Huethorst, Eline (2022) *Development of small, engineered heart tissues and their acute response to implantation.* PhD thesis.

http://theses.gla.ac.uk/82668/

Development of small, engineered heart tissues and their acute response to implantation.

Eline Huethorst
BSc, MSc, MRes

Submitted in the fulfilment of the requirements for the degree of Doctor of Philosophy

January 2022

Institute of Cardiovascular and Medical Sciences
College of Medical, Veterinary and Life Sciences
University of Glasgow

Abstract

Introduction: Human induced pluripotent stem cell derived cardiomyocytes (hiPSC-CMs) are a great source of human cardiac cells and can be combined with biomaterials to form engineered heart tissues (EHTs). Implantation of EHTs into the myocardium after a myocardial infarction (MI) is a promising strategy to regenerate the scar area. However, the ongoing challenge is the lack of electrical and mechanical coupling of the graft to the host tissue. Moreover, to replace the number of lost cells after an MI, current EHTs are large (cm-scale) and consist of >10^7 cells, resulting in extremely high costs. Therefore, the aim of this study was to develop a cost-efficient platform based on the implantation of small EHTs (<50,000 hiPSC-CMs) grafted into the rabbit myocardium *in vitro*, and subsequently to assess the electrophysiological adaptations of the hiPSC-CMs to the surrounding myocardium using of fluorescent indicators.

Methods: The EHTs (mm-scale) consisted of commercially available hiPSC-CMs (45.000 cells) seeded on top of a recombinant collagen-like peptide hydrogel (22 kPa; 6 mm diameter; 350 µm thick). Excitation-contraction coupling (ECC) properties of the EHTs were assessed *in vitro*. Adult male rabbits were euthanized and, subsequently, the heart was excised and placed on a Langendorff rig. EHTs were stained a fluorescent calcium indicator prior to implantation to track their activity. Calcium traces of the EHT and the ECG of the rabbit heart were compared during analysis.

Results: Incorporation of fibronectin into the hydrogel improved cell adhesion and resulted in viable EHTs for at least 7 days. EHTs were not able to follow high pacing frequencies comparable to the intrinsic rate of the rabbit heart, most likely because of slower calcium handling. HiPSC-CMs seeded on the hydrogel showed an improved (“twitch”-like) contraction profile in comparison to cells seeded on rigid matrixes that showed a multi-phasic time-course. Once implanted, EHTs were viable for at least 90 min and calcium transients could be recorded for this time, however, there were no signs of electrical coupling during the experiment.

Conclusion: With this work, a novel *ex vivo* platform has been developed to investigate functionality of implanted cells within the myocardium in the acute phase post-implantation. This platform can be used to investigate many factors that might affect the integration and survival of implanted cells during the acute phase in a cost-effective way and is therefore a good intermediate step between *in vitro* and *in vivo* experiments.

Table of Contents

Abstract ii
List of Tables x
List of Figures xi
Acknowledgements xiii
Author's declarations xv
Publications and abstracts xv
  Published: xv
  Conference abstracts: xv
  Manuscript in preparation: xv
List of abbreviations xvi
Chapter 1 Introduction 1
  1.1 Healthy cardiac physiology 2
    1.1.1 Cardiac anatomy 2
    1.1.2 Electrical conductivity within the heart 3
    1.1.3 Extracellular matrix deposition within the heart 4
  1.2 Physiology of cardiac cells 5
    1.2.1 Morphology 5
    1.2.2 Excitation contraction coupling 7
    1.2.3 Cell-cell interactions 9
    1.2.4 Cell-ECM interactions 10
    1.2.5 Mechano-chemo-transduction 11
  1.3 Human induced pluripotent stem cell-derived cardiomyocytes – an alternative cell source 11
    1.3.1 The origin of induced pluripotent stem cells 11
    1.3.2 Differentiation of hiPSCs into hiPSC-derived cardiomyocytes 12
    1.3.3 The immature phenotype of HiPSC-CMs 13
    1.3.4 HiPSC-CM maturation 15
  1.4 Myocardial infarction 16
    1.4.1 Myocardial infarction in humans 16
    1.4.2 Animal models for myocardial infarction 18
  1.5 Cardiac regeneration 19
    1.5.1 General concept 19
    1.5.2 Main challenges of cardiac regeneration 20
    1.5.3 Delivery of cells into the heart 21
  1.6 The EHT design: the best of both worlds? 23
  1.7 A novel platform to investigate EHT integration 24
  1.8 Monitoring the EHT post-implantation 24

1.9 Aims of this thesis 25
1.9.1 Main aim and objectives 25
1.9.2 Multiphasic contractile behaviour – A second theme throughout the chapters 26
1.9.3 Short overview of the chapters 26
Chapter 2 General methods 27
2.1 Cell culture 28
2.1.1 The cardiac cell source - rationale 28
2.1.2 Commercially available hiPSC-CMs 29
2.1.3 Discontinuation of Cor.4U (NCardia) hiPSC-CMs 30
2.1.4 ECM coatings to promote cell adhesion 31
2.1.5 Serum-free medium 33
2.2 Fluorescent Imaging 34
2.2.1 Optics 34
2.2.2 Voltage sensitive dyes 34
2.2.3 Genetically encoded calcium indicators 37
2.2.4 Fluorescent calcium dyes 40
2.2.5 Dual fluorescent imaging with voltage- and calcium dyes 43
2.3 CellOPTIQ: Voltage, calcium and contractility in one system 45
2.3.1 Background 45
2.3.2 Fluorescence signals representing APs and CaTs 46
2.3.3 Contractility recordings 47
2.3.4 Measuring voltage, calcium and contractility simultaneously 47
2.4 Intact rabbit heart experiments 49
2.4.1 Animals 49
2.4.2 Langendorff perfusion set-up 49
2.4.3 Tyrode’s solution 51
2.4.4 Measuring $\text{Time}_{R\text{-}T}$ from unpaced and paced rabbit hearts 52
2.5 Fluorescent immunochemistry 53
2.6 Statistical analysis 56
Chapter 3 Development of 2D hiPSC-CM patches 57
3.1 Introduction 58
3.1.1 Specific aims 59
3.2 Methods 60
3.2.1 Creation of small 2D micro-patches 60
3.2.2 Fabrication of stencils 60
3.2.3 hiPSC-CM seeding into stencils 62
3.2.4 Assessment of 2D patch morphology 63
3.2.5 Contractility recordings 64

3.3 Results 66
3.3.1 Morphology of 2D micro-patches 66
3.3.2 Morphology of the 2D micro-patches 67
3.3.3 2D patch functionality 69
3.3.4 Comparison of two commercially available hiPSC-CM lines. 75
3.3.5 Contractility but not voltage signals, from hiPSC-CMs vary across a monolayer 76
3.3.6 Spatiotemporal analysis reveals local variations and complexity of movement 77
3.4 Discussion and conclusion 82
3.4.1 Silicone stencils as a mould for small cardiac patches 82
3.4.2 Novel application of the MM contractility tool 82
3.4.3 Complex contractile behaviour observed in hiPSC-CM monolayers is probably of mechanical origin 83
3.4.4 Overall conclusion 84
Chapter 4 Detachment of the 2D hiPSC-CM monolayers as a building block for EHTs 85
4.1 Introduction 86
4.1.1 Background 86
4.1.2 Specific aims 88
4.2 Chapter specific methods 88
4.2.1 Thermosensitive dishes with PIPAAm coating 88
4.2.2 HiPSC-CMs culture protocol 88
4.2.3 Methods for transferring the monolayer 89
4.2.4 Assessment of contractility and electrophysiology 90
4.3 Results 90
4.3.1 Using a thermosensitive culture dish to detach intact hiPSC-CM monolayers 90
4.3.2 Contractile behaviour of the micro-patches before, during and after transfer 93
4.3.3 Voltage recordings from transferred micro patches one week after transfer 99
4.4 Conclusion and discussion 99
4.4.1 Thermoresponsive dishes to create free floating hiPSC-CM sheets . 99
4.4.2 The effect of cold temperatures on the hiPSC-CMs 100
4.4.3 Comparing the two different detachment methods. 101
4.4.4 Other applications with PIPAAm 103
4.4.5 Physiology of free-floating monolayers 103
Chapter 5 Properties of EHTs with a support structure made of recombinant collagen-like peptide hydrogel support structure 105
5.1 Introduction 106

5.1.1 Aims 108
5.2 Chapter specific methods 109
5.2.1 RCP-MA hydrogel synthesis 109
5.2.2 Cell seeding on top of the hydrogel...................................110
5.2.3 ß-adrenergic stimulation of hiPSC-CMs 111
5.2.4 RNA isolation and qRT-PCR...112
5.3 Results 113
5.3.1 RCP-MA synthesis and properties......................................113
5.3.2 Development of a method to create the ideal support structure ..113
5.3.3 Cor.4U cells but not CDI cells attach to the RCP-MA hydrogel......115
5.3.4 Optimizing the RCP-MA hydrogel 116
5.3.5 EHT functionality measurements.......................................120
5.3.6 HiPSC-CM contractility on flexible substrates is comparable to those seeded on glass...122
5.3.7 Single hiPSC-CM only show twitch-like contraction profiles independent on substrate stiffness..124
5.3.8 Effect of inotropic intervention 126
5.3.9 The relationship between substrate stiffness and stress-activated pathways 127
5.3.10 Computational model to investigate the biological findings......129
5.4 Discussion and conclusion 129
5.4.1 Different hydrogel stiffnesses 130
5.4.2 Contraction time-course changes on flexible substrates 130
5.4.3 Responses of hiPSC-CMs to ISO on rigid and flexible substrates 131
5.4.4 Overall conclusion and future implications...........................132
Chapter 6 EHT implantation: Optimization of implantation techniques 133
6.1 Introduction 134
6.1.1 Aims and sub-aims...136
6.2 Chapter specific materials and methods 136
6.2.1 Loading the intact rabbit heart with FluoVolt 136
6.2.2 EHT culture 137
6.2.3 Intramyocardial implantation of EHTs.................................137
6.3 Results 138
6.3.1 Choosing the most suitable calcium indicator: Cal520-AM vs Cal590-AM 138
6.3.2 Relation between calcium transient and APD_{90} in hiPSC-CMs *in vitro* 141
6.3.3 Staining the intact rabbit heart with the fluorescent voltage sensitive dye FluoVolt 146
6.3.4 Electrophysiology of the intact rabbit heart: ECG vs APs 149

6.3.5 The gradual optimization of the EHT implantation procedure......154
6.3.6 Implanting Cal520 loaded EHTs into the myocardium................157
6.4 Conclusion and discussion..161
6.4.1 Dual imaging of Cal590-AM and FV only achieved *in vitro*, not *in vivo* 162
6.4.2 The use of Time$_{R-T}$ as a placeholder for APD values..................163
6.4.3 The change in AP shape and amplitude post-incision................163
6.4.4 The ability of hiPSC-CMs to follow high pacing frequencies.........164
6.4.5 Limitation...166
Chapter 7 General discussion..167
7.1 The impact of the COVID-19 pandemic.....................................168
7.2 The development of small micro-patches. 168
7.3 Assessment of the effects of detachment and transfer of small monolayers 170
7.4 The use of a biomaterial as support structure for cell delivery 171
7.5 The establishment of an optical set-up to monitor the EHT post-implantation using fluorescent dyes 171
7.6 Optimization of the implantation technique 172
7.7 Inability of the human EHT to follow high pacing frequencies of the rabbit myocardium 173
7.8 Limitations...174
7.8.1 Recording signals from one EHT per experiment 174
7.8.2 Estimation of APD$_{90}$ values 174
7.8.3 Fluorescent dyes are only viable short-term 175
7.8.4 Elimination of contraction through contraction uncouplers.........175
7.8.5 Limitations of the Langendorff perfusion system......................175
7.9 Future directions 176
7.10 Multiphasic contractile behaviour – A second theme throughout the chapters...177
Final conclusion...177
Chapter 8 Appendix..178
8.1 Computational model to investigate the biological findings of the multiphasic contractile behaviour of hiPSC-CMs on rigid surfaces 179
8.1.1 Introduction 179
8.1.2 Mathematical model 181
8.1.3 Results...182
8.1.4 Conclusion and discussion 187
8.2 Cardiac differentiation of hiPSCs (Secondment in the Sullivan's Lab, Oslo, Norway) 188
8.2.1 Introduction 188
8.2.2 Methods 189

8.2.3 Results..195
8.2.4 Discussion and conclusion 199
Reference list 200

List of Tables

TABLE 2.1 LIST OF ECM PROTEINS TO PROMOTE CELL ADHESION. 32
TABLE 2.2 BMCC COMPOSITION 33
TABLE 2.3 SPECIFICS OF FLUORESCENT CALCIUM INDICATORS 43
TABLE 2.4 TYRODE'S SOLUTION COMPOSITION 52
TABLE 2.5 OVERVIEW OF USED ANTIBODIES AND PROBES 55
TABLE 2.6 OVERVIEW OF OBJECTIVES USED ON THE EVOS MICROSCOPE AND CELLOPTIQ 56
TABLE 3.1 OVERVIEW OF CELL NUMBER FOR COR.4U (NCARDIA) AND ICELL/ICELL^2 (FCDI) HIPSC-CM SEEDING INTO STENCILS. 62
TABLE 3.2 ELECTROPHYSIOLOGY OF COR.4U HIPSC-CM SEEDED IN STENCILS OF 1 2 OR 3 MM AND IN DIFFERENT CELL DENSITIES (100,000, 200,000 OR 400,000 CELLS/CM^2). 71
TABLE 3.3 CONTRACTILITY VALUES COR.4U HIPSC-CMS SEEDED IN STENCILS OF VARIOUS DIAMETER (1, 2 AND 3 MM). 74
TABLE 4.1 SUCCESS RATE WHEN USING THE FORCE PIPETTING METHOD TO TRANSFER 3 MM 2D MONOLAYERS. 91
TABLE 6.1 AVERAGE VALUES OF APS AND CORRESPONDING CALCIUM TRANSIENTS IN HIPSC-CMS PACED AT DIFFERENT PACING FREQUENCIES. 145
TABLE 6.2 APD_{90}/CAT_X RATIO'S FOR HIPSC-CMS. 145
TABLE 6.3 LOOKUP TABLE FOR FORMULAS TO CALCULATE THE APD_{90} FROM THE CAT_{50} FOR VARIOUS PACING FREQUENCIES OR CYCLE LENGTHS. 146
TABLE 6.4 AVERAGE VALUES OF TIMER-T AND APD50 TO APD90 AT DIFFERENT PACING FREQUENCIES (IN MS). 152
TABLE 6.5 THE RATIO BETWEEN APD AND $TIME_{R-T}$ FOR EVERY PACING FREQUENCY AND IR. 152
TABLE 6.6 IMPLANTATION CRITERIA FOR EVALUATING IMPLANTATION SUCCESS. 155
TABLE 8.1 COMPONENTS OF E8 CULTURE MEDIUM (200 ML). 190
TABLE 8.2 PRIMARY AND SECONDARY ANTIBODIES 193
TABLE 8.3 OVERVIEW OF GENES FOR RT-QPCR 194
TABLE 8.4 SELECTED PRIMERS FOR RT-QPCR 194

List of Figures

FIGURE 1.1 CARDIAC ANATOMY. 3
FIGURE 1.2 BASIC DIAGRAM SHOWING KEY ORGANELLES OF A CARDIOMYOCYTES AND EXCITATION CONTRACTION COUPLING. 6
FIGURE 1.3 ION CHANNEL ACTIVATION IN A) NODAL CELLS AND B) VENTRICULAR CARDIOMYOCYTES. 8
FIGURE 1.4 SARCOMERE SHORTENING........9
FIGURE 1.5 MORPHOLOGY OF CARDIAC CELLS. 14
FIGURE 2.1 EXCITATION/EMISSION SPECTRA OF VARIOUS VOLTAGE SENSITIVE DYES (A) AND CALCIUM INDICATORS (B). 36
FIGURE 2.2 DIAGRAM SHOWING THE ACTIVATION OF GCAMP. 38
FIGURE 2.3 CONFOCAL IMAGES SHOWING FROM HIPSC-CMS TRANSFECTED WITH AAV6-CMV-GCAMP-6F. 39
FIGURE 2.4 FLUO-4 BRIGHTNESS OVER TIME. 41
FIGURE 2.5 GCAMP-6F VS FLUO-4 SIGNALS RECORDED ON THE CELLOPTIQ SYSTEM. 41
FIGURE 2.6 COMBINED EX/EM SPECTRA OF FLUOVOLT AND CAL590-AM. 44
FIGURE 2.7 DIAGRAM SHOWING THE FILTER SET FOR FLUORESCENT IMAGING OF CAL520, FLUOVOLT AND CAL590. 45
FIGURE 2.8 VOLTAGE, CALCIUM AND CONTRACTILITY PARAMETERS EXPLAINED. 46
FIGURE 2.9 SIMULTANEOUS RECORDED VOLTAGE, CALCIUM AND CONTRACTILITY TRACES. 48
FIGURE 2.10 LANGENDORFF PERFUSION SET-UP. 50
FIGURE 2.11 METHOD OF CALCULATING TIME R-T. 52
FIGURE 3.1 MANUFACTURING OF SILICONE STENCILS. 61
FIGURE 3.2 DIAGRAM SHOWING THE PROCEDURE OF SEEDING HIPSC-CMS INTO STENCILS IN COMPARISON TO THE CONTROL, WHICH IS A STANDARD 96 WELL-PLATE. 62
FIGURE 3.3 SPATIOTEMPORAL ANALYSIS OF THE TOTAL HIPSC-CMS MONOLAYER. 65
FIGURE 3.4 SUCCESS RATE OF THE USE OF 1 MM, 2 MM AND 3 MM STENCILS TO CREATE SMALL 2D HIPSC-CM MONOLAYERS. 67
FIGURE 3.5 IMMUNO-HISTOCHEMISTRY FOR F-ACTIN (GREEN) AND DNA (DAPI, BLUE) OF MONOLAYERS FROM DIFFERENT CELL DENSITIES AND DIAMETERS. 68
FIGURE 3.6. THE MORPHOLOGY OF SMALL CARDIAC PATCHES MADE WITH DIFFERENT STENCIL SIZES (1, 2 AND 3 MM) AND CELL DENSITIES (1X 2X AND 4X). 69
FIGURE 3.7 EFFECT OF CENTRIFUGING HIPSC-CMS ON THEIR PHYSIOLOGY. 70
FIGURE 3.8 GENE EXPRESSION PROFILES OF VARIOUS GENES CODING FOR ION CHANNELS. 72
FIGURE 3.9 COMPARISON OF ELECTROPHYSIOLOGY BETWEEN HIPSC-CMS PATCHES OF COR.4U (NCARDIA, DARK GREY) AND ICELL^2 (FCDI, LIGHT GREY) HIPSC-CMS. 76
FIGURE 3.10 COMPARISON OF CONTRACTILITY PARAMETERS BETWEEN HIPSC-CMS PATCHES OF COR.4U (NCARDIA, DARK GREY) AND ICELL^2 (FCDI, LIGHT GREY) HIPSC-CMS. 76
FIGURE 3.11 CONTRACTILITY, BUT NOT VOLTAGE SIGNALS, FROM HIPSC-CMS VARY ACROSS A MONOLAYER. 77
FIGURE 3.12 SPATIOTEMPORAL ANALYSIS OF CONTRACTILE BEHAVIOUR OF HIPSC-CMS REVEALS LOCAL VARIATIONS OF MOVEMENT. 79
FIGURE 3.13 CELL DENSITY DOES NOT MODULATE THE COMPLEX CONTRACTILE BEHAVIOUR ON FIXED SUBSTRATES. 80
FIGURE 3.14 ISOLATED CELLS ONLY SHOW SINGLE CONTRACTION PROFILES. 81
FIGURE 4.1 PIPAAM COATING THERMORESPONSIVE CULTURE DISH. 87
FIGURE 4.2 ANIMATION EXPLAINING THE EXPERIMENTAL CELL-DETACHMENT PROCEDURE. 89
FIGURE 4.3 BRIGHTFIELD AND FLUORESCENT IMMUNOCHEMISTRY IMAGES OF TRANSFERRED MONOLAYERS. 92
FIGURE 4.4 BRIGHTFIELD IMAGES SHOWING THE MORPHOLOGY OF MONOLAYERS BEFORE, DURING AND AFTER DETACHMENT FROM THE RIGID SUBSTRATE. 93
FIGURE 4.5 THE SPONTANEOUS BEATING FREQUENCY OF A) ALL TRANSFERRED MONOLAYERS OR B) ONLY MONOLAYERS WITH SPONTANEOUS BEATING ACTIVITY. 94
FIGURE 4.6 THE CONTRACTILE BEHAVIOUR MEASURED FROM THE WHOLE MONOLAYER. 95
FIGURE 4.7 THE CHANGE IN CONTRACTILITY TRANSIENTS OVER TIME, BEFORE, DURING AND AFTER TRANSFER. 96
FIGURE 4.8 SPATIOTEMPORAL ANALYSIS OF CONTRACTILITY OF MONOLAYERS ATTACHED AND DETACHED TO RIGID SURFACES. 97
FIGURE 4.9 MAP ANALYSIS OF CONTRACTILITY OF MONOLAYERS DURING DETACHMENT AND ATTACHMENT TO RIGID SURFACES. 98

FIGURE 4.10 ELECTROPHYSIOLOGY OF HIPSC-CM MONOLAYERS ON DAY 7 AFTER DETACHMENT (RE-ATTACHED). 99
FIGURE 5.1 SCHEMATIC OF THE CHEMICAL REACTION OF RCP-MA CROSSLINKING. 110
FIGURE 5.2 SEEING HIPSC-CMS ON TOP OF HYDROGEL. 111
FIGURE 5.3 RCP-MA PROPERTIES AND FABRICATION. 114
FIGURE 5.4 DIFFERENCES IN CELL ADHESION BETWEEN HIPSC-CMS FROM DIFFERENT COMMERCIAL SOURCES. 116
FIGURE 5.5 INCREASING RCP-MA CONTENT (W/V) DOES NOT ENHANCE CELL ADHESION. 117
FIGURE 5.6 IMPROVEMENT OF CELL ADHESION AFTER ADDITION OF A ECM-COATING. 118
FIGURE 5.7 EFFECTS OF FN INCORPORATION INTO THE HYDROGEL IN ADDITION TO HYDROGEL COATING WITH FN. 119
FIGURE 5.8 VOLTAGE RECORDINGS OF HIPSC-CMS SEEDED ON EITHER RCP-MA$_{50}$, RCP-MA$_{100}$ OR GLASS SUBSTRATES. 120
FIGURE 5.9 CAL520 CA^{2+} RECORDINGS IN SPONTANEOUS BEATING HIPSC-CM SEEDED ON FLEXIBLE AND RIGID SUBSTRATES. 121
FIGURE 5.10 GENERAL HIPSC-CM MONOLAYER CONTRACTILITY OF CELLS SEEDED ON HYDROGEL VS GLASS. 122
FIGURE 5.11 SPATIOTEMPORAL CONTRACTILITY ANALYSIS OF HIPSC-CMS SEEDED ON RCP-MA HYDROGELS. 123
FIGURE 5.12 SPATIOTEMPORAL ANALYSIS OF HIPSC-CMS SEEDED ON FLEXIBLE VS RIGID SURFACES. 124
FIGURE 5.13 CONTRACTILITY ANALYSIS OF SINGLE CELLS SEEDED ON EITHER GLASS OR HYDROGEL (RCP-MA$_{100}$). 125
FIGURE 5.14 THE EFFECT OF ISOPRENALINE ON THE TIME-COURSE COMPLEXITY OF HIPSC-CM SEEDED ON DIFFERENT SUBSTRATE STIFFNESSES. 128
FIGURE 6.1 DIFFERENCES IN OPTICS BETWEEN A 40X OBJECTIVE AND THE LIGHT GUIDE. 139
FIGURE 6.2 CAL520 *VS* CAL590 *IN VITRO*. 140
FIGURE 6.3 MEASUREMENT OF CAL520 FLUORESCENCE ON THE CELLOPTIQ SYSTEM VS THE WHOLE HEART SET-UP. 141
FIGURE 6.4 THE ABILITY OF HIPSC-CMS TO FOLLOW HIGH PACING FREQUENCIES. 142
FIGURE 6.5 THE RELATION BETWEEN HIPSC-CM APS AND CALCIUM TRANSIENTS *IN VITRO*. 144
FIGURE 6.6 FV INCUBATION. FV WAS INCUBATED FOR 20 MIN USING A RECIRCULATION METHOD. 147
FIGURE 6.7 THE EFFECT OF THE INCISION AND IMPLANTATION PROCEDURE ON THE AP SHAPE AND FLUORESCENCE. 148
FIGURE 6.8 EXAMPLE APS FROM THE MYOCARDIUM, BEFORE (A) AND AFTER AN INCISION (B), ALONG THE CORRESPONDING ECG. 149
FIGURE 6.9 EXAMPLE APS FROM THE RABBIT LEFT VENTRICLE. 150
FIGURE 6.10 AVERAGE TIMER-T AND APDS AT VARIOUS PACING FREQUENCIES. 151
FIGURE 6.11 THE RELATIONSHIP BETWEEN TIME$_{R-T}$ AND APD$_{90}$ OF THE RABBIT MYOCARDIUM. 151
FIGURE 6.12 SUCCESS RATE OF THE INTRAMYOCARDIAL IMPLANTATION TECHNIQUE. 154
FIGURE 6.13 OVERVIEW OF THE FINAL EHT IMPLANTATION PROTOCOL. 156
FIGURE 6.14 EXAMPLE CALCIUM TRACES OF IMPLANTED EHTS. 157
FIGURE 6.15 EHTS PERFORMANCE. 158
FIGURE 6.16 THE CHANGE IN TIME$_{R-T}$ AND CAT$_{50}$ DURING THE COURSE OF THE EXPERIMENT, MEASURED FROM THE RABBIT ECG AND EHT, RESPECTIVELY. 160
FIGURE 6.17 APD$_{90}$ VALUES OF EHT AND LV DO CONVERGE BUT DO NOT OVERLAP. 161
FIGURE 8.1 DIAGRAMS SHOWING THE MODEL FOR THE CELL ARRANGEMENT ON THE STIFF (A) AND SOFT (B) SUBSTRATES. 179
FIGURE 8.2 MATHEMATICAL MODEL SPECIFICS. 180
FIGURE 8.3 (PREVIOUS PAGE) THE EFFECT OF VARIATION IN INTRACELLULAR CALCIUM AND NUMBER OF CONTRACTILE UNITS ON THE COMPUTED MOTION BY THE MODEL PRESENTED. 185
FIGURE 8.4 COMPUTATIONAL MODEL SHOWING THE COMPLEX CONTRACTILE BEHAVIOUR AS SEEN IN BIOLOGICAL SAMPLES. 186
FIGURE 8.5 DIFFERENTIATION OF FIBROBLASTS TOWARDS HIPSCS AND HIPSC-CM MAINTENANCE. 190
FIGURE 8.6 DIFFERENTIATION PROTOCOL AS DESCRIBED BY LIAN ET AL. 191
FIGURE 8.7 IMMUNOFLUORESCENT STAINING FOR STEM CELL MARKERS. 195
FIGURE 8.8 ASSESSMENT OF THREE DIFFERENT CELL SEEDING DENSITIES AS PREPARATION FOR HIPSC DIFFERENTIATION TOWARDS CMS. 196
FIGURE 8.9 ASSESSMENT OF THREE DIFFERENT CHIR CONCENTRATIONS AND CELL SEEDING DENSITIES. 197
FIGURE 8.10 BRIGHTFIELD IMAGES OF REPLATED HIPSC-CMS. 198
FIGURE 8.11 OVERVIEW OF HIPSC AND HIPSC-CM DIFFERENTIATION AND REPLATING PROCESSES. 199

Acknowledgements

As this thesis is written up, and my PhD comes to an end, it is time to thank those who I could not have done this without.

First of all, I would like to show my gratitude my supervisors Prof. Godfrey Smith and Prof. Nikolaj Gadegaard for their supervision and advice throughout this project. A special thanks to Prof. Smith, who is an inspiration and who has guided me through my personal development as a scientist. I cannot thank you enough.

Also a big, big thanks to Dr. Francis Burton for helping me with the data analysis and advice on the majority of my experiments.

This whole journey would not have been the same without my lab mates, Quentin, Sara, Alessandro, Miriam, Annabel and Aline. Furthermore, I would like to thank everybody from the Smith lab for all the help and motivation. Especially the (scientific) discussions over lunch, the inside jokes, personalized memes and extra-curricular experiments. I feel like I have made friends for a lifetime.

Also, a special thanks to the technical staff, Aileen and Mike, who I could always turn to with questions and request. Like magic, they would always find and retrieve a very useful piece of equipment from a random location somewhere in the lab if I needed it.

Also, a massive thank you to my dearest lab friends from the BIG lab, Marie and Iliyana, who both have great minds and spirits. Their attitude towards science sets an example and their craziness is contagious.

I am very grateful for all the dearest friends in the Netherlands that kept in touch through all those years while I was in Scotland. Your support in the form of texts, calls, cards, visits and presents was of immense value and I cannot thank them enough. To my oldest friends who I know for the better part of my life: Nynke and Liesbeth. To the gang from undergrad: Angela, Marloes, Eva, Lizette, Floor and Joyce. And to my travel buddy and bunny admirer: Esther.

Also, the biggest thanks to my love Angel. Even though you were only around for the last years of my PhD, these where the hardest. So, thank you for being my rock and sticking around through my crazy times.

And last but not least, I would like to say a massive thank you to my parents, Jacqueline and Rene, and my sister Lisanne, who have supported, motivated and guided me throughout my whole life and who were there for me in during the happy and difficult times. I literally could not have done this without them. And after almost 5 years of living here, I think my parents love Scotland even more than I do.

Author's declarations

The work presented in this thesis is original and my own except where otherwise acknowledged. None of the work presented has been submitted for the fulfilment of any other degree. Some results during the period of research have been published in a peer reviewed journal or presented in abstract form and are detailed below.

Publications and abstracts

Published:

1. Huethorst E, Cutiongco MF, Campbell FA, Saeed A, Love R, Reynolds PM, et al. Customizable, engineered substrates for rapid screening of cellular cues. Biofabrication. 2020 Feb 7;12(2):025009. PubMed PMID: 31783378. Epub 2019/11/30. eng.

2. Huethorst, E., Mortensen, P., Simitev, R. D., Gao, H., Pohjolainen, L., Talman, V., Ruskoaho, H., Burton, F. L., Gadegaard, N. & Smith, G. L. 2021. Conventional rigid 2D substrates cause complex contractile signals in monolayers of human induced pluripotent stem cell-derived cardiomyocytes. The Journal of Physiology, 2021, n/a. https://physoc.onlinelibrary.wiley.com/doi/full/10.1113/JP282228

Conference abstracts:

1. Eline Huethorst* 1, 2, Francis Burton2, Nikolaj Gadegaard1, Godfrey Smith2. Substrate flexibility ameliorates the contraction-relaxation cycle in human iPSC derived cardiomyocytes. World BIomaterials Congress 2020. Virtual congress. WBC2020-2626.

2. Huethorst E, Burton FL, Gadegaard N, Smith GL. Flexible Substrate is Key to Appropriate Contractile Behaviour of hiPSC Derived Cardiomyocytes. Biophysical Journal. 2020 2020/02/07/;118(3, Supplement 1):326a-7a.

3. Huethorst E, Burton F, Gadegaard N, Smith G. Substrate affects contractile behaviour of hiPSC derived cardiomyocytes. Physiology 2019; Aberdeen, UK: The Physiological Society; 2019.

Manuscript in preparation:

Planned

1. E Huethorst, A Kelly, A Campbell, F. Burton, G Smith. Acute integration of small EHTs into the rabbit myocardium. Planned.

List of abbreviations

AP	Action potential
APD	Action potential duration
APD_{50}	Action potential duration at 50% repolarisation
APD_{75}	Action potential duration at 75% repolarisation
APD_{90}	Action potential duration at 90% repolarisation
BMCC	Bohlen Modified Complete Culture
BSA	Bovine serum albumin
CaT	Calcium transient
CaT_{50}	Calcium transient width at 50% of the amplitude
CaT_{60}	Calcium transient width at 60% of the amplitude
CaT_{70}	Calcium transient width at 70% of the amplitude
CaT_{75}	Calcium transient width at 75% of the amplitude
CaT_{80}	Calcium transient width at 80% of the amplitude
CaT_{90}	Calcium transient width at 90% of the amplitude
CD	Contraction duration
CICR	Ca^{2+} induced Ca^{2+} release
CL	Cycle length
CM	Cardiomyocyte
DI	Diastolic interval (= CL – APD_{90})
Di-4-ANEPPS	Di-4-butyl-amino-naphthyl-ethylene-pyridinium propyl-sulfonate
DMEM	Dulbecco's Modified Eagle Medium
DMSO	Dimethyl sulphoxide
Dn_{90}	90% of contraction relaxation
ECC	Excitation-contraction coupling
ECG	Electrocardiogram
ECM	Extracellular matrix
EHT	Engineered heart tissue
EMA	European Medicines Agency
ESC	Embryonic stem cell
Ex/Em	Excitation/emission spectrum
FDA	Food and Drug Administration

FCDI	FUJIFILM Cellular Dynamics, Inc.
FoV	Field of view
FN	Fibronectin
FS	Fractional shortening
FV	FluoVolt
hERG	human *Ether-a-go-go*-related gene
hESC-CM	human embryonic stem cell derived cardiomyocytes
hiPSC-CM	human induced pluripotent stem cell derived cardiomyocyte
HR	Heart rate
$I_{Ca\text{-}L}$	L-type Ca^{2+} current
IR	Intrinsic rate
ISO	Isoprenaline
LA	Left atrium
LAD	Left anterior descending artery
LAP	Lithium phenyl(2,4,6-trimethybenzoyl) phosphinate
LED	Light-emitting diode
LTCC	L-type Ca^{2+} channel
LV	Left ventricle
MM	MUSCLEMOTION algorithm
NA	Numerical aperture
NCX	Na^{2+}/Ca^{2+} exchanger
PBS	Phosphate buffered saline
$PBS^{-/-}$	Phosphate buffered saline without Mg^{2+} and Ca^{2+}
$PBS^{+/+}$	Phosphate buffered saline with Mg^{2+} and Ca^{2+}
PDMS	Polydimethylsiloxane
PIPAAm or PNIPAM	Poly(N-isopropyl acrylamide)
PFA	Paraformaldehyde
PMT	Photomultiplier tube
PRRP	Post repolarisation refractory period
PSC	Pluripotent stem cell
PVDF	Poly-vinylidene difluoride
RA	Right atrium
RCP-MA	Methacrylated recombinant collagen-like peptide
RGD	Arg-Gly-Asp tripeptide (cell adhesion moiety)
RT	Room temperature

RV	Right ventricle
RyR	Ryanodine receptor
SERCA	Sarco-endoplasmic reticulum Ca^{2+}-ATPase
SNR	Signal-to-noise-ratio
SR	Sarcoplasmic reticulum
TCP	Tissue culture plastic
$Time_{R-T}$	Time (ms) between the R and T wave of the ECG
TRise	Upstroke time (ms) from 10% to 90% depolarisation
TTP	Time to peak contraction
T_x	Transplantation
Up_{90}	Time to 90% contraction
VT	Ventricular tachycardia
V_m	Membrane voltage
WD	Working distance

Chapter 1 Introduction

1.1 Healthy cardiac physiology

1.1.1 Cardiac anatomy

The myocardium of the heart is a highly organized tissue that has the vital function of pumping blood to peripheral tissues of the body. The two linked chambers (atrium and the ventricle), are positioned on either side of the heart, separated by the septum in the centre (Figure 1.1A and B). All large blood vessels, which include the aorta, the pulmonary vein, the pulmonary artery, and the vena cava inferior/superior are connected to the base of the heart. The apex is found distal from the cardiac base. The left side of the heart (left ventricle (LV) and left atria (LA)) provides the peripheral tissues with oxygen-rich blood, whereas the right side (right ventricle (RV) and right atria (RA)) recirculates the blood towards the lungs, where CO_2 is exchanged for O_2. Because the peripheral circulation operates at a higher arterial pressure compared to the pulmonary circulation, the myocardium of the LV is thicker and generates a higher luminal pressure compared to the RV. The left- and right coronary arteries branch of from the aorta and provide the left and right side of the heart with blood, respectively (Figure 1.1A). Additionally, the left coronary artery branches into the left anterior descending (LAD) coronary artery and the circumflex coronary artery.

Other important cardiac structures are the cardiac valves that separate the atria and ventricles (bicuspid- and mitral valve), or the ventricles with the vasculature (aortic- and pulmonary valve) so that pressure can be built-up within the ventricles (Figure 1.1B).

Finally, the myocardium forms the larger part of the contractile muscle mass. The endocardium and epicardium form the inner endothelial and outer epithelial layers, respectively, that protect the heart from sheer stresses during cyclic contraction. The electrophysiology of the endo-, myo- and epicardium is slightly different (Lachaud, 2019b, Antzelevitch and Fish, 2001, Antzelevitch et al., 1991). Additionally, CMs and ECM components are organized in a laminar fashion and radial alignment that slowly changes their direction endocardium towards to the epicardium for optimal contraction and cardiac output (Pope et al., 2008, Legrice et al., 1995). Finally, the pericardium is a thin tissue that surrounds the heart and forms an extra protective layer against sheer stresses experienced during systole and diastole.

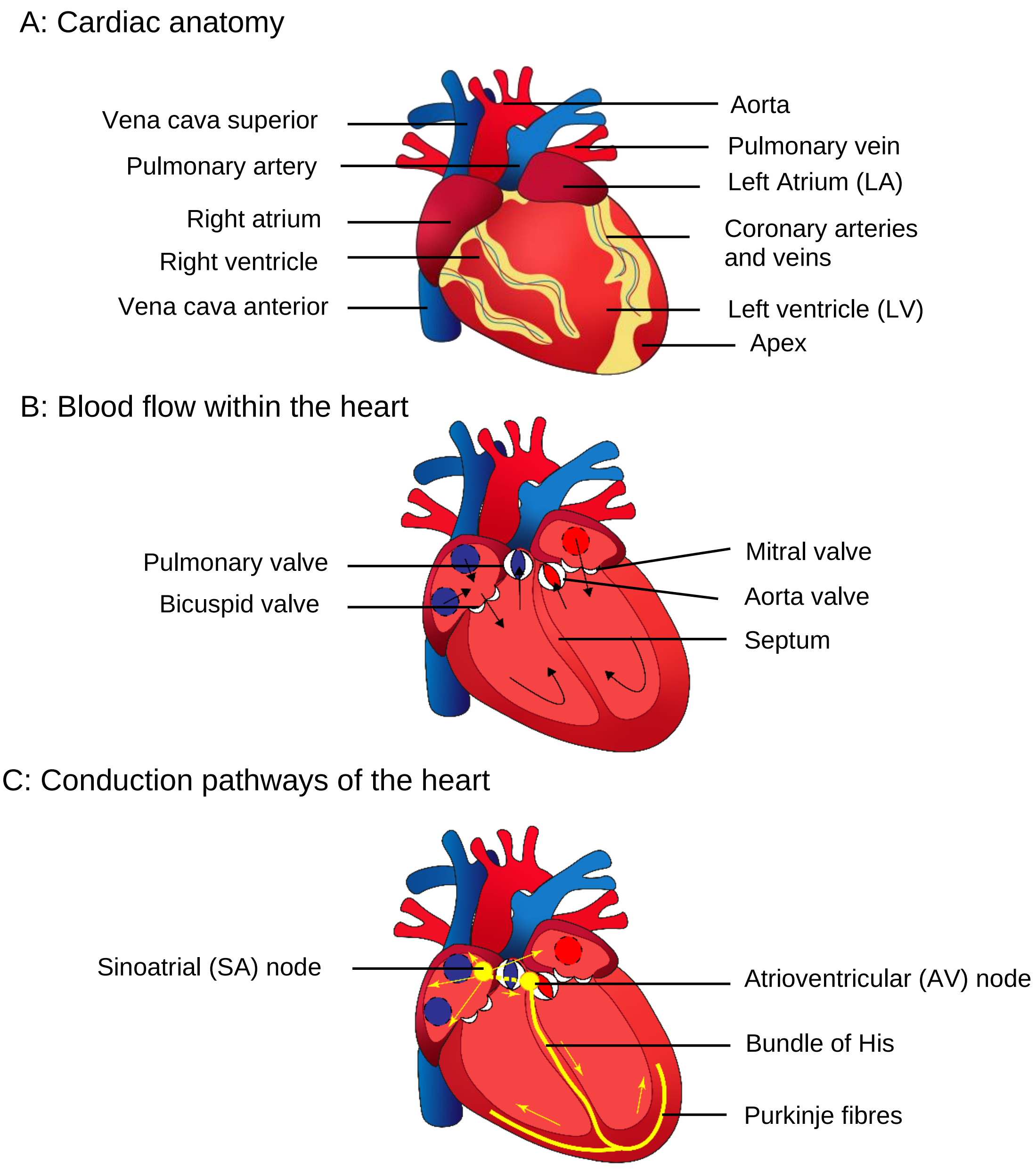

Figure 1.1 Cardiac anatomy.
A) the anatomy of the heart from the outside. B) The blood flow within the heart is regulated by valves (white). Black arrows indicate direction of blood flow. C) The conduction pathway of the heart. Yellow arrows indicate direction of conduction.

1.1.2 Electrical conductivity within the heart

The myocardium within each chamber contracts close to synchronously by orchestrated electrical pulses generated by spontaneously active pacemaker cells within the sinoatrial (SA) node, located in the right atrium (Figure 1.1C).

Pacemaker cells are innervated by the sympathetic and parasympathetic nervous system to induce a faster or slower heartbeat, respectively.

The electrical signals run from the SA node through a defined conduction system towards the peripheral cardiomyocytes (Figure 1.1C). The bundle of His functions as a primary conduction pathway and runs from the SA to the atrial-ventricular (AV) node, activating the atria simultaneously via smaller branches. The AV-node is positioned between the atria and the ventricles and assures a timed delay between the depolarization of both chambers. From here, the bundle of His branches into the left and right bundle branches, which form the main gateway for conducting the electrical pulses further towards the apex to excite the left and right ventricles, respectively. The Purkinje fibres branch from the bundle of His to electrically activate the peripheral cells within the myocardium. Depolarized CMs propagate the electrical signals by depolarizing adjacent cells through gap junctions, resulting in an orchestrated wave of depolarization and therefore contraction. The process of transforming electrical signal into contraction, also known as excitation-contraction-coupling, will be explained in more detail in paragraph 1.2.2.

1.1.3 Extracellular matrix deposition within the heart

The structural components of the cardiac extracellular matrix (ECM) changes during development to comply with the changing load of the growing heart and body, e.g. an altered matrix deposition and increased crosslinking. Collagen is the main ECM protein within the heart, but other ECM proteins, such as fibronectin (FN), laminin, proteoglycans and elastin, can also be found (Frangogiannis, 2017). Collagen is presented in the heart as fibres (collagen types 1 and 3), such as the gross ECM, or as a network (collagen type 4) such as the basal membrane. It can therefore be classified into three different components: epimysium, endomysium and the perimysium, that surround the entire muscle, individual myocytes and capillaries, and interconnecting groups of myocytes, respectively (Legrice et al., 1995, Pope et al., 2008).

The perimysium primarily defines the laminar and anisotropic 3D organisation of the CMs within the myocardium and is therefore important for the mechanical performance of the heart (Williams et al., 2014, Pope et al., 2008). Due to the mechanical differences between the RV and LV, the perimysium is different between both sides. For example, the RV contains more and larger clefts or "gaps" in between the cardiac fibres compared to the LV (Kelly et al., 2018). In contrast, the LV consists of more compact myocardium with less clefts, especially subepicardial (Pope et al., 2008). This results in extremely tight connections between the CM and ECM that can withstand higher pressures than the RV. Furthermore, the length of ECM fibres and the number of CMs per area changes gradually and inversely between the subepicardial layer, mid sections and endocardial layers (Legrice et al., 1995).

1.2 Physiology of cardiac cells

Cardiomyocytes (CMs) are the contractile cells located in the heart and form the main population of the myocardium in terms of mass. Fibroblasts, however, form the majority of the non-CM population in the heart. Other cell types that are found in the heart are macrophages, endothelial cells (vasculature) and cardiac progenitor cells.

1.2.1 Morphology

CMs are rod-shaped and elongated and are positioned in an anisotropic organization within the myocardium that benefits the efficiency of their collective contractile function. To cope with the timed beating of the heart, every CM is equipped with cell organelles that work closely together to benefit efficiency and performance.

Firstly, the sarcoplasmic reticulum (SR) functions as a reservoir for Ca^{2+}, similar to the endoplasmic reticulum (ER), which is important during excitation-contraction-coupling (ECC) (Figure 1.2)(Bers, 2002). Calcium is released from the SR into the intracellular space mainly through the ryanodine receptor (RYR) channel and is extruded from the intracellular space through the SERCA pump. Alternatively, Ca^{2+} can be transported into the cell or out of the cell through the Na^{+}/Ca^{2+}-exchanger (NCX). The process of ECC will be discussed in more detail in section 1.2.2.

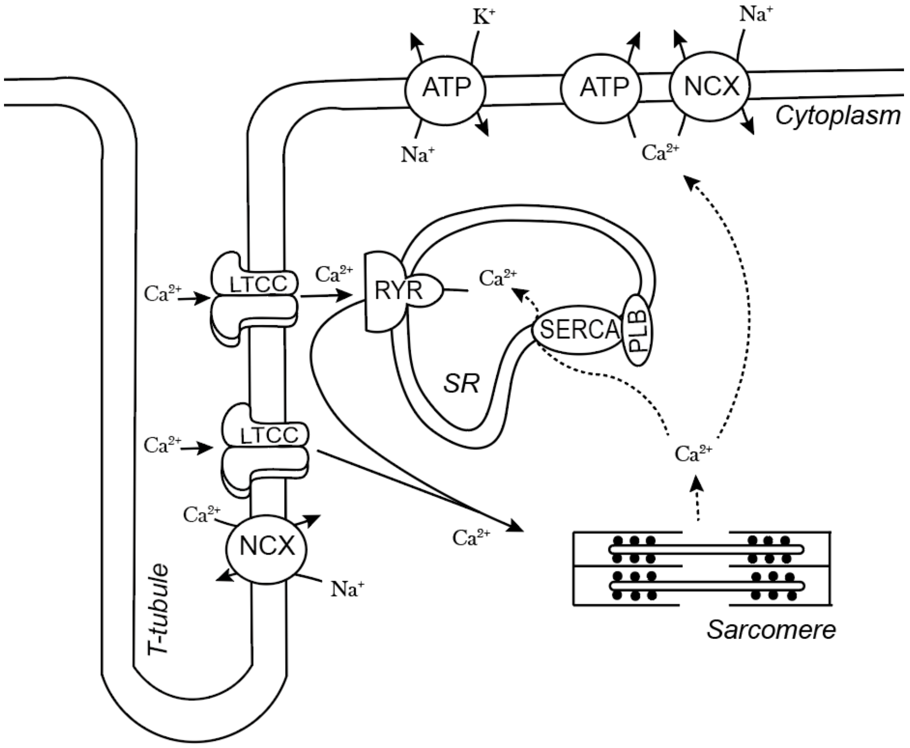

Figure 1.2 Basic diagram showing key organelles of a cardiomyocytes and excitation contraction coupling.
RYR: Ryanodine receptor. LTCC: L-Type Calcium Channel. NCX: Sodium calcium exchanger. SERCA: Sarcoplasmic/Endoplasmic Reticulum Calcium ATPase. PLB: Phospholamban. ATP: ATPase. Bold lines: calcium influx. Dashed lines: calcium efflux. The diagram design is based on a figure from the review of Bers (Bers, 2002).

Secondly, CMs have sarcomeres that function as contractile units of the cell and are aligned along the major cell axis for efficient contractility. Contraction can be defined as the shortening of the sarcomere length through transient sliding interactions between actin (thin) and myosin (thick) filaments. Myosin consists of two heavy chains and two light chains. Each heavy chain consists of a globular head region and a α-helix tail that coils around the other heavy chain, forming a dimer. The light chains are located near the neck of the heavy chain dimer, completing the myosin II molecule. Actin filaments contain tropomyosin complexes that are binding places for the globular heads of myosin and which are inhibited in the absence of Ca^{2+}. Sarcomere shortening is an active process which requires ATP and thus a CM has above average number of mitochondria within the cell. The Z-discs define the extremities of the sarcomere and consists of α-actinin. Myosin is anchored to the Z-band through the flexible molecule titin. Additionally, actin is anchored to the cell membrane through costamers and focal adhesion complexes that form the basis of rigidity sensing pathways allowing the cell to adapt to their surroundings (Pandey et al., 2018).

Thirdly, CMs have T-tubules, which are intracellular folds of the plasma membrane that bring various ion channels, such as the LTCC and the RYR, in proximity to each other to accelerate intracellular processes, including excitation contraction coupling.

1.2.2 Excitation contraction coupling

For synchronous contraction of the myocardium, rapid activation of a group of cells is needed. This process is called excitation-contraction-coupling (ECC) and consists of three main parts: 1) electrophysiology, 2) Ca^{2+} handling and 3) sarcomere shortening or contraction (Bers, 2002). These will be explained in the next section.

1.2.2.1 Electrophysiology

The membrane potential of CMs is regulated through selective permeable ion channels for Na^+, K^+ and Ca^{2+}. The magnitude of the ion current depends on the direction of ion movement into or out of the cells and varies with each ion channel type (Grant Augustus, 2009). These changes in membrane potential are illustrated in the form of an action potential (AP).

The electrical signal originates from the SA-nodes, where specialized pacemaker cells depolarize spontaneously. Their electrophysiology and AP shape are therefore slightly different from that of general ‘worker’ CMs as shown in Figure 1.3A. HCN channels are responsible for the funny (f)-current (I_f) that plays a major role in the automaticity of cardiac cells, such as immature CMs and cells located in the SA node (Mesirca et al., 2014).

During diastole, the membrane potential has a steady state of -90 mV (phase 4 Figure 1.3A) and this is maintained by the inward-rectifier potassium current (I_{k1}) through the inward-rectifier potassium channel ($K_{ir}2.1$) (Grant Augustus, 2009) (Figure 1.3B). However, if an adjacent cell depolarizes, a positive current of this cell flows through the gap junctions (connexin 43, Cx43) into this cell, causing an increase in membrane potential and, if the depolarizing threshold is reached, subsequently induces depolarization.

Under the influence of depolarised adjacent cells, the membrane potential crosses the depolarization threshold, initiating Na^{2+} influx (I_{Na}) through the voltage sensitive Na^{2+} channel $Na_V1.5$. This causes rapid depolarization of the CMs (phase 0) and the propagation of the cardiac impulse to other cells. The rapid depolarization is followed by a rapid repolarization, that marks the noticeable peak and phase 1 in the action potential (AP) of the adult ventricular CM (Figure 1.3B) (Grant Augustus, 2009). Subsequently, opening of the voltage gated L-type Calcium channel ($I_{Ca,L}$, LTCC) causes a balance between the influx through the LTCC and efflux that results in a plateau phase (phase 2). Finally, opening of the I_{kr} and I_{k1} channels enhances the efflux of potassium ions, resulting in repolarization (phase 3).

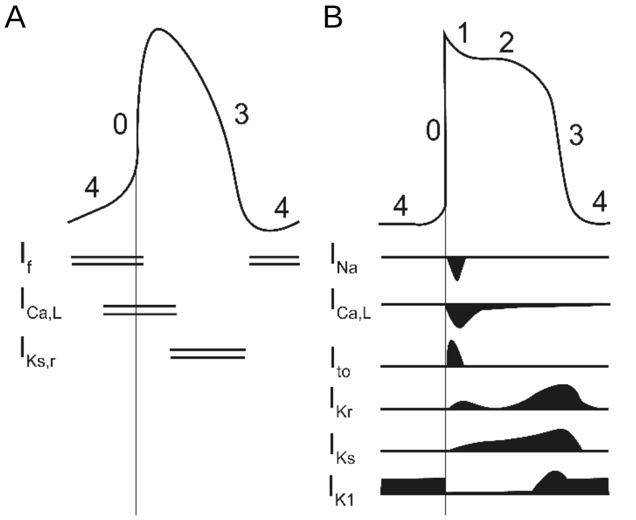

Figure 1.3 Ion channel activation in A) nodal cells and B) ventricular cardiomyocytes. Vertical line indicates rapid depolarization. Horizontal lines in (A) indicate opening of ion channels. The diagram design is based on a figure of Grant et al. (Grant Augustus, 2009).

1.2.2.2 Calcium handling

Voltage sensitive ion channels, such as the L-type Ca^{2+} channel (LTCC), are located on the cell membrane and within T-tubules, internal folds of cell membrane (Figure 1.2). LTCCs activated upon changes in membrane potential, followed by a small influx of Ca^{2+} that consequently activates the ryanodine receptor (RYR2) that is located on the SR. The space in between the LTCC and RYR2 is called the dyad and is important for efficient ECC.

The activation of RYR2 with the small influx of Ca^{2+} initiates a larger influx of Ca^{2+} from the SR into the cytoplasm (Figure 1.2). The increase in intracellular Ca^{2+} enhances binding of Ca^{2+} to the troponin complexes on the actin filaments, initiating conformational changes within this complex that unblock the binding site for the myosin head. Consequentially, myosin binds to actin, followed by sarcomere shortening. During relaxation, Ca^{2+} is actively extruded from the cytoplasm through the sarcoplasmic reticulum Ca^{2+}-ATPase (SERCA) pump on the SR and the Na^{2+}/Ca^{2+} exchanger (NCX) on the plasma membrane.

1.2.2.3 Sarcomere shortening

Binding of Ca^{2+} to the troponin complexes on the actin filaments causes conformational changes within this complex that unblock the binding site for the myosin. Consequentially, the globular head of myosin binds to the tropomyosin region on the actin filament, whereafter hydrolyzation of ATP by myosin drives conformational changes, resulting in the movement of myosin heads along the actin filament, creating a sliding motion, decreasing the distance between Z-lines and therefore decreasing sarcomere length.

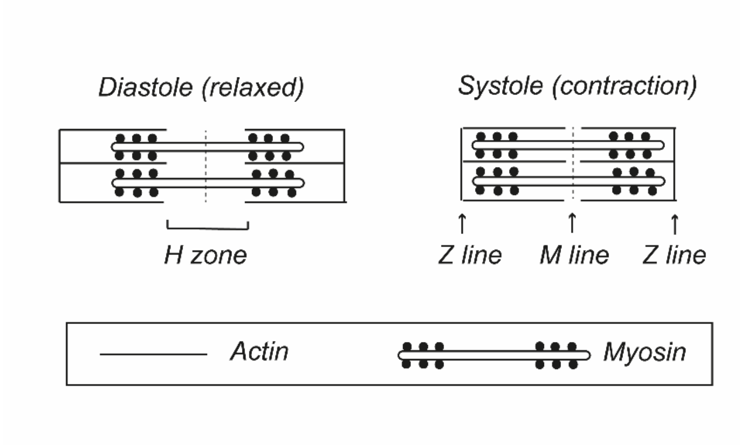

Figure 1.4 Sarcomere shortening

1.2.3 Cell-cell interactions

CMs are interconnected through intercalated discs (IDs), a staircase-like organization that can be found at the transverse ends of the cells (Manring et al., 2018, Vermij et al., 2017). The IDs form the basis for electrical and mechanical crosstalk between cells and consists of three main junctional complexes: the desmosomal junctions, adherens junctions and gap junctions. Desmosomal junctions provide structural support during the stresses encountered during every contraction-relaxation cycle and is thus important for tissue integrity. The adherens junctions function as stress receptors by facilitating the transmission of contractile forces between myocytes. Finally, the gap junctions are pores that directly connect the cytoplasm of two adjacent cells, facilitating electrical coupling (Giepmans, 2004). One gap junction exists of 12 connexins (Cx), 6 from each cell, of which Cx43 is the main type found in cardiac tissue. The mechanical stresses caused by the contraction-relaxation cycle affect the expression of connexins and proteins located in desmosomal- and adherens junctions (Gutstein et al., 2003). In addition to this, it is important to note that each junction is a protein complex, that dynamically interacts with other intra- and intercellular proteins, however, this goes further than the extent of this thesis and will not be explained (Monemian Esfahani et al., 2019, Saucerman et al., 2019).

1.2.4 Cell-ECM interactions

Besides their interactions with adjacent cells, CMs also bind to their surrounding ECM through cell adhesion complexes in the cell membrane (Pandey et al., 2018, Ward and Iskratsch, 2020, Santoro et al., 2019, Samarel, 2005, Geiger et al., 2009). Integrins are heterodimeric transmembrane molecules, that consist of an α and β subunit. There are many subtypes of the α and β subunits, and thus in a range of various integrin heterodimers (Santoro et al., 2019). The extracellular part of the integrin binds to specific binding moieties within ECM molecules of which the most universal one is the Arg-Gly-Asp (RGD) moiety. Binding sites on collagen molecules for collagen-specific integrins are encoded by GxOGEx, such as GFOGER or GLOGEN (Barczyk et al., 2010). The cytoplasmic region of the integrin heterodimer binds to protein complexes called “focal adhesions” that connected to the cytoskeleton (Santoro et al., 2019). Therefore, the adhesion complexes, including the integrins and the focal adhesions, enable crosstalk between the ECM and the cells. They play an important role in tissue remodelling (Saucerman et al., 2019) and various cellular processes, including differentiation (Santoro et al., 2019), cardiogenesis (Zeng et al., 2013), disease (Pandey et al., 2018) and cardiac electrophysiology (Sengupta et al., 2019).

1.2.5 Mechano-chemo-transduction

Both cell-cell and cell-ECM adhesions sense mechanical changes in the cellular environment, such as stretch. This mechanism is called mechano-chemo-transduction and acts like a feed-back system for the actively contracting cardiac tissue to adapt to these changes in the cellular niche (Chen-Izu and Izu, 2017). Upon tissue stretching, the integrins but also stretch-activated ion channels such as the LTCC, activate a cascade of intracellular pathways that eventually activate gene expression of cytoskeletal proteins (α-actinin), sarcomeric proteins (myosin), adhesion junctions (Yonemura et al., 2010) and gap junctions (Saucerman et al., 2019, Yonemura et al., 2010, Ward and Iskratsch, 2020, Iskratsch et al., 2014). Mechano-chemo-transduction can therefore lead to morphological and, eventually, functional changes within the cell and on tissue level (Saucerman et al., 2019). Studies investigating the effects of substrate stiffness on the contractility of cardiomyocytes have found changes in sarcomere organization (Ribeiro et al., 2020, Jacot et al., 2008, Heras-Bautista et al., 2014, Rodriguez et al., 2011, Ribeiro et al., 2015), myofibril formation and/or organization (Ribeiro et al., 2015, Engler et al., 2008, Feaster et al., 2015), calcium handling (Jacot et al., 2008, Rodriguez et al., 2011, Van Deel et al., 2017, Boothe et al., 2016) and force generation (Ribeiro et al., 2020, Rodriguez et al., 2011, Ribeiro et al., 2015). Similarly, an increased myocardial stiffness alters the contractile function of the CMs and induces and/or enhances myocardial disease (Sewanan et al., 2019).

1.3 Human induced pluripotent stem cell-derived cardiomyocytes – an alternative cell source

1.3.1 The origin of induced pluripotent stem cells

The sparse pool of adult CM from human origin limits scientific research in the cardiac field. The discovery of how to grow and maintain human embryonic stem cells (ESC) in vitro and (Thomson et al., 1998), later, how to differentiate them into cardiomyocytes (Kehat et al., 2004) increased the possibilities in cardiac research. One disadvantage, however, are the ethical issue concerning the use of human embryos for scientific purposes (Mancuso, 2003).

In 2007 the induced pluripotent stem cell (iPSC) was discovered by Takahashi et al, first in mouse (Takahashi and Yamanaka, 2006) and later in human cells (Takahashi et al., 2007). Induced PSCs are dedifferentiated somatic cells, often fibroblasts, that have obtained pluripotent abilities through epigenetic changes that can be initiated by the transcription factors Oct, Sox2, Klf4 and c-Myc (Takahashi et al., 2007). This includes the ability to proliferate and differentiate into the three germ lineages: endoderm, mesoderm and ectoderm (Takahashi et al., 2007). In this way, no human embryos are used, and thus ethical issues are bypassed. Moreover, an additional and important benefit of hiPSCs over hESCs is that patient derived cells offer possibilities to mimic pathologies of human genetic disorders in a dish (Garg et al., 2018) and develop personalized treatment, be it for hereditary disease, cancer or cardiac regeneration. However, these new technologies bring new ethical difficulties, such as the sensitivity of the genetic information and the autonomy, privacy and exploitation of cell donors (Lensink et al., 2021). Nonetheless, hiPSCs embody a promising alternative cell source for hESCs.

1.3.2 Differentiation of hiPSCs into hiPSC-derived cardiomyocytes

Human iPSC can be differentiated into many different cell types including hiPSC-derived cardiomyocytes (hiPSC-CM) through delicate cardiac differentiation protocols (Lian et al., 2013, Burridge et al., 2015, Mummery Christine et al., 2012, Breckwoldt et al., 2017). These protocols have been refined and improved over the years and vary in the differentiation method (embryonic body (EB) formation vs monolayer), the culture media, the culture substrate, the mesoderm induction stage and the cardiac specification stage (Fujita et al., 2019). Major optimization factors are the seeding density, the number of days of pluripotent growth and the concentration of CHIR99021, a small molecule and GSK3ß inhibitor, which is used to activate the canonical Wnt/ß-catenin signalling (Lian et al., 2013).

Once hiPSC are differentiated into cardiomyocytes (CM) they start to beat spontaneously and to express cardiac markers like cardiac troponin (cTnT), Nkx2.5 and myosin heavy chain (MHC) (Lian et al., 2013, Karakikes et al., 2015). Simultaneously, the hiPSC-CM stop expressing the afore mentioned stem cell markers and are thought to lose their proliferation capacity (Lian et al., 2013), although there is evidence that hiPSC-CM do proliferate *in vivo* (Chong et al., 2014).

The quality and purity of the hiPSC-CMs depend on the donor and differentiation protocol and optimization is needed for every stem cell line (Prajapati et al., 2021, Pekkanen-Mattila et al., 2009, Mannhardt et al., 2020), however, batch-to-batch variation might still happen (Huo et al., 2017). To obtain a purer population of CMs, purification of the hiPSC-CMs by using glucose free medium supplemented with lactate, based on the distinct differences in aerobic and anaerobic metabolism between cardiac and non-cardiac cells (Tohyama et al., 2013).

The duration of the differentiation process is typically 14 days on top of the pre-culture and passaging of hiPSCs (Fujita et al., 2019) and is thus a laborious and expensive process. Alternatively, hiPSC-CMs can be bought directly from companies such as NCardia or FujiFilm Cellular Dynamics International (FCDI), who perform the hiPSC culture, cardiac differentiation, and all necessary quality checks, like genetic screens and karyotyping.

HiPSC-CMs are usually grown in a monolayer format on standard tissue culture plastic (TCP) or glass substrates, which have a Young's Modulus of greater than 1 GPa (Travers et al., 2016), 3-4 orders of magnitude stiffer than the native myocardium. To ensure cell adherence to the underlying structure, the plastic or glass surface is coated with a thin layer of ECM components such as fibronectin (FN) (Blinova et al., 2018). These coatings do not alter the overall stiffness of the cell-surface interface, which thus remains inappropriately high for the normal function of the hiPSC-CMs and can result in the loss of hiPSC-CM contractility (Heras-Bautista et al., 2014).

1.3.3 The immature phenotype of HiPSC-CMs

Compared to adult CMs, hiPSC-CMs are relatively immature (Karbassi et al., 2020), which is characterized by an isotropic organization of myofilaments (Yang et al., 2014), an underdeveloped sarcoplasmic reticulum (Li et al., 2014, Hwang et al., 2015), the absence of t-tubules and a foetal gene expression profile

(Karbassi et al., 2020, Kane et al., 2015). Consequently, the cellular physiology, including Ca^{2+} handling, electrophysiology and contractility, is affected (Karbassi et al., 2020).

In immature hiPSC-CMs, ion channels that are involved in the electrophysiology are less expressed and are more randomly distributed across the plasma membrane and the SR, resulting in an altered AP shape. HiPSC-CMs have initially a small SR Ca^{2+} storage, that gradually increases during long-term culture to a similar size to that of adult ventricular CMs from mouse or rabbit (Hwang et al., 2015). However, the lack of T-tubules and random localization of ion channels creates inefficient calcium handling (Lieu et al., 2009), including Ca^{2+} release from the SR, which affect the contraction dynamics of the cell.

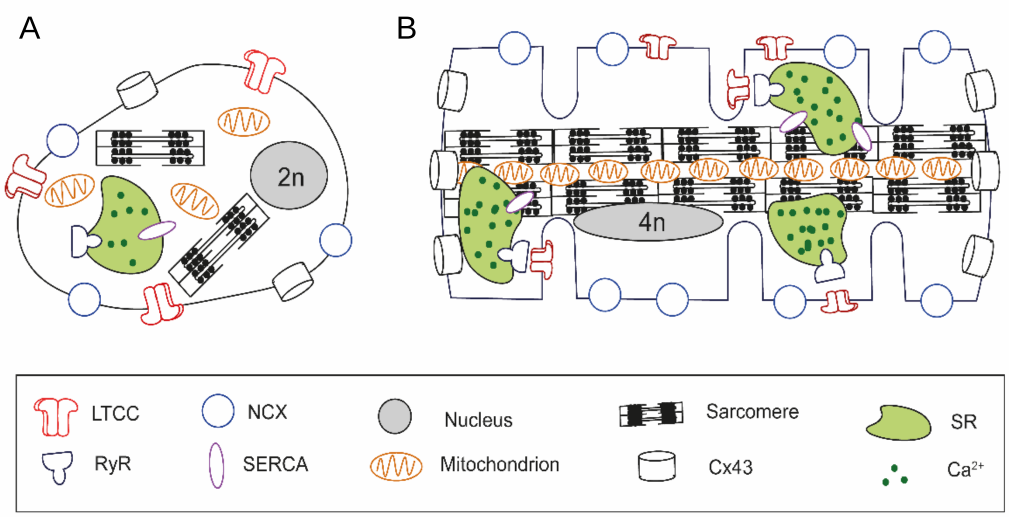

Figure 1.5 Morphology of cardiac cells.
A) the immature morphology of an hiPSC-CM. B) the mature and highly organized structure of an adult CM. The figure design was based on a figure from Karbassi et al (Karbassi et al., 2020).

Another difference between adult- and immature CMs is that hiPSC-CMs are diploid and able to proliferate (Chong et al., 2014), while adult CMs go through a cell cycle without dividing, resulting in a multi nucleated and/or polyploid cell (Senyo et al., 2013). In addition to this, hiPSC-CMs are relatively plastic, meaning that they adapt to a changing environment more easily compared to adult CMs and as a result, they can be kept in culture for multiple months in contrast to isolated adult CMs. These characteristics can be used to expand hiPSC-CMs *in vitro* (Buikema et al., 2020) or to repopulate the heart with CMs (Chong et al., 2014).

At the tissue level, the hiPSC-CMs generate a functional syncytium with properties similar to the adult myocardium, but that are fundamentally different. Firstly, hiPSC-CM derived tissue has a reduced contractile force per cross-sectional area ((Breckwoldt et al., 2017, Ulmer et al., 2018, Mannhardt et al., 2020). Secondly, the LV contains a highly organized structure in regard to fibre orientation that generates a longitudinal and transverse anatomy, however, there is no or limited orientation in hiPSC-CM derived tissue (Jackman et al., 2018, Shiba et al., 2014). Thirdly, the conduction velocity in hiPSC-CM based tissue is lower than the adult cardiac tissue and shows no anisotropy. Under normal conditions, longitudinal conduction velocity in the LV is approximately ~70 cm/s and transverse ~35 cm/s (Myles et al., 2011, Walker et al., 2007), compared to a homogeneous velocity value 10-20 cm/s in hiPSC-CM monolayers (Herron et al., 2016), which is similar to the conduction velocity in regions of ischemia (Walker et al., 2007). These differences between hiPSC-CMs and adult CMs, regarding tissue structure and properties have implications for electrical stability in a myocardium containing significant amounts of hiPSC-CMs as areas of slow conduction are a known source of ventricular arrhythmias (Chong et al., 2014, Shiba et al., 2012, Shiba et al., 2016, Liu et al., 2018). Therefore, maturation of hiPSC-CM might be necessary to improve physiological properties of hiPSC-CM derived tissues.

1.3.4 HiPSC-CM maturation

PSC-CMs can develop a more mature phenotype through exposure to biochemical (Parikh et al., 2017), topographical (Huethorst et al., 2016), electrical and/or mechanical stimulation (Ronaldson-Bouchard et al., 2019, Ronaldson-Bouchard et al., 2018, Yang et al., 2014). For example, Parikh et al. found that stimulation with thyroid and glucocorticoid hormones enhanced T-tubule formation in hiPSC-CMs, and therefore increasing the spatially and temporarily uniform calcium release within the cell and coupling between RyR2 and LTCC (Parikh et al., 2017). In addition to this, Ronaldson-Bouchard et al. showed that electrical stimulation upregulates genetic profiles associated with maturation and enhances mitochondrial development (Ronaldson-Bouchard et al., 2018). Moreover, culturing hiPSC-CMs on artificially or naturally made topographical grooves further improves anisotropy and elongation and results in a more mature contractile profile (Huethorst et al., 2016, Ribeiro et al., 2015). These maturation protocols could improve the characteristics of hiPSC-CMs to obtain a tissue with a closer resemblance to the native myocardium.

Nonetheless, one current controversy is whether the myocardium itself could function as a bioreactor, as all the elements for hiPSC-CM maturation are readily present (Scuderi and Butcher, 2017). Recent literature supports this hypothesis (Kadota et al., 2017) and thus maturation of hiPSC-CMs *in vivo* might be the next logical step.

1.4 Myocardial infarction

1.4.1 Myocardial infarction in humans

1.4.1.1 Disease progression

Coronary artery disease (CAD) can result in myocardial infarction (MI), which is the obstruction of a coronary artery restricting the blood flow towards the underlying tissue and results in massive cell death (Thygesen et al., 2012). Due to a lack of proliferative cells (Senyo et al., 2013), the heart is not able to replace the dead myocardium with healthy CMs and blood vasculature and replaces it with a relatively thin, collagenous scar instead. The disease progression of MI is a dynamic process and is generally divided into three stages: inflammation, wound healing and remodelling/maturation of the scar (Richardson et al., 2015).

During the first few days post MI, CMs undergo necrosis which is followed by an inflammation response and wound healing process (Frangogiannis, 2014). Inflammatory cells invade the ischemic zone and initiate resorption of necrotic tissue and structural remodelling of the scar by disrupting existing ECM architecture and replacing it with a provisional matrix consisting of various ECM proteins, including fibronectin.

The initial inflammatory response is followed by a healing phase dominated by myofibroblasts that lasts several weeks (Travers et al., 2016, Frangogiannis, 2015). The sudden increase in myofibroblasts is a combination of migration and proliferation of existing myofibroblasts and the (de-) differentiation of other cell types. Myofibroblasts are characterized by increased α-smooth-muscle-actin (α-

SMA) expression that generally accompanies elevated migration and contractile force as well as an increased expression of ECM proteins (Shinde et al., 2017).

Finally, during the maturation stage, the scar is stabilized by ECM crosslinking, fibroblast quiescence and vascular maturation (Frangogiannis, 2017). This scar is stiffer than the healthy myocardium (100 kPa vs 50 kPa, respectively (Ward and Iskratsch, 2020, Ramadan et al., 2017, Travers et al., 2016, Frangogiannis, 2014)) and lacks the contractility needed for normal physiology. The unaffected areas of the myocardium need to compensate for the loss of function, causing hypertrophy in these areas. Additionally, changes in pressure and volume load activate various stress-activated pathways affecting the cardiac ECM architecture and CM functionality (Li et al., 2014, Sewanan et al., 2019), altering the ventricular geometry and contractility to become more dilated and less contractile. Moreover, the scar tissue has different electrical properties than healthy myocardial tissue, changing the conduction pathway and velocity of electrical signals, that can lead to ventricular arrhythmias.

1.4.1.2 Scar morphology

All MI scars consist of an infarct zone (IZ) and a border zone (BZ), which bridges the IZ with the healthy myocardium. The BZ has therefore different physiological properties compared to the IZ. The morphology of the MI scar depends on the location (proximal vs distal) and duration (permanent vs reperfusion) of the coronary occlusion, on the anatomy of the coronary vessels and on the remodelling process afterwards. For example, scars can be transmural, covering the full myocardial wall, or non-transmural, whereas other scars can be described as “patchy” and contain strands of healthy myocardium (Jackson et al., 2003).

1.4.1.3 Current treatments and interventions

Current treatments for CAD include percutaneous coronary intervention and bypass surgery (Ramadan et al., 2017, Tully and Bishop, 2021), often accompanied by pharmaceutical intervention, such as statins or inhibitors of the renin-angiotensin-aldosterone system, to reduce adverse cardiovascular events in patients with CAD. Major factors in deciding on the best management approach are the anatomic extent and complexity of CAD along with other factors such as the patient’s overall health and preference, the LV function and operative risk (Ramadan et al., 2017).

During percutaneous coronary artery intervention, a balloon is placed in the jugular artery and propelled through the aorta and the left or right ostium towards the blocked area (Tully and Bishop, 2021). When located the balloon is inflated, widening the coronary artery and releasing the blockage so that the artery is reperfused. To maintain the blood flow, a stent is placed in the blocked area.

In cases where the blockage in the coronary artery is severe and cannot be solved by percutaneous intervention, a bypass surgery is performed (Tully and Bishop, 2021). Here, vascular graft, e.g. the saphenous vein or the left internal mammary artery, is placed between the aorta and the distal part of the blocked coronary artery, providing the underlying myocardium with blood.

1.4.2 Animal models for myocardial infarction

1.4.2.1 Small animal models vs large animal models

Because the MI is such a dynamic process, animal models are often used to investigate disease characteristics. But even though the general concept of the three phases is similar between animal models, there are some differences. For example, each disease phase is shorter in small animal models (mice and rats) compared to larger animal models (sheep, dogs and pigs) and humans (Jugdutt et al., 1996, Dewald et al., 2004). Also, the increase in collagen deposition and therefore the scar thickness varies between species (Gao et al., 2012, Jugdutt et al., 1996). In addition to this, the cardiac electrophysiology of large animals is more comparable to that of a human than that of small animals. However, from the small animal models, the rabbit model has the most comparable electrophysiology to that of human (Ellermann et al., 2020) and would therefore be apt to assess EHT survival and integration.

1.4.2.2 Animal models for MI

In animal models, the MI is induced by physical occlusion of the coronary artery, e.g. the left anterior descending (LAD) coronary artery, that is accessed by opening the thoracic cavity. Depending on the anatomy of the animal and the experimental needs, the coronary artery is occluded permanently through either a ligation (Myles et al., 2011, Ichimura et al., 2020) or cryofreezing (Weinberger et al., 2016, Shiba et al., 2014) or temporary occluded by releasing the ligation after a certain amount of time, which is also known as ischemia reperfusion injury (Chong et al., 2014, Laflamme et al., 2007). Generally, ischemia reperfusion model results in a smaller, more patchy infarct and restricted LV remodelling (Pluijmert et al., 2020, Chong et al., 2014). The size of the induced MI needs to compromise around 40% of the left LV, because smaller MI’s (5-30%) do not reflect the dynamic changes in cardiac physiology (Pfeffer et al., 1979) and animals with MI’s larger than 60% have an increased risk of death.

An alternative and less invasive method for inducing an MI in animals is by access through the carotid artery, similar to angioplasty procedures (Ziv et al., 2012, Isorni et al., 2015, Morrissey et al., 2017, Li et al., 2021). Here, ethanol or a coil can be used to induce a permanent MI, whereas a balloon can be used for ischemia-reperfusion. One limitation is that this procedure can only be done in animals with relatively large coronary arteries as wires and catheters need to pass through.

1.5 Cardiac regeneration

1.5.1 General concept

Regenerative medicine uses biomedical cues to regenerate diseased or damaged tissues within the body. More specifically, cardiac regeneration aims to convert the MI scar into healthy contractile cardiac tissue, for example by repopulating the myocardium with healthy cells (Weinberger and Eschenhagen, 2020, Shiba, 2020). Other tactics focus on biochemical and/or biophysical cues to enhance vascularization (Munarin et al., 2020) and/or proliferation (Khan et al., 2015), or to inhibit cell death (Fiedler et al., 2019). Also combinations of cells, biochemicals and biomaterials are currently assessed, for example by functionalizing biomaterials with growth factors (Chow et al., 2017) or using a biomaterial as carrier for cell delivery (Burgess et al., 2021). However, because the large number of CMs that died as a consequence of the MI needs to be replaced, most cardiac regeneration approaches focus on the transplantation of cells into the damage region and/or border zone. Nonetheless, it is important to keep the complex mechanical and electrophysiological organization of the heart in mind while exploring various approaches for cardiac regeneration to obtain the best results.

1.5.2 Main challenges of cardiac regeneration

The massive cell death following an MI and the millions of healthy CMs that have to replace these is one of the main challenges that have to be overcome within regenerative medicine. Fortunately, recent research has found methods to up-scale in vitro culture of hiPSC and hiPSC-CM (Ronaldson-Bouchard et al., 2018, Tohyama et al., 2013) .

Another main challenge, more specific to cardiac regeneration, is the low rate of clear electrical coupling of the implanted cells to the host myocardium (Gerbin et al., 2015, Weinberger and Eschenhagen, 2020, Menasché, 2018, Shiba, 2020, Shiba et al., 2014, Jackman et al., 2018, Weinberger et al., 2016). Transplanted EHTs often improve the functionality of the heart after an MI (Shiba et al., 2016, Shiba et al., 2012, Jackman et al., 2018, Weinberger et al., 2016, Pecha et al., 2019) but in the absence or with incomplete coupling that could eventually lead to ventricular tachycardia (VT) (Shiba et al., 2016, Shiba et al., 2012, Liu et al., 2018). To improve hiPSC-CM integration, it is important to understand the factors that promote cell survival and electromechanical coupling.

Factors that affect mechano-electrical coupling could be, but are not limited to, the implantation method (Gerbin et al., 2015), the graft size (Chong et al., 2014), the presence of electromechanical stimuli from the surrounding myocardium (Scuderi and Butcher, 2017) and/or paracrine factors from implanted cells (Zhu et al., 2018, Tachibana et al., 2017). Studies have shown that intramyocardially implanted grafts do electromechanically couple with the host in contrast to ectopically implanted grafts (Gerbin et al., 2015). Additionally, *in vivo* studies showed that the electromechanical stimulus of the myocardium enhances maturation of injected cells, showing enhanced maturation markers and reduced automaticity (Chong et al., 2014). Interestingly, hESC-CMs at the border of the graft area show higher maturation levels compared to cells within the core of the graft (Chong et al., 2014), suggesting that a smaller EHT with a higher surface-core-ratio will arguably be less likely to initiate arrhythmias.

1.5.3 Delivery of cells into the heart

In general, there are currently two main approaches to deliver hiPSC-CM into the myocardium, which are the injection of a cell suspension into the myocardium or ectopically transplantation of 3D engineered heart tissues (EHTs) onto the surface of the epicardium (Yang et al., 2014, Zimmermann, 2017). Both methods have their own advantages and disadvantages, which will be discussed below.

1.5.3.1 Injection

One advantage of hiPSC-CM injection is the relative easiness and precision of the cell delivery method. Upon injection, cells might be mixed with a pro-survival cocktail containing growth factors and/or small molecules to enhance survival and integration. One small molecule used is the ROCK inhibitor Y-27632, that reversibly inhibits contraction and, in this way, enhances the integration of the cells (Zhao et al., 2019). Additionally, cells could be injected in multiple smaller doses or one big dose, as desired. The second advantage is that injected hiPSC-CMs have shown to electro-mechanically couple to the myocardium (Shiba et al., 2012, Gerbin et al., 2015, Shiba et al., 2016).

However, studies that transplanted hiPSC-CMs through injection show that only a fraction (<10%) of the implanted cells is retained around the implantation site; the majority migrates or dies soon after implantation (Zhao et al., 2019, Shiba et al., 2012, Shiba et al., 2016). This is potentially caused by cell death or migration, for example into the blood stream and consequently anywhere else in the body. This is undesirable, mainly because of unknown side effects, but also because of the high cell number needed to retain enough cells within the myocardium, increasing the costs. The current number of injected cells is 10^7-10^9 cells per animal, but slightly varies for the animal size.

1.5.3.2 Engineered heart tissue

Engineered heart tissues (EHTs), consisting of hiPSC-CMs, are cultured and developed *in vitro* prior to implantation. EHTs are commonly designed to cover major parts of the infarct zone and are therefore quite large (cm-scale) and therefore long culture times are inevitable (Jackman et al., 2018, Gao et al., 2018, Weinberger et al., 2016). The development and culture of EHTs is therefore more complicated (and probably expensive) compared to the injection of cells, but the cell-cell and cell-matrix adhesion lower cell death and cell loss post-implantation, and thus resulting in a higher cell retention.

Most EHTs do not have a vasculature and are dependent on the diffusion of culture medium (*in vitro*) or extracellular fluids (*in vivo*) into the construct so that nutrients and oxygen can reach all cells within the EHT, including those in the core. This is especially important for *in vivo* studies where cells are implanted into an hypoxic environment. HiPSC-CMs within the EHTs do express VEGF (Zentilin et al., 2010) and show increased vascularization compared to control (Yeung et al., 2019). However, infiltration of capillaries happens over several weeks, as a result of intracellular cues that accompany hypoxia and cell death (Jabbour et al., 2021). To maximize the graft size while preventing developing a hypoxic core, the diffusion of nutrients can be enhanced, for example by the use of water absorbing materials such as hydrogels (Matsuo et al., 2015b), by altering the EHT shape (thin and/or porous scaffold designs) (Jabbour et al., 2021, Jackman et al., 2018) or by enhancing vascularization using vascular endothelial growth factor (VEGF) (Zentilin et al., 2010).

Unfortunately, there is no guarantee that EHTs do integrate into the myocardium after transplantation. Compared to cell injection, EHTs show in general a lower success rate regarding mechano-electrical coupling to the host myocardium (Shiba et al., 2016, Weinberger et al., 2016, Gerbin et al., 2015, Jackman et al., 2018, Shiba et al., 2012, Matsuo et al., 2015a, Shiba et al., 2014), suggesting that single cells or cellular aggregates are more able to form molecular connections to the host myocardium. The underlying reason could be that EHTs are often transplanted ectopically potentially preventing cellular integration.

Thus, neither implantation of hiPSC-CMs through injection or EHTs has optimal results. Therefore, a transplantation method with an optimal graft size vs cell retention is therefore needed.

1.6 The EHT design: the best of both worlds?

By implanting multiple small (<3 mm) EHTs into the myocardium, the advantages of both the cell injection and EHT implantation approach are combined, forming a potential regenerative solution with optimal cell retention and integration (Gerbin et al., 2015). Additionally, implanting smaller constructs to investigate factors that improve cellular integration into the myocardium might be a conscientious approach as less resources are needed during the experimental phase in comparison to large EHTs.

Cell-cell adhesions are important for CM functionality and long-term survival (Salameh and Dhein, 2013, Vermij et al., 2017, Moore et al., 2008, Li et al., 2017, Chopra et al., 2011). Therefore, the preferred method to create small (mm-scale) EHTs is a monolayer format through cell-sheet engineering (Kitala et al., 2020, Kawecki et al., 2016, Matsuo et al., 2015a). To support the monolayer, the cells could be seeded on a biomaterial such as a hydrogel: a peptide network that is highly permeable and can absorb large amounts of fluids. Hydrogel properties, such as stiffness and degradation time, are easily tuneable (Zhao et al., 2020, Weinberger et al., 2017, Pandey et al., 2018, Bar and Cohen, 2020) and functionalization by covalent binding of bioactive molecules makes them attractive biomaterials.

Even though the aim of this thesis is to create small constructs, this design allows for easy upscaling in two ways. Firstly, the diameter of the 2D-sheets could be increased from mm-scale to cm-scale (Matsuo et al., 2015b). Secondly, constructs could be stacked on top of each other to create a thicker ETH. Here, incorporation of the hydrogel helps to enhance diffusion of nutrients to the cells, which has shown to improve cell viability (Matsuo et al., 2015a, Haraguchi et al., 2012, Matsuo et al., 2015b).

1.7 A novel platform to investigate EHT integration.

Until the right method for cardiac regeneration is found, a platform to test EHTs on their ability to integrate and survive would be extremely useful to limit experimental costs, such as an *ex vivo* study. Using the *ex vivo* approach, some of the challenges that were otherwise encountered during the *in vivo* studies could be closely investigated and, hopefully, solved, saving time and money. Importantly, *ex vivo* assessment of cardiac constructs before proceeding to *in vivo* studies contributes to the three R's for laboratory animal welfare, by refining the experimental procedures and therefore ultimately reducing the number of animals used.

Using smaller EHTs and thus a smaller number of cells, various parameters could be tested in parallel to find the optimal conditions relatively quickly and efficiently. When these conditions are found, small EHTs could be upscaled to fit their purpose. In the case of small cardiac patches, upscaling is easily done by increasing cell sheet diameter, and/or stacking the cell sheets (Matsuo et al., 2015a, Miyagawa et al., 2005).

1.7.1.1 Langendorff perfusion system

The Langendorff perfusion system (Langendorff, 1895) is a good method to test the implantation and integration of cardiac constructs *ex vivo* for a couple of reasons. Firstly, hearts mounted on the Langendorff perfusion rig are viable for multiple hours, and thus provides enough time to perform experiments. Secondly, parameters such as systemic pressure, flow and contractility are controlled. Thirdly, our lab is experienced with intact rabbit heart models and the Langendorff set-up. Finally, an optical set-up can be placed next to the Langendorff perfusion rig, so that the activity of the implanted EHT can be monitored closely.

1.8 Monitoring the EHT post-implantation

Monitoring the activity and physiology of the implanted EHT is key to investigate their acute response to both the implantation process and the myocardial environment. To accomplish this, the EHT can be loaded with fluorescent dyes prior to implantation, that fluoresce upon increase in intracellular calcium concentrations or changes in membrane potential. Once implanted, the fluorescent signals from the EHT could be recorded and compared with the ECG derived from the myocardium. Nonetheless, with the correct optical set-up and two voltage sensitive dyes with distinct Ex/Em spectra, calcium transients and/or action potentials (APs) from the heart and EHT could be recorded synchronously as well. In this way, the local electrical activity of the implantation site can be monitored rather than the general electrical activity of the myocardium and will result in a more direct comparison between the EHT and the myocardium.

Currently available voltage sensitive dyes have low dynamic ranges (<10%), compromising the intensity of the recorded signal and the length of the experiment. Two novel small molecule calcium indicators Cal520-AM and Cal590-AM have a relatively high dynamic range (~400% *vs* FV), fast kinetics and long-lasting fluorescence and are therefore useful for *ex vivo* studies (Tada et al., 2014, Kopljar et al., 2018, Tischbirek et al., 2017). Moreover, the Ex/Em spectrum of Cal590-AM does not overlap with the Ex/Em spectrum of FV, enabling simultaneous imaging of the EHTs and myocardium.

1.9 Aims of this thesis

1.9.1 Main aim and objectives

The main aim of this PhD project is to develop a platform in order to investigate the acute integration and survival of small EHTs after implantation into the myocardium. This aim is addressed by the following 4 objectives:

1) The creation of small 2D hiPSC-CM monolayers with less than 50.000 cells which will function as building blocks for the small EHTs.

2) The development of a small EHT, where two approaches will be explored: a) scaffold-free EHTs and b) EHTs where a biomaterial is used as a scaffold to deliver the cells into the myocardium.

3) Establishment of an optical set-up to monitor the EHT post-implantation using fluorescent dyes.

4) Assessment of the functionality of EHTs in the first hours post-implantation.

1.9.2 Multiphasic contractile behaviour – A second theme throughout the chapters

During the initial experiments, an interesting observation of complex multiphasic contractile behaviour of hiPSC-CMs was made. These features were non-physiological compared to “twitch”-like transients, and it was hypothesized that rigid surfaces, like TCP and glass, could be the underlying cause. The investigation into the origin of these distinct time-courses will be another theme throughout this thesis.

1.9.3 Short overview of the chapters

The 4 sub-aims are divided over 4 results chapters. The first result chapter, Chapter 3, describes the creation of small 2D hiPSC-CM monolayers. Here, the first observation and investigation of the multiphasic (complex) contractile behaviour are discussed as well. Then, in Chapter 4, various methods to detach and transfer intact hiPSC-CM monolayers are explored, where after three candidate hydrogels will be assessed to be used as a carrier material for hiPSC-CM implantation in Chapter 5. In parallel, Chapter 4 and Chapter 5 also discuss whether the multiphasic contractile behaviour is also present in free-floating monolayers (Chapter 4) and hiPSC-CMs seeded on flexible surfaces (Chapter 5). Finally, the optimization of the implantation protocol as well as the imaging techniques are described in Chapter 6 and are concluded with EHT implantation experiments, assessing the acute integration of the hiPSC-CMs into the intact rabbit heart.

Chapter 2 General methods

2.1 Cell culture

2.1.1 The cardiac cell source - rationale

A high number of cardiomyocytes is needed for the generation of engineered heart tissues (EHTs), however, the source of adult human cardiac cells is extremely limited. Therefore, pluripotent stem cell derived cardiomyocytes (PSC-CMs) are generally used as a cell source for the creation of cardiac constructs. This group of cells vary in their origin (embryonic or induced) and in their availability (commercial vs non-commercial).

2.1.1.1 Embryonic vs induced PSC-CMs

Human induced PSC-CMs (hiPSC-CMs) are developed by dedifferentiating somatic cells, generally fibroblasts, into pluripotent stem cells, followed by a cardiac differentiation protocol. This results in a mixed population of ventricular-, atrial- and nodal CMs and the ratios within each cell line may vary. Embryonic stem cell derived cardiomyocytes (ESC-CMs), are generated through a similar method, but here embryonic stem cells are subjected to cardiac differentiation. Ethical regulations restrict the use of human embryos for research, and therefore, the use of hiPSC-CMs is favoured over the use of hESC-CMs for the experiments described in this thesis.

2.1.1.2 Commercial vs non-commercial cell source

HiPSC-CMs can be either obtained from commercial sources or developed non-commercially. Generally, non-commercially developed cells are a more economic cell source, because commercially available cells and the complementary cell culture medium can be extremely expensive. The protocols for the dedifferentiation and differentiation processes can be found in the literature (Lian et al., 2013), making hiPSC-CMs more accessible to less well funded labs.

The big disadvantage, however, these protocols include regular assessment of stem cell- and cardiac markers through various techniques, including immunohistochemistry, gene expression profiling and karyotyping, which can also become expensive and labour intensive. More importantly, there is no guarantee for successful differentiation and a risk of batch-to-batch variation.

In contrast to non-commercially derived hiPSC-CMs, commercial hiPSC-CMs can be bought directly from various suppliers, who guarantee high-quality hiPSC-CMs with low batch-to-batch variation. These cells are relatively expensive but grant more time for experimental procedures that lead to answering the main aim. Therefore, commercially available hiPSC-CMs were used during experimental procedures.

2.1.2 Commercially available hiPSC-CMs

hiPSC-CMs were bought from two commercial providers: 1) Cellular Dynamics International (CDI) and 2) NCardia. HiPSC-CMs from both cell lines are derived from fibroblasts from a female, caucasian donor and are reprogrammed using the defined transcription factors described by Yamanaka et al (Takahashi et al., 2007). Both companies claim to deliver 99-100% pure cardiomyocytes. The expression of major cardiac genes and drug response of both hiPSC-CM cell lines were evaluated and compared by (Huo et al., 2017). They found that both lines have an immature profile comparable to a embryonic heart. Also, small differences were seen between both hiPSC-CM lines. Specifics of both cell types are described below.

2.1.2.1 FUJIFILM Cellular Dynamics, Inc.

Two generations of hiPSC-CMs were obtained from FUJIFILM Cellular Dynamics, Inc. (FCDI), namely ICell and ICell^2. ICell^2 is the enhanced version of ICell as it has a faster recovery after thawing. Both cell types were derived through the retroviral transduction of the four reprogramming factors. However, no retroviral gene expression was detected by PCR before and after the dedifferentiation process, ensuring that the hiPSC-CMs cannot produces viral particles.

ICell and ICell^2 hiPSC-CMs were cultured according to the manufacturer's protocol. In brief, cells were stored in liquid nitrogen upon receipt. Cells were thawed for 4 min at 37°C and transferred to a 50 ml tube, where after 4 ml of plating medium was added dropwise. Cells were counted manually using a haemocytometer and tryphan blue, centrifuged at 300g for 5 mins and resuspended in maintenance medium to obtain the desired concentration. HiPSC-CMs were seeded on fibronectin coated dishes and cell culture medium was changed every other day. For some experiments, ICell^2 were seeded in a T75 flask or 6 well-plate and replated between 4 and 7 days after thawing and plating. Here, cells were washed twice with PBS$^{-/-}$ and incubated with 1 ml (6-well plate) or 3 ml (T75) Accumax^{TM} solution (A7089, Sigma) at 37° for 6 min. Detachment was confirmed under the microscope and when sufficient, where after cells were collected with excess amount of warm maintenance medium and counted. Then, cells were centrifuged at 300g for 5 min and the cell pellet was carefully resuspended in the correct amount of medium.

2.1.2.2 NCardia

The Cor.4U® hiPSC-CMs from NCardia are dedifferentiated using a non-viral method. They are classed as genetically modified organisms (GMO) and should be handled according to local biosafety regulations. To ensure high-quality cardiomyocytes, Cor.4U® hiPSC-CMs are tested for cardiac markers, e.g. Cx-43 and cardiac α-actinin, and normal electrophysiological properties after differentiation.

Cor.4U® cardiomyocytes were handled and maintained according to the manufacturer's protocol. In brief, hiPSC-CMs were stored in liquid nitrogen once received. Cryovials were placed on dry ice for transport, thawed until for 2 min at 37°C. Then, cells were transferred to a 50 ml tube, where after 4 ml of Cor.4U® maintenance medium was added dropwise. The number of viable hiPSC-CMs was counted using a haemocytometer, where after cells were centrifuged at 300g for 5 mins and resuspended to obtain the desired concentration. HiPSC-CMs were seeded on fibronectin coated dishes and cell culture medium was changed every other day.

2.1.3 Discontinuation of Cor.4U (NCardia) hiPSC-CMs

Unfortunately, internal investigations within the NCardia company revealed hiPSC-CMs were actually from embryonic origin, resulting in the discontinuation this cell line in March 2019 (Braam, 2019), approximately 18 months after the start of this study and after a considerable amount of work had been completed using this cell line. For ethical and institutional/regulatory reasons, the UoG did not grant us a licence to culture embryonic cells or cells derived from embryonic origin in our laboratories as alternatives can be used. Therefore, it was decided to continue this work using only hiPSC-CMs from FCDI. This means that some experiments described in this thesis are done with hiPSC-CMs from both companies, and part of the experiments only with hiPSC-CMs from NCardia or FCDI. Captions of figures and tables will state which cell type was used.

2.1.4 ECM coatings to promote cell adhesion

2.1.4.1 Fibronectin

Fibronectin (FN) is an ECM protein that binds to a wide variety of other ECM proteins, including collagen and other FN molecules (Kubow et al., 2015). In addition to this, FN is a ligand for various integrins, allowing the binding of many cell types. Because of these properties, FN is often used as a coating for cell culture dishes. The extensive experience in our lab with FN and hiPSC-CM has shown that hiPSC-CMs bind and spread greatly on FN coated dishes. Thus, FN could be seen as a positive control in cell adhesion studies.

The general protocol for coating dishes with FN is as follow: FN (bovine, 33010018, Gibco) was diluted 1:100 in PBS$^{+/+}$. The following volumes per well were used: 70 ul (96 well-plate), 300 ul (glass area of 35 mm MatTek dishes), 0.5 ml (12 well-plate), 1 ml (6 well-plate) and 5 ml (T75 flask).

2.1.4.2 Other ECM proteins

During some studies, other ECM proteins were tested. In Table 2.1, all ECM proteins used are listed.

Table 2.1 List of ECM proteins to promote cell adhesion.

ECM protein	Company	Reference #	Concentration or dilution	Note
Fibronectin (FN)	Gibco	33010018	1:100	Bovine origin. Used for coating and to mix with the RCP-MA hydrogel
Laminin	BioLamina	LN 521	1:100	
Cellnest	FUJIFILM Europe B.V.	16461438	0.1%	Same recombinant collagen-like peptide as the RCP-MA hydrogel
Geltrex	Life Technologies	A1413302	1:100	Also used for hiPSC culture

2.1.5 Serum-free medium

For most experimental procedures, the maintenance medium was replaced for BMCC medium. BMCC medium is serum-free and phenol-red-free, which is important to avoid potential protein-binding of test compounds to serum component and to prevent interference with fluorescent microscopy, respectively. BMCC is home-made and its composition is shown in Table 2.2.

Table 2.2 BMCC composition

Compound	**Molecular weight (g/mol)**	**Final concentration (mM)**
$CaCl_2$ (1M solution)	NA	1.490
$MgSO_4$*7H20	246.47	0.81
KCl	74.55	4.4
$NaHCO_3$	84.01	36
NaCl	58.00	77.59
Na2HO4P	141.96	0.91
Na_2SeO_3-$5H_2O$	263.00	0.0001
KNO_3	101.11	0.0008
D-Glucose (Dextrose)	180.16	25
HEPES	238.30	25.03
*Phenol Red^^*	*376.40*	*0.04*
Sodium Pyruvate	110.05	1
Total Na		**115.5**
Total K		**4.4**
Total Ca		**1.49**

2.2 Fluorescent Imaging

2.2.1 Optics

HiPSC-CMs are cultured in monolayers, meaning that fluorescent recordings represent a number of cells rather than one CM. The number of cells within the frame, and thus the averaged amplitude and time-course of the transients, depend on the magnification that was used. Additionally, the maximum spatial resolution of a microscope is the numerical aperture (NA) of the objective lens, which is expressed as the amount of light collectable by a microscope objective and the broadness of the light cone that is able to go through the lens and reach the sample when in focus (Bootman et al., 2013). The NA and the magnification of the objective lens are often inversely proportional to each other and determine the working distance. Because the full frame is occupied by cells, the total fluorescence is relatively high, making it is possible to use a 40x objective with a lower NA objective to enhance the working distance. In this way, recordings can be made from cells seeded on either thick TCP or thin glass, so a wider range of culture dishes can be used. All objectives used are air objectives and an overview of them is shown in Table 2.6.

Other important factors that affect the recorded fluorescent signal is the dynamic range of the fluorescent dye or probe. The dynamic range is calculated by subtracting the background fluorescence from both the peak- (F) and baseline (F_0) fluorescence, whereafter both values are divided (F/F_0). This approach also normalizes loading differences and makes it therefore possible to compare experiments. However, it is important to note that some factors cannot be compensated for, such as photobleaching and compartmentalization (Bootman et al., 2013).

2.2.2 Voltage sensitive dyes

2.2.2.1 FluoVolt^{TM}

FluoVolt^{TM} (FV) (Ex/Em: 480/535 nm) is a fast-acting voltage sensitive fluorescent probe that records membrane potentials by photo-induced electron transfer (Asakura et al., 2015), a process whereby a fluorescent reporter is enhanced or quenched by an electron-rich donor through a membrane spanning molecular wire. A change of membrane electric field alters the rate of electron transfer, and, in turn, the intensity of the emitted fluorescence has a fast response (within sub-milliseconds) and is capable of 25% fractional change in fluorescence per 100 mV change. This is higher than other fast response probes, like RH237 or Di-4-ANEPPS (Fluhler et al., 1985) that have a fractional change of 2-10%. Additionally, FV is less cytotoxic (Miller et al., 2012, Salerno et al., 2020) and has a smaller Ex/Em spectrum compared to RH237 and Di-4-ANEPPS, which are shown in Figure 2.1A. Moreover, our lab has good experience with FV during *in vitro* experiments with several cardiac cell lines, including adult CMs and hiPSC-CMs (Cor.4U, ICell and ICell^2).

FV has been used *in vitro* (Herron et al., 2016, Saleem et al., 2020) and in *ex vivo* (Salerno et al., 2020) studies with isolated mice hearts, but never in intact rabbit hearts. In contrast, DI-4-ANEPPS has been used for intact rabbit heart experiments before, however, its broad Ex/Em spectrum and, more importantly, probability to induce arrythmia’s make it a lesser candidate for *ex vivo* rabbit heart studies than FV (Salerno et al., 2020).

The FV membrane potential kit comes also with the PowerLoad^{TM} Concentrate that enhances cell loading and can therefore be classed in the same category as pluronic acid that is used to load hiPSC-CMs with calcium indicators.

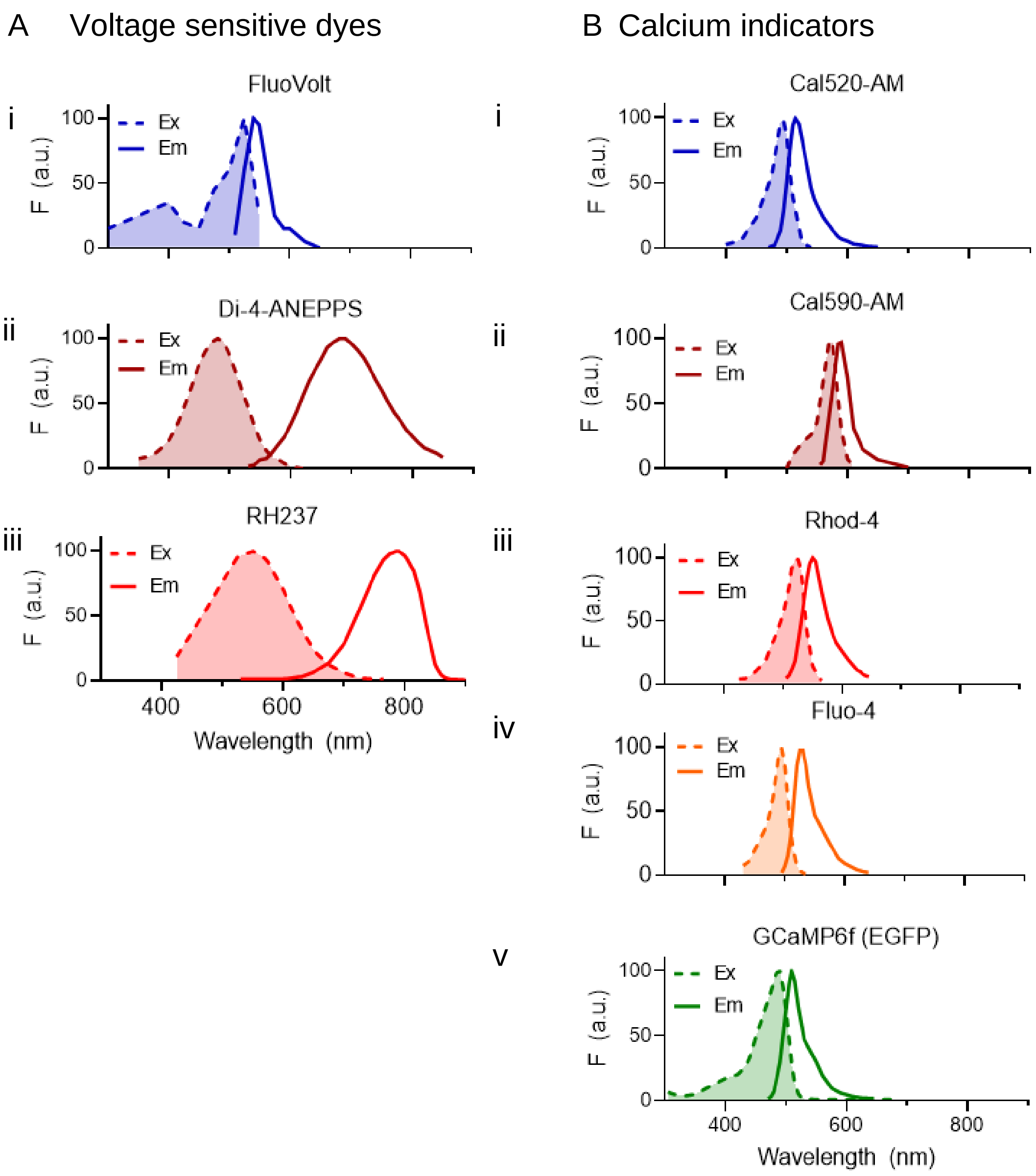

Figure 2.1 Excitation/emission spectra of various voltage sensitive dyes (A) and calcium indicators (B).
The voltage sensitive dyes are: FluoVolt (Ex/Em: 480/535 nm) (Ai), Di-4-ANEPPS (Ex/Em: 482/686 nm) (Aii) and RH237 (Ex/Em: 550/786 nm) (Aiii). The calcium indicators are: Cal520-AM (Ex/Em: 493/515 nm) (Bi), Cal590-AM (Ex/Em: 574/588 nm) (Bii), Rhod-4 (Ex/Em: 523/551 nm) (Biii), Fluo-4-AM (Ex/Em: 495/528) (Biv) and GCaMP6f (Ex/Em: 489/511) (Bv). GCaMP6f has the same fluorescent spectrum as enhanced green fluorescent protein (EGFP). Ex/Em spectra are taken from examples shown in the spectrum viewer on the AAT Bioquest website, except from the Ex/Em spectrum of FluoVolt, which is taken from the thesis of Dr. Quentin Lachaud (Lachaud, 2019a).

2.2.2.2 General protocol for FluoVolt^{TM} loading *in vitro*

HiPSC-CM were incubated in BMCC medium for at least one hour and subsequently loaded with FluoVolt^{TM} Dye (1:1000) and Powerload^{TM} Concentrate (1:100) for 20 minutes at 37°C. Action potentials (APs) were recorded on the CellOPTIQ system.

2.2.2.3 General protocol for FluoVolt^{TM} loading *ex vivo*

The protocol for FV loading into intact rabbit hearts was established and optimized during these studies and the results are described in Chapter 6.

In brief, after placing the intact rabbit heart onto the Langendorff perfusion system and blebbistatin incubation, the flow rate was reduced from 40 ml/min to 26 ml/min (~67%) to enhance diffusion of the dye into the myocardium. In a beaker, 100 ml Tyrode's with blebbistatin was combined with previously mixed pluronic acid (0.05%) and FV (1:4000). This beaker was connected to the circuit through a secondary tube, which was enabled during incubation. The dye was recirculated, meaning that cardiac effluent was collected, filtered, and added to the original beaker. The total incubation time was 20 min, similar to that of *in vitro* studies. The experimental set-up will be explained later in paragraph 2.4.2 and an overview is shown in Figure 2.10A.

2.2.3 Genetically encoded calcium indicators

To track the activity of the EHT once it is implanted into the myocardium, cells could be genetically modified with a genetically encoded calcium indicator (GECI) (Kaestner et al., 2014). GECI's are stably expressed for a long timeframe (weeks-months) and are therefore ideal for implantation studies. One particular interesting GECI is GCaMP, which has a high signal-to-noise ratio (Nakai et al., 2001). GCaMP is based on an EGFP sequence that bridges two halves of a calmodulin molecule. In the presence of Ca^{2+}, the calmodulin binds to the M13 peptide and folds, activating the EGFP molecule that subsequently becomes fluorescent (Figure 2.2). There are multiple generations of GCaMP with each different brightness and kinetics. GCaMP-6f is the 6th generation of GCaMP molecules and has relatively fast kinetics (Chen et al., 2013). Importantly, GCaMP-variants have been used for *in vitro* (Saleem et al., 2020) and *in vivo* (Shiba et al., 2012, Kadota et al., 2017, Jackman et al., 2018) studies with promising results.

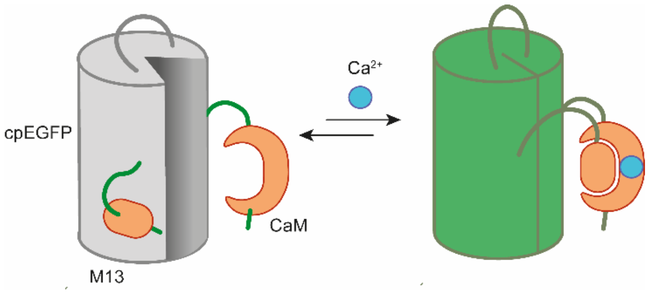

Figure 2.2 Diagram showing the activation of GCaMP.
cpEGFP = circularly permuted enhanced GFP. CaM = calmodulin. M13 = CaM interacting peptide.

2.2.3.1 Development of a GCaMP-6f hiPSC-CM cell line

A GCaMP hiPSC-CM cell line would be ideal as it would stably express GCaMP long-term and it could serve a unlimited source of hiPSC-CMs. Therefore, it was decided to establish a lab where hiPSCs could be maintained and differentiated towards cardiomyocytes. The new hiPSC lab was based in the lab of Prof. Nikolaj Gadegaard and the hiPSC-CM cell line, as well as support and guidance, were obtained from the Dr. Gareth Sullivan, who is based in the University of Oslo, Norway. The protocols and results regarding hiPSC culture and differentiation towards cardiomyocytes are shown in Chapter 8.2. Unfortunately, this work was too laborious and time consuming and went beyond the main aim of my thesis. Therefore, it was decided to stop with the culture differentiation of the non-commercial hiPSCs from the Sullivan Lab.

2.2.3.2 Transfection of commercial hiPSC-CMs with GCaMP-6f

Transfection of commercial hiPSC-CMs with GCaMP-6f is a good alternative to the GCaMP cell line. An aliquot of AAV6-CMV-GCaMP6f viral particles was kindly provided by the Eschenhagen lab in Hamburg to try and transfect our hiPSC-CMs (Saleem et al., 2020). The plasmid is ensembled by the lab and consists of the AAV6 backbone, which is known to infect cardiac cells relatively well and a cytomegalovirus (CMV) promotor that drives the GCaMP6f expression.

The transfection protocol was adapted from the Eschenhagen lab. In brief, human iPSC-CM (Cellular Dynamics International (N=1) and Axiogenesis (N=1), 5 wells per group) were plated according to the manufacturers protocol. Cells were transfected at day 2 after plating with a MOI ranging from 10^3-10^7 and in addition a negative control without transfection. After 3 days, medium with the virus was replaced for fresh culture medium. On days 6-10 GCaMP6f signals were recorded using the CellOPTIQ® system using the 480nm wavelength LED. Subsequently on day 10, cells were incubated with the fluorescent calcium indicator Fluo-4-AM (5 µM), which served as a positive control. Fluo-4 signals were also recorded with the 480nm LED.

Unfortunately, the transfection rates were not high enough and signals could only be recorded from some cells using the confocal microscope as shown in Figure 2.3. Moreover, no GCaMP-6f signals could be recorded on the CellOPTIQ system (Figure 2.5) and it is therefore unlikely that we could record signals on the *ex vivo* set-up, which uses an optical system with a lower NA.

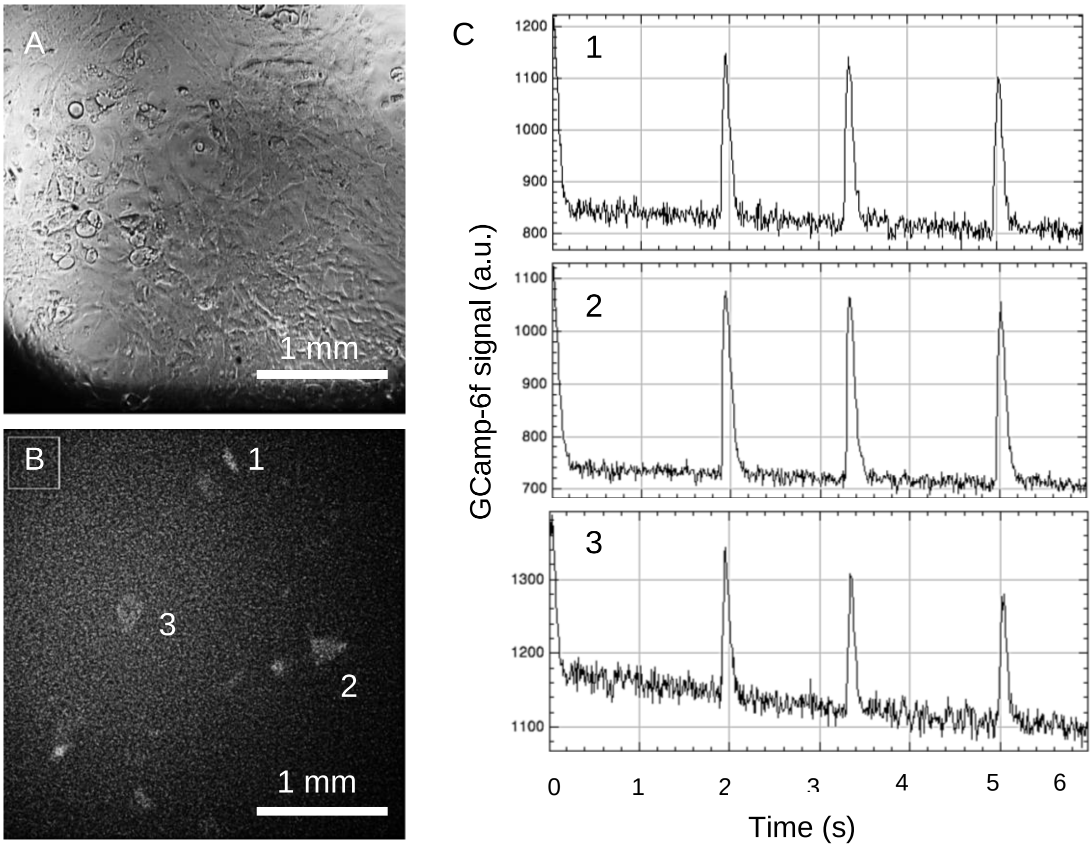

Figure 2.3 Confocal images showing from hiPSC-CMs transfected with AAV6-CMV-GCaMP-6f.
A) Brightfield image of hiPSC-CMs showing that the cells formed a monolayer. B) Fluorescent image (470nm Ex) of the same location as panel (A), showing 3 fluorescent cells – an indication of cells being transfected with AAV6-CMV-GCaMP-6f. C) GCaMP6F intensity in time from the same 3 cells indicated in panel (B). Image is taken on day 10 after plating. Cells were transfected with an MOI of 10^7, but other MOI’s had similar results. HiPSC-CMs were from NCardia (Cor.4U), however similar results were seen for CDI cells (ICell^2).

2.2.4 Fluorescent calcium dyes

2.2.4.1 Fluo-4, AM

As we were unable to record calcium transients using GCaMP-6f, it was decided to use calcium dyes instead. Fluo-4-AM is a fluorescent calcium indicator that is bright, has a high rate of cell permeation and has a large dynamic range and is therefore another candidate for reporting calcium concentrations (Gee et al., 2000).

Human iPSC-CM (Cor.4U, NCardia®) were plated and maintained according to the manufacturers protocol in a cell density of 30,000 cells/well (100,000 cells/cm^2, standard cell density). On day 7, cells were washed with BMCC culture medium (serum free). Then, cells were loaded with 5 µM Fluo-4, AM (Thermo Fisher Scientific, F14201) (1mM stock in DMSO) dissolved in BMCC medium and incubated for 20 min at 37°C, where after cells were washed with and kept in fresh BMCC medium. The Fluo-4 decay in time was measured on the CellOPTIQ system. Fluo-4 signals were recorded every 5 minutes for 3 hours (36 runs, $N_{wells} = 5$, $N_{experiment} = 1$) using the 480nm LED. Even though Fluo-4 is bright at the start of the experiment, this brightness is reduced to 50% after 1.5 hours (Figure 2.4). This is potentially not enough for implantation studies where lower NA optics are used and the light will be scattered by the myocardium. Therefore, Fluo-4AM is also unsuitable for implantation studies.

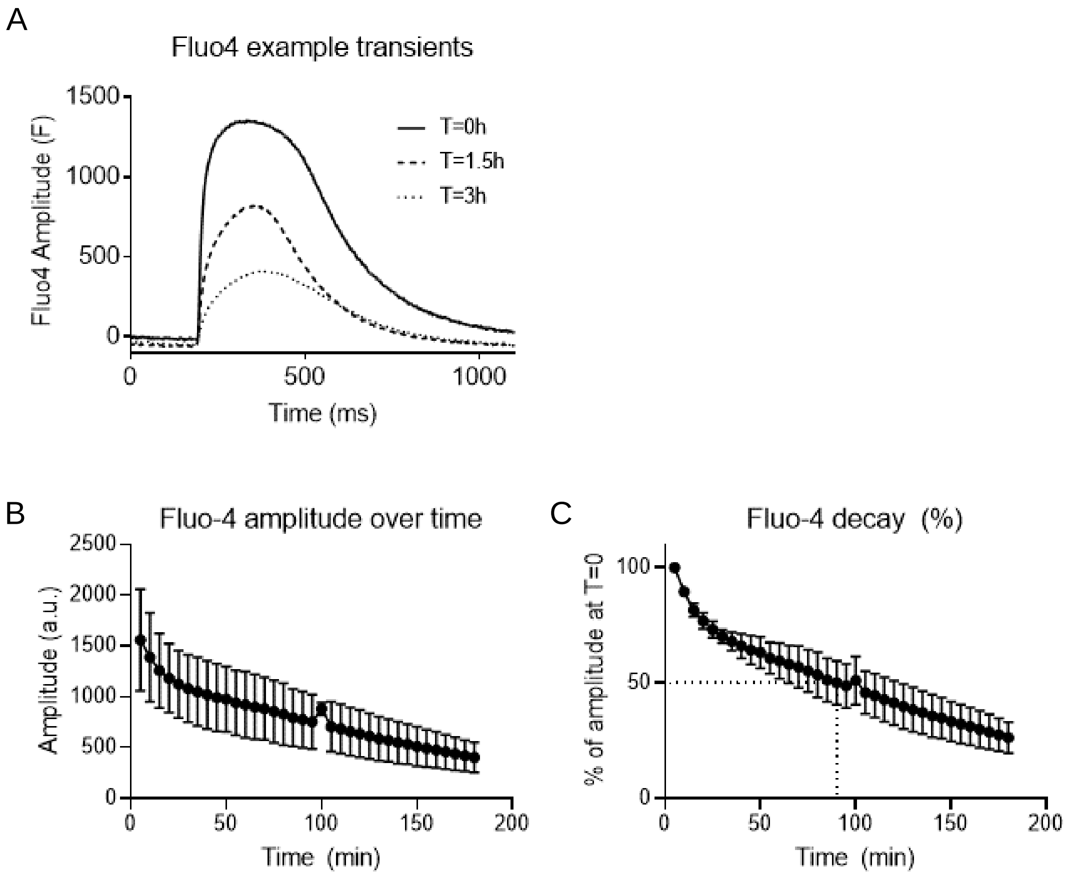

Figure 2.4 Fluo-4 brightness over time.
A) 3 example transients from the same location at different time points, namely at the start (T=0), halfway the experiment (T=1.5h) and at the end of the experiment (T=3). B) the amplitude of the Fluo-4 signal. C) the percentage of Fluo-4 signal compared to the start of the experiment. Results are from 3 independent experiments with 5 wells per experiment and plotted as mean±SD.

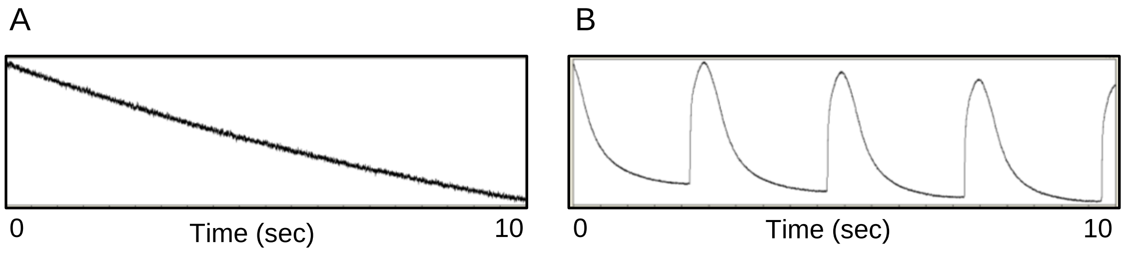

Figure 2.5 GCaMP-6f vs Fluo-4 signals recorded on the CellOPTIQ system.
A) GCaMP-6f signal. B) Fluo-4 signal. Results are taken from CDI cells (ICell^2) on day 11 after plating.

2.2.4.2 Cal-520^{TM}, AM

Cal520-AM (Ex/Em: 493/515) is a novel small molecule calcium indicator with impressive kinetics, brightness and a long-lasting stable amplitude signal and thus a long experimental window (Tischbirek et al., 2017, Tada et al., 2014). More importantly, it has the smallest effect on hiPSC-CMs functionality when compared to other calcium indicators (Kopljar et al., 2018) and is therefore a good candidate for *in vitro* and *ex vivo* studies.

HiPSC-CM were incubated in BMCC medium for 2-24 hours, where after they were incubated in BMCC with 0.02% pluronic acid-F127 (Biotium, 59000-F) (stock 10% w/v in H_2O) and 1, 3 or 5 µM Cal-520®, AM (AAT Bioquest, 21130) (5 mM or 1 mM stock in DMSO). Cal-520®, AM dye was incubated for 30 min at 37°C where after cells were washed with and kept in BMCC medium. Recordings were made on the CellOPTIQ system (paragraph 2.3).

2.2.4.3 Cal-590^{TM}, AM

Cal-590-AM is a small molecule calcium indicator similar to Cal-520, but it has slightly slower kinetics and a more red-shifted Ex/Em spectrum of 574/588 nm (Zhao Q, 2015). Because of the latter, Cal590-AM (AAT Bioquest, 20511) could be combined with fluorescent dyes that have a GFP-like Ex/Em spectrum, such as FV, and it could be used for 2-P-fluorescence (Tischbirek et al., 2017). The staining protocol is the same as for Cal-520-AM.

Table 2.3 Specifics of fluorescent calcium indicators

Dye	Molecular weight (g/mol)	Ex/Em (nm)	Dissociation constant (K_d, nM)	Reference
Cal520™-AM	1102.95	493/515	320	(Tada et al., 2014, Tischbirek et al., 2017, Lock et al., 2015, Kopljar et al., 2018)
Fluo-4AM	1069.95	494/506	335	(Gee et al., 2000, Lock et al., 2015)
GCaMP-6f	-	492/515	90	(Chen et al., 2013, Helassa et al., 2016, Lock et al., 2015)
Cal590™-AM	1266.81	574/588	561	(Tischbirek et al., 2017, Zhao Q, 2015)
Rhod-4-AM	1015.96	523/551	451	(Lock et al., 2015)

2.2.5 Dual fluorescent imaging with voltage- and calcium dyes

Because the ECG only provides a global measure of the electrical signal within the myocardium, it is useful to record the electrical activity from the myocardium directly surrounding the implantation site. Thus, it would be ideal to use two different voltage sensitive dyes to stain both the EHT and the myocardium, allowing for direct comparison of the electrophysiology of both tissues and therefore integration. However, the dynamic range and Ex/Em spectra of currently available dyes make this extremely challenging, especially when recording fluorescent signals from a small target tissue, such as the EHTs from this study.

Alternatively, differential combinations of voltage sensitive dyes and calcium indicators have been used *in vitro*, *in vivo* and *ex vivo* to study electrophysiology and calcium handling of the same tissue (Swift et al., 2019), or examine electrophysiological integration of implanted cells within the host tissue (Jackman et al., 2018, Gao et al., 2018). Here, combinations used are RH237 with Cal520-FF (Gao et al., 2018), RH237 with GCaMP6 (Jackman et al., 2018) and RH237 with Rhod2-AM (Swift et al., 2019). However, to our knowledge, FV has not been used in combination with a calcium dye despite its relatively high dynamic range and narrow Ex/Em spectrum.

The Ex/Em spectrum of the novel calcium indicator Cal590-AM (Paragraph 2.2.4.3), is 590/630 nm and could therefore be combined with FV (Ex/Em: 480/535 nm) as shown in Figure 2.6. The protocol for dual loading is practically a combination of the protocols for each dye. In brief, cells were incubated with BMCC medium prior to cell loading and subsequently incubated with FV (1:1000), pluronic acid (0.02%) and Cal590-AM (2µM) for 30 min at 37°C.

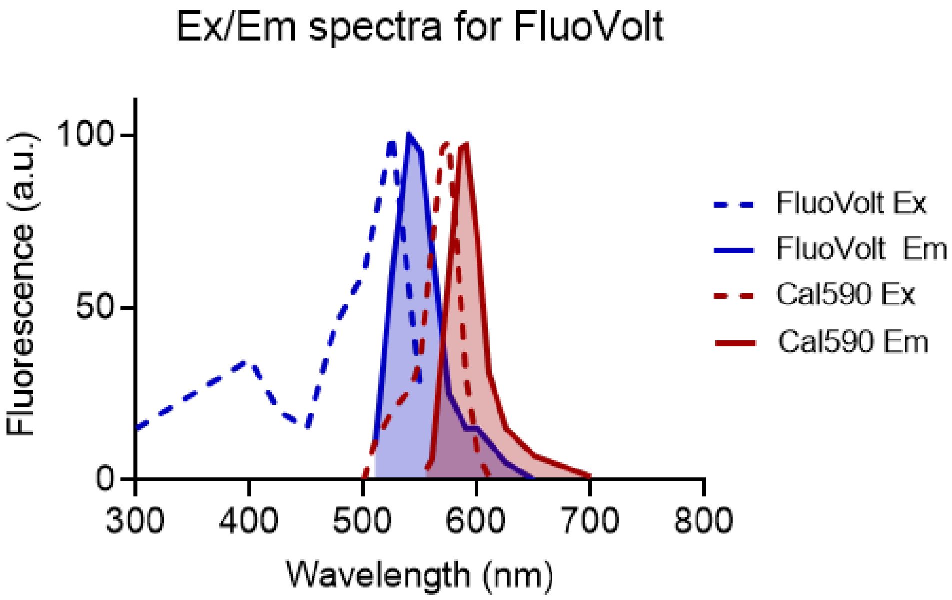

Figure 2.6 Combined Ex/Em spectra of FluoVolt and Cal590-AM.

2.3 CellOPTIQ: Voltage, calcium and contractility in one system

2.3.1 Background

The CellOPTIQ system is designed to record voltage, calcium and contractility transients from cardiac cells. An overview of the set-up is shown in Figure 2.7 and an overview of objectives used is shown in Table 2.6. During course of each experiment, culture dishes were placed in an on-stage incubator to maintain an environment with 5% CO_2 and 37°C. The system is set-up to record either calcium or voltage traces simultaneously with contractility recordings. Additionally, there is a possibility to electrically pace the cells at fixed rates, usually with 2 ms impulses at 40mV.

To assure alignment of signals, the amplitude of the brightfield light increases for a short amount of time (approximately 2 ms) in parallel with electrical pacing. This short peak is visible on channel 3 of the CellOPTIQ system and does therefore not interfere with recorded signals on channel 1 (FV and Cal520) and channel 2 (Cal590). However, a spike is visible on the recorded video frames for contractility, but because of their short nature, these can be filtered out during analysis, so only a small artefact remains (Figure 2.9B).

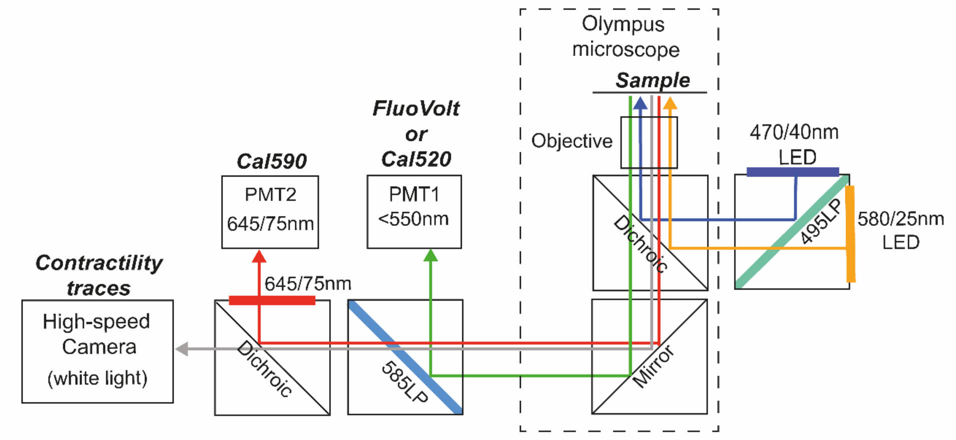

Figure 2.7 Diagram showing the filter set for fluorescent imaging of Cal520, FluoVolt and Cal590.
FluoVolt and Cal520 are excited using the 470/40nm excitation filter, where after emitted light is filtered by the dichroic 550LP filter. Cal590 is excited using the 580/25nm filter and emitted light is passed through the 550LP filter and subsequently reflected by a dichroic mirror and filtered through a 645/75nm emission filter. Fluorescent signals are recorded at 10kHz using PMTs. The dichroic mirror passes white light allowing for simultaneous contractility recordings. Cal590 and FluoVolt can be recorded simultaneously, enabling simultaneous voltage, calcium and contractility recordings.

2.3.2 Fluorescence signals representing APs and CaTs

APs and calcium transients (CaTs) were recorded using a 40x objective (NA = 0.6), correct filter sets, photomultiplier tube (PMT) and a sensor with an acquisition rate of 10kHz. Recorded traces were analysed using CellOPTIQ software, which calculated the beating frequency along with various parameters by averaging multiple transients, as shown in Figure 2.8A and B. For APs these were: the depolarization time (TRise) and action potential duration at 90% of repolarisation (APD_{90}). From the CaTs, only the calcium transient duration at 50% of the amplitude (CaT_{50}) was measured.

To measure contractility, bright field image stacks are recorded and analysed using the MM contractility tool (Sala et al., 2018). Besides the beating frequency, the following parameters are measured during contractility analysis: contraction time (Up_{90}), relaxation time (Dn_{90}), amplitude and the contraction duration at 50% of the amplitude (CD_{50}) as shown in Figure 2.8C.

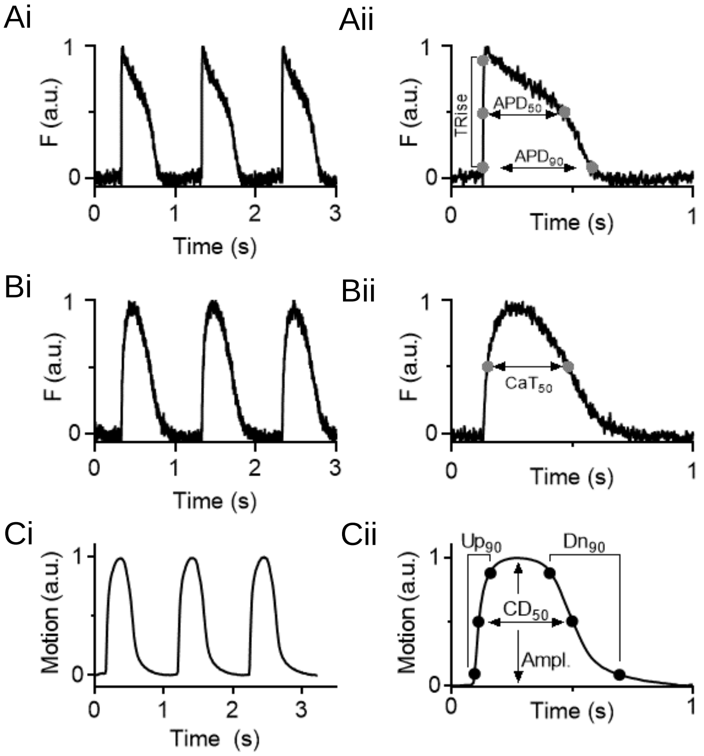

Figure 2.8 Voltage, calcium and contractility parameters explained.
A) APs in sequence (Ai) and isolated (Aii). AP parameters are the TRise, APD_{50} and APD_{90}. B) CaTs in sequence (Bi) and isolated (Bii). CaT parameter is the CaT_{50}. C) Contractility traces in sequence (Ci) and isolated (Cii). Contractility parameters are Up_{90}, Dn_{90}, CD_{50} and the amplitude.

2.3.3 Contractility recordings

Recordings for contractility were made on various timepoints (day 0-7) and cells were kept in a controlled environment of 37°C and 5% CO_2, unless stated otherwise. Brightfield video recordings were made using a high-speed camera (Hamamatsu ORCA-flash 4.0 V2 digital CMOS camera C11440-22CU) (100 fps, 600 x 600 pixels) and either the 4x (NA = 0.13), 10x (NA = 0.4) or 40x (NA = 0.6) objective (Table 2.6).Video frames were analysed using the open source MUSCLEMOTION (MM) contractility algorithm published by Sala et al (Sala et al., 2018), which measures movement as a function of pixel intensity and has been verified against a number of other measures of mechanical function (Sala et al., 2018). The beat frequency, amplitude, contraction time (Up_{90}), relaxation time (Dn_{90}) and the contractility duration at 50% of the peak (CD_{50}) were measured.

2.3.4 Measuring voltage, calcium and contractility simultaneously

The vectors of ECC, voltage, calcium and contractility, were measured simultaneously to find their direct relationship. HiPSC-CMs were loaded with FV (voltage) and Cal590-AM (calcium) for 30 min at 37°C. Transients were recorded simultaneously, by automatically alternating the respective LEDs on/off with 1 ms intervals, so that only one LED emits light at a time. Because of the fast turnover and fast acquisition rate of 10 kHz, a high-resolution recording can still be achieved. Because white light is used for the contractility recordings, a red filter was placed in front of this LED to prevent PMT saturation. Example traces of simultaneously recorded voltage, calcium and contractility traces during an *in vitro* experiment on the CellOPTIQ system are shown in Figure 2.9A and B.

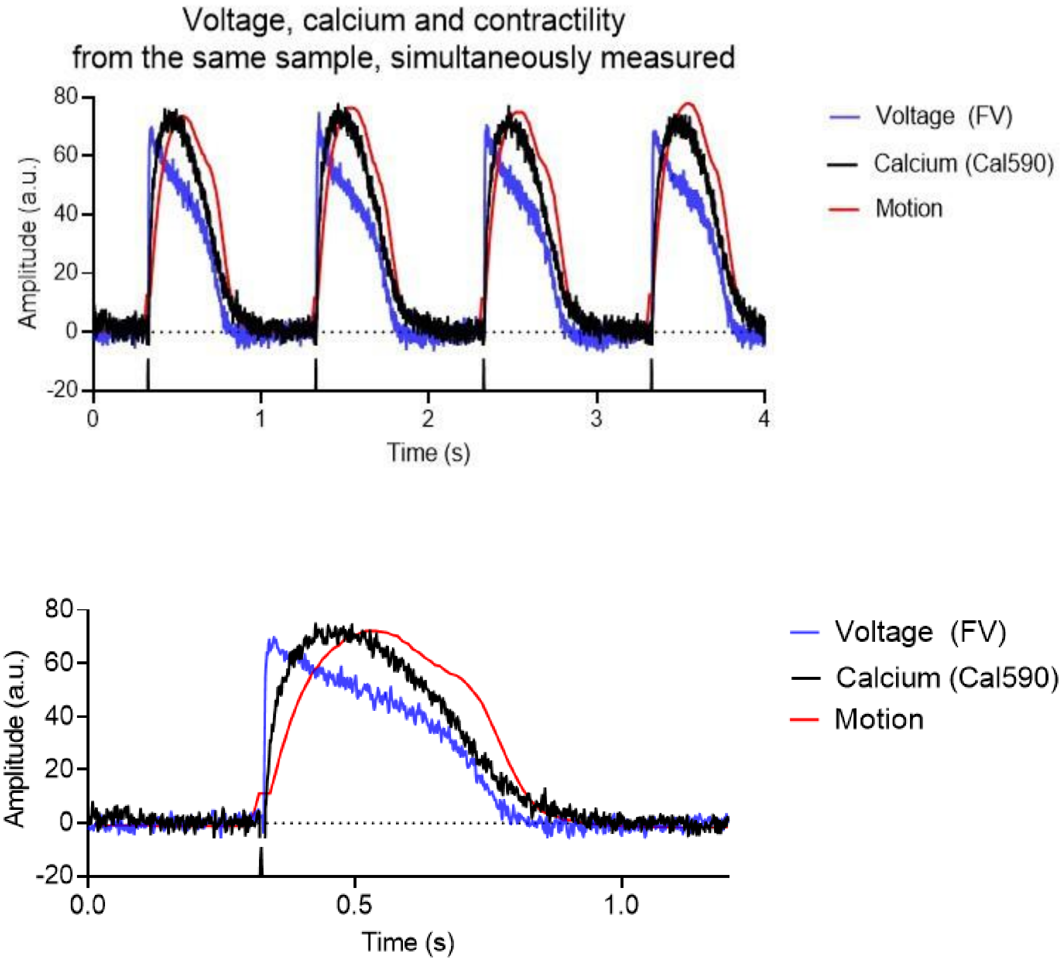

Figure 2.9 Simultaneous recorded voltage, calcium and contractility traces.
A) Multiple-second recording of voltage (FV, blue), calcium (Cal590, black) and contractility (bright light, red) transients. B) close-up of one ECC cycle, emphasizing the delay between the different events. Transients were recorded on the CellOPTIQ system. HiPSC-CMs were paced at 1Hz.

2.4 Intact rabbit heart experiments

2.4.1 Animals

For this work, healthy adult male New Zealand White rabbits (2.5-3.5 kg) were used. All animal experiments were approved by the British council for Animal Research and were conducted in accordance with the UK Animals (Scientific Procedures) Act 1986 under project Licence (7008835). Animals were purchased from Envigo (Huntingdon, UK). All rabbit heart isolations were done by technicians Aileen Rankin and Michael Dunne.

2.4.2 Langendorff perfusion set-up

Isolated Langendorff-perfused hearts are widely used to investigate cardiac electrophysiology as it is a relatively straightforward technique. Its design keeps the heart stable for a couple of hours, thus giving us enough time to investigate the physiology of EHTs post-implantation.

Rabbits were anesthetized with an intravenous (IV) injection of 0.5mL/kg Euthatal (200mg/mL, sodium pentobarbitone, Rhoe Merieux Inc, Athens, GA, USA) mixed with 500 U of heparin (CP Pharmaceutical Ltd, Wrexham, UK) via the left marginal ear vein. The absence of pain reflexes was checked by pinching in between the toes of the rabbit and, once confirmed, the heart was excised and placed into ice cold heparin substituted Tyrode's solution to inhibit muscle contraction. Hearts were subsequently placed onto the Langendorff perfusion system with care to avoid air bubble formation that could cause in ischemia when entering the coronary arteries. During the experiment, the heart was perfused with Tyrode's solution at a constant flow of 40 ml/min, unless otherwise indicated. A simplified diagram of the whole setup is shown in Figure 2.10A.

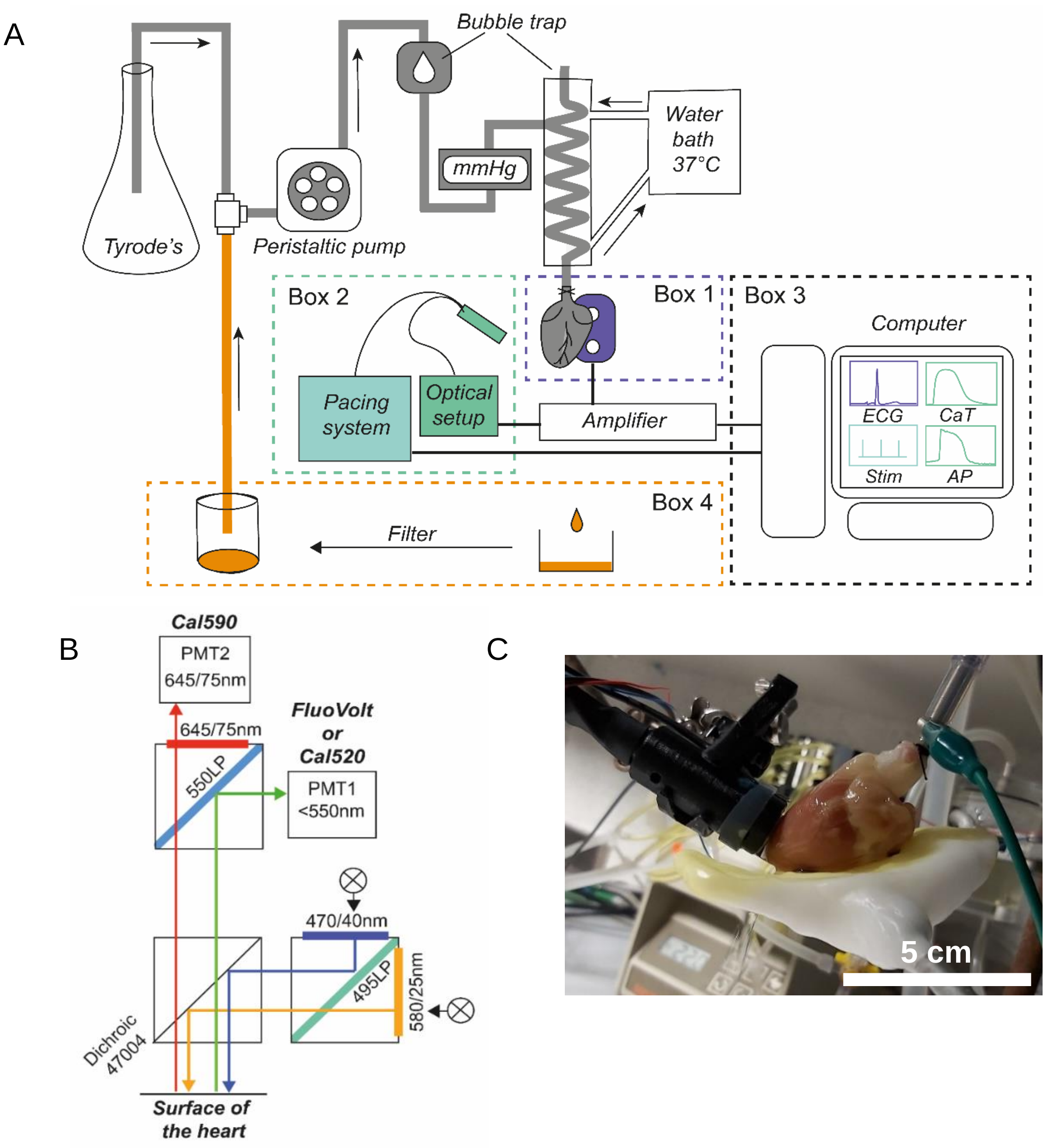

Figure 2.10 Langendorff perfusion set-up.
A) Simplified diagram of the total setup. Parts are highlighted in different colours and/or boxes. The general setup (grey), consists of the heart being placed on the rig, where warmed (37°C) Tyrode's solution is pumped from a 5L conical flask towards the heart using a peristaltic pump. Two bubble traps are placed in the system to prevent air bubble formation, that could induce blockage of coronary capillaries. Additionally, there is a pressure meter (mmHg) to monitor the systemic pressure. The heart is placed onto a cradle that contains two electrodes (box 1) to record the ECGs. Fluorescent signals are recorded using the lightguide and optical setup (box 2) which is explained in more detail in diagram (B). Pacing electrodes were attached to the base of the light guide for field stimulating. Fluorescent signals, as well as the ECGs, were amplified before recording and displayed on the computer along with the simulation impulses (box 3). During FV incubation and recirculation, the effluent of the heart is collected, filtered and recirculated through the system (box 4). B) A simplified, but detailed diagram depicting the optical setup for the *ex vivo* experiments (box 2), including all filters used. C) A photo of the heart attached to the rig and placed on top of the cradle. The light-guide is placed on the surface of the heart as it would be during fluorescent recordings and/or electrical pacing of the heart and EHTs.

Once the heart was attached to the Langendorff set-up, hearts were incubated with 10 nM blebbistatin (Stock in DMSO, 1760, Tocris). Blebbistatin inhibits binding of myosin-II to the actin filaments, by blocking the adenosine triphosphatases (ATPases) in an actin-detached state (Kovács et al., 2004). In this way, blebbistatin pharmacologically uncouples excitation-contraction pathways and minimizes motion artefacts. An alternative excitation-contraction uncoupler is 2,3-butanedione monoxime (BDM), however, BDM affects the AP time-course and hearts incubated with BDM are more susceptible for sustained arrythmias and is therefore unsuitable for these studies (Lou et al., 2012). After blebbistatin incubation, experimental procedures could start.

To record electrocardiograms (ECGs) the rabbit heart was placed into a cradle with 2 electrodes as shown in Figure 2.10A and C. Fluorescent signals from the EHT (calcium transients) or the heart (action potentials) were recorded using the optical setup (Figure 2.10B), including a light guide (NA = 0.2), LEDs, excitation-, emission-, dichroic filters, PMTs and the LabChart software (v8.1.16, AddInstruments) (Figure 2.10A).

2.4.3 Tyrode's solution

Tyrode's solution with 25 mM glucose is used to perfuse the heart during the experiment. To assure a pH of 7.4, the Tyrode's solution is additionally buffered with 5 mM HEPES. Sodium acetate, glucose, $CaCl_2$ and HEPES are added to the solution on the day. $CaCl_2$ is added after bubbling the solution with 95% O_2 and 5% CO_2 for minimal 20 min, otherwise, calcium could precipitate from the solution and cause obstructions in the coronary vasculature of the heart, resulting in ischemia. Solutions were filtered prior to cardiac perfusion. An overview of all compounds compromising Tyrode's solution can be found in Table 2.4.

Table 2.4 Tyrode's solution composition

Compound	Volume for 10L (g)	Final concentration (mM)
NaCl	53.94	93
$NaHCO_3$	16.8	20
Na_2HPO_4	1.42	1
$MgSO_4$	2.463	1
KCl	3.72	5
$C2H_3NO_2$ (sodium acetate)	16.4	20
D-Glucose (dextrose)	45.15	25
$CaCl_2$ (1M solution)	18 ml	1.8
HEPES (500 mM stock, pH 7.4 @ 37°C)	100 ml	5

2.4.4 Measuring Time$_{R-T}$ from unpaced and paced rabbit hearts

During intact rabbit heart experiments, the heart is electrically paced using two electrodes. This electrical impulse can be observed in the ECG as a peak with an amplitude many times larger than the ECG. Further, the electrical stimulus changes the ECG time-course, so that the time-course is different from that of ECGs from unpaced hearts, as shown in Figure 2.11. Nonetheless, the R-wave and T-wave are still distinguishable and thus the Time$_{R-T}$ can be calculated in both paced and unpaced rabbit hearts.

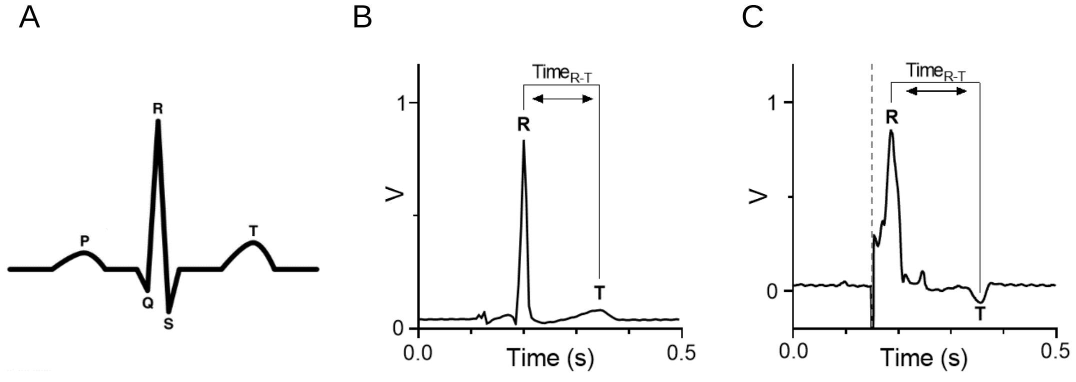

Figure 2.11 Method of calculating Time R-T.
A) A classic multiple-lead ECG. B) An ECG trace from an unpaced rabbit heart used for baseline recordings. C) An ECG trace from a paced rabbit heart at 2.5 Hz (400ms interval). Dotted gray line indicates pacing stimulus. Traces are normalized for better comparison. R-wave and T-wave are indicated with an R and T respectively.

2.5 Fluorescent immunochemistry

Fluorescent immunohistochemistry is an imaging method that uses primary and secondary antibodies, tagged with a fluorescent tag, or a fluorescent probe, to target and visualize specific proteins of interest in tissue slices or cell cultures.

For immunofluorescence, a relatively standard protocol was used. In brief, cells were fixed for 10 minutes with 2% paraformaldehyde (PFA), washed 3x with PBS and permeabilized with 0.2% Triton X for 10 minutes at room temperature. In the case of membrane targeted antibodies, cells were incubated with those before permeabilization. Then, cells were washed 3x with 1% BSA/PBS, where after antigens were blocked with 10% goat serum in 1% BSA/PBS for 1.5 hour at room temperature, to avoid background noise during imaging, and washed again 3x with 1% BSA/PBS. Then, the primary antibody was diluted in 1% goat serum in 1% BSA/PBS and incubated overnight at 4°C. The next day, cells were washed 3x with 1% BSA/PBS, where after the secondary antibody was diluted in PBS and incubated for one hour at room temperature. DAPI was used to stain the cells, but depending on the brand, was included during the incubation with the secondary antibody, or incubated for 2 min afterwards. Finally, cells were washed 3x with PBS to remove all excess antibodies and DAPI.

An overview of antibodies and probes is given in Table 2.5. Images were made using either the EVOS2 FL Auto or the confocal microscope. The objectives used are given in

Table 2.6. Image analysis was done using ImageJ v1.51j8 or CellProfiler v3.0.0.

Table 2.5 Overview of used antibodies and probes

Name	Company	Category number	Dilution
Primary antibodies			
Rabbit-anti-Sox2	Stemgent	09-0024	1:100
Rabbit-anti-Oct4	Stemgent	09-0023	1:100
Rabbit-anti-Nanog	Stemgent	09-0020	1:100
Rabbit-anti-α-actinin	Abcam	Ab137346	1:50
Mouse-anti-α-actinin	Sigma	A7732	1:500
Mouse-anti-α-actinin	Abcam	Ab9465	1:200
Mouse-anti-cTnnT	Abcam	Ab8295	1:200
Mouse-anti-Integrin α2	R&D	MAB1233	?
Rabbit-anti-Integrin α5	Abcam	Ab150361	1:200
Rabbit-anti-Connexin 43	Abcam	Ab11370	1:100-1:10000
Mouse-anti-N-Cadherin	Thermo Fisher Scientific	MA1159	1:500
Secondary antibodies			
Dialight-488 Goat-anti-Rabbit	Thermo Fisher Scientific	35552	1:200
Alexa Fluor-488 Goat-anti-Mouse	Invitrogen	A11001	1:500
Alexa Fluor-647 Goat-anti-Mouse	Invitrogen	A21235	1:500
Alexa Fluor-488 Goat-anti-Rabbit	Invitrogen	A11034	1:500
Alexa Fluor-647 Goat-anti-Rabbit	Invitrogen	A21245	1:500
Probes			
Wheat Germ Agglutinin-Alexa 594 (NB: added prior to permeabilization)	Invitrogen	W11262	1:100
Rhodamine Phalloidin (conjugated F-Actin)	Thermo Fisher Scientific	R415	1:50
Nuclear stains			
Nucblue fixed cell stain	Life Technologies	R37606	2 drops in 1 ml
DAPI	Thermo Fisher Scientific	62247	1:1000

Table 2.6 Overview of objectives used on the EVOS microscope and CellOPTIQ

Objective	Magnification	Numerical aperture (NA)	Working distance (mm)
EVOS			
EVOS^{TM} Phase-contrast	10x	0.25	9.2
EVOS^{TM} Plan Fluorite	10x	0.30	8.3
EVOS^{TM} Phase-contrast	20x	0.40	3.1
EVOS^{TM} Plan Fluorite (LWD)	40x	0.65	2.8
EVOS^{TM} Plan Fluorite (SWD)	40x	0.75	0.72
CellOPTIQ			
Olympus PLN2X	2x	0.06	-
Olympus UPLFLN4X	4x	0.13	17.0
Olympus UPlanSApo	10x	0.4	3.1
Olympus LUCPlanFL N	40x	0.6	2.70-4.00
Olympus UPlanSApo	40x	0.95	0.18
Whole heart set-up			
Light guide	NA	0.2	

2.6 Statistical analysis

All data are expressed as mean ± standard deviation (SD). Comparison between multiple groups of data was made with a one-way ANOVA and followed by the appropriate *post hoc* test for that data set. Data was paired when appropriate, however, sometimes missing values prohibited the ability to pair data during statistical tests. A two-tailed p-value less than 0.05 was considered significant. All statistical analysis was done using Graphpad Prism (version 8.0.2). Group sizes are denoted as N for the number of experiments and n for the number of samples. Here, samples could be hydrogels, monolayers or dishes.

The Brown Forsythe and Bartlett's Test showed significance meaning that the data was nonequally distributed. Therefore, a Kruskal Wallis test was performed with a Dunn's multiple comparison test as Post Hoc test. Groups were compared to both the centrifuged control group and the non-centrifuged control group. A p-value <0.05 was considered statistically significant.

Chapter 3 Development of 2D hiPSC-CM patches

3.1 Introduction

Cardiac cells and/or biomaterials can be used to develop engineered heart tissues (EHTs), which in turn could be implanted into the myocardium.

EHTs are commonly designed to cover major parts of the infarct zone and are therefore quite large (cm-scale). In order to establish an EHT of sufficient size, these constructs contain large numbers of cells, namely tens of millions of cells each (Jackman et al., 2018, Gao et al., 2018, Weinberger et al., 2016, Kadota et al., 2020). This means that perhaps hundreds of millions of cells are needed for a complete study to test various conditions associated with cell integration and survival. Labs investigating such features typically require systems in place to generate many millions of hiPSC-CMs and many labs have successfully established protocols for hiPSC differentiation into a pure population of CMs (Breckwoldt et al., 2017, Lian et al., 2013, Burridge et al., 2015). However, these are expensive, laborious and time-consuming protocols. Moreover, small differences in culture protocols, such as the type of coating proteins, growth factors or donor cells used, affect the differentiation efficiency and functionality of the hiPSC-CMs (Prajapati et al., 2021) and result in batch-to-batch variations as well as variations between different labs (Mannhardt et al., 2020, Prajapati et al., 2021).

The alternative is using a commercial hiPSC-CM cell line, where all differentiation and culture protocols are done by the company as well as the quality control (Huo et al., 2017). Moreover, commercial cells have a minimal batch-to batch variation which allows for better comparison between experiments and between labs. The biggest disadvantage is their price tag of approximately $2,000 for 5 million cells, and this makes them an unattractive cell source for larger EHTs. For example, for study with 25 EHTs, where each EHTs consists of 10 million cells, the costs of this study would be around $100,000 for cells alone.

The development of smaller EHTs that contain less than 50,000 cells could be a solution to overcome these problems. For example, the same study with 25 small EHTs of 50,000 cells each, would cost $500 instead of $100,000, only 0.5% of the initial costs. In this way, more constructs can be used to test more factors involved with cellular integration and survival in the myocardium for an efficient use of resources. To investigate whether EHT size affects graft integration and survival, small EHTs could be upscaled by simply increasing cell sheet diameter, and/or stacking the cell sheets (Matsuo et al., 2015a, Miyagawa et al., 2005).

Even though large EHTs have been investigated extensively there is no evidence that large EHTs have a benefit over multiple smaller EHTs while there is evidence that large EHTs have difficulty coupling to the host myocardium (Weinberger et al., 2016, Matsuo et al., 2015a, Shiba et al., 2014). In contrast, cell delivery through injection has shown to improve cellular integration and electrical coupling (Gerbin et al., 2015), suggesting that single cells or cellular aggregates are more able to form molecular connections to the host myocardium. However, besides construct size, graft size is determined by the number of cells implanted, but also by the number of cells that survive (Weinberger and Eschenhagen, 2020). Studies that transplanted hiPSC-CMs by injection show that only a fraction (<10%) of the implanted cells is retained around the implantation site; the majority migrates or dies soon after implantation (Zhao et al., 2019). Thus, neither implantation of hiPSC-CMs through injection or large EHTs has optimal results. Therefore, a transplantation method with an optimal graft size vs cell retention is therefore needed, for example small EHTs of mm-scale with <50,000 cells.

In this chapter, commercially available hiPSC-CMs will be used to develop small monolayers (≤3 mm) that could be used as building blocks for small EHTs. The focus will be on the success rate of the production method, the number of cells within the patch, and the consistency of the patch. Further, it is important to assess whether the development of the small patches does not have any adverse effect on its physiology. Therefore, the electrical activity and contractility of the hiPSC-CMs will be compared to monolayers produced using the standard culture method.

3.1.1 Specific aims

The aim of this chapter is to find a method for the development of small (≤3mm) hiPSC-CM monolayers that will form the building blocks for the small EHTs. This main aim can be broken down into sub-aims:

1) Can we use silicone stencils to create 1, 2 and 3 mm monolayers and what is the success rate?

2) What is the morphology and cell retention of the monolayers and is there a difference when using various stencil sizes or cell seeding densities?

3) Is the functionality of the hiPSC-CM within the monolayers comparable to those within the standard 96 well-plate?

3.2 Methods

3.2.1 Creation of small 2D micro-patches

Small 2D micro-patches are desired for two different reasons. Firstly, aggregates of a relatively small number of cardiac cells have shown to enhance cellular integration into the host myocardium over larger constructs, e.g. cardiac patches (Gerbin et al., 2015). Secondly, small patches could increase the experimental throughput and limit the experimental costs.

3.2.2 Fabrication of stencils

To create small cardiac micro-patches (1, 2 or 3 mm in diameter), polydimethylsiloxane (PDMS, silicone) inserts were designed and developed by Dr. Xie He. PDMS is widely used for cell culture purposes, for example as material for inserts or as a softer substrate (Sengupta et al., 2019, Pandey et al., 2018).

In brief, a mould for the stencils was created using a 4x4 array of magnets, stainless steel pegs with a diameter of 1, 2 or 3 mm and a 96 well plate as shown in Figure 3.1A-C. The pegs were made by the UoG workshop. PDMS (Sylgard-184, 761036, Sigma) was prepared by mixing component A and B, in a 1:10 ratio. A vacuum pump was used to extract the air from the silicone, where after the PDMS was poured into the mould and allowed to set for a couple of hours at 60°C. When set, stencils were removed from the mould and cut to ±7 mm heights, to simplify cell seeding with a large enough lumen for the cell suspension. To create stencils with different outer diameter, a half-area (Ø = 5 mm) or a standard 96-well plate (Ø = 6.4 mm) were used for thin and thick stencils, respectively (Figure 3.1D and E).

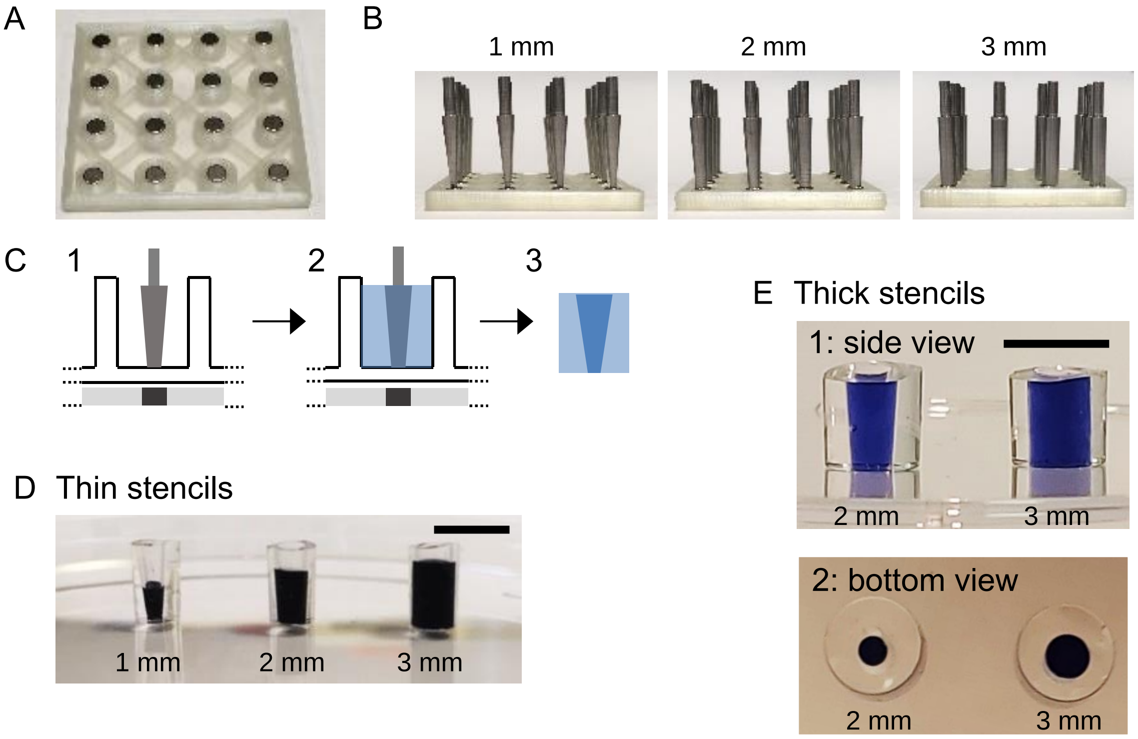

Figure 3.1 Manufacturing of silicone stencils.
A) 4x4 3D printed grid with magnets. B) 1, 2 and 3 mm stainless steel pegs on top of the 4x4 grid. C) Diagram of stencil preparation using PDMS. D) Examples of 1, 2 and 3 mm thin stencils. E) Examples of 2 and 3 mm thick stencils, where image 1 shows the side view of the stencils and image 2 shows the bottom view of the stencils with the lumen area. Scalebars represents ~7 mm. Trypan Blue was used as a colorant.

3.2.3 hiPSC-CM seeding into stencils

Before cell seeding, stencils were sterilized with 70% EtOH overnight and exposed to UV light for another 20 minutes. Excess fibronectin was removed from the culture plates, obtaining a dry culture well so tight seal is created between the culture dish and the silicone stencil. HiPSC-CMs were thawed and maintained as described in paragraph 2.1.2, however, seeding into the stencil was done using long and thin 200 µl pipette tips that are also used for western-blots.

Different cell seeding densities were used depending on experimental needs and stencil diameter. As manual cell counting using the haemocytometer can be unreliable when using very concentrated or diluted cell suspensions, aliquots of the 4x cell density were diluted 4 times (5 µl suspension with 15 µl of medium) prior to cell counting to assure correct seeding densities. A diagram of hiPSC-CM seeding is shown in Figure 3.2 and an overview of all cell seeding densities and cell suspension is shown in Table 3.1.

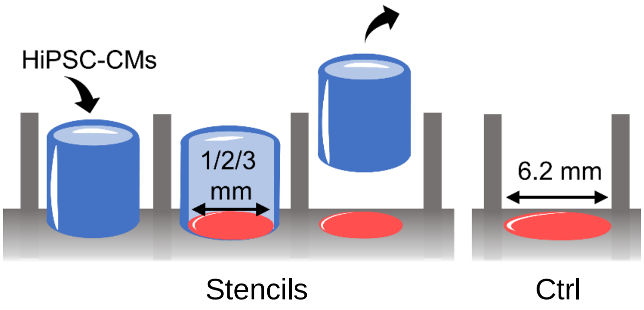

Figure 3.2 Diagram showing the procedure of seeding hiPSC-CMs into stencils in comparison to the control, which is a standard 96 well-plate.

Table 3.1 Overview of cell number for Cor.4U (NCardia) and ICell/ICell^2 (FCDI) hiPSC-CM seeding into stencils.

HiPSC-CM source		**Cor.4U (NCardia)**			**ICell and ICell^2 (FCDI)**		
Cell seeding density		1x	2x	4x	1x	2x	4x
Stencil size	Area (mm^2)						
1 mm	0.8	756	1,512	3,023	1,260	2,520	5,040
2 mm	3.1	3,023	6,047	12,094	5,039	10,078	20,156
3 mm	7.1	6,803	13,605	27,211	11,338	22,675	45,350
Full well of 96 well-plate	31.2	30,000	60,000	120,000	50,000	100,000	200,000

Seeding volume stencils (µl)	7	14	30	7	14	30
Cell suspension (cells/ml)	225,000	450,000	900,000	375,000	750,000	1,500,000

3.2.4 Assessment of 2D patch morphology

3.2.4.1 Fluorescent immunochemistry

Cells were fixed for 10 minutes with 2% paraformaldehyde (PFA), washed 3x with PBS and permeabilized with 0.2% Triton X for 10 minutes at RT. After 3 wash steps with 1% BSA/PBS, cells were blocked with 10% goat serum in 1% BSA/PBS for 1.5 hour at RT and subsequently washed 3x with 1% BSA/PBS. Phalloidin-Rhodamine (R415, Invitrogen, 1:50) was used as an F-actin stain and was incubated for 1.5 hours at RT, followed by a 2-minute incubation with DAPI (R37606, Life technologies, 1:1000). Cells were washed and stored in PBS until imaging. Images were made with the RFP, DAPI and brightfield channels, using the EVOS2 FL Auto and a 10X objective (Plan Fluor 10X/0.3, ∞/1.2).

3.2.4.2 Image analysis using CellProfiler Software

CellProfiler software (v.3.0.0) was downloaded from the website and a pipeline was created for image analysis. First, pictures were reduced in size and cropped to the desired size. Primary objects (nuclei) were located based on size and pixel intensity and the secondary objects (cells) were located based on the primary objects and pixel intensity. Because the aim is to calculate the area covered by cells, it was not important where borders between cells were drawn. The perimeter of the 2D patch was calculated by smoothening the RPF-channel picture (displaying cells), and a primary object was located based on size. Output from all the objects (nuclei, cells and 2D patch perimeter) were collected in an excel sheet. The pipeline was created to work on all images, however, the pipeline needed some adaptations for a small selection of images, e.g. threshold for pixel intensity. Also, all images were cropped to exclude a ring of scattered fluorescent light on the outside of the well, though some images needed more cropping.

3.2.4.3 Calculations for 2D patch coverage and size

The total area of the silicone stencils with a lumen diameter of 1, 2 or 3 mm (N=10) was measured, using three methods: 1) ink stamp method, 2) addition of fluorescein and 3) making a bright field image. For the ink stamp method, the bottom side of the stencil was coloured with dark ink, pressed against a 10 cm dish and imaged. All images were made using the EVOS 2 FL Auto microscope using a 10X objective (Plan Fluor 10X/0.3, ∞/1.2) and with either the GFP settings (method 2) or bright field settings (methods 1 and 3). The area of the stencil was calculated using ImageJ.

3.2.5 Contractility recordings

Recordings for contractility were made on various timepoints (day 0-7) and cells were kept in a controlled environment of 37°C and 5% CO_2, unless stated otherwise. Brightfield video recordings were made using a high-speed camera (Hamamatsu ORCA-flash 4.0 V2 digital CMOS camera C11440-22CU) (100 fps, 600 x 600 pixels) and either the 4x (NA = 0.13), 10x (NA = 0.4) or 40x (NA = 0.6) objective.Video frames were analysed using the open source MUSCLEMOTION (MM) contractility algorithm published by Sala et al (Sala et al., 2018), which measures movement as a function of pixel intensity and has been verified against a number of other measures of mechanical function (Sala et al., 2018). The beat frequency, amplitude, contraction time (Up_{90}), relaxation time (Dn_{90}) and the contractility duration at 50% of the peak (CD_{50}) were measured.

For spatiotemporal analysis, video frames were subdivided into 30x30 grid squares, each of approximately 40x40 µm, and each analysed with the MM algorithm, resulting in a spatiotemporal analysis and is explained in Figure 3.3. Additional measurements were derived from the spatiotemporal analysis: the number of peaks within one time-course and the start time (TStart), measured as the time to 50% of the amplitude during the contraction phase. Dispersion (spread) of TStart and CD_{50} values was estimated as the difference between 10th and 90th percentile, to exclude outliers (Figure 3.3E).

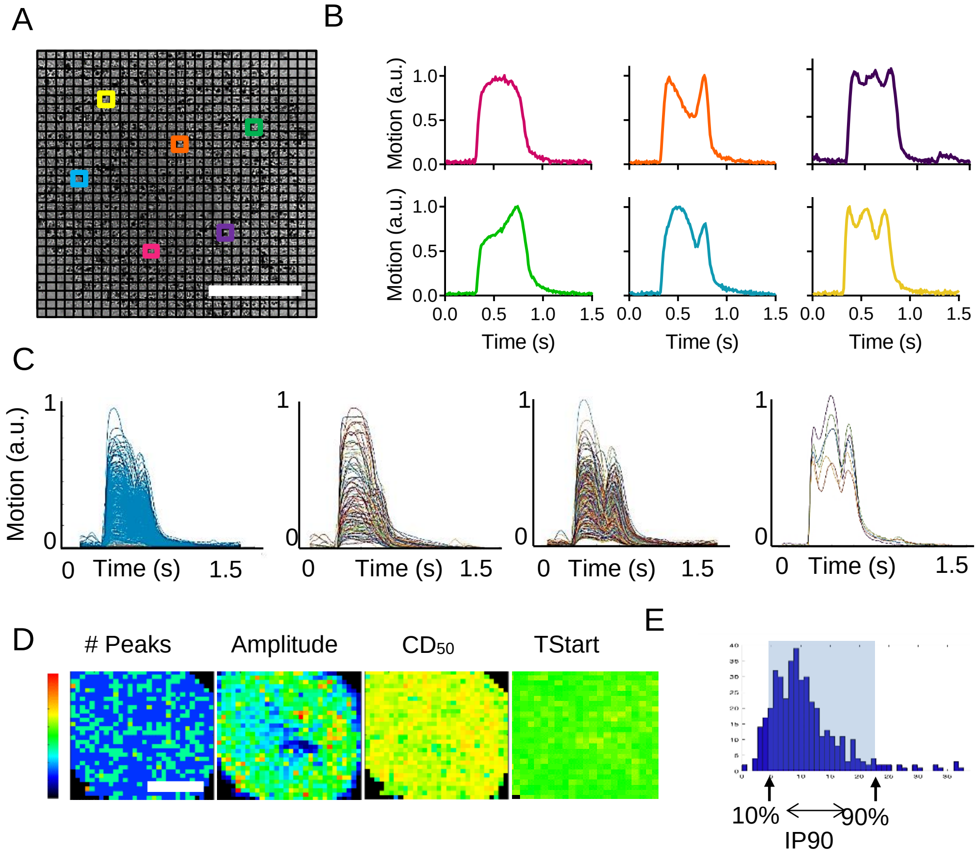

Figure 3.3 Spatiotemporal analysis of the total hiPSC-CMs monolayer.
A) Video frames were subdivided into 30x30 grid squares. Each grid square (~40x40 µm) was analysed using the MM algorithm (Sala et al. 2017)(Sala et al., 2018), resulting in 900 individual data points. B) Various contractile profiles are seen at different locations within one monolayer as represented by the colour-schemed traces (panels A and B). We observed transients containing one peak (Bi and Bii), two peaks (Biii and Biv) and more than two peaks (Bv and Bvi). C) All traces obtained from one video. D) All traces obtained from one video with one peak. E) All traces obtained from one video with two peaks. F) All traces obtained from one video with more than two peaks. G) Values for various measurements are plotted in a heatmap. (i) the number of peaks (scalebar 1-3 peaks), (ii) amplitude (scalebar 0-8000 a.u.), (iii) contraction duration at 50% of the amplitude (CD$_{50}$) (scalebar 0-1200 ms), and (iv) the start times (TStart) (scalebar 0-600 ms). H) the 10th-90th percentile difference (IP90) was calculated for CD$_{50}$ and TStart values to obtain a more realistic average within one group and thus allowing us to compare different groups. Scalebars represent 1 mm.

3.3 Results

3.3.1 Morphology of 2D micro-patches

Three stencil sizes of 1, 2 and 3 mm were tested to create small hiPSC-CMs monolayers of 1 2 and 3 mm in diameter, respectively. Ideally, the 2D patch has a circular shape, with an area similar to the area of the stencil. This means that for 2D patches made with either the 1 mm, 2 mm or 3 mm stencils, the monolayer surfaces should in theory be 0.79 mm^2, 3.14 mm^2 and 7.07 mm^2, respectively.

The shape of the hiPSC-CM patch depends on the cell seeding performance and the tight seal between the silicone stencil and the culture plate. Touching the silicone with the pipette tip during cell seeding might compromise the seal between the stencil and the culture plate and induce a leak. Additionally, a small air bubble could form on the bottom of the stencil, preventing cell adhesion on those locations. These situations might result in bigger or smaller patches.

The success rate of the cell seeding procedure was assessed. The appearance of the hiPSC-CMs monolayers was divided in 4 categories: 1) a good patch with a circular shape and correct size, 2) a patch smaller than expected, 3) a larger patch and 4) no patch at all. The success rate was calculated accordingly for every stencil size.

As shown in Figure 3.4, more than half of the 2 mm and 3 mm patches were good (53.4% and 66.7%, respectively), where only 28.9% of the 1 mm patches were considered good. Importantly, in 34.4% of the 1 mm stencils did not result in a 2D patch, in comparison with 2.2% and 0% of the 2 mm and 3 mm stencil groups, respectively. This indicates that the 1 mm stencil is too small for cell seeding procedures. Approximately 20% of both the 2 mm and 3 mm patches were slightly bigger as a result of a leaking stencil, in comparison to ~ 9% in the 1 mm stencil group.

These results indicate that the 1 mm stencil is too small for the creation of small hiPSC-CM patches. In contrast, the 2 mm and 3 mm stencils are large enough and result in well-defined monolayers.

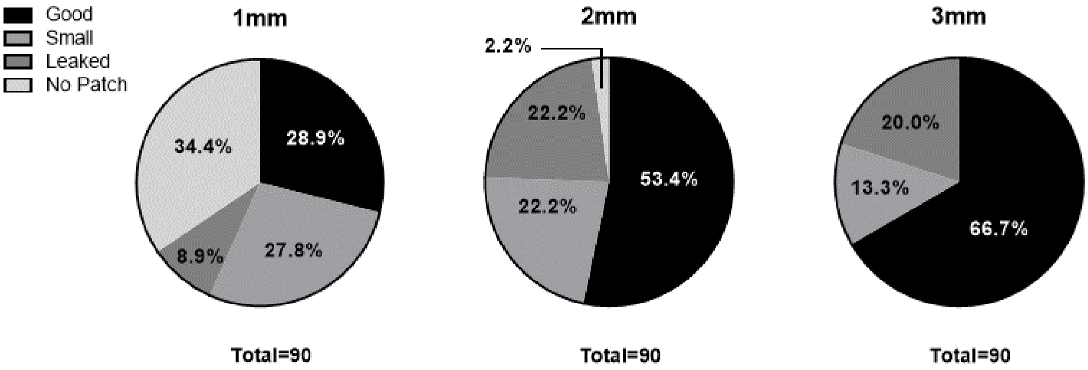

Figure 3.4 Success rate of the use of 1 mm, 2 mm and 3 mm stencils to create small 2D hiPSC-CM monolayers.
Monolayers were classed as 1) good, 2) small (because of air bubble or leak), 3) leaked and larger and 4) no patch at all.

3.3.2 Morphology of the 2D micro-patches

In Figure 3.5, examples of good small hiPSC-CMs patches are shown for every stencil size and cell seeding density. In addition to this, the effect of centrifuging on patch morphology was also tested, because NCardia advises to not centrifuge hiPSC-CMs as this can harm the cells and obscure experiments and results. However, during our experiments the cell suspension needs to be centrifuged to obtain concentrated cell suspensions for seeding into the small lumen of the stencils.

The average patch size of 2 mm and 3 mm patches was not significantly smaller than their respective theoretical value of 3.14 mm^2 and 7.07 mm^2 (Figure 3.6A). However, 1 mm patches were significantly smaller. With increasing cell densities, an increase in cell number and cell coverage was expected. The coverage of the patch area by cells is lower when normal (1x) cell seeding densities were used (Figure 3.6B). Doubling the cell seeding density did result in a coverage comparable to control. Increasing this further to a 4x normal cell density did not increase the coverage any further but resulted in a thicker layer as also seen in Figure 3.5. The used cell densities were not affected by stencil size.

Interestingly, increasing the seeding cell density did not have a linear relationship with cell retainment as a relatively lower percentages of cells was retained in the 2x and 4x cell seeding density groups (Figure 3.6C and D). This was 16-44% and 18-27% for the double and quadruple cell densities, respectively. The 1x cell density group resulted in the highest percentage of nuclei remained (29-57%) and this was closest to the control groups (53%). Stencil size slightly influences the number of nuclei remaining, as most nuclei were observed in the 3 mm stencil followed by the 2 mm stencil (Figure 3.6C).

Finally, centrifuging did not have any adverse effects on area coverage, the number of nuclei within the patch and the cell retention rate.

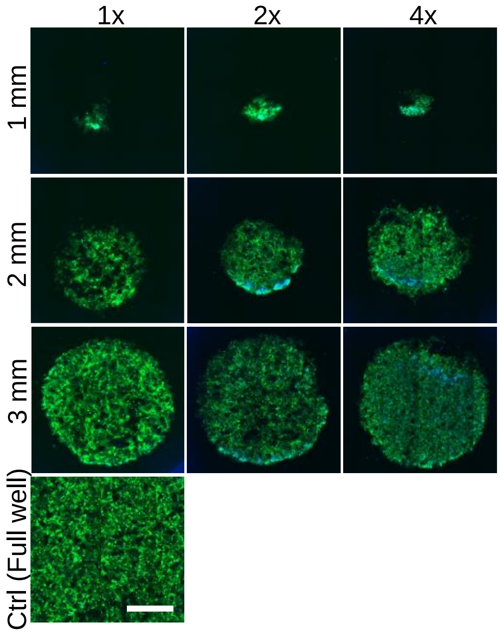

Figure 3.5 Immuno-histochemistry for F-actin (green) and DNA (DAPI, blue) of monolayers from different cell densities and diameters.
Cells seeded in a well of a 96 well-plate served as a control. Scale bar indicates 1 mm.

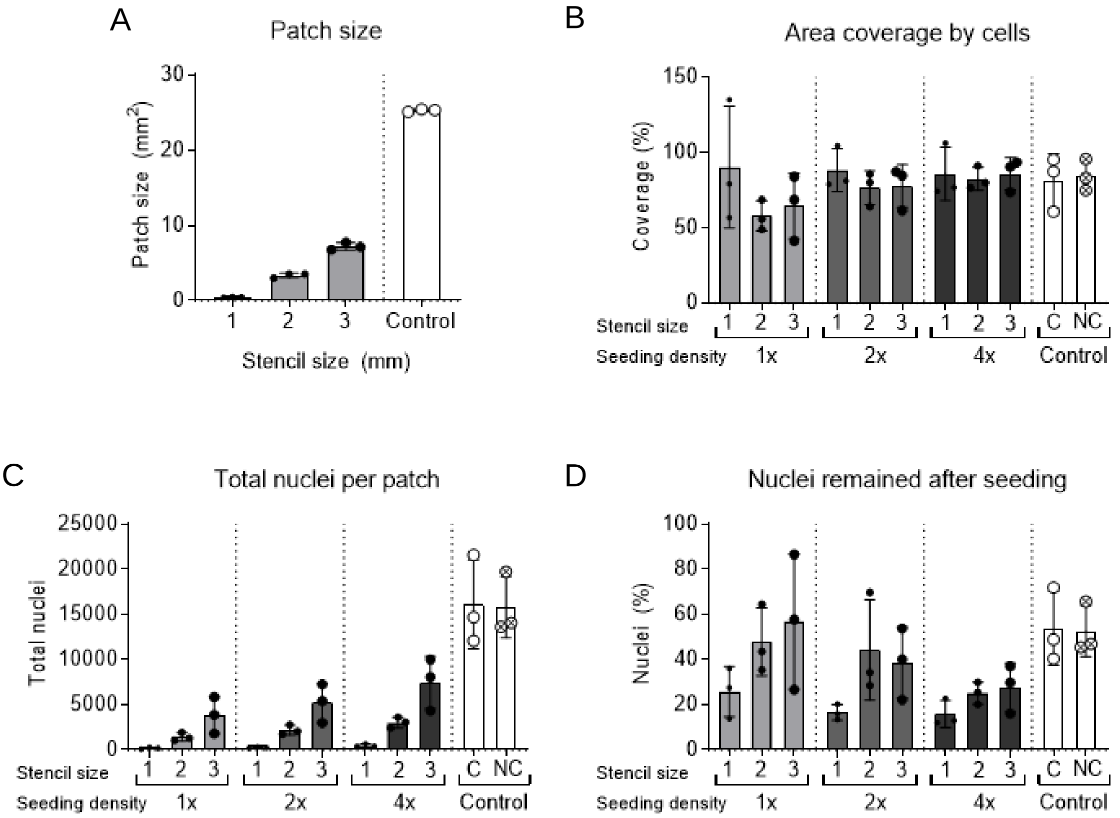

Figure 3.6. The morphology of small cardiac patches made with different stencil sizes (1, 2 and 3 mm) and cell densities (1x 2x and 4x).
Patches were assessed on A) patch size, B) the average area coverage by cells calculated as total patch area divided by area covered by cells, C) the total number of nuclei per patch and D) the percentage of nuclei remained after seeding. N = 3, n = 9-30. C = centrifuged control. NC = non-centrifuged control.

3.3.3 2D patch functionality

3.3.3.1 Centrifuging hiPSC-CMs prior to cell seeding does not affect their functionality

On day 4 after stencil removal, the monolayers were assessed on their electrophysiology and the results are shown in Figure 3.7. These data show that there are no significant differences for all electrophysiology parameters (Figure 3.7A) and most of the contractility parameters (Figure 3.7B) between centrifuged cells and cells that were not centrifuged. Here, only the contraction time (Up90) shows a small significant difference between both groups, however, this is biologically irrelevant. Therefore, it can be assumed that centrifuging does not have any adverse effect on the Cor.4U hiPSC-CMs.

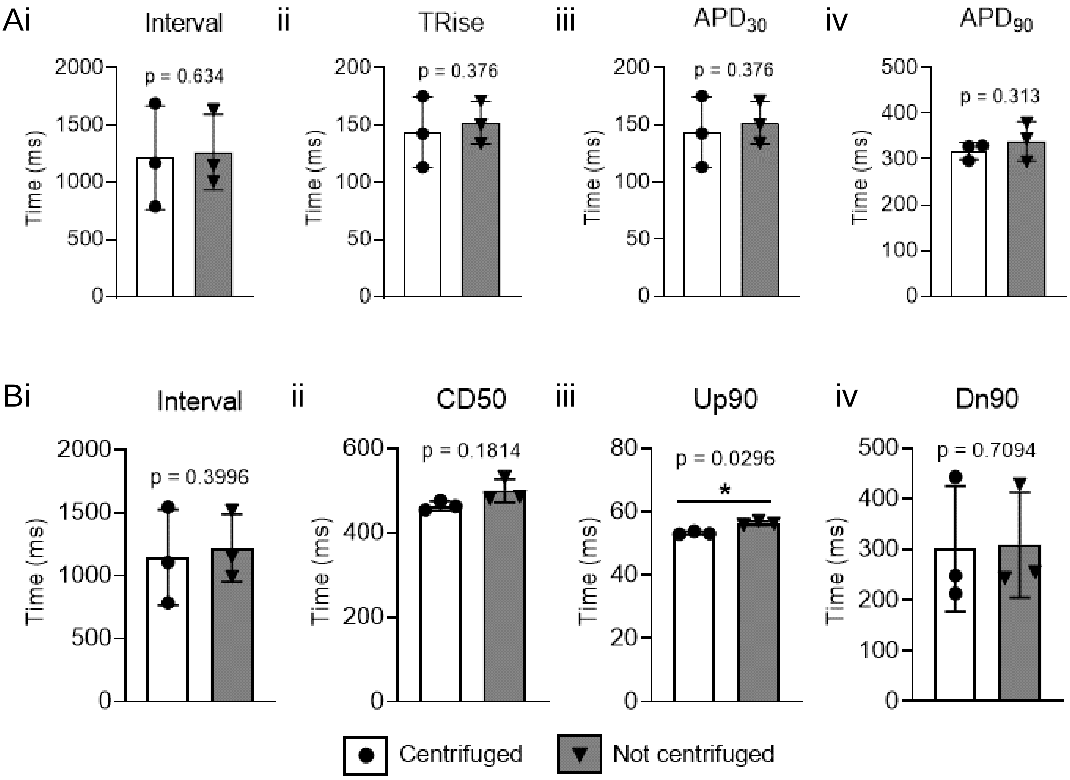

Figure 3.7 Effect of centrifuging hiPSC-CMs on their physiology.
A) Changes in electrophysiology. B) Changes in contractility. Experiments were done with Cor.4U hiPSC-CMs. N=3, n=9.

3.3.3.2 HiPSC-CMs seeded in stencils have a similar APD compared to control

The electrophysiology of the hiPSC-CMs was measured for all stencil sizes (1, 2 and 3 mm) and cell densities (1x, 2x and 4x the standard cell density) and results are shown in Table 3.2. All test groups had a similar spontaneous beating frequency compared to control, as were the TRise, APD$_{30}$, APD$_{50}$ and APD$_{90}$. This indicates that the stencils do not have a negative effect on the electrophysiology of hiPSC-CMs. Therefore, we can assume that the stencil sizes and cell densities tested here do not affect the electrophysiology of hiPSC-CMs when compared to standard culture conditions.

Table 3.2 Electrophysiology of Cor.4U hiPSC-CM seeded in stencils of 1 2 or 3 mm and in different cell densities (100,000, 200,000 or 400,000 cells/cm^2).

2D patches were statistically compared to hiPSC-CMs cultured in standard 96 well-plates. HiPSC-CMs used are from NCardia. N = 3, n=20-30.

Seeding density		Normal (1x)			Double (2x)			Quadruple (4x)			Control
Stencil size		1 mm	2 mm	3 mm	1 mm	2 mm	3 mm	1 mm	2 mm	3 mm	
	N	3	3	3	3	3	3	3	3	3	3
	n	24	29	30	28	30	30	20	30	30	18
Mean Interval	Mean	1397	1062	1126	1350	1146	1178	1350	1277	1315	1238
	(±SD)	±175.1	±228.8	±267	±170	±269.3	±270.2	±307.9	±330.1	±520.6	±388.5
	p value	0.8079	0.7275	0.9604	0.9608	0.9879	0.9978	0.9602	0.9996	0.9943	NA
TRise	Mean	10.93	9.272	10.28	11.19	8.479	9.547	9.984	9.517	9.754	8.852
	(±SD)	±4.382	±2.458	±6.498	±5.627	±2.371	±4.788	±2.439	±2.805	±5.111	±2.542
	p value	0.5271	0.9996	0.852	0.405	0.9996	0.9969	0.9493	0.9971	0.9866	NA
APD$_{30}$	Mean	224.4	192.4	198.1	223.5	208.3	189.8	219.2	215.7	173.3	147.7
	(±SD)	±15.66	±14.5	±21.11	±9.217	±19.11	±17.82	±34.44	±34.21	±14.57	±24.75
	p value	0.1032	0.22	0.2398	0.22	0.2398	0.1032	0.2398	0.2398	0.2398	NA
APD$_{50}$	Mean	298.7	261.6	269.2	289.4	278.1	262.9	283	280.2	245.9	224.8
	(±SD)	±18.22	±30.98	±38.07	±24.09	±41.08	±20.77	±68.79	±70.87	±32.3	±12.23
	p value	0.0848	0.223	0.2765	0.0677	0.246	0.0584	0.5548	0.6079	0.5516	NA
APD$_{90}$	Mean	375.7	335.7	352.3	378.5	354.9	353.8	346.2	347.5	332.4	328.7
	(±SD)	±46.98	±28.25	±30.3	±63.19	±32.65	±37.71	±65.1	±72.13	±37.66	±30.15
	p value	0.4814	0.9997	0.9581	0.4197	0.929	0.9416	0.9925	0.9896	0.9998	NA

Even though the average values were not statistically significant, an interesting trend is seen where the APD_{30} and APD_{50} values, but not the APD_{90}, of the micro-patches were longer compared to those of the control monolayer, suggesting an altered AP shape that is not related to beating rate and that results in a more prominent plateau-phase; a feature of mature CMs.

A small gene expression study was performed to try and explain some of the trends seen in AP shape. Gene expression was assessed for 5 genes coding for ion channels that have a relatively big influence on the AP shape, namely: the rapid delayed rectifier potassium current (I_{kr}) involved in depolarization (phase 0), the funny current (I_f) involved in stem cell automaticity (phase 0), inward sodium channel (I_{Na}) (phase 1), the L-type calcium channel ($I_{Ca.L}$)(phase 2)and the inward rectifier potassium current (I_{K1})(phase 3).

As shown in Figure 3.8, gene expression for all 5 ion channels were all upregulated compared to control, however not significantly. The most upregulated channel is the sodium channel, which is activated during phase 0, the depolarization phase, and not during repolarization. Also, the L-type calcium channel, which is activated during phase 2, is slightly upregulated (~ 1.4x).

It was not possible to obtain additional data points because of the discontinuation of Cor.4U hiPSC-CMs. From this moment, it was decided to continue with the ICell^2 hiPSC-CMs from FCDI.

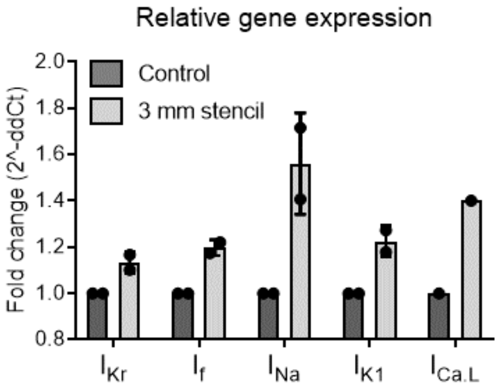

Figure 3.8 Gene expression profiles of various genes coding for ion channels. HiPSC-CMs were seeded in 3mm stencils seeded using the double cell density and values were compared to the control: a full well seeded in the normal cell density. Experiments were done with Cor.4U hiPSC-CMs. N=1 or 2 with 2 technical replicates each.

3.3.3.3 Contractile profiles of hiPSC-CMs seeded in stencils is similar to that of standard seeding procedures.

Then, also the contractility of hiPSC-CM micro-patches was assessed and the average values ±SD are shown in Table 3.3. There were no significant changes for the contraction time, relaxation time and CD_{50} between test groups versus control. This indicates that neither cell density nor stencil size affects the contractile behaviour of hiPSC-CMs.

Table 3.3 Contractility values Cor.4U hiPSC-CMs seeded in stencils of various diameter (1, 2 and 3 mm).
Values are compared to a fully seeded 96 well-plate with normal (1x) cell density.

Seeding density		Normal (1x)			Double (2x)			Quadruple (4x)			Control
Stencil size		1 mm	2 mm	3 mm	1 mm	2 mm	3 mm	1 mm	2 mm	3 mm	
	N	3	3	3	3	3	3	3	3	3	3
	n	24	29	30	28	30	30	20	30	30	18
Contraction time	Mean	63.71	61.49	57.28	58.18	58.1	59.97	62.1	53.71	60.74	54.82
	(±SD)	±7.129	±8.677	±7.913	±2.195	±6.007	±10.89	±7.49	±16.14	±10.75	±0.2517
	p value	0.4046	0.6956	0.9972	0.9883	0.9899	0.8814	0.6123	0.9997	0.7944	NA
Relaxation time	Mean	311.7	259.8	270.1	311.8	273	281.2	285.1	262.6	302.4	305.2
	(±SD)	±13.76	±23.13	±39.78	±23.72	±30.6	±18.7	±42.89	±34.85	±98.94	±113.2
	p value	0.9998	0.8145	0.9403	0.9998	0.9619	0.9929	0.9971	0.8558	>0.9999	NA
CD_{50}	Mean	392.8	380.8	395.7	389.9	415.1	403.7	385.1	393.1	390	394.5
	(±SD)	±54.15	±46.77	±74.83	±55.94	±58.24	±44.59	±74.98	±92.54	±62.64	±77.07
	p value	0.9999	0.9632	>0.9999	0.9996	0.767	0.9966	0.9946	0.9999	0.9996	NA

3.3.4 Comparison of two commercially available hiPSC-CM lines.

Because of the discontinuation of Cor.4U cells, hiPSC-CMs from FCDI would be used from now on and therefore the effect of the stencils on their functionality was assessed and compared to those of the Cor.4U hiPSC-CM patches. It was decided to assess only the 3 mm diameter micro patches, because this size resulted in the highest success rate. Nonetheless, the cell seeding density might affect the physiology of the cells and therefore all three seeding densities were tested.

First the electrophysiology of the cells was assessed, and averages are shown in Figure 3.9. ICell^2 patches were beating at a higher frequency (not significantly) compared to the Cor.4U cells, but this was similar across all densities (Figure 3.9A). Neither cell density nor cell type influenced the TRise on average as shown in Figure 3.9B. In contrast to the decreased APD_{30} and APD_{50} values in Cor.4U cells, seeding ICell^2 in stencils did not alter the APD values. Therefore, no further PCR experiments were performed for the FCDI hiPSC-CMs.

Then, contractile behaviour of ICell^2 hiPSC-CMs was analysed as shown in Figure 3.10. No differences were seen in contraction time, relaxation time and CD_{50} between all cell densities, indicating that stencil size did not affect contractility. In addition to this, no differences were seen in relaxation time and CD_{50} between both cell types. The only difference seen was an increased contraction time in ICell^2 patches (Figure 3.10A).

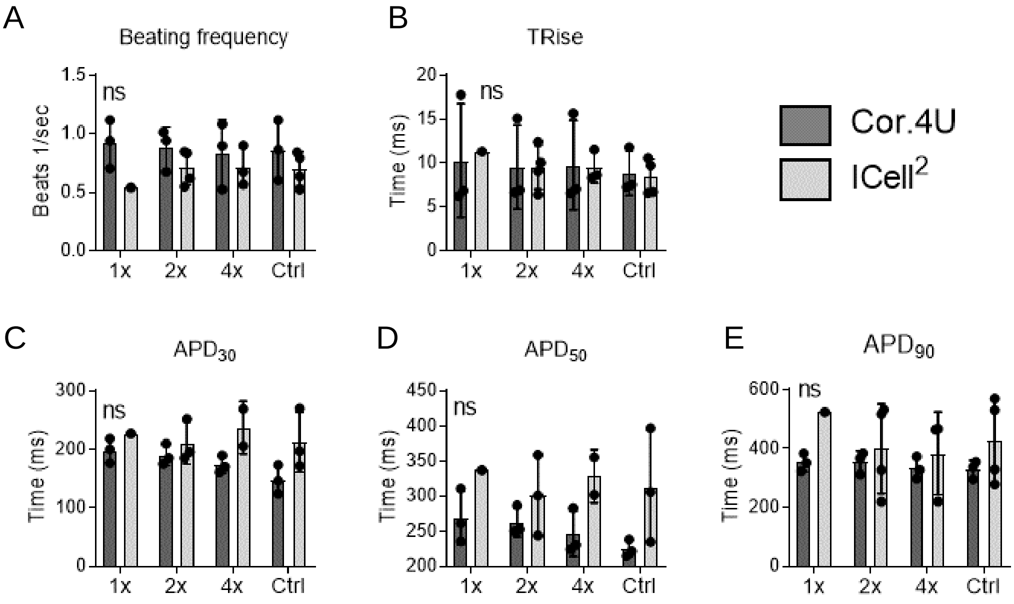

Figure 3.9 Comparison of electrophysiology between hiPSC-CMs patches of Cor.4U (NCardia, dark grey) and ICell^2 (FCDI, light grey) hiPSC-CMs.
A) Beating frequency. B) TRise. C) Action potential duration at 30% of the amplitude (APD$_{30}$). D) Action potential duration at 50% of the amplitude (APD$_{50}$). E) Action potential duration at 90% of the amplitude (APD$_{90}$). Only 3 mm stencils were used. N = 3 experiments, n= 9 for control and n = 20-30 for test groups.

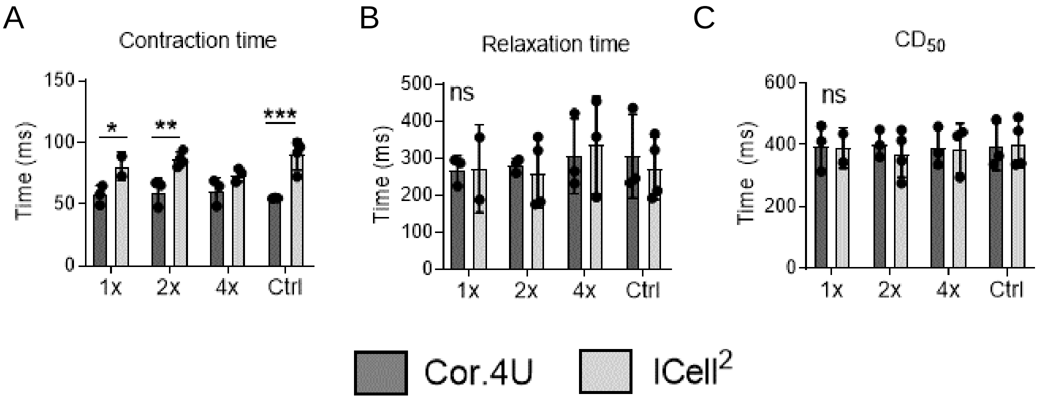

Figure 3.10 Comparison of contractility parameters between hiPSC-CMs patches of Cor.4U (NCardia, dark grey) and ICell^2 (FCDI, light grey) hiPSC-CMs.
A) Contraction time. B) Relaxation time. C) Contraction duration at 50% of the amplitude (CD$_{50}$).

3.3.5 Contractility but not voltage signals, from hiPSC-CMs vary across a monolayer

Figure 3.11 shows typical contractility and voltage signals from hiPSC-CMs seeded as a monolayer on tissue culture plastic (TCP). Fluorescence signals (voltage) and video images (contractility) were recorded in sequence from three discreet regions of approximately 300x300 µm, as shown in Figure 3.11A and segments of these recordings are shown in Figure 3.11B. The voltage traces from each location shown in Figure 3.11Bi-iii illustrate comparable profiles with a very similar uniform shape and duration. In contrast, the contractility traces in the three locations are different, showing complex time-courses with single- or multiple peaks (Figure 3.11Biv-vi). This is highlighted in the overlaid plots of Figure 3.11C and D. These data suggest that the complex contractile profile is not a consequence of non-uniform electrical coupling, but rather are mechanical in origin.

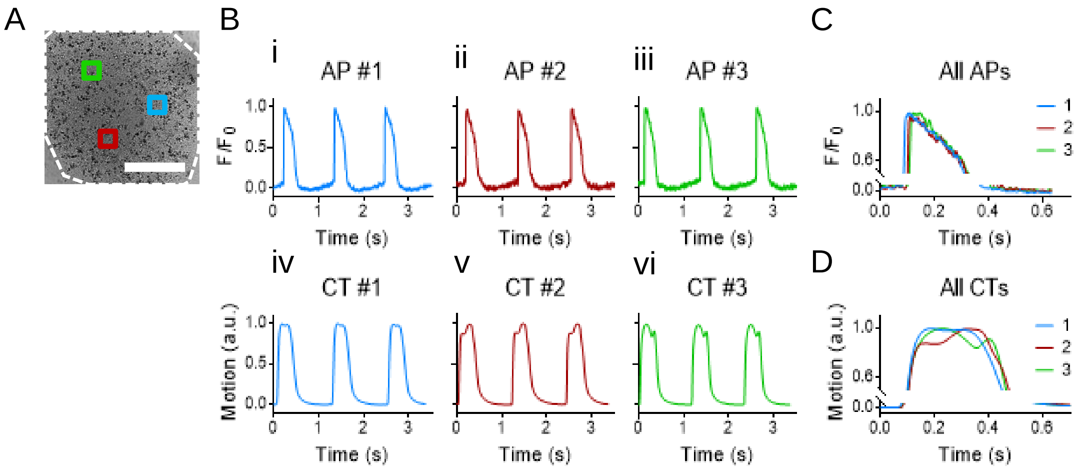

Figure 3.11 Contractility, but not voltage signals, from hiPSC-CMs vary across a monolayer. A) Example of 3 different locations within a 2D micro-patch indicated with blue, red and green squares. The white dotted line indicates the outer line of the patch. Scalebar is 1 mm. B) Action potentials (AP) (top row, panels i-iii) and contractility traces (CT)(bottom row, panels iv-vi) recorded on three different locations within one well (blue, green and red inserts in panel A). APs and CTs with the same colour are recorded on the same location. APs show comparable profile on all three areas within the well, however, contractility traces show three different profiles. C) Overlay of the three APs. D) Overlay of the three CTs.

3.3.6 Spatiotemporal analysis reveals local variations and complexity of movement

3.3.6.1 Improved MM algorithm analyses adjacent areas in parallel

The complex contractile behaviour is also visible from video recordings (data not shown). There are areas in the video frame showing double movement (centre) next to areas with single movement (left and right sides). To shed light on this contractile behaviour, the video frame was divided into 3x3 grid-squares, each of 100x100 μm, as shown in diagram Figure 3.12A. The MM algorithm was then applied to each grid square, resulting in 9 different but simultaneous contractility traces. In Figure 3.12B, all 9 traces generated by the MM algorithm are displayed together, showing the synchronicity at the start of the contractile phase, followed by contractile profiles that differed in shape. In Figure 3.12C, all 9 traces are placed in correspondence to their position in the 3x3 grid. The simple, “twitch-like” transients occur adjacent to complex transients with multiple peaks. This is also visible in Figure 3.12D, which shows a heatmap for the number of peaks (1). Likewise, heatmaps for the amplitude (2), the start time (TStart) (3) and the contraction duration at 50% of the amplitude (CD_{50}) (4) are shown (Figure 3.12D). These heatmaps also clarify that areas with relative high values for amplitude, TStart or CD_{50} are located adjacent to areas with relatively low values, emphasizing the local variation in contractility. Lastly, the average contractility transient is shown in Figure 3.12E which displays a complex profile that is constant from beat-to-beat, similar to that seen in Figure 3.11B. These data suggest that the contractile behaviour of hiPSC-CMs monolayers seeded on rigid substrates exhibit complex contractile patterns that vary locally (100 µm range).

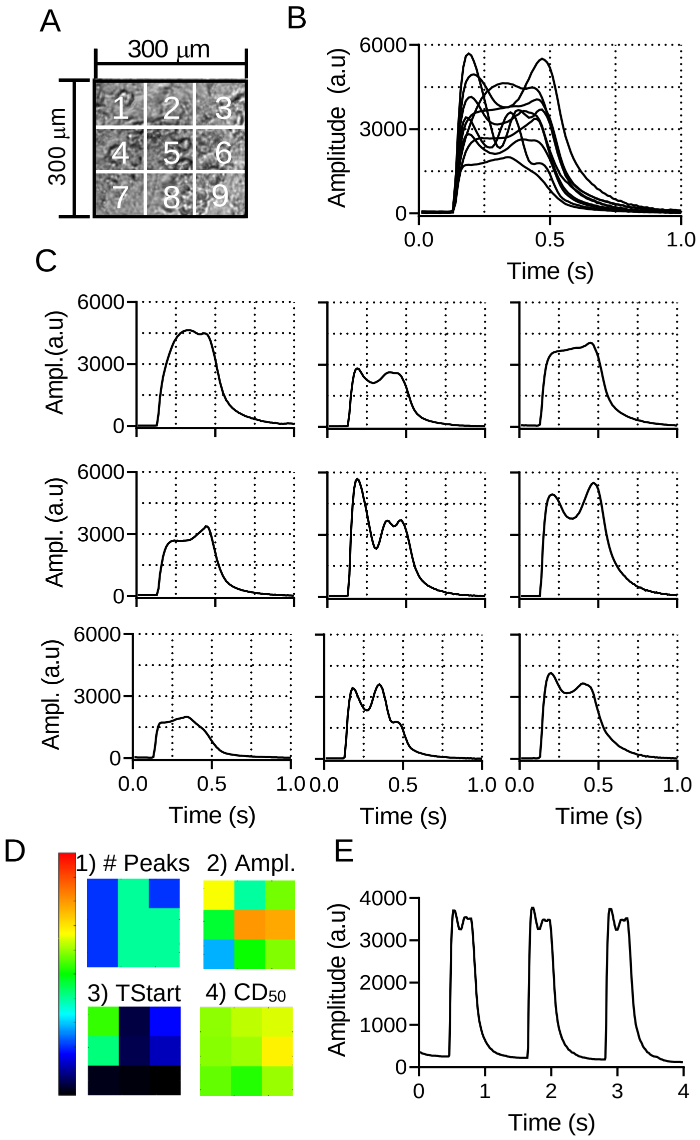

Figure 3.12 Spatiotemporal analysis of contractile behaviour of hiPSC-CMs reveals local variations of movement.
A) 300 x 300 µm fields of view were subdivided in 3 x 3 grid-squares of 100 x 100 µm, where after the MM algorithm was applied to every grid-square. B) All traces from each grid-square (9 in total) were overlapped. C) All traces from each grid-square were placed in their corresponding location shown in panel A. D) Heatmaps indicating 1) the # peaks, 2) the amplitude of the events, 3) the start time (TStart) and 4) the contractile duration at 50% of the amplitude (CD_{50}) (scalebars are 0-5 peaks, 0-7000 a.u., 0-40 ms and 0-600 ms, respectively). E) The contractility trace taken from the whole area (300 x 300 µm).

3.3.6.2 Local variations in movement are independent of cell seeding density

Increasing the cell seeding density did not affect the complexity as shown in Figure 3.13. Like the standard (1x) cell density, the average traces of the 2x and 4x cell seeding densities showed a complex time-course and were similar to the ones seen in Figure 3.11 and Figure 3.12. The spatial analysis revealed similar complex contractile behaviour at all three cell seeding densities, with both single-peaked and multiple-peaked transients in every region. This data indicates that cell seeding density does not modulate the complex contractile behaviour on fixed substrates.

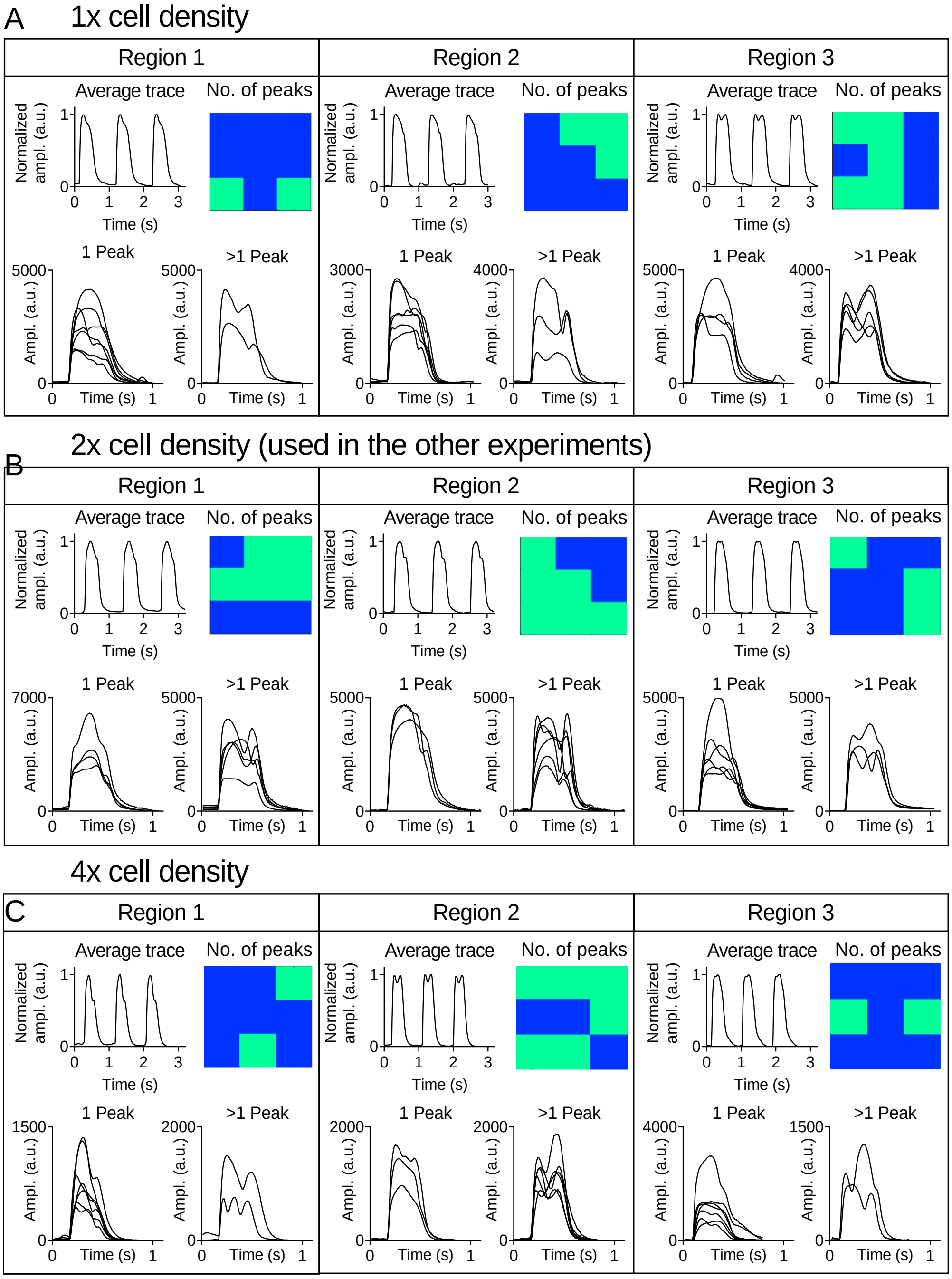

Figure 3.13 Cell density does not modulate the complex contractile behaviour on fixed substrates.
HiPSC-CMs seeded in 1x (A), 2x (B) or 4x (C) the cell density suggested by the manufacturer. For each cell density, example traces are shown from three distinct regions of the same micro-patch. These include 1) the average contractile trace recorded from the whole area (top left panel), 2) a heatmap showing the location of grid-squares with either 1 (blue) or >1 peak (light green) (top right), 3) the traces with 1 peak (bottom left) and 4) the traces with >1 peak (bottom left). Recordings are from Cor.4U hiPSC-CMs (NCardia) on day 2 after stencil removal.

3.3.6.3 Isolated hiPSC-CMs only show “twitch-like” contractility profiles

The origin of the complex behaviour might be differential attachment of the monolayer to the underlying substrate and not the behaviour of individual cells. Evidence for this are the MM records from isolated single hiPSC-CMs on glass substrates. As shown in Figure 3.14A and B, individual isolated cells on glass show single-peaked contraction as expected from the standard ECC model. Thus, complex contractile behaviour only arises in a mechanically linked sheet of cells on glass or plastic substrates.

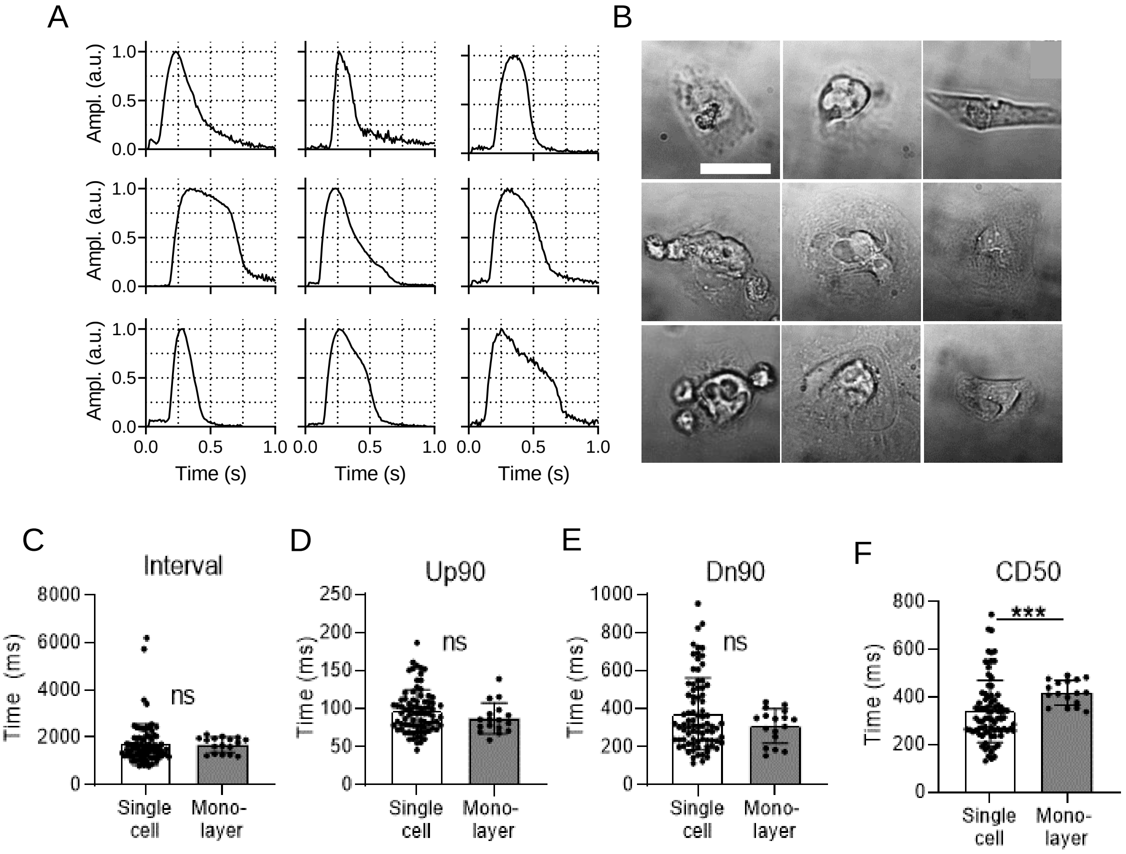

Figure 3.14 Isolated cells only show single contraction profiles.
Contractility traces (A) and corresponding brightfield images (B) of isolated iPSC-CMs (ICell^2 (FCDI)) seeded on glass. Recordings taken on day 4 or 5 after stencil removal. Scalebar indicates 50 µm. Data points of 82 single cells (white bars) and 17 micro-patches (3 mm; grey bars) showing the averages of contractility parameters (C-F). C) Interval, D) contraction time (Up90), E) Relaxation time and F) CD50. Statistical significance was assessed using an unpaired two-sided T-Test for Up90 and a Mann-Whitney test for Interval, Dn90 and CD50 as the data points did not follow a Gaussian distribution.

Further analysis of the contractility transients revealed no statistical differences for the interval, Up90 and Dn90 when compare them to values obtained from micro-patches (Figure 3.14C-E). However, the contraction duration was significantly shorter in single cells, supporting the hypothesis that isolated cells on TCP experience less resistance and restriction during contraction.

3.4 Discussion and conclusion

3.4.1 Silicone stencils as a mould for small cardiac patches

In this chapter, small hiPSC-CM patches were tested against standard cell culture and optimized for cell seeding density and stencil size. It was found that 2 mm or 3 mm stencils resulted in hiPSC-CM patches with similar morphology and physiology compared to standard culture methods. The success rate when using these stencils is high enough (over 60%) to use for future experiments, especially because this is partially determined by experience and is therefore expected to increase further in time. In contrast, the lumen of the 1 mm stencils was too small and consequently resulted stencil leakage and therefore cell loss. Therefore, 1 mm stencils will not be included in future experiments. Both the 2 mm and 3 mm stencils resulted in high success rates, and will therefore be used for future studies to develop small EHTs.

Further, the cell density that is normally used for hiPSC-CM culture did not result in a similar coverage as the standard culture method, and the underlying reason is not known. Therefore, higher cell densities are needed for a solid monolayer. Interestingly, there was not a linear gain in the number of nuclei remained with increasing cell density, indicating a saturation of cell adhesion between 2x and 4x the normal cell density. Therefore, the double cells density has our preference for future 2D patches, however, the 4x density will not yet be excluded.

3.4.2 Novel application of the MM contractility tool

The muscle motion (MM) algorithm as published by Sala et al (Sala et al., 2018), is capable of analysing contractility of 2D and 3D hiPSC-CM cultures and isolated adult CMs. It is a non-invasive way to measure the contractile behaviour of cells as it is based on the relative change in pixel intensity of bright field video frames in time. It could therefore be compared to other contractility analysis tools that are found in literature (20, 21). However, the MM algorithm gives only an average contractility of the field of view and spatial differences are thus overlooked. Instead, in this study, video frames were divided into grid-squares and each grid-square was analysed with the MM algorithm, generating local contractility profiles within one monolayer as shown in Figure 3.12. It has been tested on magnifications from 4x to 40x; the range of magnifications that are used in our laboratory. However, in contrast to the publication of Sala et al (Sala et al., 2018), this tool was not tested on 3D cultures or isolated cardiomyocytes. There are alternative commercial methods to perform a spatiotemporal analysis, such as the Sony SI8000 system, however, this system is very expensive and thus not as accessibly as the spatiotemporal MM.

3.4.3 Complex contractile behaviour observed in hiPSC-CM monolayers is probably of mechanical origin

The multi-peaked contractile events analysed using the MM algorithm represented marked phasic changes in the movement of areas of the hiPSC-CM monolayer with respect to the TCP surface during the contraction (Figure 3.12 and Figure 3.13). This indicates marked heterogeneity of cell-to-cell motion across areas of the monolayer in the contractile phase. This heterogeneity occurs despite homogeneous AP signals across the same monolayer.

In the contractile phase induced by the close to synchronous APs, the complex movement events appear to be mechanical and to arise from differential adhesion between the substrate and the monolayer. Here, it is important to note that multiphasic contractile behaviour was not observed in isolated cells and was independent of cell density. In elegant studies of intracellular forces and movement in cell pairs, Maruthamuthu *et al.* showed that uniform forces were experienced between cell-cell and cell-substrate interfaces resulting in differential movements across these two types of interfaces depending on their relative stiffness (Maruthamuthu et al., 2011). Variation in adhesion or local substrate stiffness could be due to the very different local stiffness characteristics caused by ECM remodelling and de novo ECM deposition by the hiPSC-CMs (Antia et al., 2008).

3.4.4 Overall conclusion

From these studies, it was found that the 2 mm and 3 mm stencils using either the 2x or 4x cell densities would be useful for the development of small EHTs. Furthermore, the observation that hiPSC-CM exhibit a different contraction profile across the monolayer, independently from APs, ignited our interest and will be further investigated during the next chapters.

Chapter 4 Detachment of the 2D hiPSC-CM monolayers as a building block for EHTs

4.1 Introduction

4.1.1 Background

Cell sheet engineering plays a big role for the regeneration of tissues, like the myocardium, cornea and skin. By placing *in vitro* cultured cell sheets onto the diseased areas the function of the recipient tissue can be improved (Kitala et al., 2020, Kawecki et al., 2016, Matsuo et al., 2015a). Importantly, due to the thin nature of the cell sheets, all cells are exposed to nutrients through diffusion and thus enabling the development large patches (i.e. centimetres in area) (Gao et al., 2018, Jackman et al., 2018, Matsuo et al., 2015a). Moreover, thicker tissues can be engineered by stacking those initial cell sheets (Matsuo et al., 2015a, Haraguchi et al., 2012), showing the versatility of cell sheet engineering.

A key technique in cell sheet engineering are the thermoresponsive dishes, which are coated with a thermoresponsive polymer. One of the most explored polymer is poly(N-isopropyl acrylamide) (PIPAAm), pioneered by the Okano lab (Yamada et al., 1990, Okano et al., 1993). An alternative thermoresponsive polymer is poly[tri(ethylene glycol) monoethyl ether methacrylate] (P(TEGMA-EE)) (Dworak et al., 2013), but this is less well studied and not commercialized like PIPAAm. Upon cooling, the PIPAAm polymer changes its chemical structure from hydrophobic (37°C) to hydrophilic (<32°C) (Yamada et al., 1990, Okano et al., 1993). This chemical shift gently disrupts cell-substrate bonds, but not cell-cell adhesions, resulting in detachment of a fully intact monolayer or cell sheet as shown in Figure 4.1. Importantly, subcellular ECM proteins are not affected by this method, which is in contrast to conventional enzymatic or mechanical harvesting, where cell-cell and cell-matrix adhesions as well as the subcellular matrix are disrupted (Kitala et al., 2020, Kawecki et al., 2016). It is likely that maintaining the integrity of the cell sheet, including the subcellular ECM, has benefits for the survival of hiPSC-CMs and therefore their regenerative potential (Zhao et al., 2020). Hence, using thermoresponsive dishes might be a good approach to form small EHTs as proposed in this thesis.

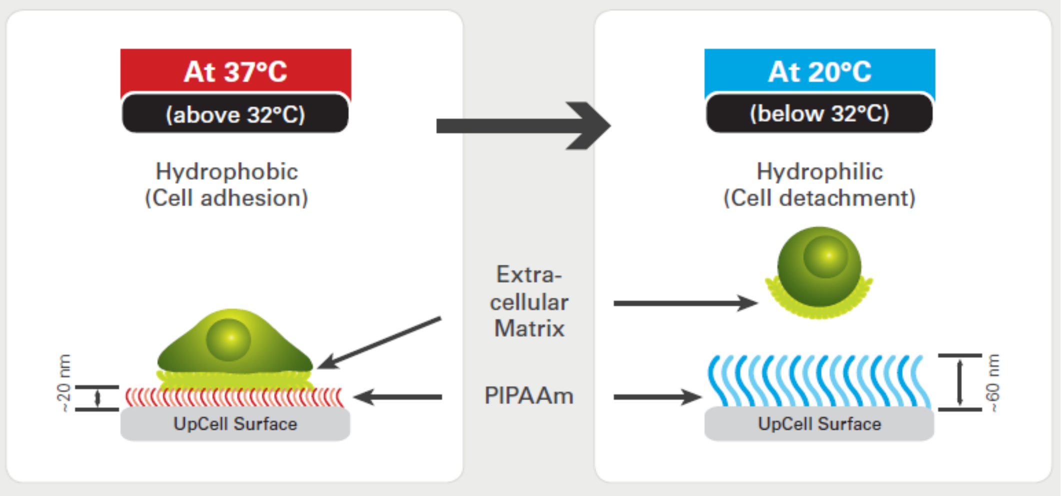

Figure 4.1 PIPAAm coating thermoresponsive culture dish.
Diagram adapted from the UpCell (Nunc) brochure.

In literature, there are two main methods described to detach the monolayers and transfer them to a new culture dish. Firstly, a hydrophobic membrane, such as polyvinylidene fluoride (PVDF), could be used as a makeshift/substitute cell adhesion substrate (Kawecki et al., 2016, Shimizu et al., 2002a). Secondly, force pipetting, which uses hydraulic forces to gently detach the monolayer (Matsuo et al., 2015a, Kawecki et al., 2016). The membrane method has some advantages over force pipetting, because it is less harmful to the cells and the membrane can function as a support structure during transfer, maintaining the cell sheet size. However, this method is more time consuming and there is no guarantee that the cells will form bonds to the membrane prior to cell sheet transfer (Kawecki et al., 2016). Also, removing the monolayer from the membrane afterwards, e.g. during transplantation or when stacking multiple monolayers, is complicated (Haraguchi et al., 2012). Force pipetting, on the other hand, is relatively quick and straight forward, but might damage the cell sheet more than the other method, affecting cell viability. Also, the shape of the monolayer might deform or shrink after detachment without a membrane (Haraguchi et al., 2012, Matsuo et al., 2015a, Baek et al., 2020). However, giving the successful results in literature, both methods will be tested on the transfer of small hiPSC-CM monolayers for the development of small EHTs.

In this chapter, the small monolayers that were developed in Chapter 3 will be cultured on the commercially available NUNC UpCell PIPAAm coated dishes, whereafter the two detachment methods, PVDF membrane and force pipetting, will be assessed to confirm the most suitable method for detachment and transfer of small hiPSC-CM monolayers in order to use them as building blocks for EHTs. Here, the focus lays on the success rate of both method as well as the monolayer size and functionality after detachment and transfer.

4.1.2 Specific aims

The main aim of this chapter is to assess methods to detach and transfer small hiPSC-CM monolayers for future assembly and/or implantation. In addition to this, the complex contractile behaviour of hiPSC-CMs as seen in Chapter 3 will be investigated. The more specific aims are:

1) Seeding the hiPSC-CMs on thermosensitive culture dishes and test optimal detachment/transfer method.

2) To test the success rate of the transfer method by monitoring the number of transfers and the number of surviving monolayers.

3) To assess the morphology and functionality of the patches after detachment and during re-attachment.

4) Determine whether the complex contractile behaviour seen in Chapter 3 is also present in detached monolayers.

4.2 Chapter specific methods

4.2.1 Thermosensitive dishes with PIPAAm coating

PIPAAm is commercialized and readily coated dishes are available from various suppliers. The dishes that were used during these studies were Nunc dishes with UpCell surface (60 mm, Z688835-30EA; 96 well-plate, Z694347; Merck).

4.2.2 HiPSC-CMs culture protocol

On day -4, 3 mm stencils were placed onto FN-coated (10 µg/ml, bovine, Gibco) thermosensitive PIPAAm-dishes and Cor.4U hiPSC-CMs (NCardia) were seeded inside either the 2 mm or 3 mm diameter stencils in a 2x cell density ($2x10^5$ cells/cm^2). HiPSC-CMs were maintained in a controlled environment with 5% CO_2

and at 37°C. Two days after plating, stencils were removed and covered with fresh maintenance medium, where after cells were cultured for 2 more days before the start of the experiment (day 0). Culture medium was changed every 2-3 days, which was supplied by the hiPSC-CMs manufacturer.

On day 0, cells were cooled to 25°C for 1 hour under culture conditions with 5% CO2 and allowed to detach from the surface of the dish. Then, cell sheets were lifted off the dish using either a membrane or by force pipetting, as explained below. An overview of the detachment protocol is shown in Figure 4.2.

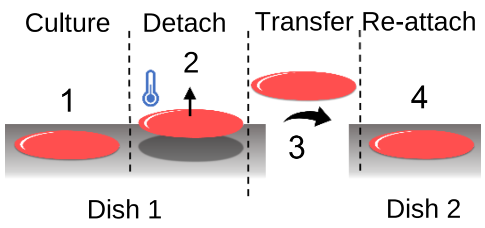

1. HiPSC-CMs culture on thermo-sensitive dish (C)
2. Detach micro-patch by cooling temperature (D)
3. Transfer cell patch (T)
4. Allow reattachment on days 1-7 (R)

Figure 4.2 Animation explaining the experimental cell-detachment procedure.
Cell were culture on a thermosensitive dish (C), where after the plated was cooled to 25°C, allowing the cell sheet to detach while maintaining cell-cell adhesions (D). Then, the cell sheet was transferred to a new culture dish (T) and allowed to re-attach to the new culture dish (R).

4.2.3 Methods for transferring the monolayer

4.2.3.1 PVDF membranes

The manufacturer of the commercialized thermosensitive UpCell NUNC culture dishes recommends polyvinylidene difluoride (PVDF) membranes, which are also used in the westernblot technique during the protein transfer step. However, the PVDF membranes are delivered with the larger NUNC dishes (6 well-plate), but not with the 96-well plates which were used here. Therefore, standard westernblot PVDF membranes were cut into shape, sterilized and used instead to transfer cells.

PDVF membranes with 0.2 µm pores (Novex, LC2002, Life Technologies) were sterilized using EtOH, where after the membrane was either placed in a sterile environment for the EtOH to evaporate (dry membrane) or directly placed in sterile PBS (wet membrane). After cooling the culture dishes for 90 min at room temperature, PVDF membranes were placed on top of the monolayer and incubated for another 30 min at room temperature. Subsequently, membranes with attached monolayers were transferred to a second culture dish using tweezers and incubated for 30-40 min at 37°C, allowing detachment from the membrane and attachment to the new fibronectin coated culture dish. Then, fresh warm culture medium was added, and the membrane removed.

4.2.3.2 Force-pipetting

With the force-pipetting method, the culture dish was cooled for 30-40 minutes where after the monolayer was carefully detached by pipetting culture medium underneath the cell sheet. After detaching, hiPSC-CM sheets were transferred to a new FN coated standard glass tissue culture dish using a 1 ml pipette. Cells were allowed to attach without medium at 37°C for 10 min, where after maintenance medium was added.

4.2.4 Assessment of contractility and electrophysiology

Contractility recordings were made before cooling, during cooling as the monolayer is detaching, directly after transfer and on days 1, 3,5 and 7 after transfer. The video frames were assessed using the MM contractility software, including the spatiotemporal analysis method. Additionally, APs were recorded on the CellOPTIQ system on day 7 using FV as voltage sensitive dye. Detailed description of contractility- and electrophysiology recordings are written in the methods chapter (Chapter 2).

4.3 Results

4.3.1 Using a thermosensitive culture dish to detach intact hiPSC-CM monolayers

4.3.1.1 2D Transfer of hiPSC-CMs using PVDF membranes

First, monolayer detachment using a PVDF membrane is tested as this method was suggested by the manufacturer. Membranes were placed on top of the monolayer and incubated for 40 min at room temperature (RT). Soaking the PVDF membrane in advanced resulted in 10% of the monolayers being transferred, in contrast to 0% of the dry membranes (data not shown). This percentage is too low for further investigation and other methods for the transfer of monolayers needed to be explored.

4.3.1.2 Transfer of hiPSC-CM monolayers using force pipetting

Force pipetting could be used as an alternative to the PVDF membrane transfer method. With force pipetting, the monolayers were also incubated at RT to release the cell-substrate bonds and were subsequently released from the culture dish by pipetting some medium underneath/beside the monolayer. This might damage the cells slightly, however, is relatively quick and easy compared to the PVDF membrane method. After complete detachment, the cell sheet is transferred to a new culture dish using a 1 ml pipet.

Using the pipetting method, 49% of the monolayers was transferred of which 52% was viable. This means that only 25% of the initially seeded monolayers was successfully transferred to a new culture dish. This is slightly higher compared to the membrane method (10%), however neither are completely satisfactory. Table 4.1 gives an overview of the success rates.

Table 4.1 Success rate when using the force pipetting method to transfer 3 mm 2D monolayers.
After transfer, monolayers were included when spontaneous beating was observed and excluded when cell death was observed over time.

	Seeded monolayers	**Successful transfer**	**From transferred monolayers**		**Success rate**	
Exp. #	N seeded	N transferred	N incl.	N excl.	From seeded monolayers	From transferred monolayers
1	7	7	6	1	86% (6/7)	86% (6/7)
2	24	10	3	7	13% (3/24)	30% (3/10)
3	12	0	0	0	0% (0/12)	-
4	20	14	7	7	35% (7/20)	50% (7/14)
Total	63	49% (31/63)	16	15	25% (16/63)	52% (16/31)
Exp. 1 2 4	51	61% (31/51)	16	15	31% (16/51)	52% (16/31)

In Figure 4.3A and B, brightfield and fluorescent immunochemistry images of successfully transferred 2 mm and 3 mm monolayers are shown. Some monolayers were quiescent upon cooling, directly after transfer and/or at day 1, but all samples regained their spontaneous beating ability at day 3. Other samples exhibited either loss off cells, no-uniform/partially contractions, disproportionately folded/malformed monolayers or cell death and were for these reasons excluded from further analysis (Figure 4.3C). Therefore, a transfer where the monolayer was spontaneously beating at day 3 after transfer and held a desirable shape and size was considered a successful transfer.

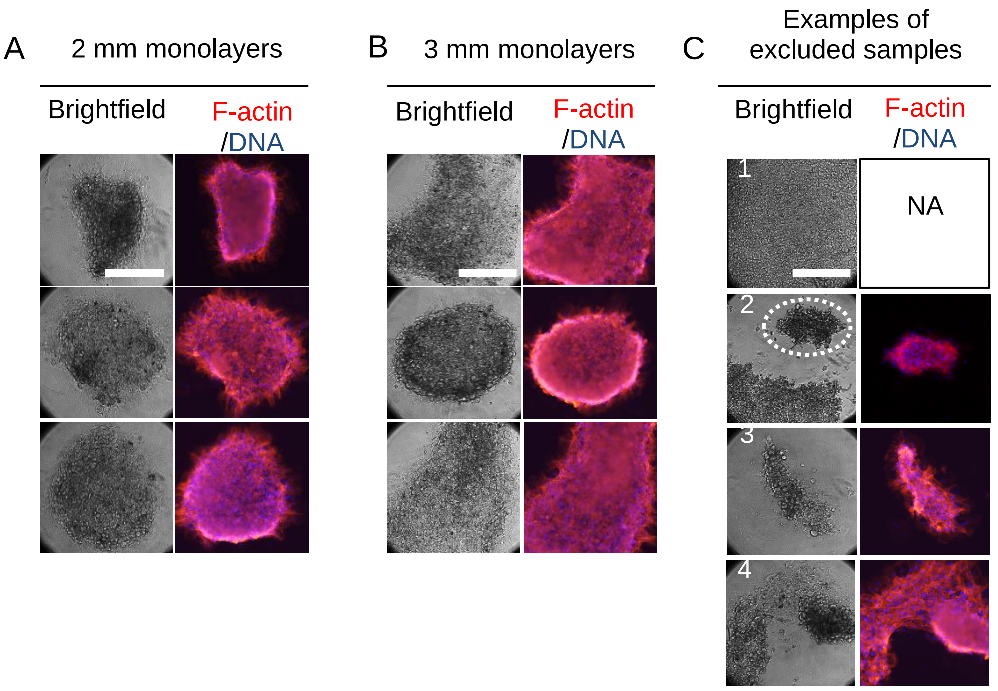

Figure 4.3 Brightfield and fluorescent immunochemistry images of transferred monolayers. A) Three examples of 2 mm monolayers after a successful transfer. B) Three examples of 3 mm monolayers after a successful transfer. C) Examples of excluded samples because of (1) cell death, (2) partial cell death, (3) detached/floating monolayer or (4) malformed/folded shapes. In figure C2, dotted lines indicate area with beating cells. All images were taken on day 7 after transfer. Scalebars indicate 400 µm.

4.3.1.3 Morphology of successfully transferred tissues in time

At the start of the experiment, hiPSC-CMs formed a confluent monolayer as shown in Figure 4.4,which was maintained during detachment. After the transfer, however, monolayers were significantly smaller (<1 mm) and were sometimes folded, which is shown in both Figure 4.3 and Figure 4.4. Interestingly, these folds disappeared over time, indicating remodelling of the micro-patch shape. Additionally, the cells at the perimeter of the patch spread, an indication of cell adhesion to the new substrate.

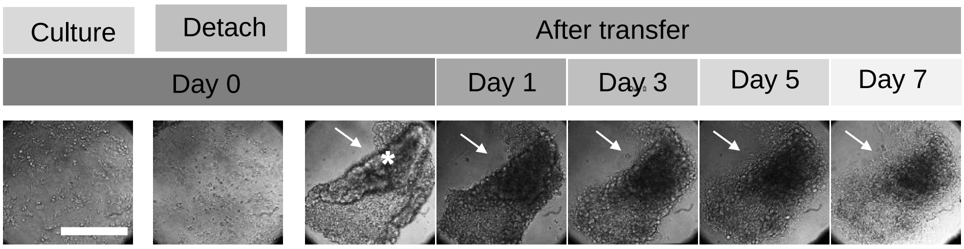

Figure 4.4 Brightfield images showing the morphology of monolayers before, during and after detachment from the rigid substrate.
Monolayers were allowed to re-attach to a new TCP culture dish. Scalebar represents 400 µm. White arrows indicate cell spreading over time during reattachment. Asteriscs indicates area where the cell sheet is folded.

4.3.2 Contractile behaviour of the micro-patches before, during and after transfer

4.3.2.1 Spontaneous beating frequency

Contractile behaviour of the monolayers was assessed before, during and after transfer at various time points. Figure 4.5 shows the spontaneous beating frequency throughout the procedure with (Figure 4.5A) and without (Figure 4.5B) quiescent monolayers. At day 0, the spontaneous rate was reduced to approximately 60% of control on lowering the temperature to 25°C. On detachment a considerable number of samples turned quiescent while others returned a normal spontaneous beating frequency (Figure 4.5A). By day 1 at 37°C, spontaneous activity had returned in the majority of the samples and the rate reduced gradually over the 7 days in culture.

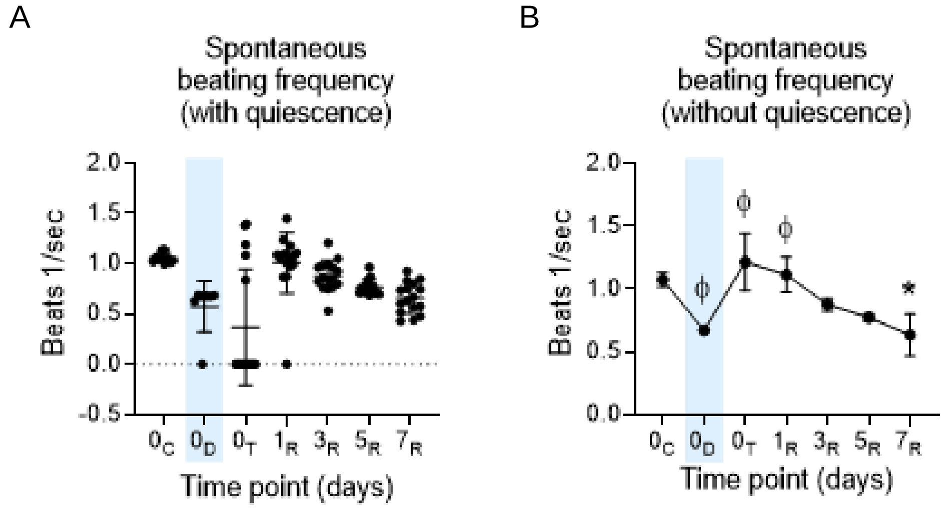

Figure 4.5 The spontaneous beating frequency of A) all transferred monolayers or B) only monolayers with spontaneous beating activity.
Φ indicates a timepoint with excluded values because of quiescence. * Indicates p value < 0.05. Blue line indicates the colder temperature during detachment. N = 3; n = 16. Cor.4U (NCardia) hiPSC-CMs were used for this experiment.

4.3.2.2 The overall contractile behaviour of the hiPSC-CM monolayer

First, the contraction of the whole monolayer was assessed. The contraction time, relaxation time and contraction duration did all increased during detaching and can be explained by the slower beating frequency shown in Figure 4.5, which is most likely caused by the reduced temperature during this experimental stage. The contraction time increased from 50 ms to 75 ms upon cooling and slowly decreased to start values during reattachment (Figure 4.6A). In contrast, the relaxation time was similar to the start values directly after transfer and at day 1, but increased gradually during reattachment as shown in Figure 4.6B. The amplitude of the contractility transient was slightly increased during cooling but was similar to the control on all other time points (Figure 4.6C). The change in mean contractile duration at 25, 50 and 75 percent of the amplitude (CD_{25}, CD_{50} and CD_{75}, respectively) was slightly lower than start values, but slowly increased during reattachment, however, not significantly (Figure 4.6D-F).

These changes in contractility can also be observed in the contractility transients. Two examples are shown in Figure 4.7 where the temporary change of the contractility time-courses is shown. Interestingly, the average contractility profile of the monolayer was twitch-like before transfer, but was multi-phasic after transfer. Further, these graphs show the difference in contractility time-course at different temperatures and that the contractile duration is prolonged upon cooling.

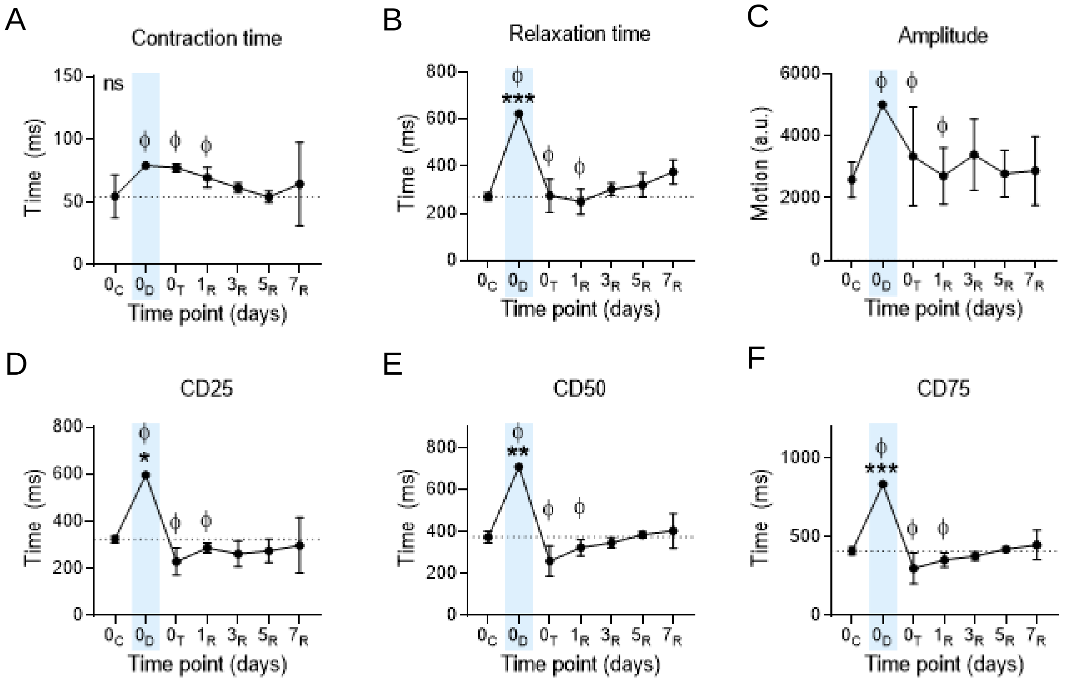

Figure 4.6 The contractile behaviour measured from the whole monolayer.
A) Contraction time. B) Relaxation time. C) Amplitude. D) contractile duration at 25% of the amplitude (CD_{25}). E) contractile duration at 50% of the amplitude (CD_{50}). F) contractile duration at 75% of the amplitude (CD_{75}). φ indicates a timepoint with excluded values because of quiescence. * indicates p value < 0.05. Blue line indicates the colder temperature of 25°C during detachment. N = 3; n = 16. Cor.4U (NCardia) hiPSC-CMs were used for this experiment.

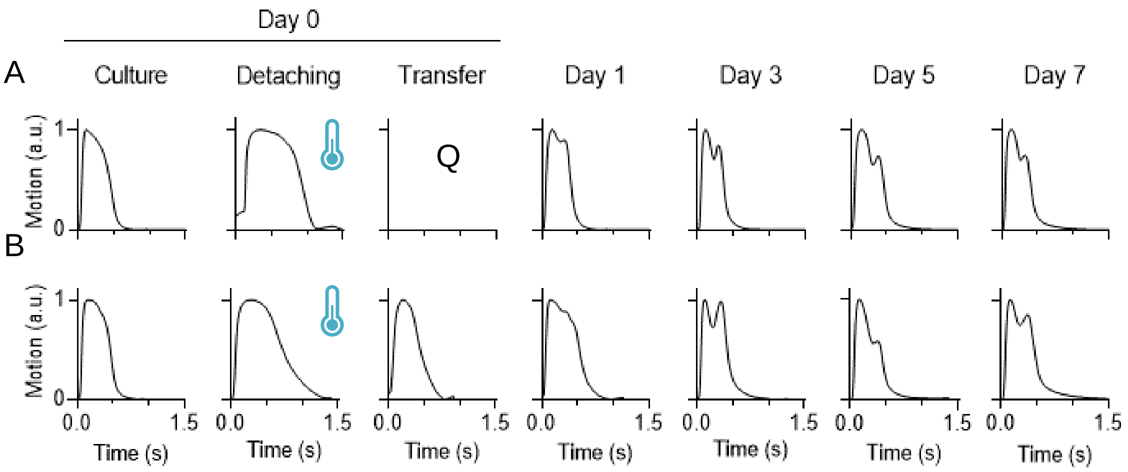

Figure 4.7 The change in contractility transients over time, before, during and after transfer. Contractility transients of two examples are shown: A) traces from the sample shown in Figure 4.4. and B) traces from a sample without quiescence and thus a trace for every time point. Contractility transients are taken with a 10x objective. Q indicates quiescence. Thermometer symbol indicates colder temperature of 25°C during detachment.

4.3.2.3 Spatiotemporal analysis reveals local variation in motion over large area

As discussed in the previous chapter (Chapter 3), hiPSC-CM contractility can vary locally. For this reason, the contractility of the monolayers was assessed using spatiotemporal analysis where the whole frame area was subdivided in 30x30 grid-squares, each analysed with the MM algorithm. The effects of attachment and detachment of the hiPSC-CM monolayers to/from the tissue culture dish on the complexity and heterogeneity of the contraction profiles, are shown in Figure 4.8 and Figure 4.9.

Figure 4.8A indicates that on average 54±15% of the grid-squares displayed single-peaked transients at the start of the experiment. The percentage of single peaks increased towards the maximum (% 1-peak: 86±15% after detachment) and correspondingly the percentage of transients with more complex contractile behaviour dropped towards zero after detachment (% >1-peak: 14±15% after detachment). This profile was maintained for 24h, but over the subsequent 2 days, the percentage of grid-squares showing single peaks declined back towards the control value (% 1-peak: 53±24% on day 3) and was maintained until day 7 (% 1-peak: 45±10%), while the grid-squares displaying more complex behaviour increased correspondingly.

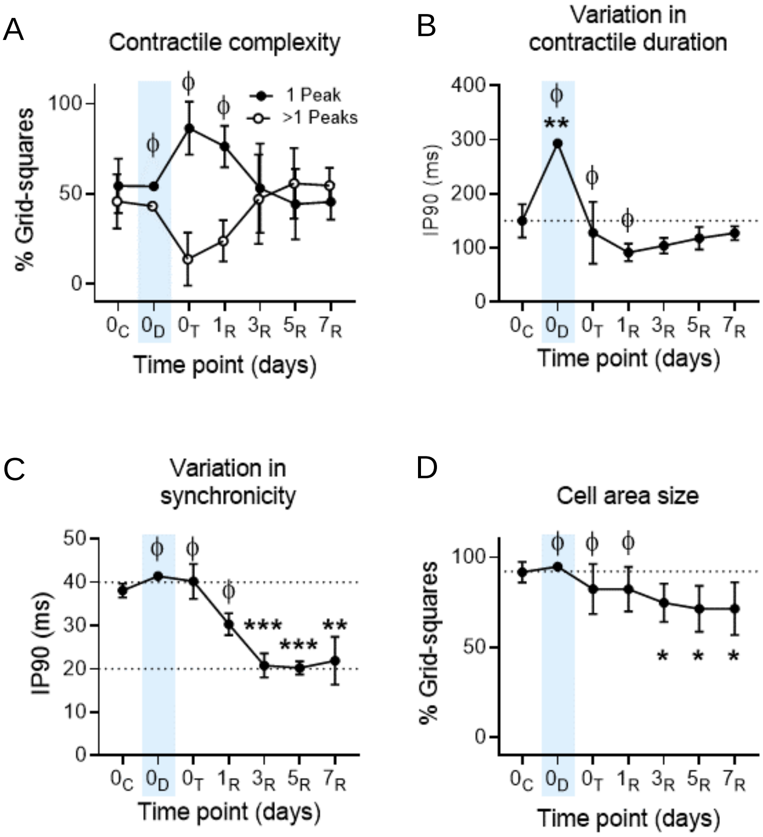

Figure 4.8 Spatiotemporal analysis of contractility of monolayers attached and detached to rigid surfaces.
A) Contractility complexity. B) Variability of the contractile duration (CD_{50}) expressed as IP90 in ms. C) Variability in synchronicity (TStart) expressed as IP90 in ms. D) Cell area size calculated as percentage of grid-squares analysed. Φ indicates a timepoint with excluded values because of quiescence. N = 3; n = 16. Cor.4U (NCardia) hiPSC-CMs were used for this experiment.

Figure 4.8B shows the variability in contractile duration, expressed as IP90, before, during and after detachment from the rigid substrate. Before detachment, mean IP90 for CD_{50} was 150±31 ms and this approximately doubled on cooling, which is most likely caused by the lower temperature and the slower spontaneous beating frequency (Figure 4.5). Within the first day after detachment, mean IP90 for CD_{50} decreased significantly to 90±31 ms but increased again to 127±13 ms on day 7, indicating increased heterogeneity in contractile events when cells are attached to the culture dish.

An indication of the synchronicity of contraction is given by the IP90 of TStart values (Figure 4.8C). There is no change in synchronicity of the monolayer activation on cooling and detaching, but from day 1 through to day 7 after monolayer transfer, the IP90 values were significantly lower than the control (IP90 = 38±2 ms on day 0, 21±3 ms on day 3, 22±6 ms on day 7), indicating an increased synchronicity after transfer. The increased synchronicity is sustained and can therefore not be explained by the level of attachment to the culture substrate. When looking at the total monolayer area, expressed as % of grid-squares analysed, we can see a gradual decrease in area size, which is significantly smaller on days 3-7 compared to day 0 before detachment (Figure 4.8D and Figure 4.9). This can also be observed when looking at the brightfield images shown in Figure 4.3 and Figure 4.4. This decrease in area size, hints towards a more 3D like structure and thus increased syncytium of cells (more cell-cell contact) and could explain the sustained increased synchronicity in contractility (Figure 4.8C).

An example of the map analysis of one sample is shown in Figure 4.9 and shows the change in area size (A-D), number of peaks (B), IP90 of CD_{50} (C) and IP90 of TStart (D) in time.

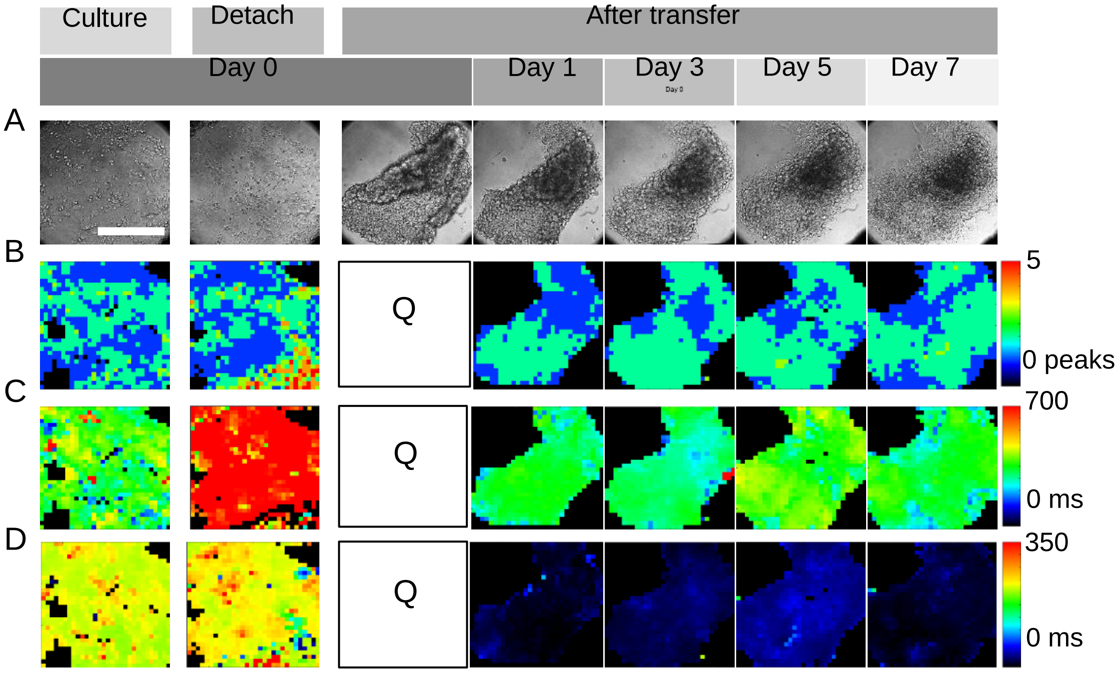

Figure 4.9 Map analysis of contractility of monolayers during detachment and attachment to rigid surfaces.
A) Example brightfield images showing the morphology of the monolayers in time, which are the same as shown Figure 4.4. B-D) Heatmaps for the number of peaks (B), the contraction duration (C) and the start time (D) of monolayers, before, during and after detachment. Scalebar represents 400 µm and Q indicates quiescence.

4.3.3 Voltage recordings from transferred micro patches one week after transfer

The electrophysiology of the reattached monolayer was measured on day 7 and results are shown in Figure 4.10. Interestingly, the spontaneous beating frequency and the TRise were comparable to the values of samples that were cultured in a standard fashion as described in Chapter 3. However, the APD_{90} was significantly increased in re-attached monolayers (APD_{90} = TCP: 354±48 ms, re-attached: 448±8 ms, p = 0.0134).

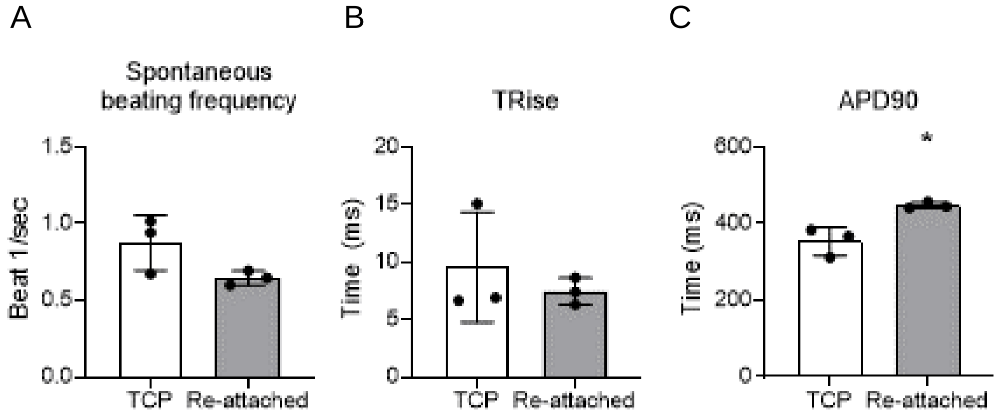

Figure 4.10 Electrophysiology of hiPSC-CM monolayers on day 7 after detachment (re-attached).
Values are compared to values those of hiPSC-CM monolayers seeded on TCP that were discussed in Chapter 4. A) Spontaneous beating frequency. B) TRise. C) Action potential duration at 90% of the amplitude (APD_{90}). N = 3; n = 16. Cor.4U (NCardia) hiPSC-CMs were used for this experiment.

4.4 Conclusion and discussion

4.4.1 Thermoresponsive dishes to create free floating hiPSC-CM sheets

In this chapter, NUNC UpCell dishes with the thermoresponsive PIPAAm coating were used to detach intact hiPSC-CM sheets, which could be used as building block for cardiac EHTs. These dishes have shown to be successful for the development of cardiac patches for cardiac regeneration of the infarcted myocardium in research (Matsuo et al., 2015a, Tsuruyama et al., 2019) and clinical studies (Miyagawa et al., 2017). The main advantage is the non-invasive way of cell harvesting by simply incubating the culture dish at room temperature. In this way, the subcellular ECM remains intact and forms an ideal niche for the hiPSC-CM, promoting cell survival and integration after implantation (Zhao et al., 2020).

4.4.2 The effect of cold temperatures on the hiPSC-CMs

To detach the cellular sheet, the PIPAAm coated dish was placed for 30-60 minutes at room temperature. This may be damaging to CMs, however, others have showed that using this method for cell sheet engineering using CMs is possible and results in viable cell sheets (Matsuo et al., 2015a). Moreover, damage caused by short-term hypothermia has shown to be reversible in adult CMs and it is likely that this is the case for hiPSC-CMs as well (Mcglynn, 2017). From these data, it is known that the APD of hypothermic cardiomyocytes is prolonged (Dietrichs et al., 2020), and the contraction time-course slows down at low temperatures (Bers et al., 1989), caused by a reduced calcium sensitivity of the myofilaments (Harrison and Bers, 1989). It is therefore not surprising that longer contraction durations, and consequently a decreased spontaneous beating frequency, were observed during incubations at room temperature. Importantly, hiPSC-CM monolayers showed contraction at a similar spontaneous beating frequency soon after being relocated in a 37°C environment, an indicator for good recovery.

4.4.2.1 Non-thermoresponsive alternatives to PIPAAm

Nonetheless, there is a search for isothermal alternatives for PIPAAm. A recent publication by Baek et al. describes a chemical coating from which monolayers can detach within minutes in isothermal conditions (Baek et al., 2020). Here, the surface energy that is important for cell adhesion, is changed by replacing the cell culture medium for a Mg^{2+} and Ca^{2+} free buffer, such as $PBS^{-/-}$. Importantly, the subcellular niche of the detached cells is not affected. This method could be a great alternative for cell types that are sensitive to temperature changes. However, the coating reduces, although not significantly, the number of focal adhesions per cell as well as the focal adhesion density (Baek et al., 2020). This could have implications for spontaneously beating cardiac cells that need sufficient binding to a substrate to support the contractile forces. Moreover, intervention with relatively low Ca^{2+} concentration and subsequent reinstitution of calcium ions leads to significant morphological changes, a phenomenon known as the calcium paradox (Zimmerman et al., 1967). Temporarily substituting maintenance medium with low calcium containing medium as a method for detachment could thus lead to irreversible damage. Therefore, detaching using PIPAAm would be the least damaging method of the two.

4.4.3 Comparing the two different detachment methods.

Two proposed methods for sheet detachment and transfer were explored. The first method tested was based on hydrophobic PVDF membranes and was suggested by the manufacturer and could maintain monolayer size and shape. However, this technique is less used with CMs (Shimizu et al., 2002a). Unfortunately, on average, only 10% of the monolayers bound to the membrane and transferred to a new culture dish. The second method, simply pipetting, is more often used for cardiac cells (Haraguchi et al., 2012, Matsuo et al., 2015a, Shimizu et al., 2002b, Miyagawa et al., 2005). This technique resulted in 25-31% successful transfers and was thus slightly more successful than the membrane technique. Unfortunately, both methods resulted in a suboptimal percentage of viable transfers, thus other ways to create small EHTs should be explored.

4.4.3.1 The PVDF membrane technique

The low success rate could be caused by one or multiple reasons. Despite the recommendation of the manufacturer to use PVDF membranes in combination with PIPAAm (Kawecki et al., 2016, Shimizu et al., 2002a), some practical issues were experienced. Firstly, the small size of the monolayers might have limited the efficacy of cell adhesion to the PVDF membrane. For example, the manufacturer of the UpCell dishes emphasizes the importance of preventing air bubbles between the cells and the membrane is emphasized . With a smaller surface, the effect of one air bubble is many times larger than on a larger surface.

Secondly, the PVDF membrane was relatively thick and stiff, what diminishes the surface contact with the monolayer. Attempts to improve membrane flexibility by soaking the membrane in culture medium did not gain positive results (data not shown), potentially because of the high hydrophobicity of PVDF. Another rationale to soak the membrane into culture medium was to bind proteins to the membrane that would enhance cell adhesion (Park et al., 2020). According to the manufacturer, emersion of PVDF into EtOH activates the surface chemistry, however, this did not enhance binding either (data not shown). Kawecki et al found that an alternative membrane called SUPRATHEL, a medical approved membrane as treatment for burn wounds, had a superior detachment rate over PVDF membranes (88% vs 72%) (Kawecki et al., 2016). However, it is important to note that there was still cell loss and these studies were done on fibroblast and dermal cells, not CMs.

Thirdly, the incubation time at low temperatures could have been too short for sufficient cell detachment. Kawecki et al assessed the detachment after 24h of incubation, many hours more than used in our studies. Nonetheless, protocols with larger cell sheets showed cell detachment within one hour as well (Haraguchi et al., 2012). The long incubation times make this a time-consuming process, especially when stacking cell sheets. But more importantly, when exposing cells to relatively cold temperatures and a reduced nutrient supply for a longer period of time might increase the risk of reduced cellular viability.

4.4.3.2 The force pipetting technique

Force pipetting resulted in a higher success rate compared to the PVDF membrane, as this technique was faster and more controllable. However, it was too aggressive for the small cardiac monolayers. The unsuccessful detachments and transfers were mainly caused by patch rupture, which would presumably be less significant in larger patches. Moreover, patches detached and transferred using this technique significantly reduced in size, which is also observed by others (Shimizu et al., 2002b, Miyagawa et al., 2005, Haraguchi et al., 2012). They shrank from 3 mm to <1 mm, deforming from a monolayer to spheres, which are unsuitable for the development of small EHTs. Arguably, monolayers of a larger diameter could be used so that the final is big enough for cell sheet stacking. However, this will significantly increase the number of hiPSC-CMs needed, while one of the aims was to minimize cell numbers. Therefore, a backbone, e.g. a biomaterial, might be an alternative approach to increase the survival- and success rate (Haraguchi et al., 2012).

In short, both the PVDF membrane and the force pipetting techniques are not suitable for small hiPSC-CM patches. Therefore, other ways of transferring the hiPSC-CM monolayer should be considered.

4.4.4 Other applications with PIPAAm

Besides the many cell types tested with the PIPAAm coating for cell sheet engineering, A recent study by Zhao et al. presented a novel thermosensitive three-block peptide microspheres, based on the PIPAAm thermo-responsiveness. These microspheres form a liquid at room temperature but a hydrogel at 37°C (Zhao et al., 2020). Encapsulation of cardiac cells onto these microspheres was possible and after myocardial implantation through injection the retention rate of almost 20% in contrast to 2% when injected the cells alone. These data are highly supportive of the importance of a support structure of cells before implantation and a conformation that injection of single cells is not achieving desirable results for cardiac regeneration (Zhao et al., 2020).

4.4.5 Physiology of free-floating monolayers

The successfully transferred monolayers using the pipetting method were analysed further on morphology and physiology, namely voltage and contractility using fluorescent recordings and brightfield videoframes, respectively.

4.4.5.1 Contractility

Although the overall contractility of detached hiPSC-CM monolayers was not significantly different from adhered monolayers, some of the hiPSC-CM monolayers became quiescent after detachment. Most of them recovered within 1 day and were beating with a similar pace to that before detachment and to other patches from the same experiment. This indicates that the pipetting technique might have reversibly and irreversibly harmed some patches. The comparable physiology of patches that survived, indicates that they recovered after the transfer process.

4.4.5.2 Spatiotemporal analysis

In Chapter 3 we hypothesized that the multiphasic contractile behaviour is caused by the rigid surface the cells adhere to. Here, we observed that this complex contractile behaviour disappears upon detachment but reappears when the monolayer attaches to the new culture dish. This confirms that this complexity is indeed of a mechanical origin. Interestingly, although the IP90 values for CD_{50} were similar across the monolayers during the experiment, the IP90 values for TStart were permanently and significantly decreased after detachment, suggesting a more synchronous contraction. The underlying reason could be an increased cell-cell coupling, caused by the reduced diameter and folding of the sheet as shown in Figure 4.4 and Figure 4.8, respectively.

4.4.5.3 Electrophysiology

Interestingly, re-attached monolayers did display a relatively long APD_{90} (~450 ms), compared to those on a rigid substrate, especially considering their relatively fast spontaneous beating frequency of almost 2 Hz (Figure 4.10). The reason for this is unclear and might be related to the more 3D-like structure and associated electrical syncytium that develops after detachment (Lemme et al., 2018, Lemoine et al., 2017).

4.4.5.4 Conclusion

Taken together, neither the membrane technique nor the pipetting technique have shown to be useful for the development of small EHTs. Therefore, other methods, such as the use of a biomaterial backbone, should be explored instead.

Additionally, these data show that the complex contractile behaviour, described previously in Chapter 3, is abolished on detachment of the monolayer from the TCP substrate, but reappears during re-attachment. This suggests that the attachment to the rigid TCP affects the contractile behaviour of hiPSC-CMs.

Chapter 5 Properties of EHTs with a support structure made of recombinant collagen-like peptide hydrogel support structure

5.1 Introduction

The myocardial stiffness changes during developmental stages and in disease. For example, the human neonatal myocardium has a Young's Modulus around 10 kPa but this increases over time to approximately 50 kPa for a healthy adult heart (Ramadan et al., 2017, Travers et al., 2016, Ward and Iskratsch, 2020). Cardiac fibrosis, present in some cardiac disease states, increases this stiffness even further to approximately 100 kPa (Ward and Iskratsch, 2020, Ramadan et al., 2017, Travers et al., 2016). Stiffening of the myocardium is mainly caused by deposition of more or different types of ECM proteins by myofibroblasts, and the resulting alterations in myocardial stiffness affect the functionality/contractility of cardiomyocytes *in vivo* (Li et al., 2014).

Like other cell types, cardiomyocytes bind to their surrounding ECM and to neighbouring cells through cell adhesion complexes in the cell membrane (Pandey et al., 2018, Ward and Iskratsch, 2020, Santoro et al., 2019, Samarel, 2005, Geiger et al., 2009). Both cell-cell and cell-ECM adhesions sense mechanical changes in the cellular environment and lead to functional changes within the cell via activation of overlapping intracellular pathways (Pandey et al., 2018, Del Rio et al., 2009, Monemian Esfahani et al., 2019, Izu et al., 2019, Yonemura et al., 2010, Saucerman et al., 2019, Iskratsch et al., 2014, Wickline et al., 2016). Studies investigating the effects of substrate stiffness on the contractility of cardiomyocytes have found changes in sarcomere organization (Ribeiro et al., 2020, Jacot et al., 2008, Heras-Bautista et al., 2014, Rodriguez et al., 2011, Ribeiro et al., 2015), myofibril formation and/or organization (Ribeiro et al., 2015, Engler et al., 2008, Feaster et al., 2015), calcium handling (Jacot et al., 2008, Rodriguez et al., 2011, Van Deel et al., 2017, Boothe et al., 2016) and force generation (Ribeiro et al., 2020, Rodriguez et al., 2011, Ribeiro et al., 2015). However, these studies were mostly done with single cells, and overlooked the additional role of cell-cell coupling and intercellular force transmission (Monemian Esfahani et al., 2019, Yonemura et al., 2010).

HiPSC-CMs are usually grown in a monolayer format on standard tissue culture plastic (TCP) or glass substrates, which have a Young's Modulus of greater than 1 GPa (Travers et al., 2016), 3-4 orders of magnitude stiffer than the native myocardium. To ensure cell adherence to the underlying structure, the plastic or glass surface is coated with a thin layer of ECM components such as fibronectin (Blinova et al., 2018). These coatings do not alter the overall stiffness of the cell-surface interface, which thus remains inappropriately high for the normal function of the hiPSC-CMs and can result in the loss of hiPSC-CM contractility (Heras-Bautista et al., 2014). Softer substrates that mimic the native stiffness of the myocardium could be used as a culture substrate to cells to contract without physical restrictions, such as hydrogels.

Hydrogels are peptide networks that are highly permeable and absorb large amounts of fluids. They are created through a crosslinking process of smaller peptides. For example, methacrylated side chains can be cross-linked when exposed to light irradiation and a photoinitiator, resulting in a covalently bound peptide network with long-lasting mechanical properties. More complex hydrogels can be made by peptide functionalization or through combining various compounds together, such as other ECM proteins (Saldin et al., 2017), cell adhesion moieties (Jia et al., 2016) and therapeutic agents (Burgess et al., 2021, Chow et al., 2017).

In addition to their usefulness during *in vitro* studies, hydrogels are also widely used for tissue engineering because of their versatility (Zhao et al., 2020, Weinberger et al., 2017, Bar and Cohen, 2020, Majid et al., 2020). Two main concepts are currently used: 1) the injection of a hydrogel, followed by *in situ* regeneration and 2) *in vitro* development of a 3D construct followed by implantation. Generally, natural peptides are more desired for implantation studies than synthetic materials as they contain natural peptide sequences that closely resemble essential properties of the native ECM, such as cell adhesion and ECM remodelling (Majid et al., 2020). A good example of a hydrogel made of a naturally derived peptide is Gel-MA; a methacrylated gelatine peptide hydrogel (Yue et al., 2015). However, the drawbacks of naturally derived peptides are the batch-to-batch variation and the risk of pathogen transmission, such as prions (Asher, 1999).

To overcome these problems, recombinant peptides based on natural molecules could be used instead. Methacrylated recombinant collagen-like peptide (RCP-MA) is a recombinant peptide based on human collagen I and is commercially available from Fujifilm as Cellnest (Parvizi et al., 2016, Parvizi et al., 2018, 2020, Tytgat et al., 2019). RCP-MA has already been used for *in vivo* studies as micro-sphere for cell delivery (Parvizi et al., 2016) and as perivascular scaffold (Parvizi et al., 2018). The peptide is made through yeast fermentation, followed by purification steps that remove host cell proteins which could potentially induce immune responses. RCP-MA contains arginine-glycine-aspartic acid (RGD) tripeptide sequences that are needed for cell adhesion to the hydrogel (Tytgat et al., 2019). The methacrylated sidechains allow for crosslinking and the methacrylation level determines the density of the hydrogel network and thus the final stiffness of the hydrogel (Figure 5.1) (Tytgat et al., 2019). In this way, the hydrogel could be tuned to mimic the native stiffness of the heart. Moreover, collagen type-1 is the main ECM protein of the myocardium, which makes RCP-MA based hydrogels interesting for EHT development and cardiac regeneration.

There are different ways of using hydrogels for cell culture: 1) mixing cells within the hydrogel, creating a 3D structure and 2) seeding cells on top of a hydrogel in a 2D format. Cell-cell adhesions is important for CM function and their long-term survival (Salameh and Dhein, 2013, Vermij et al., 2017, Moore et al., 2008, Li et al., 2017, Chopra et al., 2011), so encapsulating cells in a biomaterial requires a fine cell:material ratio. Seedings cells on top of a pre-made hydrogel might therefore be a good alternative approach for the development of an engineered heart tissues (EHT). Some advantages of seeding cells on top of a hydrogel over encapsulating cells inside the hydrogel include: 1) no UV-light damage to the cells while crosslinking the RCP-MA, 2) hydrogels can be pre-soaked in culture medium to enhance cellular viability and perhaps adhesion, 3) guaranteed cell-cell connections which is beneficial to cellular physiology and survival and 5) better time-management as hydrogels can be pre-made and stored in in the fridge. This format can be up scaled if needed, simply by increasing the hydrogel's diameter and/or stacking hydrogel/cell layers on top of each other, where the hydrogel benefits the diffusion of nutrients to the cells located in the core of the constructs (Matsuo et al., 2015a).

5.1.1 Aims

Although a certain number of cells is needed to regenerate the heart and up-scaling might therefore be inevitable. During the previous chapter, a small cardiac patch (<50,000 hiPSC-CMs) was developed. This methodology will form the basis of the EHT that will be developed during this chapter, and which has the following properties:

1) That the EHT consists of commercially available hiPSC-CMs and a readily available biomaterial.

2) That the hiPSC-CMs form a discrete monolayer of cells so that cell-cell connections are maintained.

3) That the biomaterial has a comparable stiffness to the native myocardium and does not affect hiPSC-CM functionality.

4) That the biomaterial can be shaped into a thin layer of ~300 µm thick.

5) That the EHT is stable *in vitro* for at least a week.

6) That the EHT can function as a building block for future upscaling.

5.2 Chapter specific methods

5.2.1 RCP-MA hydrogel synthesis

Three variants of RCP-MA were kindly provided by FUJIFILM Manufacturing Europe B.V., namely 20%, 50% and 100% methacrylated RCP-MA (RCP-MA_{20}, RCP-MA_{50} and RCP-MA_{100}). These result in hydrogels with a Young's Modulus (E') of 1.0, 12.7 and 22.6 kPa for RCP-MA_{20}, RCP-MA_{50} and RCP-MA_{100}, respectively, after UV-crosslinking (Figure 5.3A). Rheology measurements were performed by Suzan van Dongen and Bas Kluijtmans from FujiFILM Europe B.V., using an Anton Paar Rheometer.

It was suggested by FujiFILM Europe B.V. to use lithium phenyl(2,4,6-trimethylbenzoyl) phosphinate (LAP, L0290, Tokyo Chemical Industry UK Ltd. (TCI)) as a crosslinking agent for our studies. LAP is a free radical photo-initiator used to initiate free radical chain polymerization upon light exposure and is combined with RCP-MA to produce a photopolymer. LAP is preferred over other crosslinking agents, such as Irgacure 2959, for biological applications due to its increased water solubility, increased polymerization rates with 365 nm light and absorbance at 400 nm allowing for polymerisation with visible light. The improved polymerization kinetics reduce initiator toxicity and increase cell viability.

Upon receipt, freeze-dried RCP-MA was stored in the freezer. RCP-MA was dissolved in PBS$^{+/+}$ to obtain a 10% w/v concentration and incubated for at least 1 hour at 37°C. LAP (L0290, Tokyo Chemical Industry Co., Ltd) was dissolved in PBS to get a 2.5% w/w solution, followed by a 30 min incubation at 37°C. Per 1000 µl of 10% RCP-MA (w/v), 26 µl LAP and 50 µl of PBS$^{+/+}$ or fibronectin (FN, bovine, 33010018, Gibco) was added. The mixture was pipetted into a mould and exposed to UV-light (365nm) at a light intensity of 10 mW/cm^2 for 2-5 minutes using the Omnicure series 1500 crosslinker. Hydrogels could set for another couple of minutes, where after they were either directly used for an experiment or incubated in 100 µg FN/ml PBS$^{+/+}$ overnight. In later experiments, hydrogels were soaked into plating medium for approximately an hour.

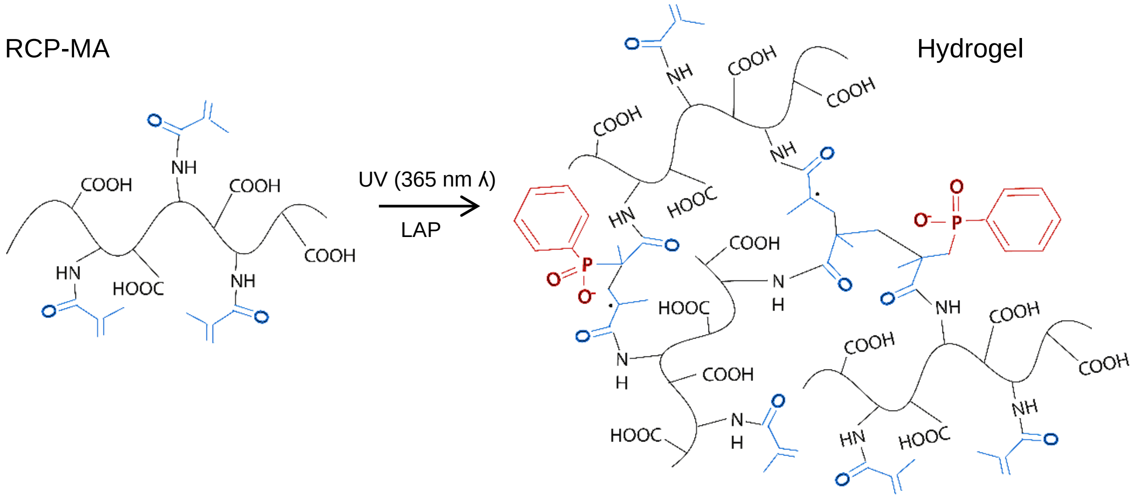

Figure 5.1 Schematic of the chemical reaction of RCP-MA crosslinking.
RCP-MA is crosslinked using LAP photoinitiator and UV light (365 nm wavelength). The RCP base sequence is shown in black. Methacrylate side groups are shown in blue and the number of methacrylated sidechains determine the stiffness of the hydrogel. Residual of LAP photoinitiator is shown in red.

5.2.2 Cell seeding on top of the hydrogel

For most experiments, hydrogels of 350 µm and a 6 mm diameter were used. Prior to cell seeding, the hydrogels are soaked in culture medium for approximately an hour. Then, the hydrogels are carefully place in a 35 mm glass dish (P35G-1.5-14-C, MatTek corporation) and a thick 3 mm stencil is placed on top of the hydrogel. Here, a tight seal is created, preventing the cell suspension from leaking after cell seeding. Without touching the stencils, ~22,500 (double) or ~45,000 (quadruple) hiPSC-CMs are seeded inside each stencil, on top of the hydrogel. After 2 days, stencils are removed, and 2 ml maintenance medium is added to each dish and replaced every 3 days. The result is a 6 mm diameter hydrogel with a 3 mm diameter hiPSC-CM monolayer. The ~1.5 mm rim can be used for EHT handling during future implantation studies. An overview of the procedure is shown in Figure 5.2.

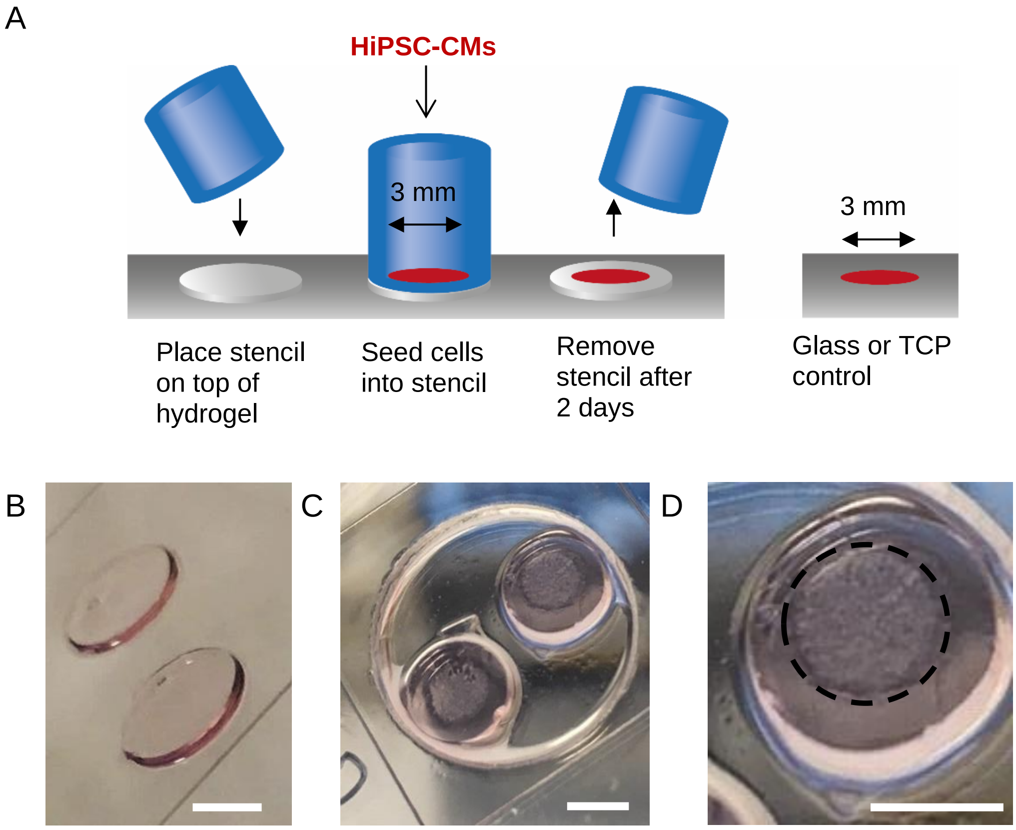

Figure 5.2 Seeing hiPSC-CMs on top of hydrogel.
A) Diagram showing the procedure of seeding hiPSC-CMs on top of hydrogels using thick stencils. In some experiment, a glass or TCP surface is used as a control, so the stencil is just placed directly onto the TCP or glass surface. B) Hydrogels pre-soaked in plating medium. C) Two examples of hydrogels with hiPSC-CMs seeded on top. D) a close-up of one of the hydrogels. Black dotted lines indicate area with cells. The outer rim that does not contain cells is also visible. Scalebars indicate 3 mm.

5.2.3 β-adrenergic stimulation of hiPSC-CMs

Isoprenaline (ISO) is an ß-adrenergic receptor agonist. In adult CMs ISO has a inotropic, chronotropic and lusotropic effect, however, these effects are sometimes absent in hiPSC-CMs (Pillekamp et al., 2012, Chen et al., 2015, Liu et al., 2007). These contradictory results are most likely caused by the immature state of the hiPSC-CMs (Karbassi et al., 2020), but also the hiPSC donor/source and the cardiac differentiation protocol, resulting in a variety of genotypes and phenotypes, might be an underlying reason for the difference in ISO response between hiPSC-CM lines (Huo et al., 2017, Mannhardt et al., 2020).

ISO studies were performed on the CellOPTIQ system (paragraph 2.3). ISO (15627, Sigma Aldrich) was dissolved and diluted in PBS until a 1000x stock solution and kept at 4°C until further use. First, the baseline contractility of EHTs or hiPSC-CM monolayers were recorded. Then, an aliquot of the 1000x stock solution was diluted 100x in BMCC medium to obtain a 10x stock, followed by replacing 10% of the BMCC in the dish with either 10x ISO stock solution (final concentration of 300 nM or 1 µM) or a vehicle (BMCC medium), followed by a 5 min incubation period. Subsequently, contractility was recorded to measure the effect of ISO. All recordings were done at spontaneous rate or at fixed rates of 1, 1.2 or 1.5 Hz. Glass dishes (MatTek) served as a control.

5.2.4 RNA isolation and qRT-PCR

In collaboration with a Finish cardiovascular research lab, expert in gene expression profiling of hiPSC-CMs, the expression of natriuretic peptide A (NPPA) and natriuretic peptide B (NPPB) mRNA was studied as described previously (36). Endothelin-1 (ET-1) upregulates the expression of NPPA and NPPB in hiPSC-CMs and was therefore used as a positive control (36). Cells were lysed in 400 µl of Trizol reagent (Invitrogen, Carlsbad, CA, USA) and stored at -80°C. Total RNA was isolated using the Phase Lock Gel Heavy tubes (Quantabio, Beverly, MA, USA) according to the manufacturer’s instructions and RNA concentration and quality was analysed using NanoDrop 1000 (Thermo Fisher Scientific, Waltham, MA, USA) spectrophotometer. cDNA was synthesised from 50–250 ng of total RNA in 10 µl reactions with Transcriptor First Strand cDNA Synthesis Kit (Roche, Basel, Switzerland) according to the manufacturer's protocol using random hexamer primers and MJ Mini Personal thermal cycler (Bio-Rad). The cDNA was diluted 1:9 in PCR grade H2O, of which 4.5 µl was used for qPCR analysis. Commercial TaqMan® Gene Expression Assays for NPPA (Hs00383230_g1), NPPB (Hs01057466_g1), ACTB (4333762F), and eukaryotic 18S rRNA (4352930E), all from Thermo Fisher Scientific, were used with LightCycler® 480 Probes Master reagent (Roche) according to manufacturer's instructions. Analysis was performed on a LightCycler® 480 Real-Time PCR System (Roche). Two technical reactions were used for each reaction, and the average of technical replicates was used in the analysis. To confirm absence of PCR contamination, no-template controls were used. The ΔΔCt method was used to analyse the relative gene expression. First, the quantification cycle (Cq) values of NPPA and NPPB were normalised to the average of the Cq values of reference genes ACTB and 18S rRNA of the same sample, whereafter the obtained ΔCq values were normalised to the ΔCq values of control sample.

5.3 Results

5.3.1 RCP-MA synthesis and properties.

Rheology measurements for the Young's modulus (E') were done by FujiFilm Europe B.V. and were 2, 10 and 22 kPa for the RCP-MA$_{20}$, RCP-MA$_{50}$ or RCP-MA$_{100}$, respectively, as shown in Figure 5.3A (2020, Parvizi et al., 2016). To test the properties of the hydrogel in solution, mixtures of RCP-MA$_{20}$, RCP-MA$_{50}$ or RCP-MA$_{100}$ hydrogels were placed into PBS overnight. The next day, significant swelling of the hydrogel was seen in the RCP-MA$_{20}$ group and RCP-MA$_{50}$, but not in the RCP-MA$_{100}$ hydrogel (Figure 5.3B). The amount of swelling is thus related to the number of crosslinks and the water uptake capacity of the hydrogel decreases with increasing concentration because of the formation of a more densely crosslinked network due to the higher number of photo-crosslinkable functionalities present (Tytgat et al., 2019). Further, RCP-MA$_{100}$ was the least flexible, followed by RCP-MA$_{50}$ and RCP-MA$_{20}$ as shown in Figure 5.3C. More specifically, RCP-MA$_{20}$ was too soft to maintain its shape and does therefore not have the right properties to function as a support structure for hiPSC-CM implantation.

5.3.2 Development of a method to create the ideal support structure

Different moulds were tested for RCP-MA crosslinking. Firstly, a 96 well-plate was used as mould, however, this resulted in meniscus formation instead of a flat hydrogel. This was especially visible when using small quantities of 200 μl or 500 μl needed to make think hydrogels, which created a ring-shaped hydrogel

(Figure 5.3D). A second method is to use the stencil for both hydrogel crosslinking and subsequent seeding of hiPSC-CMs. Unfortunately, this method resulted in a low success rate, because it is extremely easy to accidentally move a stencil when pipetting liquids, e.g. the hydrogel mixture or hiPSC-CMs (Figure 5.3E). Therefore, the third method of using coverslips and a silicone mould is the best method to make hydrogels (Figure 5.3F and G). Here, the silicone mould is placed on top of a sterile glass microscope slide, the RCP-MA solution is added to the mould and a glass coverslip is placed on top while preventing air-bubble formation. This method results in hydrogels of approximately 350 µm thick (Figure 5.3G) and has a high accuracy and reproducibility. Additionally, the shape and size of the hydrogel could be easily amended by developing a new silicone mould.

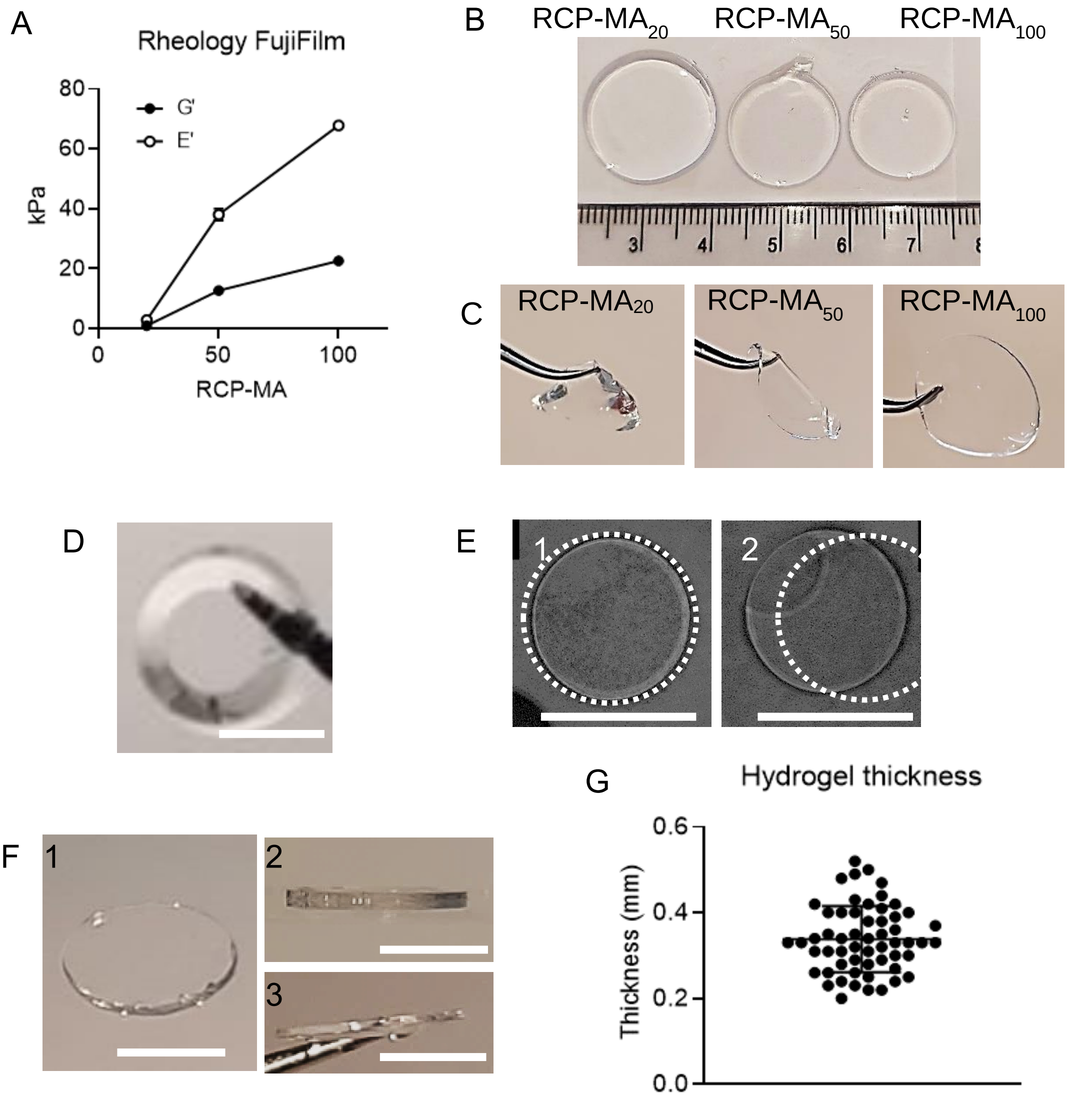

Figure 5.3 RCP-MA properties and fabrication.

A) The stiffness of the 20% 50% and 100% methacrylated RCP-MA in G’ and E’, measured by FujiFILM Europe B.V. B and C) Macroscopic photos of the three types of hydrogel made with the same 1.5 cm mould. B) The size of the hydrogel after 1 day in PBS. C) When picking up the hydrogels with forceps the stiffness of the hydrogel becomes visible. D) Crosslinking of RCP-MA inside a 96 well-plate causes meniscus formation of the hydrogel. E) Examples of hydrogel crosslinking and cell seeding inside a stencil where (1) the stencil stayed in place during both procedures and (2) where the hydrogel was malformed and the stencil moved during cell seeding, resulting in a misalignment. White dotted line indicates where the hiPSC-CMs are located. F) (1) top view, (2) side view, (3) side view after picking up with tweezers. Scale bar represents 3 mm. G) Crosslinking of RCP-MA inside a silicone mould results in a thin hydrogel of approximately 350 μm ($N_{Experiments}$ = 8; $n_{Hydrogels}$ = 48).

5.3.3 Cor.4U cells but not CDI cells attach to the RCP-MA hydrogel

HiPSC-CMs (Cor.4U and ICell^2) were seeded on RCP-MA$_{100}$ hydrogels and glass substrates and cultured for a couple of days. Soon after cell seeding it was found that hiPSC-CMs from Cor.4U (NCardia) did adhere to the hydrogel, and no difference was seen between glass and the RCP-MA$_{100}$ groups (Figure 5.4A). In contrast, the ICell^2 (FCDI) hiPSC-CMs did not spread when seeded on the RCP-MA$_{100}$ hydrogel, but did spread on FN coated glass (Figure 5.4B). This suggests that these two hiPSC-CM lines have different cell adhesion complexes.

No direct comparison has been made between the adhesion molecules of both hiPSC-CM types so far, only regarding their ion channel expression and functionality during drug screening in 2D (Huo et al., 2017) and 3D (Mannhardt et al., 2020). However, a report on the website of NCardia, published in 2019, stated that their hiPSC-CM cell line contains a embryonic finger print (Braam, 2019). In other words, their cell line is derived from hESC and not hiPSC. This difference in origin might explain the differences between the phenotype of hiPSC-CM lines. More importantly, the embryonic origin of the Cor.4U hiPSC-CMs was discontinued which made us change direction to use only CDI hiPSC-CMs (Braam, 2019). Because these hiPSC-CMs do not adhere to this hydrogel, we wanted to optimize the hydrogel properties to promote cell adhesion.

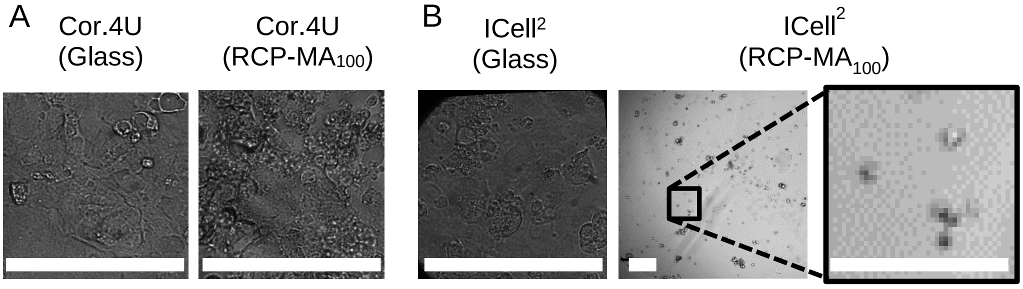

Figure 5.4 Differences in cell adhesion between hiPSC-CMs from different commercial sources.
Cor.4U (A) but not ICell^2 hiPSC-CMs (B) adhere to RCP-MA hydrogels. Images of Cor.4U cells were made on day 8 after cell seeding. Scalebars indicate 300 µm.

5.3.4 Optimizing the RCP-MA hydrogel

The underlying biological and/or biochemical reason for the inadequate cell adherence might be correlated to the presence or absence of binding moieties, such as RGD. The RCP-MA sequence contains multiple RGD sequences, supporting adhesion of many cell types, including adipose tissue derived stem cells and primary human bone marrow derived cells (Parvizi et al., 2016). However, these might be not sufficient for the adhesion of ICell^2 hiPSC-CM.

Various strategies were explored to increase cell adhesion to the hydrogel. Firstly, the RCP-MA content was increased and therefore the number of RGD moieties. Secondly, a hybrid hydrogel was created that consisting of RCP-MA and fibronectin. The experimental outcomes are described in the following sections.

5.3.4.1 Increasing the RCP-MA content 3x and 10x

To test the first hypothesis whether the number of RGD moieties was too little, the percentage (w/v) of RCP-MA$_{100}$ peptide was increased from 10% to 30% and 100%. Unfortunately, this did not improve the cell adhesion as shown in Figure 5.5. This indicates that the number of available RGD moieties does not cause the absence of ICell^2 adhesion.

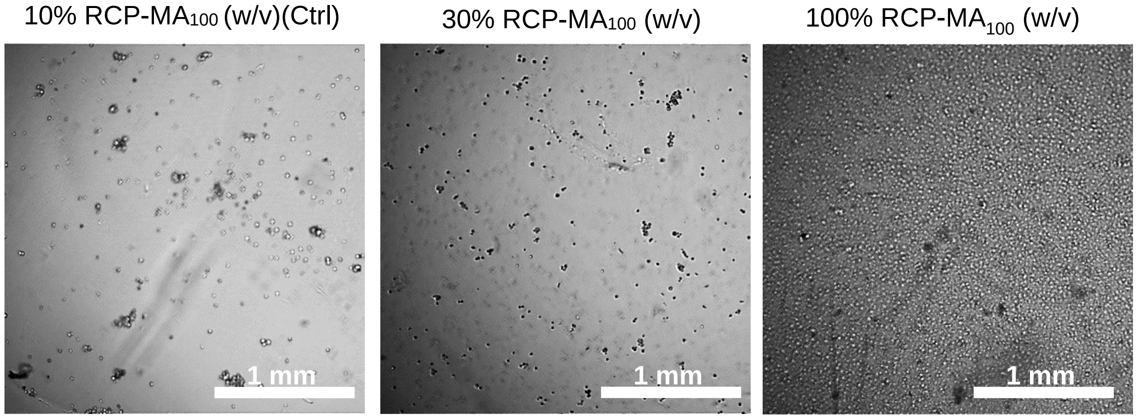

10% RCP-MA$_{100}$ (w/v)(Ctrl) 30% RCP-MA$_{100}$ (w/v) 100% RCP-MA$_{100}$ (w/v)

Figure 5.5 Increasing RCP-MA content (w/v) does not enhance cell adhesion.
These experiments were done with ICell^2 (FCDI).

5.3.4.2 Coat the hydrogel with various ECM proteins

To test whether the RCP-MA hydrogel did not have the correct cell adhesion moieties, it was decided to coat the hydrogels with different ECM peptides. Four different ECM coatings were tested, namely Geltrex, laminin, fibronectin (FN) and Cellnest (FCDI) and a non-coated hydrogel served as a control. Geltrex, laminin and FN are widely used in cell culture to coat plastic or glass surfaces prior to cell seeding. From previous data and extensive experience, hiPSC-CMs bind strongly to FN and thus FN served as a positive control. Additionally, Cellnest has the same RCP sequence as the RCP-MA hydrogels, and thus serves as an internal control.

Images that were taken 2 days after cell seeding, but before stencil removal, showed that hiPSC-CMs were present in all groups, including the control group as shown in Figure 5.6. However, hiPSC-CMs did not adhere to the Cellnest, Geltrex or control group and formed cellular aggregates instead. Coating the hydrogel with laminin resulted in a marginally improved cell adhesion, but not as good as FN, which showed similar levels of cells spreading compared to control.

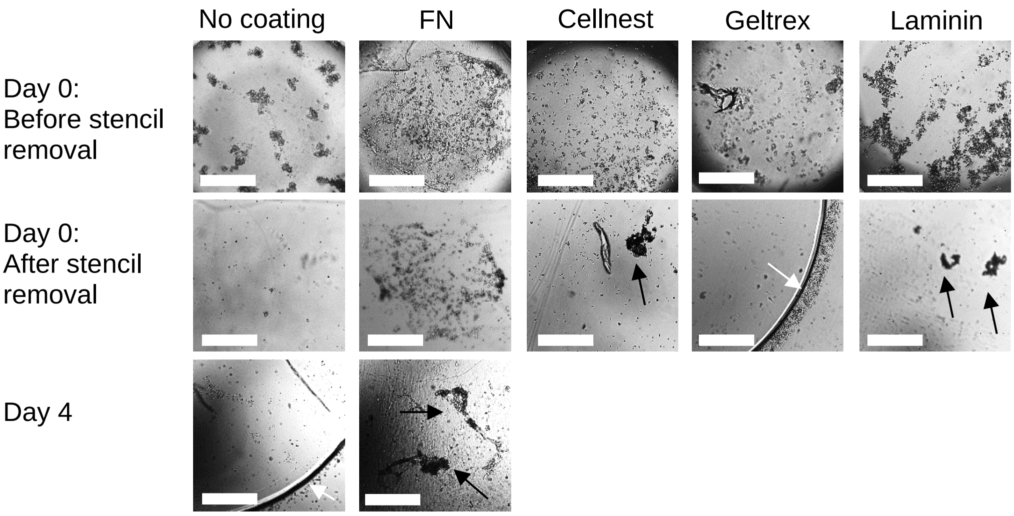

Figure 5.6 Improvement of cell adhesion after addition of a ECM-coating.
Four coatings were tested: 1) FN, 2) Cellnest, 3) Geltrex and 4) Laminin. A non-coated hydrogel served as a control. Cellnest has the same peptide sequence as RCP-MA. FN serves as a positive control. Black arrows indicate cell aggregates. White arrows indicate cell gathering along the sides of the hydrogel. Cells were seeded on day -2 and were from FCDI. Scalebars indicate 1 mm.

The removal of the stencils caused hydrogel movement and consequently resulted in cell detachment in some of the groups, such as the Geltrex group and control (Figure 5.6). The hiPSC-CMs in the laminin and Cellnest groups formed aggregates, suggesting the absence of cell adhesion to the hydrogel as well. Because Cellnest has the same peptide sequence as RCP-MA, we can conclude that this peptide sequence is not promoting ICell^2 hiPSC-CM adhesion. Only FN coated hydrogels resulted in a monolayer which was maintained after stencil removal, suggesting a relatively strong adhesion.

Further culture of the hiPSC-CMs, showed that the cells seeded on FN coated hydrogels started to lift off the hydrogel as a sheet, an indication that FN does not form strong bonds with the peptides of the hydrogel. Hence, further improvements are needed.

5.3.4.3 Incorporation of FN into the hydrogel mix to serve as an anchor to the ECM coating

The peptide sequence of FN contains a variety of bindings sites to promote adhesion to a range of ECM proteins besides cell adhesion complexes, including binding sites for other FN molecules (Antia et al., 2008). These binding sites could serve as an anchor when mixed into the RCP-MA hydrogel to prevent hiPSC-CMs detachment from the hydrogel. To achieve this, FN was combined with 10% RCP-MA (w/v) and LAP as a substitute for PBS prior to crosslinking, obtaining a new RCP-MA/LAP/FN mix. Afterwards, hydrogels were also coated with FN.

Using this new approach, strong cell adhesion was seen for the RCP-MA_{100} for at least 10 days and was comparable to that of the control group (Figure 5.7). The strong binding was especially visible during contraction as cells pulled the hydrogel (data not shown). In contrast, cell sheet detachment and cellular aggregation was seen in the RCP-MA_{50} after day 5 (Figure 5.7). Therefore, it was decided to use the RCP-MA_{100} with FN incorporated and a FN coating for future experiments.

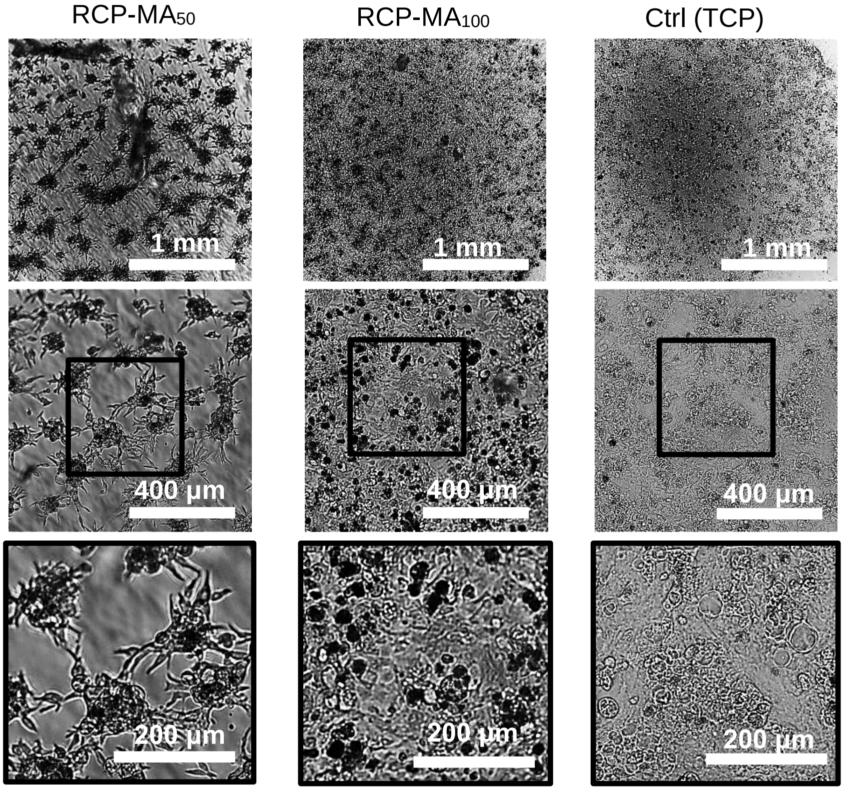

Figure 5.7 Effects of FN incorporation into the hydrogel in addition to hydrogel coating with FN.
Brightfield images of hiPSC-CMs (FCDI) seeded on RCP-MA_{50} (right column), RCP-MA_{100} (centre column), or glass substrate. Black squares indicate inserts presented in the bottom row. Recordings were made on day 5.

5.3.5 EHT functionality measurements

5.3.5.1 Voltage recordings

Voltage recordings (day 7) were made on hiPSC-CMs seeded on either RCP-MA$_{50}$, RCP-MA$_{100}$ or a glass substrate. The spontaneous beating frequency was the same for all groups, indicating comparable viability of the cells (Figure 5.8). Also, TRise, APD$_{50}$ and APD$_{90}$ were not statistically different compared to the control group. This indicates that a flexible substrate does not change the electrophysiology of the hiPSC-CMs.

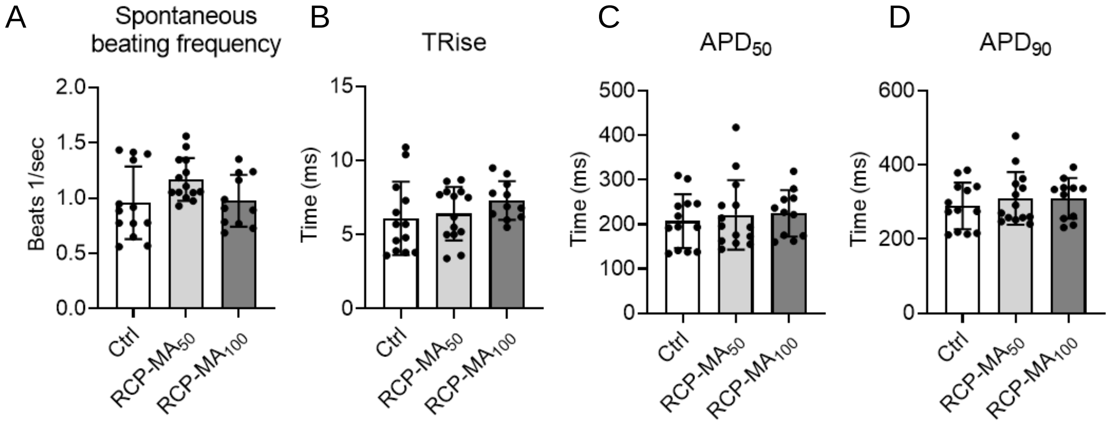

Figure 5.8 Voltage recordings of hiPSC-CMs seeded on either RCP-MA$_{50}$, RCP-MA$_{100}$ or glass substrates.
A) Spontaneous beating frequency. B) TRise. C) APD$_{50}$ and D) APD$_{90}$. $N_{Experiments}$=3; n_{Dishes}=14. No groups were statistically different. Recordings were made on day 7.

5.3.5.2 Comparison of Ca^{2+} transients

Separate measurements of intracellular Ca^{2+} indicate a similar calcium transient between rigid and flexible substrate as shown in Figure 5.9. The only changes noted was an approximately 10% increase in Width50 and Width10 of the calcium transient on flexible substrate (Figure 5.9D and E, respectively).

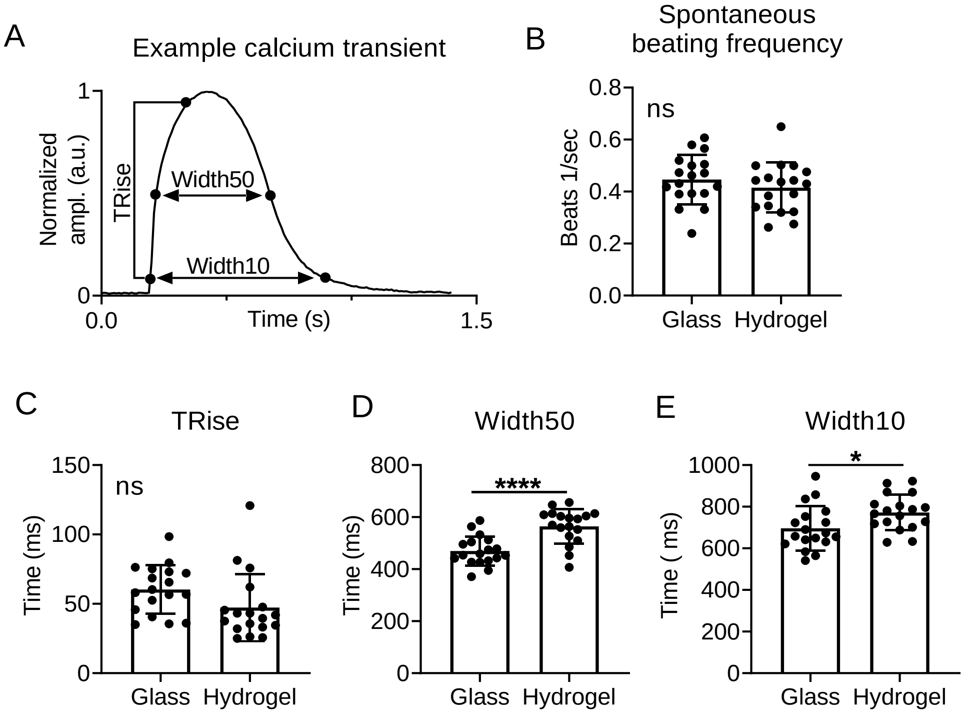

Figure 5.9 Cal520 Ca^{2+} recordings in spontaneous beating hiPSC-CM seeded on flexible and rigid substrates.
A) Diagram explaining the TRise (C), Width10 (D) and Width10 (E) measured from averaged calcium transients. B) Spontaneous beating frequency of hiPSC-CMs. C) the upstroke of the calcium transient (TRise). D) The width of the calcium transient at 50% of the amplitude (Width50). E) The width of the calcium transient at 10% of the amplitude (Width10). $N_{Experiments}$ =4 and 2 experiments, for glass and hydrogel, respectively. $N_{Samples}$ = 3 to 7 monolayers per experiment for glass and $N_{Samples}$ = 3-15 monolayers per experiment for hydrogel. Unpaired t-tests were done for the spontaneous beating frequency and Width10, but due to skewed data, a Mann-Whitney U test was done for the TRise and Width50. A p-value < 0.05 was considered significant and is indicated with *. * = p<0.05, **** = p<0.0001.

5.3.6 HiPSC-CM contractility on flexible substrates is comparable to those seeded on glass.

When looking at the contractility of the entire hiPSC-CM monolayer, no differences in spontaneous beating frequency were observed between RCP-MA$_{50}$, RCP-MA$_{100}$ and glass surfaces, indicating the patches were of comparable viability on both formats (Figure 5.10A). Changes in the amplitude signals caused by the substrate are shown in Figure 5.10B and no major trends in the contractility amplitude were seen with respect to time.

No significant differences were observed in the average contraction time (Up$_{90}$), relaxation time (Dn$_{90}$) and contraction duration (CD$_{50}$) as shown in Figure 5.10C,D and E, respectively. However, on day 7, CD$_{50}$ was significantly shorter in cells seeded on both the hydrogels compared to control CD$_{50}$ (CD$_{50}$ on RCP-MA$_{50}$: 224±8 ms RCP-MA$_{100}$: 230±9 ms, glass: 298±17 ms, P=0.04) (Figure 5.10E).

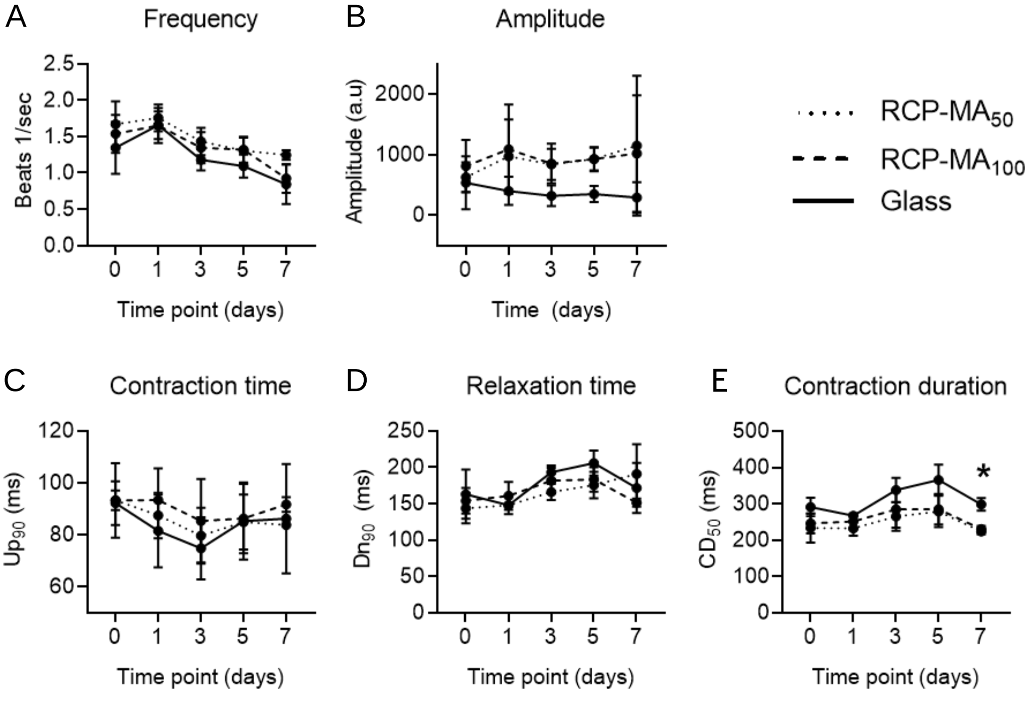

Figure 5.10 General hiPSC-CM monolayer contractility of cells seeded on hydrogel vs glass. A) Spontaneous beating frequency in beats per second. B) Contraction amplitude in arbitrary units. C) Contraction time (Up$_{90}$). D) Relaxation time (Dn$_{90}$). E) Contraction duration (CD$_{50}$). N$_{Experiments}$=3; n$_{Dishes}$=3-6 samples per group per experiment. And * indicates a p-value <0.05.

5.3.6.1 Spatiotemporal analysis of contractility

When performing the spatiotemporal analysis on these samples, analysis of the RCP-MA$_{50}$ contractility videos was difficult as the hiPSC-CMs aggregates were beating non-uniformly which complicated the analysis. This is especially clear when looking at the heatmap for the start times of the contraction shown in Figure 5.11 (middle row). In contrast, the monolayer on top of the RCP-MA$_{100}$ hydrogels showed uniform contraction and similar CD$_{50}$ compared to control (Figure 5.11, top and bottom row). Therefore, the only the RCP-MA$_{100}$ and control were analysed using this algorithm.

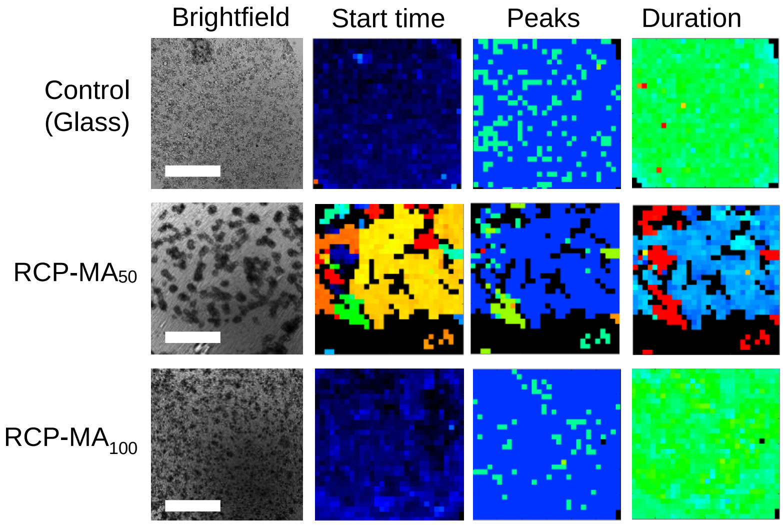

Figure 5.11 Spatiotemporal contractility analysis of hiPSC-CMs seeded on RCP-MA hydrogels.
Glass served as a control. Along brightfield images, the heatmaps for start time, the number of peaks (light blue = 1 peak; dark blue = 2 peaks; other colours = >2 peaks) and duration are shown. Scalebar = 1 mm.

In Figure 5.12A, the average percentage of grid-squares with single-peaked transients indicates cells attached to the collagen gel retain a high percentage of grid-squares with single peaks, while the cells on glass progressively developed a significant percentage of grid-squares with 2 or more peaks in each contractile event (% 1-peak on day 7 = RCP-MA$_{100}$: ~90±4%, glass: ~62±8%). No significant differences were observed in the number of grid-squares with contractile events (Figure 5.12B) or the degree of cell synchronicity (Figure 5.12C) and contraction duration (Figure 5.12D). These data indicate that hiPSC-

CMs seeded on a flexible substrate do not have a multi-peaked contractility time-course, in contrast to cells that are attached to a fixed substrate, like glass or plastic.

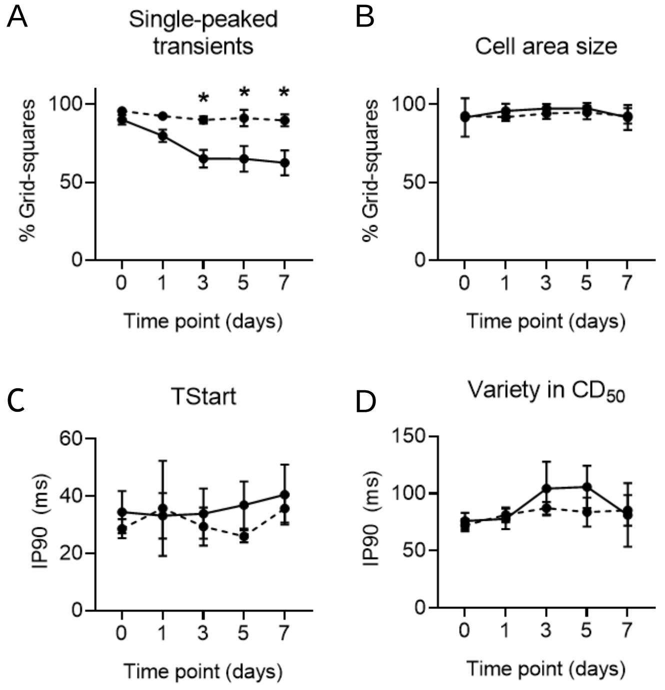

Figure 5.12 Spatiotemporal analysis of hiPSC-CMs seeded on flexible vs rigid surfaces. A) The percentage of grid-squares with only 1 peak. B) % of analysed grid-squares. C) The variety in start time (IP90 values). D) The variety in contraction duration (IP90 values). Dashed line = RCP-MA_{100} and the solid line is the glass surface.

5.3.7 Single hiPSC-CM only show twitch-like contraction profiles independent on substrate stiffness.

The origin of the multi-peaked contractile behaviour might be differential attachment of the monolayer to the underlying substrate and not the behaviour of individual cells. Evidence for this are the MM records from isolated single hiPSC-CMs on both glass and flexible substrates. As shown in Figure 5.13A and B, individual isolated cells on glass show single-peaked contraction as expected from the standard ECC model. This is also observed in isolated cells seeded on the flexible substrate (Figure 5.13C and D). Thus, complex contractile behaviour only arises in a mechanically linked sheet of cells on glass or plastic substrates.

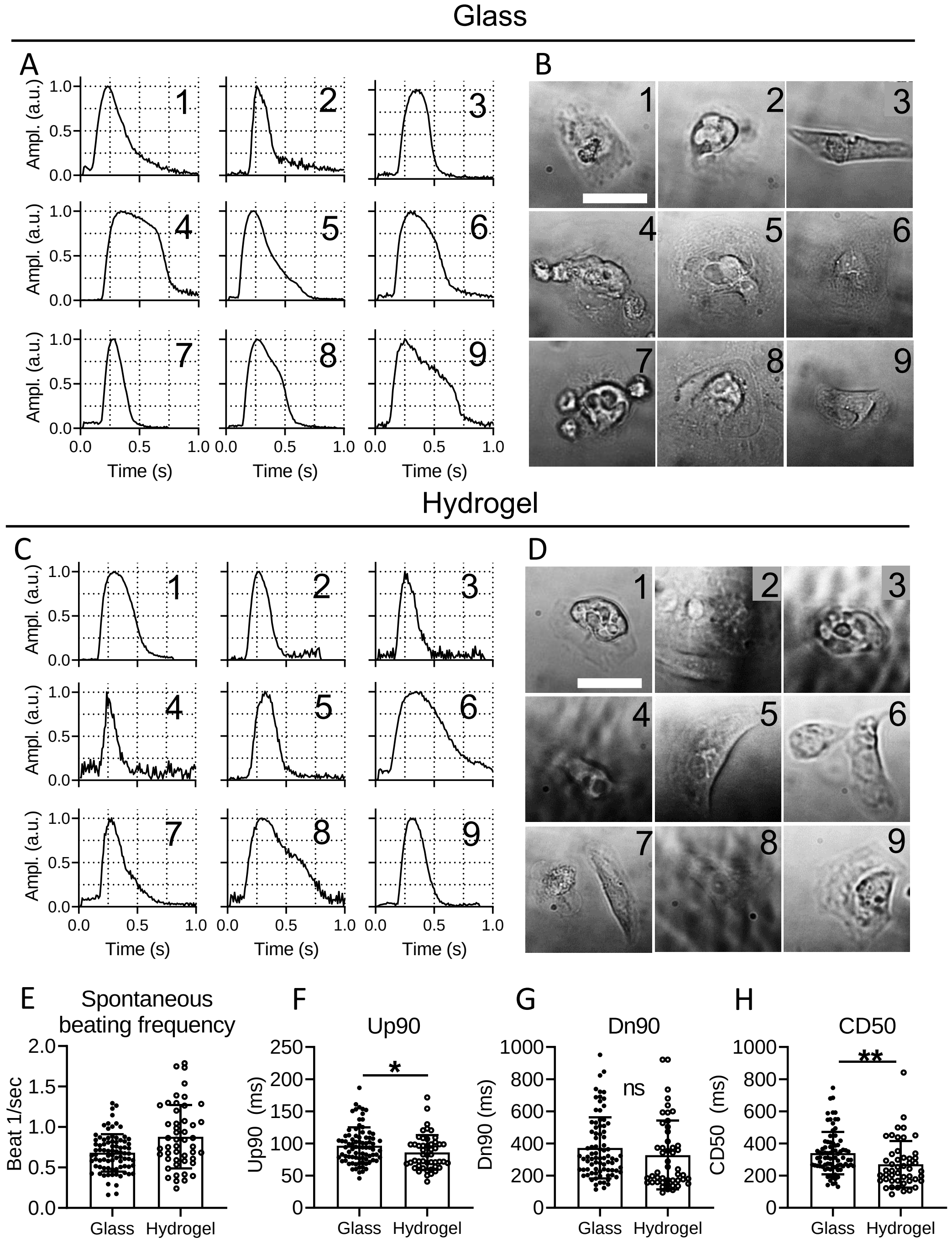

Figure 5.13 contractility analysis of single cells seeded on either glass or hydrogel (RCP-MA$_{100}$).

Transients (A, C) and corresponding brightfield images (B, D) of single cells seeded on glass surfaces (A, B) or RCP-MA$_{100}$ (C, D). E) Spontaneous beating frequency. F) Contraction time (UP$_{90}$). G) Relaxation time (Dn$_{90}$). H) Contraction duration (CD$_{50}$). *: p-value <0.05. **: p-value < 0.01. Scalebar indicates 50µm. N$_{Glass}$ = 82; n$_{Hydrogel}$ = 48; N$_{Experiments}$ = 3. Recordings were taken on either day 4 or 5 after cell seeding.

Moreover, single cells on both substrates had similar spontaneous beating frequencies and relaxation times (Dn_{90}) as shown in Figure 5.13E and G. However, the contraction time (Up_{90}) was significantly shorter in the hydrogel group (Up_{90} = RCP-MA_{100}: 86±27 ms, glass: 97±28 ms, p=0.04) (Figure 5.13F). Further, single cells seeded on a hydrogel had a significantly shorter CD_{50} compared to glass (CD_{50} = RCP-MA_{100}: 271±145 ms, glass: 340±131 ms, p<0.001)(Figure 5.13H), which was also observed in hiPSC-CM monolayers seeded on the hydrogel (Figure 5.10E). Thus, the substrate stiffness affects the contraction duration in both hiPSC-CMs monolayers and single cells.

5.3.8 Effect of inotropic intervention

To investigate whether a flexible substrate alters the effects of inotropic drugs, we incubated cells with the ß-agonist isoprenaline (ISO) (300 nM) and the contractile responses were compared to responses on a rigid substrate (glass).

As shown in Figure 5.14 the addition of isoprenaline caused a marked increase in spontaneous beating frequency in both hydrogel and glass substrates. In the steady state (5 min), the change in spontaneous frequency of contractions on hydrogel were significantly higher than that observed on glass (Δ Freq = 0.6±0.1 vs 0.8±0.1, P<0.0001). For spatial analysis, contractile parameters were measured while stimulating the cells at a fixed rate of 1 Hz, (10% higher than the maximum spontaneous rate observed in isoprenaline) to avoid the complicating influence of variable spontaneous rates on other contraction parameters.

Figure 5.14B shows the recordings of the 900 (30x30) contractile events of a typical patch seeded on glass before and after the addition of ISO. Traces were grouped into single or multiple-peaked events from which it is evident that a significant number of grid-squares contained multiple-peaked contractile events, the fraction of grid-squares with complex contractions was relatively unchanged by the addition of ISO. For the equivalent traces from the 2D-culture on a hydrogel, which is shown in Figure 5.14C, notably many fewer areas had complex contraction traces. The spatial distribution of the complex contractile events before and after ISO are shown in Figure 5.14D and E and indicate that the position and number of grid-squares with >1 peak was approximately the same before and after ISO for both substrates. Figure 5.14F summarizes the change in the percentage of grid squares with complex contractile events. No significant difference was observed on the addition of ISO and hydrogel cultures show essentially no change in the negligible number of grid-squares that demonstrate complex contractile events.

Figure 5.14G indicates that the contraction duration at a fixed stimulation rate (1 Hz) was decreased on addition of ISO in both and glass and hydrogel substrates. The extent of the decrease in contraction duration is significantly larger and more consistent on the hydrogel surface (ΔCD_{50} = hydrogel+ISO: -253±19 ms, glass+ISO: -199±53 ms, $p=0.04$). The change in the amplitude of the contractile event was also quantified in this set of measurements. As shown in Figure 5.14H, addition of ISO resulted in no significant changes in the amplitude of the contractile events for either glass or hydrogel.

In summary, the contractile time-course of 2D-cultures is unaffected by ß-adrenergic stimulation on both substrate types. ISO causes no net inotropic change in 2D cultures of hiPSC-CMs but dramatically shortened the time-course of contraction, an effect that was significantly greater in monolayers of iPSC-CMs on the flexible substrate compared to glass/plastic.

5.3.9 The relationship between substrate stiffness and stress-activated pathways

External mechanical stresses could enhance stress activated pathways, including upregulation of genes encoding the well-known hypertrophy markers NPPA and NPPB (17, 36, 43-45). Gene expression profiling of hiPSC-CMs seeded on either hydrogel or glass for NPPA and NPPB showed no statistically significant differences between each group, but both were significantly lower when compared to cells subjected to a hypertrophy assay using endothelin-1 (ET-1) (Figure 5.14I). This indicates that stiff culture substrates do not activate these mechanical stress responses within hiPSC-CMs. Moreover, the similar - lack of - stress response suggests that the multiphasic contractile behaviour is not caused by hypertrophy related mechanical stress.

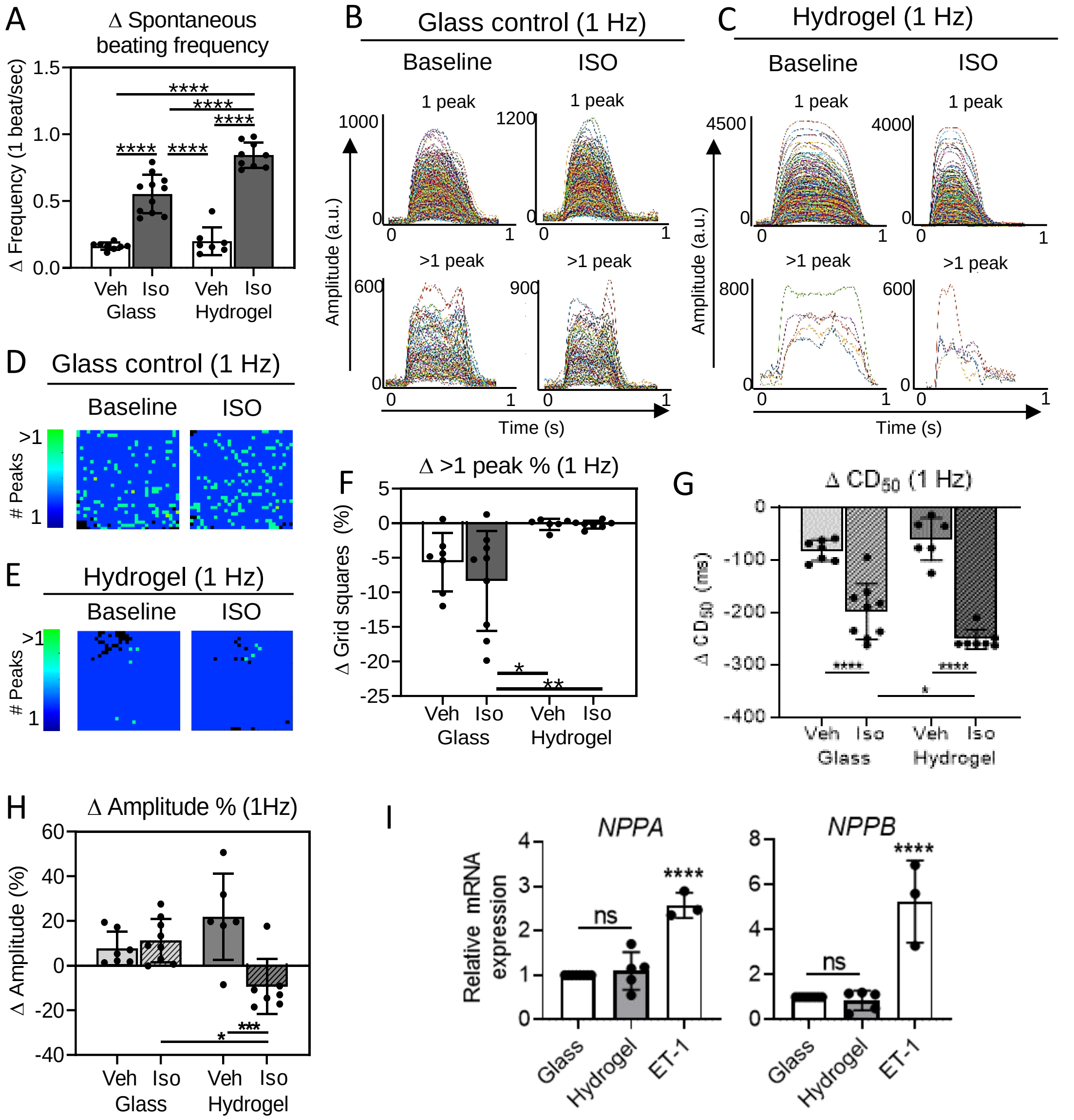

Figure 5.14 The effect of isoprenaline on the time-course complexity of hiPSC-CM seeded on different substrate stiffnesses.

HiPSC-CMs (ICell^2 (FCDI)) were seeded on either a glass substrate or a hydrogel (RCP-MA$_{100}$) and incubated with either isoprenaline (ISO, 300 nM) or vehicle (culture medium) for 5 min, where after contractility recordings were made. A) The spontaneous beating frequency of hiPSC-CMs. B) Contractility traces (900) from the spatial analysis of one representative glass control sample at baseline and after ISO incubation. Classification of the transients is based on the number of peaks (1 vs >1). C) Contractility traces (900) from the spatial analysis of one representative hydrogel sample at baseline and after ISO incubation. Classification of the transients is based on the number of peaks (1 vs >1). D and E) The distribution of grid-squares containing 1-peaked (dark blue) or multiple-peaked transients (light green) at baseline and after ISO incubation for the glass control (D) and hydrogel substrate (E). F) The change in the percentage of grid-squares containing multiple-peaked transients compared to the baseline. G) The change in average CD50 values as compared to the baseline. H) The change in amplitude as percentage of the baseline values. I) Relative gene expression for stress-activated genes NPPA and NPPB. Endothelin-1 (ET-1) treatment served as a positive control. $N_{\text{Experiments}} = 3$, $N_{\text{Samples}} = 5$ to 8 per group. Groups were compared with any other group using a one-way ANOVA with a Dunn's (A, F, G, H) or Tukey (I) post hoc test. A p-value < 0.05 was considered statistically significant and is indicated with *. * = p<0.05, ** = p<0.01, *** = p<0.001, **** = p<0.0001. All recordings were made on day 5 after stencil removal.

5.3.10 Computational model to investigate the biological findings

In collaboration with our colleagues from the mathematics department of the University of Glasgow, a mathematical model was developed to help interpret and explain the spatiotemporal features of contraction measured in the biological experiments. The model represents a one-dimensional chain of contractile units each one connected to its two neighbors with left and right ends anchored to a substrate by springs. Individual contractile units represent single hiPSC-CM cells and are described by the previously published sarcomere contraction model of Rice et al (Rice et al., 2008). For the coupling of the contractile units into a chain, the published model of Timmermann et al (Timmermann et al., 2019) is used.

The mathematical model and the results can be found in the appendix (Chapter 8.1).

5.4 Discussion and conclusion

In this chapter, an EHT was developed that fits the sub-aims presented in the introduction. In brief, the EHT is small (mm), and consists of a biomaterial and a small number of cells (<50,000 cells per EHT). The biomaterial is a recombinant collagen peptide (RCP-MA_{100}) that has a stiffness comparable to that of the native myocardium, namely ~22 kPa. Using silicone moulds, very thin hydrogels were created (~350 µm) and after some small alterations of the hydrogel synthesis, namely the addition of FN and a FN coating, hiPSC-CM could form strong adhesions to the biomaterial. The hiPSC-CMs seeded on the hydrogel showed a comparable electrophysiological and contractile behaviour as cells cultured in standard culture conditions. Moreover, their physiology was stable for over a week in culture, suggesting the hydrogel is a good biomaterial for hiPSC-CM culture and for future *in vivo* applications.

In addition, contractility was analysed in a spatiotemporal manner like in the previous chapter. Here, it was found that hiPSC-CMs cultured on soft substrates show minimal complex contractile behaviour compared to rigid surfaces. This will be discussed below.

5.4.1 Different hydrogel stiffnesses

A recombinant collagen-like peptide was assessed on its quality to function as a support material for hiPSC-CM implantation. Three RCP-MA materials with various material stiffnesses were tested, namely RCP-MA_{20}, RCP-MA_{50} and RCP-MA_{100}. From these three, RCP-MA_{100} was the most suitable as cell adhesion and functionality was similar to control, but only if the material was mixed and coated with FN. In contrast, cells seeded on RCP-MA_{50} did show cell adhesion, but no cell spreading, which was also observed by Pandey et al (Pandey et al., 2018). Because all other aspects of the gel, such as chemical sequency of RCP, the FN content and the crosslinking protocol, the lack of cell adhesion is most likely caused by the lower stiffness of RCP-MA_{50} vs RCP-MA_{100}. A recent paper from Ribeiro et al. showed that hiPSC-CMs cultured on 21 kPa acrylamide gels could generate an optimal contraction force compared to stiffer and softer gels (Ribeiro et al., 2020). However, other literature showed that a stiffness 10 kPa is optimal for intracellular protein structures and contraction efficiency of immature CMs, such as hiPSC-CMs (Engler et al., 2008, Ribeiro et al., 2015). These discrepancies might be due to phenotypical and/or genotypical differences between CM cell lines.

5.4.2 Contraction time-course changes on flexible substrates

This study showed that the contractile duration was shorter in hiPSC-CM monolayers seeded on the flexible substrate and was close to that measured from single isolated hiPSC-CMs (Figure 5.13H). This is in line with other studies that showed that contraction and relaxation velocity were impaired by matrix stiffening, including on glass, in isolated adult rat CMs (Van Deel et al., 2017). Interestingly, this was reversed when cells were transferred from stiff (100 kPa) to soft (15 kPa) substrates, indicating that the cellular adaptations to mechanical changes are not permanent. Additionally, Sewanan et al. found that hiPSC-CMs seeded on 3D decellularized ECM from stiffer hypertrophic myocardium resulted in longer relaxation time compared to ECM from healthy hearts (Sewanan et al., 2019).

Several studies have examined the contractile events of single cells cultured on flexible substrates and associated the change over time with changes in sarcomere alignment and other aspects of cell culture that reflected cell maturation (Ribeiro et al., 2020, Ribeiro et al., 2015, Jacot et al., 2008, Engler et al., 2008). None of these studies reported the complex phases of contraction as reported here and similarly, these phases were not present in recordings of single isolated hiPSC-CMs (Figure 5.13A-D). It is unlikely that maturation rather than mechanical factors provides an explanation for the more physiological time-course of monolayers seen on the flexible substrate in this study, because these changes can occur acutely (within 1 day) by simply detaching the monolayer from the underlying substrate as shown in the previous chapter (Chapter 4). Furthermore, there were no major changes in electrophysiology (APD) and contraction time-course (CaT_{50}) over time on flexible substrates, supporting the lack of an ongoing maturation process.

5.4.3 Responses of hiPSC-CMs to ISO on rigid and flexible substrates

In an initial effort to examine the consequences of the flexible substrate on the response of hiPSC-CMs on an inotropic intervention, the features of the contractile signal were examined before and after 300nM isoprenaline. As shown in Figure 5.13, the complexity of the contractile event across the monolayer was not altered by addition of isoprenaline despite the increase in spontaneous frequency. Stimulation at fixed rate allowed the comparison of the contractile time course before and after isoprenaline and demonstrated the absence of an inotropic effect but the presence of a clear lusotropic action of the drug. Also, the addition of ISO decreased the duration of contraction because of the increased rate of relaxation. Similar results of the addition of ISO have been observed in previous studies using hiPSC-CMs and hESC-CM in media with normal extracellular Ca^{2+} (Chen et al., 2015, Lewandowski et al., 2018, Pillekamp et al., 2012). The underlying mechanism is thought to be the summed effects of ß-adreno receptor mediated phosphorylation of L-type Ca^{2+} channel, contractile protein troponin-I and the SR uptake regulatory protein phospholamban. The combined result of these processes in iPSC-CMs is a limited inotropic action due to reduced contribution of the sarcoplasmic reticulum in the response due to immature status of the SR (Chen et al., 2015, Pillekamp et al., 2012, Liu et al., 2007). The response of the monolayer on flexible substrates was like that on rigid with increase in spontaneous frequency, neutral inotropic change and shorter contractile duration. Interestingly, the relative increase in both the spontaneous frequency and the decreased CD_{50} at fixed rate were greater on the flexible substrates than compared to the rigid substrate. The mechanism underlying these relatively larger chronotropic and lusotropic actions on a flexible substrate is unclear. One possible option is that the greater chronotropic and lusotropic actions are an outcome of the less complex events during the contractile phase on the flexible substrates, which allows more rapid mechanical events on the monolayer, but altered sensitivity to ISO or altered intracellular pathways may also contribute. Further work is required to fully understand the consequences of the inotropic action of drugs on the more physiological, flexible substrates.

5.4.4 Overall conclusion and future implications

Here, a small EHT was developed from RCP-MA_{100} that is approximately 350 μm thick and 6 mm in diameter and has <50k cells per construct. The area of hiPSC-CMs is 3 mm in diameter the surrounding rim can be used to easily handle the EHT during transplantation. Importantly, cell adhesion was optimized by functionalizing the RCP-MA_{100} hydrogel with FN and the hiPSC-CMs are viable for at least one week *in vitro*. In this form, the EHT will be tested in the intact rabbit heart during future experiments.

In addition to this, the overall effects of the mechanically flexible substrate on hiPSC-CMs were also studied. In summary the effects were: 1) the simpler and more physiological contractile events than that seen on a fixed substrate, 2) a shorter overall duration of contraction and 3) enhanced chronotropic and lusotropic effects on the addition of ISO. This work suggests that rigid substrates are inappropriate mechanical matrices for hiPSC-CMs culture. These findings are important for both basic research and cardiotoxicity studies that use hiPSC-CMs as a stable reliable model of human myocardium.

Chapter 6 EHT implantation: Optimization of implantation techniques

6.1 Introduction

One of the main challenges within the field of cardiac regeneration is the ability of implanted cells to integrate into the host myocardium by making direct cell-cell and cell-ECM connections with the myocardium. This is important for electrical activation of the graft by the host and thus synchronous contraction and is also known as mechano-electrical coupling (Menasché, 2018, Shiba, 2020). Absent or incomplete coupling could eventually lead to arrhythmias, including ventricular tachycardia (VT), and is thus essential for cardiac regeneration (Shiba et al., 2016, Shiba et al., 2012, Liu et al., 2018, Shiba et al., 2014). The mechano-electrical coupling can be explained in two different ways. Firstly, it can be seen as the physical coupling between two adjacent cells through physical molecular binding of two connexins for electrical coupling or two N-Cadherin for mechanical coupling, as discussed in the introduction (Paragraphs 1.2.3-1.2.5). Secondly, mechano-electrical coupling can also be seen as the effect that the electrical field and the mechanical contraction of the myocardium have on the implanted graft.

To improve hiPSC-CM integration, it is important to understand the factors that promote cell survival and electro-mechanical coupling. Factors that affect mechano-electrical coupling could be, but are not limited to, the implantation method (Gerbin et al., 2015), the graft size (Chong et al., 2014), the presence of mechano-electrical stimuli from the surrounding myocardium (Scuderi and Butcher, 2017) and/or paracrine factors from implanted cells (Zhu et al., 2018, Tachibana et al., 2017). Studies have shown that intramyocardially implanted grafts do mechano-electrically couple with the host in contrast to ectopically implanted grafts (Gerbin et al., 2015). Additionally, *in vivo* studies showed that the mechano-electrical stimuli of the myocardium enhance maturation of injected cells, showing enhanced maturation markers and reduced automaticity (Chong et al., 2014). Interestingly, hESC-CMs at the border of the graft area show higher maturation levels compared to cells within the core of the graft (Chong et al., 2014), which could be explained by either the cells being in direct contact with the host or hypoxia and/or cell death in the core of the graft ((Jabbour et al., 2021)). However, the reason is unknow but could be investigated using this platform.

Discrepancies in resting heart rate between human and small animals such as rat and guineapig might complicate mechano-electrical coupling. It has been repeatedly shown that human CMs, including hiPSC-CMs can pace up to 3 Hz (Shiba et al., 2012, Masumoto et al., 2016), which is the resting beating rate of rabbits (Wang et al., 2019), meaning that the rabbit myocardium could be a suitable platform for implantation studies of human cells.

An intermediate *ex vivo* stage for assessing the various factors that could influence hiPSC-CM integration (positively and negatively) would be useful to save time and resources. The Langendorff perfusion system is a natural choice to test the implantation and integration of cardiac constructs *ex vivo* for a three of reasons. Firstly, hearts mounted on the Langendorff perfusion rig are viable for multiple hours, and thus provides enough time to perform experiments. Secondly, our lab is experienced with intact rabbit heart models and the Langendorff set-up. Finally, an optical set-up can be placed next to the Langendorff perfusion rig, so that the activity of the implanted EHT can be monitored closely. Importantly, *ex vivo* assessment of cardiac constructs before proceeding to *in vivo* studies contributes to the three R's for laboratory animal welfare, by refining the experimental procedures and therefore ultimately reducing the number of animals used.

Tracking the activity and physiology of the implanted cells is key to investigate acute integration, for example using fluorescent dyes. Ideally, both EHT and the myocardium of the implantation site are monitored simultaneously using two voltage sensitive dyes with distinct Ex/Em spectra. However, the currently available voltage sensitive dyes have low dynamic ranges or remain within cells for short periods of time, compromising the magnitude of a recorded signal and the length of the experiment. Two novel small molecule calcium indicators Cal520-AM and Cal590-AM have a relatively high dynamic range, fast kinetics and long-lasting retention within cells and are therefore useful for *ex vivo* studies (Tada et al., 2014, Kopljar et al., 2018, Tischbirek et al., 2017). Moreover, the Ex/Em spectrum of Cal590-AM does not overlap with the Ex/Em spectrum of FV, enabling simultaneous imaging of the EHTs and myocardium.

6.1.1 Aims and sub-aims

In this chapter, a new platform will be developed to assess the acute integration of small EHTs into the myocardium. The main aim will be broken down into the following sub-aims:

1. Which fluorescent calcium indicator, Cal520-AM or Cal590-AM, has the best background to noise ratio, and is thus most suitable to use during implantation studies

2. Do the EHTs based on human iPSC-CMs follow the relatively high beating rates of the rabbit heart *in vitro*?

3. What is the best implantation method to maintain a viable and stable implant?

4. Once implanted into the rabbit heart, do the physiology of the EHTs change acutely?

6.2 Chapter specific materials and methods

6.2.1 Loading the intact rabbit heart with FluoVolt

The Langendorff perfusion system was prepared as described in the methods section (paragraph 2.4). After blebbistatin incubation, the light guide was placed onto the LV and a background recording was made. The light guide was not repositioned during the experiment.

A solution of 1.5 ml Tyrode’s, 0.5 ml 20% pluronic acid (0.1% final concentration) and 25 µl FV (1:4000 final concentration) was prepared, thoroughly mixed and added to a beaker with 100 ml Tyrode’s + blebbistatin. Then, the perfusion rate was slowly decreased from 40 ml/min to 26 ml/min, where after the solutions were changed from the 5L Tyrode’s solution + blebbistatin to the 100 ml FV mixture. FV was incubated for 20 min by recirculating the dye. Here, the effluent of the heart was collected and filtered manually using a 0.2µm filter and a syringe. Filtered effluent was placed back into the 100 ml beaker. After 20 min incubation period, the solutions were changed back to Tyrode's with blebbistatin for the rest of the experiment.

FV incubation was monitored by making 5 sec recordings using the 470nm LED and PMT2 at T=0, 5, 10, 15 and 20 min following the start of the incubation period. FV recordings were made every 30 min until the end of the experiment.

6.2.2 EHT culture

HiPSC-CM were purchased from FujiFILM Cellular Dynamics International (ICell^2, FCDI) and were seeded on 100% RCP-MA hydrogels with a 4X cell density and using 3 mm stencils (~45,000 cells/hydrogel). On day 2, stencils were removed and hiPSC-CMs were cultured for another 2-5 days in maintenance medium (FCDI). Five EHTs were prepared for each intact rabbit heart experiment to assure at least one successful implantation.

6.2.3 Intramyocardial implantation of EHTs

One day before EHT implantation, the EHT maintenance medium was replaced for BMCC medium, so EHTs could adapt to the serum free medium. On the day of implantation, EHTs were incubated with 2 µM Cal520-AM and 0.02% pluronic acid for 30 min at 37°C. Then, EHTs were washed 1x with BMCC medium and left in the incubator until further use, which was between 1 and 3 hours.

Meanwhile, the Langendorff perfusion system was prepared as described where after, the heart was placed onto the rig, assessed on its functionality (systemic pressure and ECG), and incubated with blebbistatin for 20 min. At this point the heart was ready to proceed with the implantation protocol. Prior to implantation, however, both the EHT spontaneous beating activity and Cal-520-AM loading were confirmed prior to implantation. Here, the latter was confirmed *in vitro* using the light guide system associated with the Langendorff set-up. This was used to check the fluorescence signal from the construct prior to implantation. This also allowed the comparison of the Cal520 fluorescence before and after implantation.

Once spontaneous beating activity and Cal520-AM loading was confirmed, the experiment proceeded by making an incision into the rabbit LV using a straight

15° ophthalmic knife. Using tweezers and a small scoop, the EHT was then implanted into the incision and the myocardium was repositioned over the EHTs. Then, the light guide was placed on top of the incision site, with the electrodes located on either side of the EH. Finally, the first calcium traces could be recorded using the 470 nm LED and a PMT. If no signal was recorded, the LV and EHT were electrically paced using 10V electrical impulses of 2 ms duration. If the myocardium was stimulated, but there was still no calcium signal, the light guide was repositioned. This was repeated until a clear calcium transient could be recorded. LED and PMT settings were maintained during the whole experiment and calcium transients were recorded for as long as possible, but no longer than 2.5 hours. Transients were analysed using LabChart v8 software (ADInstruments).

6.3 Results

6.3.1 Choosing the most suitable calcium indicator: Cal520-AM vs Cal590-AM

When recording fluorescence from cultured hiPSC-CMs on the CellOPTIQ system, high NA objectives (NA = 0.6) are used to optimise light collection and therefore signal strength. In contrast, the light guide has a low NA of 0.2 and is therefore less efficient in collecting light, this feature contributes to an increased signal-to-noise ratio using this optical system. In addition to this, implantation of EHTs underneath the epicardium, the intervening myocardium will scatter light and thus reduce the excited light reaching the construct and the collection of emitted light. This ultimately leads to a reduction in collected light, a decreased signal strength and an increased signal noise (Figure 6.1). Thus, it is important to choose the calcium indicator with a high dynamic range and brightest fluorescence signal to monitor the calcium signal during the EHT implantation experiments.

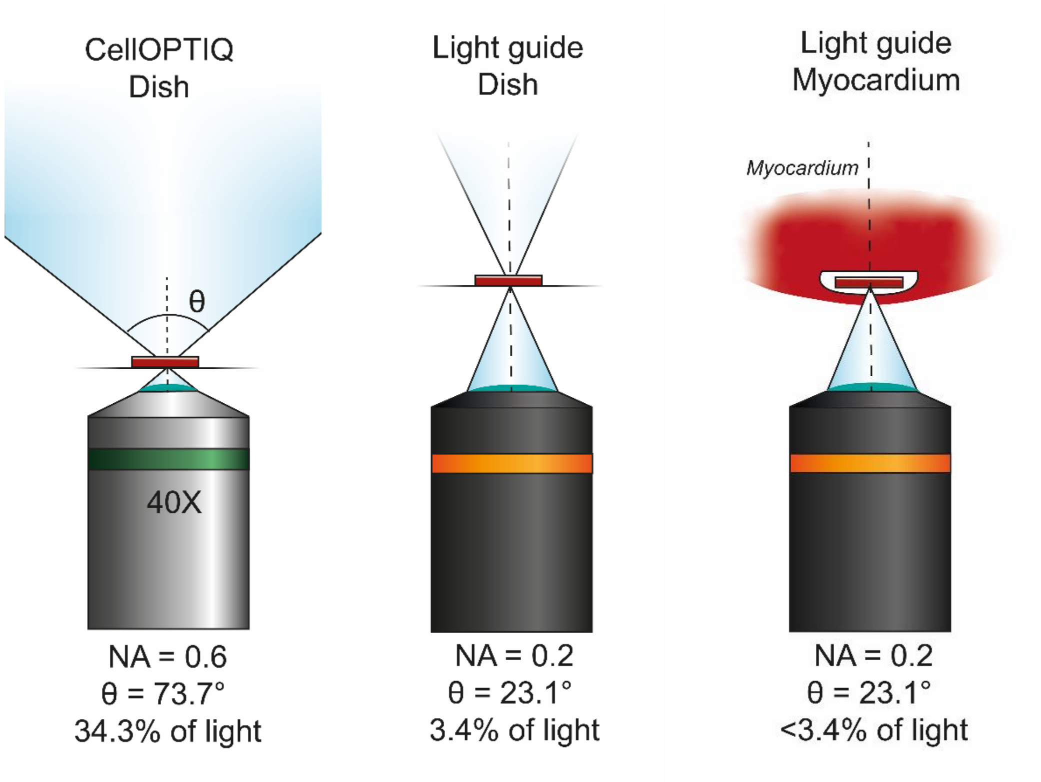

Figure 6.1 Differences in optics between a 40X objective and the light guide.
Lower NA leads to the collection of fewer light and therefore a reduction in the signal recorded. % of light can be collected through the following formulas: % of light collected = -1/2 (cos (ϴ-2)-1) where ϴ = (sin^{-1}(na)) / 2.

6.3.1.1 *In vitro* assessment of the Cal520-AM and Cal590-AM calcium indicators.

Cal520-AM and Cal590-AM are both potential calcium dyes with distinct Ex/Em spectra. Cal520-AM has a similar Ex/Em spectrum as FV (Ex/Em: Cal520-AM = 490/525 nm; FV = 522/535 nm) and therefore the correct optical filter sets are readily present in our lab. New filter sets were purchased for Cal590-AM (Ex/Em = 574/588 nm) with in mind the potential dual loading with FV to allow for simultaneous voltage and calcium recordings. Using FV to load the heart and Cal590-AM to load the EHT, the physiology of both the EHT and the myocardium surrounding the implantation site can be monitored.

To compared both calcium indicators, the difference in fluorescent intensity was measured *in vitro* on the CellOPTIQ system and using the light guide as part of the whole heart experiment set-up. In Figure 6.2 the amplitude of the fluorescent signal of both Cal520 and Cal590 is shown. This data shows a reduction in calcium transient amplitude when moving from the CellOPTIQ system to the light guide on the Langendorff set-up. Additionally, it becomes apparent that Cal520 is approximately 10x brighter compared to Cal590, using a 5x lower LED intensity. The Cal590 intensity will decrease even further after implantation and therefore, Cal590-AM is not useful to use as calcium indicator for our experiments. In contrast, Cal520-AM is bright enough and there is a possibility to increase the light intensity. Therefore, Cal520-AM is the calcium indicator of choice.

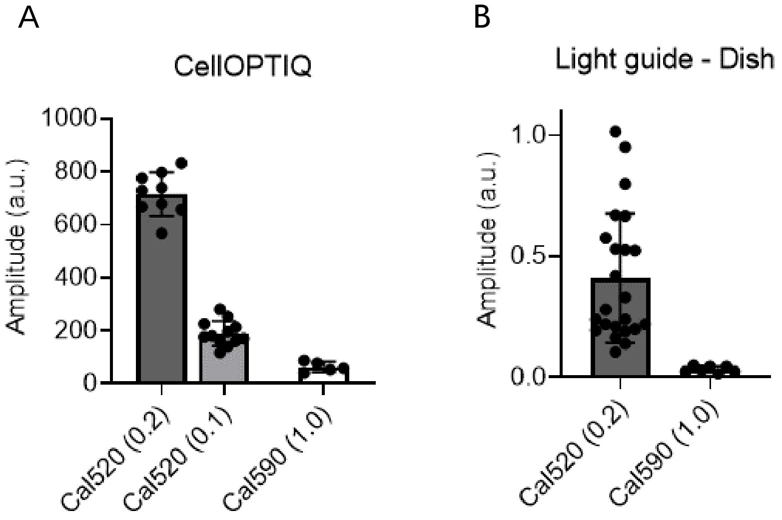

Figure 6.2 Cal520 *vs* Cal590 *in vitro*.
The difference between Cal520 and Cal590 calcium indicators when measured *in vitro* using the CellOPTIQ system (NA=0.6) (A) and using the light guide (NA=0.2) (B). Number behind every dye-indication represents the LED setting. Values of the CellOPTIQ and whole heart set-up cannot be compared 1:1.

6.3.1.2 Brightness of Cal520-AM *in vitro* vs *ex vivo* system

Further evaluation of Cal520-AM showed that the calcium transient intensity further decreased after implantation into the myocardium (Figure 6.3A), whereas the dynamic range (F/F_0) stayed relatively similar (Figure 6.3B) suggesting that the amplitude of the Ca^{2+} transient remained the same.

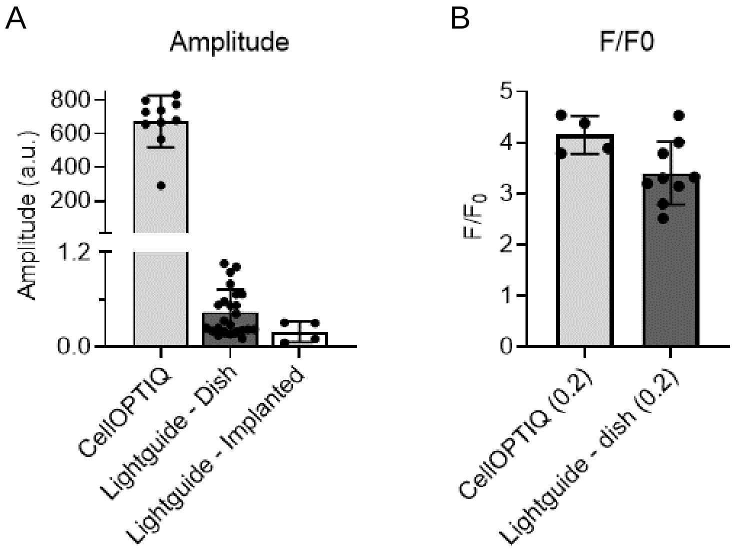

Figure 6.3 Measurement of Cal520 fluorescence on the CellOPTIQ system vs the whole heart set-up.
A) The amplitude of the Cal520 signal. A further comparison is made between the EHT pre and post implantation. B) Dynamic range. For all recordings, an LED setting of 0.2 was used.

6.3.2 Relation between calcium transient and APD_{90} in hiPSC-CMs *in vitro*

Even though Cal590-AM is most likely not suitable for the *ex vivo* experiments, it can be used to simultaneously measure voltage and calcium signals *in vitro* in order to establish the relationship between the APD_{90} and the calcium transient duration within EHTs. Knowing this relationship will help the interpretation of the recorded calcium transients *ex vivo* and the (in)ability of hiPSC-CMs to adapt acutely to the rabbit myocardium. Additionally, EHTs will be electrically paced at various pacing frequencies, ranging from 1 Hz to 3.3 Hz, to investigate the extent to which the EHTs can follow stimulus rates that approximate to the rabbit heart rate.

6.3.2.1 HiPSC-CMs paced at high frequencies (3 Hz) show alternans

The response of the hiPSC-CMs to the stimulus can be categorized into three categories: 1) hiPSC-CMs respond to every electrical stimulus, 2) hiPSC-CMs do not respond to every electrical stimulus, including skipping every other stimulus and alternating amplitude of the calcium transient, or 3) hiPSC-CM do respond to every electrical stimulus but show alternans of APD and calcium transient amplitude, indicating a borderline ability to response.

From calcium transients and APs recorded Figure 6.4 displays the percentage of EHTs that show alternans in their APs (Figure 6.4B) and/or calcium transients (Figure 6.4C). From this figure we can see that the APs follow the electrical pacing flawlessly up to and including 2.9Hz. But using 3.3Hz the majority (80%) of the EHTs follows, whereas only 10% of the EHTs shows alternans and another 10% skips every other stimulus (Figure 6.4B). In contrast, from 2.5Hz alternans can be observed in the calcium signal and evidently, this results in a higher percentage of EHTs that show alternans (approx. 30%) or do not follow the pacing stimuli (approximately 50%) at 3.3Hz (Figure 6.4C).

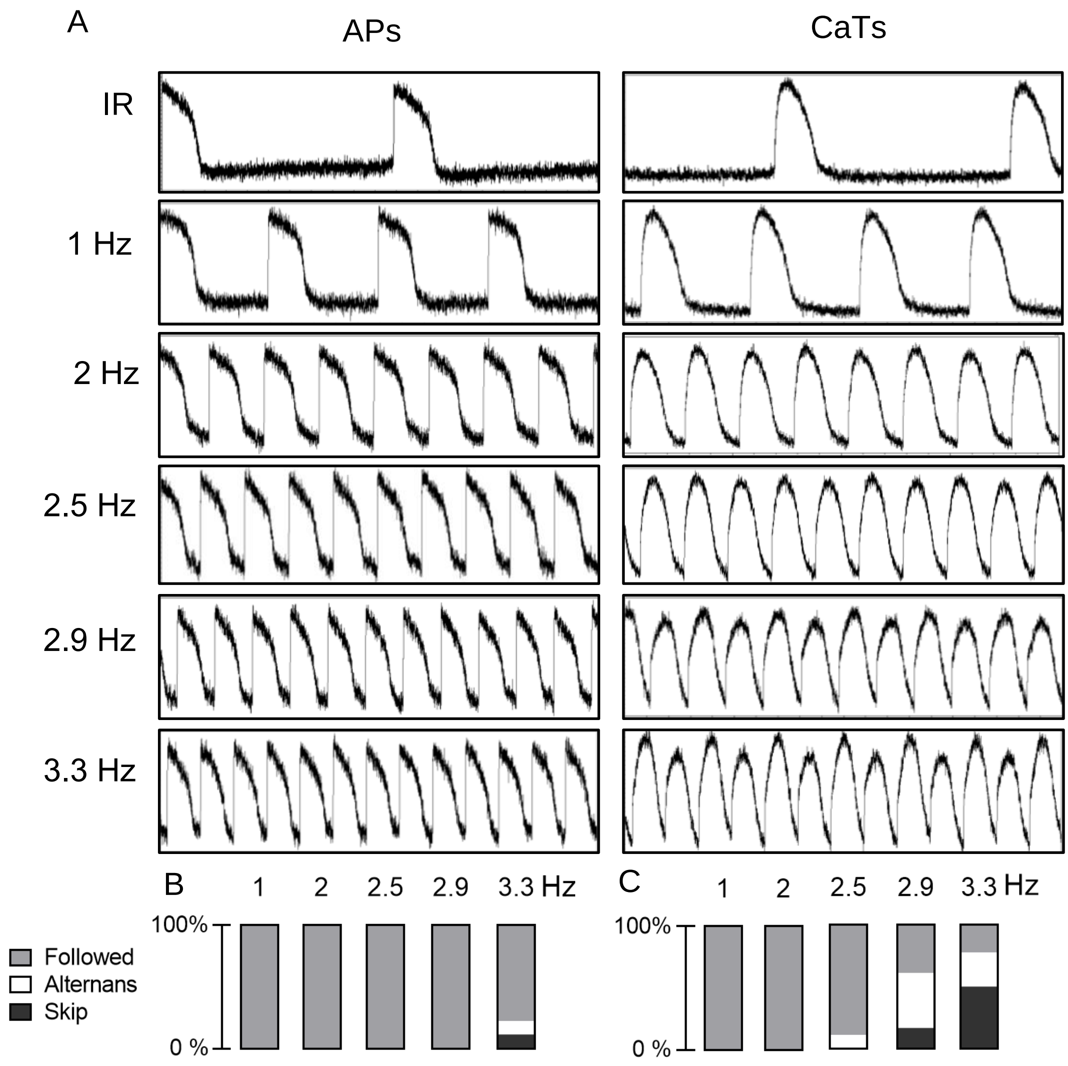

Figure 6.4 The ability of hiPSC-CMs to follow high pacing frequencies.
A) Example traces of APs (left) and CaTs (right) where APs do not show alternans, and CaTs do from approx. when paced at a fixed rate of 2.9 Hz. Recordings lasted for 4 seconds. B) APs and C) calcium transients were classified into 3 groups. HiPSC-CMs catching the pacing frequency without difficulties were classified as 'following'. HiPSC-CMs catching the pacing frequency but showed alternans were classified as 'alternans'. HiPSC-CMs that did not catch the pacing frequency and showed either extreme alternans or were skipping every other stimulus were classified as 'skip'. For voltage transients: N= 9 data points from 2 experiments. For calcium transients: N=18 data points from 6 experiments.

6.3.2.2 CaT vs APD_{90} of hiPSC-CMs, paced at various pacing frequencies

Following the excitation-contraction-coupling mechanisms, the calcium transient width follows the AP, but their relative time-course may vary at increasing cycle lengths. To explore this, EHTs were paced at different frequencies and the APs and calcium transients were measured simultaneously using FV and Cal590-AM, respectively. The results from those measurements are shown in Figure 6.5 and Table 6.1. At a beating frequency of 2 Hz the APD_{90} is on average similar to theCaT_{90}, but this changes slowly for faster pacing frequencies in a way that at 2.5 Hz, 2.9 Hz and 3.3 Hz the APD_{90} overlaps with CaT_{80}, CaT_{70} and CaT_{60}, respectively (Figure 6.5A-B). So, the calcium transient's width that corresponding with the APD_{90} decrease as pacing frequencies increase. This indicates that the EHTs calcium handling is too slow to complete a full cycle before the next electrical impulse. This explains the increased probability of calcium alternans during electrical stimulation at 2.5 Hz and higher that was shown in Figure 6.4.

All average APD_{90} values and corresponding CaTs (CaT_{50} – CaT_{90}) are shown in Table 6.1. From these values, a relationship between APD_{90} and CaT_x can be calculated as a APD_{90}/ CaT_x ratio (Table 6.2 and Figure 6.5B).

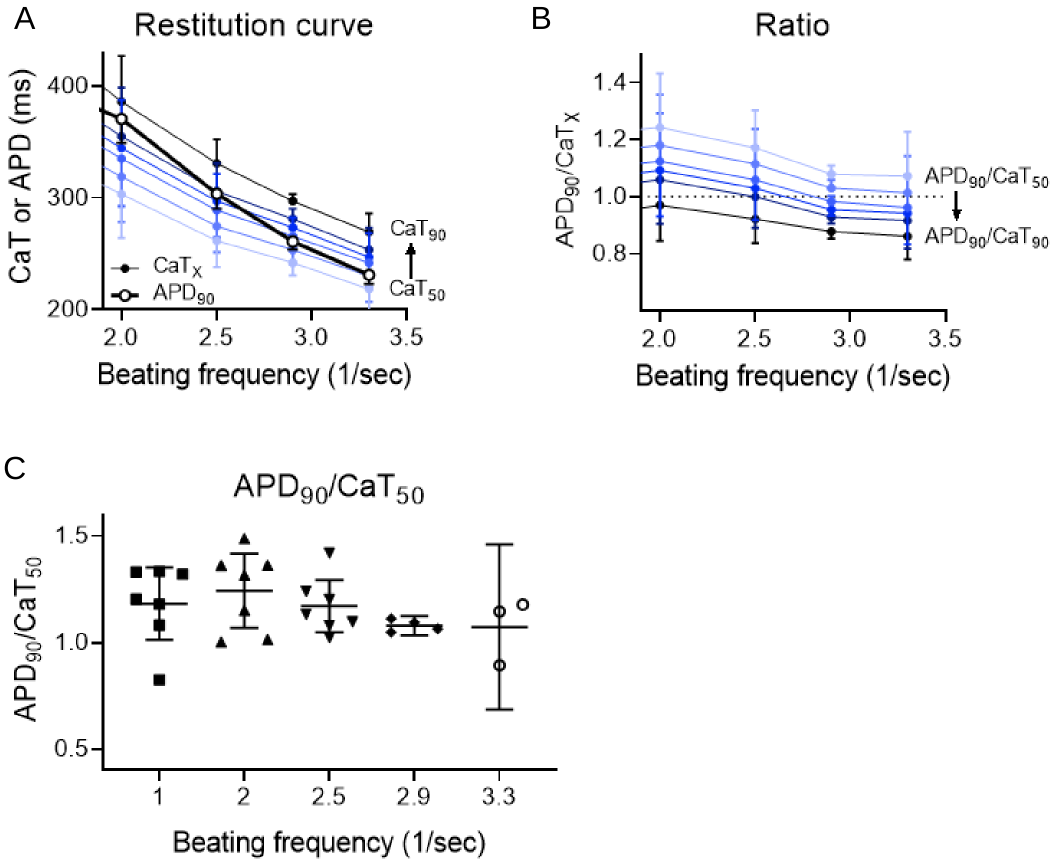

Figure 6.5 The relation between hiPSC-CM APs and calcium transients *in vitro*.
A) The average CaT_{50} to CaT_{90} (CaT_{50} - CaT_{90}; black dots, thin line) and APD_{90} (white dots, thick line) values plotted against the corresponding beating frequency. B) The ratio of APD_{90}/CaT_X. C) the APD_{90}/CaT_{50} ratios for every beating frequency with their respective 95% confidence intervals. All data is obtained from ICell^2 hiPSC-CMs cultured on hydrogel substrates. N experiments = 2. N data points = 3-7.

The CaT_{50} of the calcium transient is most of interest to calculate the APD_{90} as this is the point where the calcium decay is at maximum speed and will therefore have the least variability as an index of the duration of the calcium transient. Because relationship between APD_{90}/CaT_{50} and the cycle length is not linear, conversion of the CaT_{50} into APD_{90} values will be done with a formula for each cycle length. A lookup table with the final formulas to convert the CaT_{50} to the APD_{90} can be found in Table 6.3. These formulas will be used during the *ex vivo* implantation studies to convert the EHT calcium transient CaT_{50} into APD_{90} values.

Table 6.1 Average values of APs and corresponding calcium transients in hiPSC-CMs paced at different pacing frequencies.
Averages ± SD are shown for APD$_{90}$, CaT$_{50}$ to CaT$_{90}$. EHTs were paced at 1 Hz, 2 Hz, 2.5 Hz, 2.9 Hz and 3.3 Hz (cycle lengths of 1000 ms, 500 ms, 400 ms, 350 ms and 300 ms, respectively)

Pacing frequency (Hz)		1	2	2.5	2.9	3.3
Cycle length (ms)		1000	500	400	350	300
APD$_{90}$	Av.	443.18	370.61	303.57	260.80	230.92
	±SD	±57.74	±21.50	±13.63	±6.97	±8.18
CaT$_{50}$	Av.	397.88	310.09	265.52	247.91	218.06
	±SD	±97.55	±39.37	±23.44	±11.51	±26.63
CaT$_{60}$	Av.	410.74	319.00	274.49	253.37	229.78
	±SD	±104.73	±40.67	±23.28	±12.58	±22.80
CaT$_{70}$	Av.	435.74	335.00	288.82	265.50	241.74
	±SD	±112.63	±42.56	±24.39	±10.10	±21.67
CaT$_{75}$	Av.	450.22	344.46	297.01	273.28	246.92
	±SD	±117.44	±43.31	±24.44	±9.07	±21.24
CaT$_{80}$	Av.	467.42	355.01	305.83	280.93	253.43
	±SD	±122.41	±43.65	±25.02	±9.12	±19.73
CaT$_{90}$	Av.	477.02	358.30	308.41	283.56	253.43
	±SD	±132.72	±47.84	±28.41	±13.38	±19.73

Table 6.2 APD$_{90}$/CaT$_{x}$ ratio's for hiPSC-CMs.
Averages ± SD are shown for the ratios calculated as APD$_{90}$/CaT$_{x}$ where CaT$_{x}$ represents the CaT$_{50}$ to CaT$_{90}$. EHTs were paced at 1 Hz, 2 Hz, 2.5 Hz, 2.9 Hz and 3.3 Hz (cycle lengths of 1000 ms, 500 ms, 400 ms, 350 ms and 300 ms, respectively).

Pacing frequency (Hz)	1		2		2.5		2.9		3.3	
Cycle length (ms)	1000		500		400		350		300	
	Av.	±SD	Av.	±SD	Av.	±SD	Av.	±SD	Av.	±SD
APD$_{90}$/CaT$_{50}$	1.18	±0.18	1.24	±0.19	1.17	±0.13	1.08	±0.03	1.07	±0.16
APD$_{90}$/CaT$_{60}$	1.10	±0.17	1.15	±0.18	1.09	±0.12	1.02	±0.03	1.01	±0.13
APD$_{90}$/CaT$_{70}$	1.05	±0.16	1.12	±0.17	1.06	±0.12	0.98	±0.02	0.96	±0.11
APD$_{90}$/CaT$_{75}$	1.02	±0.16	1.09	±0.16	1.03	±0.11	0.95	±0.02	0.94	±0.11
APD$_{90}$/CaT$_{80}$	0.98	±0.15	1.06	±0.15	1.00	±0.11	0.93	±0.02	0.92	±0.10
APD$_{90}$/CaT$_{90}$	0.87	±0.13	0.97	±0.12	0.92	±0.08	0.88	±0.02	0.86	±0.08

Table 6.3 Lookup table for formulas to calculate the APD_{90} from the CaT_{50} for various pacing frequencies or cycle lengths.
Additionally, the ratio constant, the standard deviation and the confidence interval are plotted too.

Pacing frequency (Hz)	Cycle length (ms)	APD_{90}/CaT_{50} constant	±SD	Confidence Interval (ms)	Formula
1	1000	1.18	0.18	1.01 – 1.35	$APD_{90} = CaT_{50} * 1.18$
2	500	1.24	0.19	1.07 – 1.42	$APD_{90} = CaT_{50} * 1.24$
2.5	400	1.17	0.13	1.05 – 1.29	$APD_{90} = CaT_{50} * 1.17$
2.9	350	1.08	0.03	1.03 – 1.13	$APD_{90} = CaT_{50} * 1.08$
3.3	300	1.07	0.16	0.68 – 1.46	$APD_{90} = CaT_{50} * 1.07$

6.3.3 Staining the intact rabbit heart with the fluorescent voltage sensitive dye FluoVolt

6.3.3.1 FluoVolt incubation

During the Langendorff perfusion experiments, the electrophysiology of the heart is monitored using an ECG, however, this information represents the electrical conductance through the whole heart. It would be more interesting, and perhaps more informative, to (additionally) monitor the electrical signals from myocardium surrounding the implanted EHT. As explained in paragraph 6.3.1.1, simultaneous recordings with FV and Cal590-AM are not possible because of the poor SNR from the Cal590 signal from the grafted EHT. Nonetheless, FV can be loaded into the rabbit myocardium to investigate the relation between the $Time_{R-T}$ and the local APD.

From Figure 6.6, the gradual loading of the dye into the myocardium is shown. From these graphs a clear increase in fluorescent intensity in time can be observed. After 5 minutes of loading, no transient is visible, however, after 10 min of loading a small AP can be observed. After 20 min incubation, evident APs can be recorded from the rabbit myocardium, with a dynamic range (F/F_0) of ~1.10 and an amplitude of 0.05 (Figure 6.6B and C). This is in line with the literature, stating that FV has a relatively high background fluorescent and low dynamic range (Salerno et al., 2020, Scientific).

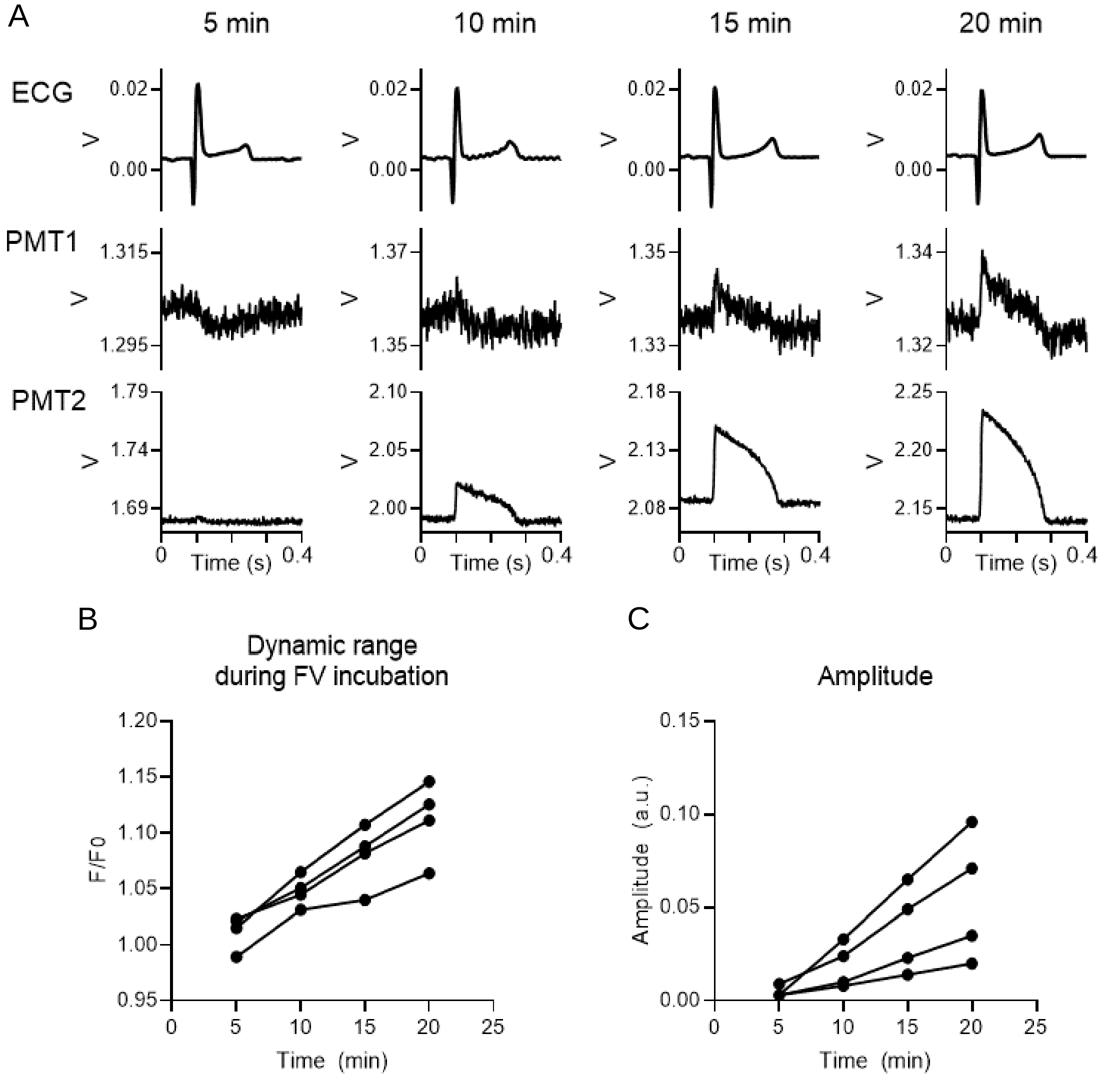

Figure 6.6 FV incubation. FV was incubated for 20 min using a recirculation method.
A) Traces showing the FV signal in time during recirculation. Traces were recorded at 1-2 min, 5 min, 10 min, 15 min and 20 min. FV traces are brightest in PMT2 but are also picked up by PMT1. B) The dynamic range (F/F_0) and C) the amplitude of the FV traces during the incubation (N = 4).

6.3.3.2 The effect of the incision and implantation procedure on the AP shape and FluoVolt signal.

The incision for EHT implantation damages the heart, but it is unknown to what extend and what the effects are for the electrophysiological signals underneath. Impaired or altered electrical signals might affect the EHT integration into the heart. It is therefore important to know if and how the electrical signals are affected by the incision and whether they recover.

Figure 6.7 shows AP recordings from myocardium post-incision indicating a reduction in both the amplitude and dynamic range of the FV signal compared to the pre-incision signal. Interestingly, both the AP amplitude and dynamic range recover in time (Figure 6.7, white spheres), but the exact duration of the recovery varies between incision, location and hearts. In some cases, however, the fluorescent levels do not recover to control levels (data not shown). Similar changes in AP amplitude were seen when performing a sham implantation.

Beside the AP amplitude, the AP shape also changed after making the incision (Figure 6.8). The usual AP time-course has a steep upstroke and slow repolarisation phase (Figure 6.8A). However, post-incision, this changes into a 2-phased upstroke and a quicker decay (Figure 6.8B). This most likely represents the combination of delayed conductance from the isolated myocardial bridge and the normal conductance from the underlying myocardium. It is important to note that the APD is not prolonged, suggesting that the initiation of the depolarization and completion of the repolarization of the cardiomyocytes within the myocardial bridge and underlying tissue is simultaneous.

These data indicate that the incision and implantation procedure temporarily affect the synchrony of the local electrical signal, as represented by AP amplitude and shape, this acute effect recovers within an hour post-incision/implantation.

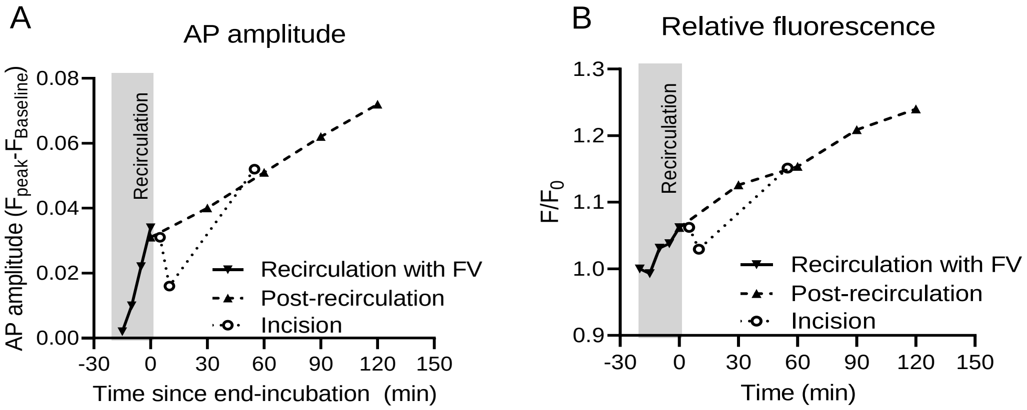

Figure 6.7 The effect of the incision and implantation procedure on the AP shape and fluorescence.

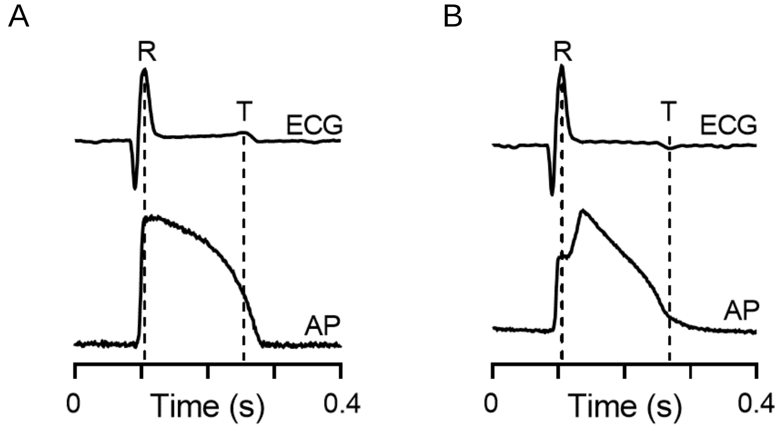

Figure 6.8 Example APs from the myocardium, before (A) and after an incision (B), along the corresponding ECG.

6.3.4 Electrophysiology of the intact rabbit heart: ECG vs APs

ECG recordings are technically accumulated extracellular signals as a result of transmembrane AP signals derived from the whole rabbit heart. ECGs could therefore serve as an indicator to determine local AP durations when the AP signals cannot be recorded, e.g. when Cal520 is used to measure EHT calcium traces thereby preventing FV to be used to record APs due to spectral overlap. The time between the peaks of the R- and T-waves of an ECG ($\text{Time}_{\text{R-T}}$) represents the time from when most left ventricular cardiomyocytes are depolarized and most cells repolarized, respectively and therefore may reflect local ventricular APD values.

6.3.4.1 The relationship between the local APD and global ECG

To find the relation between APD_{90} and $\text{Time}_{\text{R-T}}$, rabbit hearts were loaded with FV and paced at different pacing frequencies (2.5 Hz, 2.9 Hz and 3.3 Hz), where after both the ECG and APs were recorded simultaneously. Example traces of the ECGs and corresponding APs at different pacing frequencies are shown in Figure 6.9.

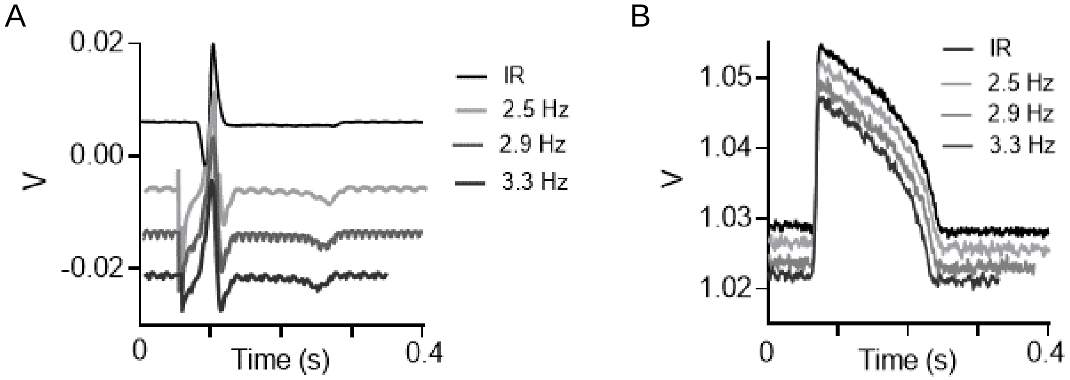

Figure 6.9 Example APs from the rabbit left ventricle.
Representable traces from ECGs (A) and APs (B) at different pacing frequencies. IR = intrinsic rate.

First, the $\text{Time}_{\text{R-T}}$ and APDs of simultaneous recordings were measured to investigate the direct relationship between the ECG and APs, respectively. Average values ±SD are shown in Figure 6.10A-D and Table 6.4. These data show that the $\text{Time}_{\text{R-T}}$, as well as the APD_{50}, APD_{75} and APD_{90}, decrease with increasing pacing frequencies. Additionally, these data show that the APD most similar to the $\text{Time}_{\text{R-T}}$ is not constant, but changes with the pacing frequency. For example, for the intrinsic rate (IR) and a pacing frequency of 2.5 Hz, the $\text{Time}_{\text{R-T}}$ corresponds with the APD_{75}, whereas for the pacing frequencies of 2.9 Hz and 3.3 Hz the $\text{Time}_{\text{R-T}}$ corresponds with the APD_{80} and APD_{90}, respectively (Table 6.4). The data from Figure 6.10 and Table 6.4 is compiled to form a restitution curve (Figure 6.11A) and shows clearly that the $\text{Time}_{\text{R-T}}$ and corresponding APD varies, depending on the cycle length. Additionally, this graph reveals the linearity of the relationship between the cycle length, APD and $\text{Time}_{\text{R-T}}$ (Figure 6.11A). This dynamic relationship becomes clearer when calculating the ratio between $\text{Time}_{\text{R-T}}$ and APD (APD/ $\text{Time}_{\text{R-T}}$) as shown in Figure 6.11B and Table 6.5.

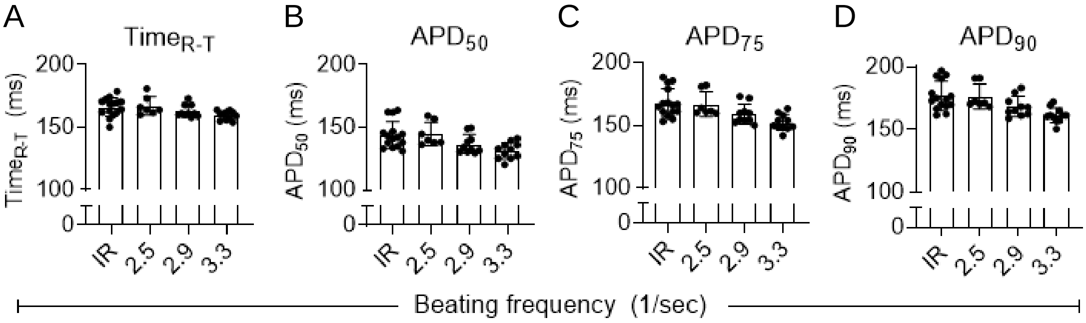

Figure 6.10 Average TimeR-T and APDs at various pacing frequencies.
A) Time$_{R-T}$. B) APD$_{50}$. C) APD$_{75}$. D) APD$_{90}$. Before pacing, recordings were made at the intrinsic rate (IR). Then, hearts were electrically paced at 2.5 Hz, 2.9 Hz and 3.3 Hz.

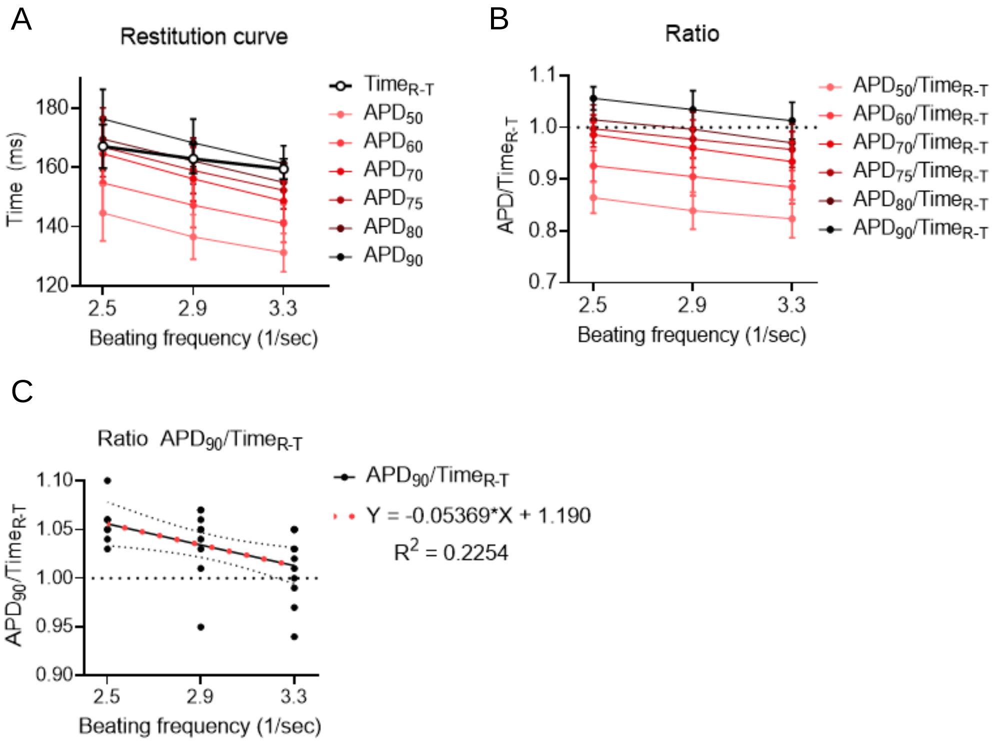

Figure 6.11 The relationship between Time$_{R-T}$ and APD$_{90}$ of the rabbit myocardium.
A) Restitution curve where the APD and Time$_{R-T}$ are plotted against the beating frequency. B) The ratio between APD and Time$_{R-T}$ plotted against the beating frequency. APDs range from APD$_{50}$ to APD$_{90}$ as indicated by the colour gradient. C) APD$_{90}$/Time$_{R-T}$ from figure (B) plotted against the linear regression curve (pink dotted line) and the 95% confidence interval. The linear regression results in a formula describing their relationship. White circles (A) and dotted line (B and C) indicate the Time$_{R-T}$. N = 3 experiments and n = 7-15 data points per experimental group.

Table 6.4 Average values of TimeR-T and APD50 to APD90 at different pacing frequencies (in ms).
N = 3 experiments and n = 7-15 data points per experimental group.

	IR (ms)		2.5 Hz (ms)		2.9 Hz (ms)		3.3 Hz (ms)	
	Average	±SD	Average	±SD	Average	±SD	Average	SD
$\text{Time}_{R\text{-}T}$	166.12	±7.36	167.11	±7.38	162.92	±4.94	159.49	±3.43
APD_{50}	143.99	±10.73	144.66	±9.45	136.59	±7.55	131.32	±6.47
APD_{60}	155.61	±11.19	154.81	±10.36	147.25	±7.54	141.17	±6.35
APD_{70}	164.73	±11.48	164.65	±9.83	156.18	±7.50	148.66	±6.80
APD_{75}	167.91	±11.25	166.90	±10.04	159.02	±7.85	152.29	±6.32
APD_{80}	171.13	±11.00	169.58	±10.57	162.21	±7.70	154.96	±6.52
APD_{90}	176.75	±11.59	176.41	±10.00	168.32	±8.03	161.36	±5.93

Table 6.5 The ratio between APD and $\text{Time}_{R\text{-}T}$ for every pacing frequency and IR.
Ratios were based on data presented in Table 6.4 and calculated by dividing the APD by their respective $\text{Time}_{R\text{-}T}$. N = 3 experiments and n = 7-15 data points per experimental group.

	IR		2.5 Hz		2.9 Hz		3.3 Hz		Average	
	Av.	±SD	Av.	±SD	Av.	±SD	Av.	±SD	Av.	±SD
$APD_{50}/\text{Time}_{R\text{-}T}$	0.87	±0.06	0.87	±0.03	0.84	±0.04	0.82	±0.04	0.85	±0.02
$APD_{60}/\text{Time}_{R\text{-}T}$	0.94	±0.06	0.93	±0.03	0.90	±0.04	0.89	±0.03	0.91	±0.02
$APD_{70}/\text{Time}_{R\text{-}T}$	0.99	±0.06	0.98	±0.03	0.96	±0.04	0.93	±0.04	0.97	±0.03
$APD_{75}/\text{Time}_{R\text{-}T}$	1.01	±0.06	1.00	±0.03	0.98	±0.04	0.95	±0.04	0.99	±0.02
$APD_{80}/\text{Time}_{R\text{-}T}$	1.03	±0.06	1.01	±0.03	1.00	±0.03	0.97	±0.04	1.00	±0.03
$APD_{90}/\text{Time}_{R\text{-}T}$	1.06	±0.06	1.06	±0.02	1.03	±0.04	1.01	±0.04	1.04	±0.02

6.3.4.2 Creating a formula to determine the local APD of the rabbit myocardium from ECG recordings

Using the APD/$\text{Time}_{R\text{-}T}$ ratio’s, a formula was developed to determine the APD from ECG recordings during future studies. Here, the APD_{90} value was chosen as parameter in the formula because 1) this represents the completion of the repolarisation phase and is therefore most representative of the $\text{Time}_{R\text{-}T}$ and 2) it is the least variable parameter during *in vitro* studies, which is important when converting the EHT’s calcium time-course duration to a corresponding APD_{90} value. Furthermore, the $APD_{90}/\text{Time}_{R\text{-}T}$ ratio simulates a linear relationship with the cycle length for 2.5, 2.9 and 3.3 Hz, so for these pacing frequencies, one formula would be sufficient to calculate the APD_{90} while taking the pacing frequency into account (Figure 6.11C).

The slope and y-intercept are 0.0005 and 0.86, respectively, which gives the following formula:

Equation 1

$$\frac{APD90}{TimeRT} = -0.0537 * Freq + 1.190$$

Rearrangement of the variables results in the following final formula that will be used to calculate the APD_{90} based on the pacing frequency and $Time_{R\text{-}T}$:

Equation 2

$$APD90 = (-0.05369 * Freq + 1.190) * TimeRT$$

6.3.5 The gradual optimization of the EHT implantation procedure

6.3.5.1 Intramyocardial implantation methods

Intramyocardial implantation can be achieved by making a superficial incision underneath the epicardium. The exact methodology, however, was optimized gradually over many experiments, and increased the success rate of the implantation drastically as shown in Figure 6.12. For example, the implantation during 5/6 final experiments were successful on the first attempt, meaning that a calcium transient could be recorded at first instance. All challenges and solutions that added to the improvement of the experimental protocol are shown in Table 6.6. These lead to an EHT implantation protocol where calcium traces could be recorded for up to 2 hours.

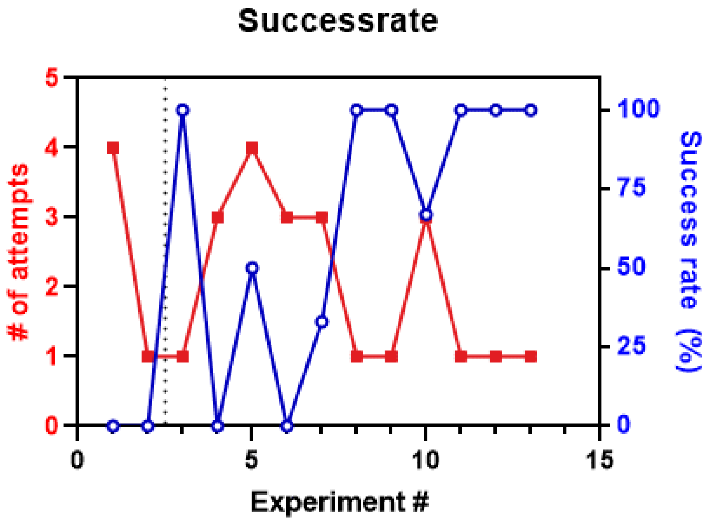

Figure 6.12 Success rate of the intramyocardial implantation technique.
Success rate (blue) is calculated as the number of successful transplantations divided by the total attempted intramyocardial implantations (red). An implantation is considered successful when a Cal520 signal can be recorded. Dotted line indicates the change from the pocket incision method to the myocardial bridge method.

Table 6.6 Implantation criteria for evaluating implantation success.
For each criterion, one or more possible challenges are listed, along with potential solutions that were implemented to address the corresponding challenge.

Subject	Challenge	Solution
Implantation method – Pocket vs myocardial bridge	A myocardial pocket fills with cardiac effluent causing the EHT to float out of the pocket	A myocardial bridge-flap is made to allow effluent drainage. The flap is also elastic and allows for better control of EHT implantation
Difficulties during implantation	A small incision equals less damage, but complicates EHT implantation, resulting in loss of constructs	Make the incision slightly bigger to assure EHT implantation
Quiescence	Cells can become quiescent during the implantation	Pace the cells to be able to record traces from the cells
Pacing stimulation	A higher voltage is needed to pace the cells than to pace the heart	Use the maximum of 10V to pace both the heart and the cells
Constant recorded signal	Cells are small area, so when moving the light guide the signal either changes or is lost	Do not reposition the light guide once a good signal can be recorded
Number of implantations per rabbit ventricle	To reduce the numbers of animals used for the experiments, multiple EHTs could be implanted. However, moving the light guide changes the calcium transient quality	Do not reposition the light-guide once a good signal can be recorded. Therefore, only one successful implantation and recording can be done per heart
Bleaching of fluorescent signal	Long term excitation of fluorophore causes fluorescent bleaching	Make short (30 sec) recordings with long intervals (20 min)
Chemical effects of Tyrode's solution	The change from BMCC culture medium to Tyrode's solution might negatively affect the hiPSC-CMs	5 mM HEPES was added to the Tyrode's buffer to guarantee a pH of 7.4
Chemical effects of cardiac effluent	Cardiac effluent might negatively affect the hiPSC-CMs	The effect of the effluent on hiPSC-CM performance was tested *in vitro* and cardiac effluent did not affect the cells negatively
AP after incision	Incision might damage the myocardium that no electrical conductance is maintained in the area	Use voltage sensitive dyes to investigate the alterations to the electrical signals from the incision site
Closing the incision	The EHT might come loose after implantation, so stitches or glue might help prevent this	Glue or stitches did not work. The new myocardial bridge served as an elastic band to maintain the position of the EHT once implanted

6.3.5.2 The final experimental design

The final implantation method is shown in Figure 6.13 and includes staining the EHT with Cal520-AM (2 µM for 30 min), implanting the construct using the myocardial bridge incision and using electrodes on either side of the light guide lens to field stimulate the EHT along with the myocardium. Moreover, it is important to avoid repositioning the light guide once a calcium signal is recorded, as this could lead to changing the calcium signal during the experiment or even losing the signal, resulting in premature termination of the experiment.

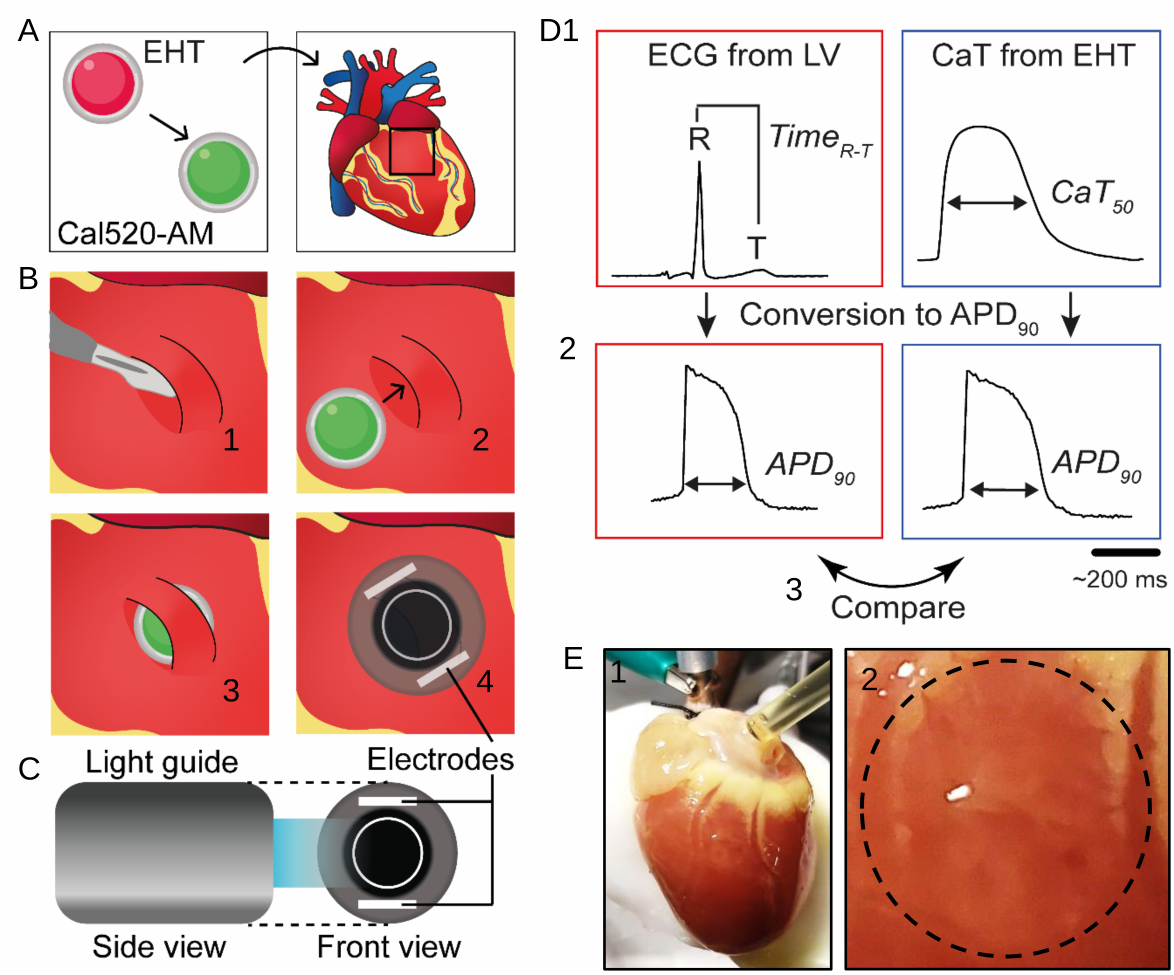

Figure 6.13 Overview of the final EHT implantation protocol.
A) EHTs are stained with Cal520-AM for 30 min prior to implantation. B) a myocardial bridge incision is made (1) and the EHT is implanted in a way that the myocardial bridge covers the hiPSC-CMs (2-3). Then the light guide is placed over the incision and EHT with the electrodes placed on either side of the myocardial bridge (4). C) Side view and front view of the head of the light guide. D) Example image of the rabbit heart with an implanted EHT. E) zoom to get a clearer view of the implantation site. White dotted lines mark the incision and black dotted circle indicates the EHT.

6.3.6 Implanting Cal520 loaded EHTs into the myocardium

6.3.6.1 Successfully implantation of EHTs into the myocardium

Using the EHT implantation protocol described in Figure 6.13, the physiology of implanted EHTs was assessed over time. Example calcium transients from implanted EHTs are shown in Figure 6.14 and are plotted along the corresponding ECG and stimulus traces. The EHTs from this specific experiment were recorded for approximately one hour and were able to follow up to a 3.3 Hz pacing frequency for the duration of the experiment.

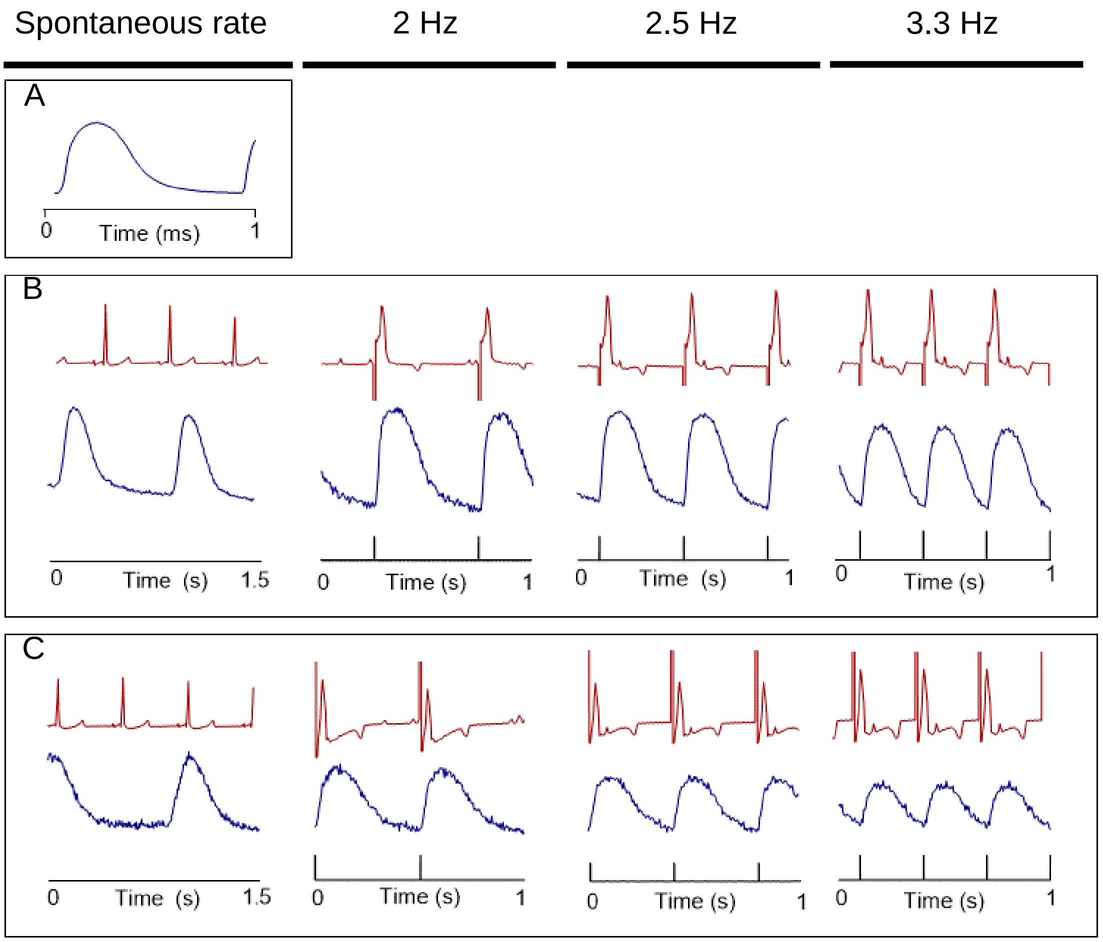

Figure 6.14 Example calcium traces of implanted EHTs.
Traces were recorded before (A), directly after (B) and approximately 1 hour after implantation (C). The traces shown are the calcium traces recorded from the EHT (blue), the ECG recorded from the rabbit myocardium (red) and the electrical pacing stimulus (black). All recordings are made with the light guide. During recordings, EHTs and heart were paced at different pacing frequencies (2, 2.5 and 3.3 Hz) along with the spontaneous rate.

No mechano-electrical coupling of the EHT with the myocardium was observed during any of the experiments. However, the spontaneous rate of implanted EHTs doubled on average after 2 hours from 0.5 Hz to 1 Hz, as shown in Figure 6.15A and B. Consequently, EHTs were less able to follow pacing at 1000ms intervals at later time points (100-150 min from implantation), but had an enhanced ability to follow 2 and 2.5 Hz pacing frequencies (Figure 6.15C). In contrast, their ability to follow 2.9 and 3.3 Hz pacing frequencies was decreased by a third to half, compared to timepoints within the first 50 min after implantation. The rabbit hearts were able to follow pacing frequencies above 2.9 Hz effortlessly, but had difficulty following lower rates (Figure 6.15C).

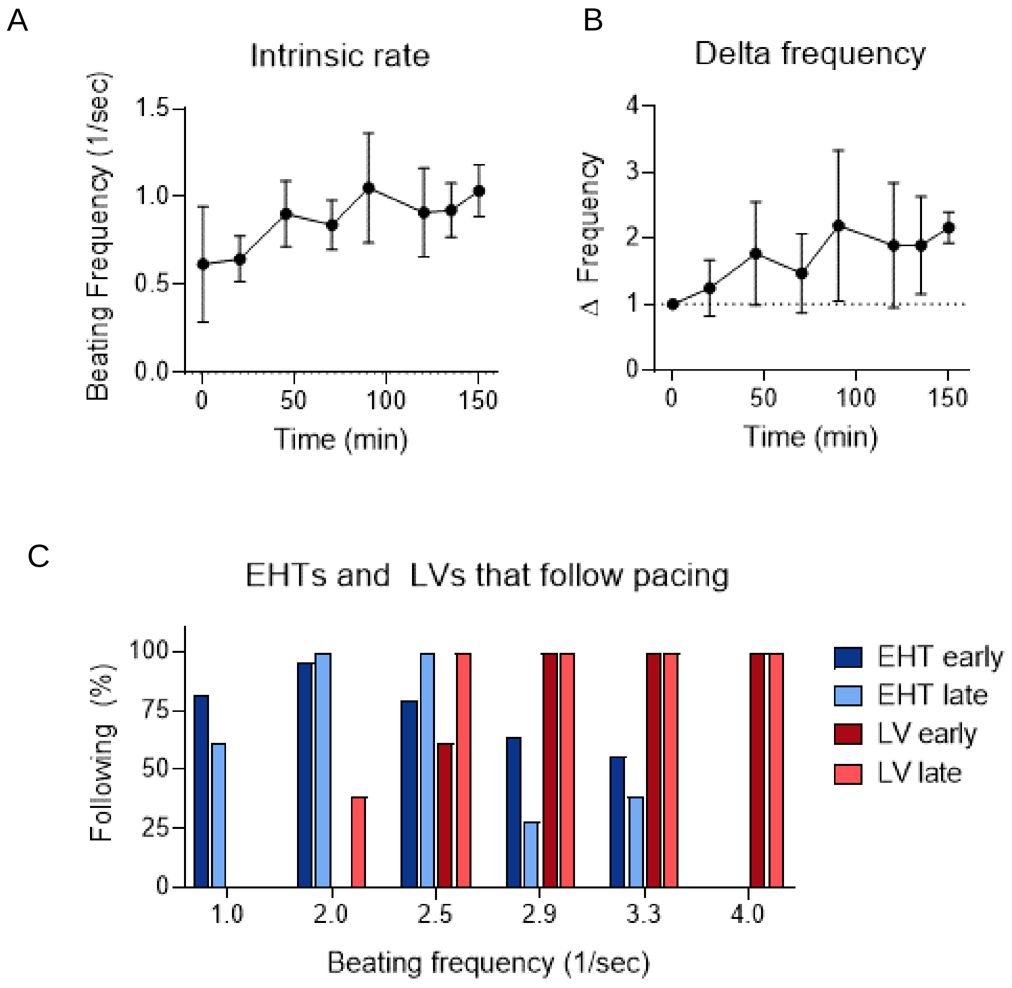

Figure 6.15 EHTs performance.
A) The spontaneous beating frequency of implanted EHTs. B) the delta beating frequency, compared to the first recording of spontaneous beating frequency. C) Here, early (0-50 min) and late (100-150 min) timepoints were combined to observe the difference between just implanted EHTs versus EHTs that were implanted for roughly 2 hours. N=5 EHTs. N per timepoint: early: 5; late: 3 for both EHT and LV.

6.3.6.2 The acute integration of EHTs into the rabbit myocardium

In Figure 6.16A, the averaged $\text{Time}_{\text{R-T}}$ were plotted, and no obvious changes were seen during the course of the experiment. This was confirmed by graphing the delta $\text{Time}_{\text{R-T}}$ as shown in Figure 6.16B. As seen before, the $\text{Time}_{\text{R-T}}$ was shorter when the myocardium was paced at higher frequencies (Figure 6.16A) Then, the individual values were converted to APD_{90} using the formula described in paragraph 6.3.4.1. and averaged values are plotted in Figure 6.16C. The APD_{90} values were approximately 170ms, 160ms and 145ms for LV paced at 2.5 Hz, 2.9 Hz and 3.3 Hz, respectively.

Then, calcium transients were recorded from the implanted EHTs and the CaT_{50} was measured. All average CaT_{50} values are shown in Figure 6.16D and indicate a small initial increase in CaT_{50}, followed by a decrease after approximately an hour of implantation, where after the values seem to stabilize. The ΔCaT_{50} values indeed show a small decrease of 5-10%, but this is not significant (Figure 6.16E). The CaT_{50} values were also converted to their respective APD_{90} values using the formula presented in paragraph 6.3.2.2., which are shown in Figure 6.16F. Here, the APD_{90} values decreased from approximately 330 ms to 190 ms at pacing frequencies of 1 Hz and 3.3 Hz, respectively.

All converted APD_{90} values of both the rabbit LV and the EHTs, paced at 2.5 Hz, 2.9 Hz and 3.3 Hz, are shown in Figure 6.16G. Interestingly, the APD_{90} of the EHTs and rabbit LV seem to converge soon after implantation, but stabilise after an hour.

When plotting the beating frequency against the diastolic interval (DI = cycle length – APD_{90}) at early (0-50 min) and late (100-150 min) time points it becomes clearer that the DI of the EHTs increases in time, while the DI for the LV remains roughly the same (Figure 6.16H and I). Consequently, the DI values of both EHT and LV converge. For example, at a 2.9 Hz pacing frequency, the difference between the diastolic interval of the LV and EHT is 72 ms within the first 50 min, but decreases to 43 ms during the final 50 min; a reduction of ~40% (Figure 6.16H and I). Although this is a large change, the DI of the EHT does not overlap with the DI of the LV, indicating a physiological limit to this adaptation.

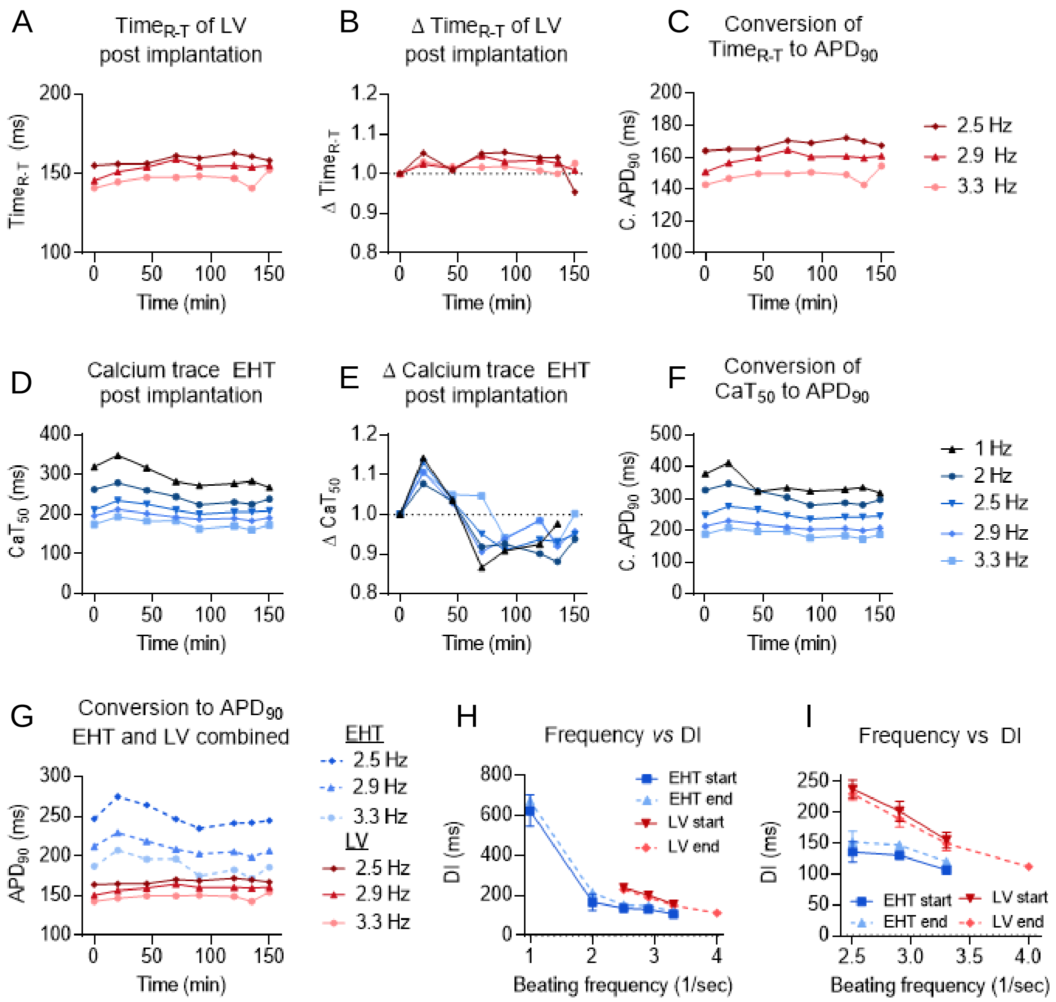

Figure 6.16 The change in Time$_{R-T}$ and CaT$_{50}$ during the course of the experiment, measured from the rabbit ECG and EHT, respectively.
A) average Time$_{R-T}$. B) ΔTime$_{R-T}$ relative to the first recording. C) the conversion of Time$_{R-T}$ to APD$_{90}$ using the formula as described in paragraph 6.3.4.1. D) The average CaT$_{50}$. E) ΔCaT$_{50}$ relative to the first recording. F) the conversion of CaT$_{50}$ to APD$_{90}$ using the formulas as described in 6.3.2.2. G) APD$_{90}$ from both EHTs and ECGs (myocardium). H) The diastolic interval plotted for every cycle length. I) The same data as graph H, but focussed on the beating frequencies of 2.5-4 Hz. N = 5 EHTs. N per time point: 0 min: 5; 20 min: 5; 45 min: 4; 70 min: 4; 90 min: 3; 120 min: 3; 135 min: 3; 150 min:2.

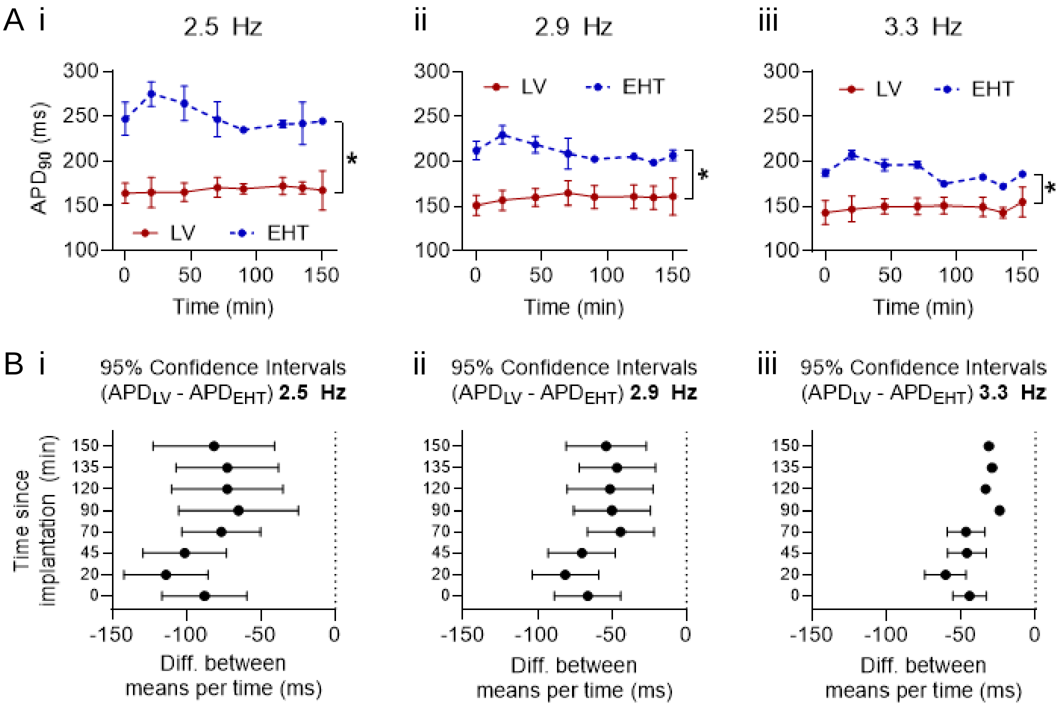

Figure 6.17 APD$_{90}$ values of EHT and LV do converge but do not overlap.
A) Converted CaT$_{50}$ and (blue, dotted) Time$_{R-T}$ (red, solid) to APD$_{90}$ values at i) 2.5 Hz, ii) 2.9 Hz, and iii) 3.3 Hz electrical stimulation. Values are shown as mean ± SD. B) 95% confidence intervals for the various timepoints post-implantation, calculated as the difference between cell means per row (LV-EHT). N = 5 EHTs. N per time point: 0 min: 5; 20 min: 5; 45 min: 4; 70 min: 4; 90 min: 3; 120 min: 3; 135 min: 3; 150 min:2.

6.4 Conclusion and discussion

In this chapter, a method was developed to implant small EHTs into the myocardium of the rabbit heart and monitor their activity for the first hours after implantation. The EHTs were stable and viable after implantation and when using Cal520-AM, calcium traces could be recorded for over two hours. To determine whether the EHT can alter its physiological characteristics towards that of the intact rabbit heart, the separate ECG from the myocardium and the calcium traces from the EHT were recorded from the intact rabbit heart and EHT, respectively. Conversion of the Time$_{RT}$ and CaT$_{50}$ to their separate APD$_{90}$ values suggests that the physiology of the EHT does change minimally whilst implanted, but does not match the physiological values of that of a rabbit heart.

6.4.1 Dual imaging of Cal590-AM and FV only achieved *in vitro*, not *in vivo*

As an alternative to dual imaging with two voltage sensitive dyes, the calcium dye Cal-590-AM and FV were initially used to stain the EHT and myocardium, respectively. Previous measurements showed that hiPSC-CMs in culture and studied on CellOPTIQ showed that this combination of dyes successfully monitored voltage and Ca^{2+} simultaneously. However, the use of both dyes during studies with the intact rabbit heart did not gain results. Multiple reasons could be the underlying cause for the differences in outcome:

Firstly, FV emits a small fraction of fluorophores at a broad spectrum, so finding a suitable filter set to selectively filter the correct signals is challenging. Multiple filter sets were tested, and clear separated Cal590 signals were recorded using a long pass filter, including the very red-shifted tail of the Cal590 signal and thus excluding a large part of the emitted light. This is no problem during *in vitro* studies, however, the signal was too small for *ex vivo* studies because of the light-scattering myocardium.

Secondly, the lightguide has a low NA compared to the 40x objective on the CellOPTIQ system and it consequently collects less light and thus results in a relatively small, recorded signal.

Thirdly, the total mass of the myocardium of the heart is many times larger than the small number of implanted cells and thus the fluorescent signal of the FV loaded myocardium and its background signal are larger than the small Cal590-AM signal. Therefore, it is possible to use FV and Cal590-AM simultaneously for *in vitro* studies, but not for intact rabbit heart experiments using this optical setup.

One approach to overcome these problems is to use an alternative imaging system. A 2-photon (2P) microscope could be used to record FV and calcium transients separately with a high SNR ratio. 2P-microscopy uses 2 photons of a near infrared wavelength to excite a fluorophore. FV has been used in 2P-microscopy before and showed a reduced toxicity compared to di-4-ANEPPS

(Salerno et al., 2020). Additionally, Cal590 could be used to record calcium transients from the EHTs (Tischbirek et al., 2017).

Alternatively, the brighter calcium dye Cal520 could be used for EHT signals in combination with the long wavelength voltage-sensitive dye PhoS to stain the rabbit heart (previously known as BeRST) (Photoswitch Biosciences) (Ex/Em: 652/680 nm) (Huang et al., 2015).

6.4.2 The use of Time$_{R-T}$ as a placeholder for APD values.

As dual fluorescent imaging with Cal590-AM and FV was not feasible, it was decided to use Cal520-AM instead of Cal590-AM. As Cal520-AM has the same Ex/Em spectrum as FV, APs could not be recorded simultaneously along with the CaTs anymore. Therefore, the APs that were recorded using FV were compared to their respective ECG, so that an estimated APD$_{90}$ could be calculated from the Time$_{R-T}$. The formula to convert Time$_{R-T}$ into APD$_{90}$ also takes the pacing frequency into account.

By converting the CaT$_{50}$ values from the EHT to APD$_{90}$, the two sets of substitute APD$_{90}$ values from both the EHT and myocardium could be compared. Although these APD$_{90}$ values are not measured directly from the EHT and the implantation site, they give a good representation of the local electrical activity. These measurements were used to estimate whether the EHT activity adapts to the activity of the myocardium and the mismatch of the electrophysiological signal between the two sites at different pacing rates.

6.4.3 The change in AP shape and amplitude post-incision

It is important that the myocardium surrounding the implantation site is still electrically active to assure myocardial function as this indicates a healthy perfused tissue surrounding the EHT. Additionally, electrical activity of the myocardium could influence hiPSC-CM maturation and integration into the myocardium (Chong et al., 2014). During the Langendorff rabbit heart experiments, APs were recorded from the implantation site, confirming the electrical activity after making an incision. However, AP shape and amplitude were different compared to pre-incision APs. Here, the AP time-course showed an additional step during the upstroke that indicates a conduction delay that is most likely a consequence of the incision (myocardial bridge) creating multiple conduction pathways. Records show a very similar AP and APD measure after making the incision, illustrating the absence of significant ischemia (Allen et al., 1989, Kléber, 1990). Furthermore, the decrease in AP amplitude was reversible and suggest only a temporarily decreased electrical activity in that area, implying that the myocardial damage caused by the incision was minimal. However, some degree of damage is to be expected when separating tissue layers.

6.4.4 The ability of hiPSC-CMs to follow high pacing frequencies.

Both the *in vitro* and *ex vivo* studies reported in this thesis show that hiPSC-CM cannot reliably follow pacing frequencies ≥2.9 Hz, which is manifest as alternans for either V or Ca^{2+} transients or as an absence of response. Alternans normally don’t happen at lower pacing rates, but only in very high paced rabbit hearts (Myles et al., 2011). Our *in vitro* study shows that alternans occur more prominently in the records of calcium transient compared to voltage. The underlying reason is most likely the poor calcium handling of the immature hiPSC-CMs, including the absence of T-tubules and dyads and a reduced expression and (almost) random localization of surface membrane and SR ion channels involved with E-C coupling (Karbassi et al., 2020, Kane et al., 2015). Additionally, the reduced calcium stores within the SR of hiPSC-CMs goes along a decreased SERCA activity and a substantial role for NCX in Ca^{2+} handling, resulting in slow calcium dynamics (Hwang et al., 2015, Itzhaki et al., 2011, Kane et al., 2015). Here, long-term culture or maturation protocols could enhance the structural organization and expression of maturity markers (Lundy et al., 2013) and therefore improve the integration of hiPSC-CMS *in vivo*.

Other small animal studies have shown that hiPSC-CMs and hESC-CMs could follow high pacing frequencies up to 5 Hz (Shiba et al., 2012, Gerbin et al., 2015), but it is important to note that these measurements were done several weeks after transplantation. *In vitro* studies have shown that mechano-electrical conditioning of hiPSC-CM enhances the CM maturation (Ronaldson-Bouchard et al., 2019, Ronaldson-Bouchard et al., 2018). Also, Chong *et al.* found evidence for *in vivo* maturation of hESC-CMs post-implantation, that includes increased myofibril alignment, prominent sarcomeres and an increased CM diameter (Chong et al., 2014). These observations were made between 14-84 days post-implantation, suggesting that maturation happens over several weeks. Interestingly, hESC-CMs that engrafted at the edge of the graft are showed an enhanced maturation status compared to CMs located in the core of the graft (Chong et al., 2014), underlining the importance of connection between implanted cells and the host. During our studies, mechanical stimuli were absent, and recordings were made within two hours after implantation, which could explain the discrepancies between the studies. Future studies are needed to clarify the effect of the mechanical and/or electrical stimuli of the heart on the maturity of implanted hiPSC-CMs (Scuderi and Butcher, 2017).

According to our studies, HiPSC-CM can follow up to 3.3 Hz, but the calcium signals show alternans, which is abnormal and indicates that the cells are at their limits of frequency. This data suggests that the EHTs cannot acutely follow the resting pace of the rabbit heart with normal ECC. Comparing the APDs indicated that 1) the rabbit APD was shorter than human EHT across all rates, even at rates of 3.3 Hz, 2) as a consequence the DI for the EHT was shorter than the rabbit at all rates, including 3.3 Hz and 3) The EHTs would not follow a pace with DI shorter than 100 ms and a similar limiting DI occurred in rabbit hearts at the higher rates of 4 Hz. Therefore, it is concluded that a minimum DI is necessary for following high pacing frequencies and this would not be possible in hiPSC-CM unless the APD shortens. Two publications show that hPSC-CM could successfully follow higher heart rates when implanted into the rat myocardium (5 and 6 Hz), but these recordings were taken 2 and 4 weeks post-implantation (Shiba et al., 2012, Gerbin et al., 2015). The electrophysiology of the implanted cells was not measured in this study, however, there was no indication of calcium alternans in their recordings, suggesting that the electrophysiology would not show alternans either. Interestingly, Gerbin *et al*. showed that hESC-CMs did not respond to *in vitro* field stimulation of 6 Hz, even after a ramp-up protocol of 6 weeks, as opposed to the *in vivo* experiments (Gerbin et al., 2015). This raises the possibility that the myocardium contains additional cues that promote mechano-electrical coupling that were not present in the *in vitro* studies. Al together, it is likely that the electrophysiology of hPSC-CMs can altered in time, but that the mechano-electrical coupling happens over several weeks rather than acutely.

6.4.5 Limitation

It was possible to record calcium transients from implanted EHTs for at least 2.5 hours post-implantation, but experiments were terminated after this timepoint because of the limited time frame where explanted heart are viable. Unfortunately, other experiments were shorter, resulting in missing data for later time points (60-150 min). The main reasons for the variability in the length of the experiments and thus the missing data-points is the loss of the Ca^{2+} signal. This could be caused by bleaching of the fluorescent dye, by accidental movement of the lightguide and/or cell death within the EHTs.

In case of cell death, the ability to (not) survive the implantation method and the myocardial environment might be related to the quality of the EHT and the hiPSC-CMs. This could skew the results as surviving EHTs might have superior electrophysiological and/or calcium handling features in order to adapt to the rabbit myocardium. It could therefore be argued to exclude the 2 EHTs with an incomplete record.

Another reason for missing data-points is the inability of EHTs to follow pacing frequencies.

Chapter 7 General discussion

The general aim of this thesis was to investigate the acute phase after implantation on the survival and integration of hiPSC-CMs into the myocardium.

> ***To meet this purpose, the specific aims of this study were to develop a cost-efficient platform based on the implantation of small EHTs (<50,000 hiPSC-CMs) grafted into the rabbit myocardium*** in vitro***, and subsequently to assess the electrophysiological adaptations of the hiPSC-CMs to the surrounding myocardium using of fluorescent indicators***.

The conclusions of each chapter as well as its limitations and the future directions are discussed below.

7.1 The impact of the COVID-19 pandemic

The SARS-Cov-2 (COVID-19) pandemic resulted in closure of the university, including all lab facilities, and caused disruption within my final year. The lab closure happened just after the *ex vivo* experiments were optimized. For my last year and final experiments, it was envisioned to repeat the *ex vivo* experiments multiple times to gain N-numbers and to do some additional experiments to investigate mechanical-coupling by washing off the ECC uncoupler. These experiments have been done subsequently but are not part of this thesis. Furthermore, I would have like to investigate *in vivo* use of these constructs allowing the EHTs to integrate for 24h or longer.

The three-month extension to make up for the delays caused by the pandemic was not enough to do all the experiments that were envisioned. Instead, only repetition of the *ex vivo* experiments was completed. To mitigate the time away from the lab, I focused on writing a paper and on writing this thesis.

7.2 The development of small micro-patches.

To achieve the main aim of this thesis, it was decided to develop small constructs to minimize the number of cells needed for one construct, and therefore maximizing the number of experiments that can be done with the same number of cells. The design of the small EHTs makes it possible to increase the EHT size, which might be necessary to investigate whether EHT size is an important factor for integration and survival of the graft. Initially, it was chosen to use a monolayer format, because upscaling can be easily done in two ways; 1) by enhancing the monolayer diameter, simply by using a wider stencil or culture dish and 2) by enhancing the EHT thickness by stacking monolayers on top of each other (Matsuo et al., 2015a).

The CMs used in this thesis are commercially available hiPSC-CMs. Their advantage is that they are ready to use after thawing and do not require quality controls to assess their purity. However, the extremely low proliferation rate of hiPSC-CMs makes this a limited cell source and commercial cells need to be bought in continuously, resulting in costly experiment. In contrast, hiPSCs do proliferate and when differentiated into CMs, could represent an unlimited hiPSC-CM source. Moreover, genetically modifying the hiPSCs with a genetically encoded calcium indicator GCaMP6f would benefit assessment of the functionality of EHTs post-implantation.

In the appendix (Chapter 8.2) the establishment of an hiPSC culture facility was discussed. The circumstances for the maintenance of this specific hiPSC line and their differentiation protocol and purification were optimized and resulted in cell lines of beating cardiomyocytes. However, the protocols for hiPSC maintenance and cardiac differentiation are time consuming and took away time, focus and resources from the main aim of this thesis. It was therefore decided to discontinue the use of the in house developed hiPSC-CM line and to continue with the commercial cells. For this reason, the in-house differentiated hiPSC-CMs were never used to create the EHTs.

The micro-patches were optimized for the cell seeding density and stencil size, where the 2 mm and 3 mm stencils achieved an acceptable success rate. Furthermore, the standard cell seeding density (Cor.4U: 100,000 cells/cm^2; ICell^2: 150,000 cells/cm^2) was not sufficient to reach a similar coverage as compared to control. Instead, a minimum of 2x the cell density is needed to seed in the stencil. This is means that approximately 6,000 cells and 14,000 cells are needed for a 2 mm and 3 mm stencil, respectively, instead of the usual 30,000 cells when seeding Cor.4U hiPSC-CMs. This means that 5x as many assays can be performed when using the 2 mm stencil and 2x as many assays when using the 3 mm stencil. Therefore, using stencils an improvement of the standard culture conditions.

After the optimization of the micro-patch, the primary cell source, Cor.4U hiPSC-CMs from NCardia, was discontinued by the manufacturer as it was found that these cells have an embryonic fingerprint in their genome (Braam, 2019). Therefore, my supervisor and I decided to continue with the ICell^2 hiPSC-CMs from FCDI, however, this also meant that new optimization was needed. Fortunately, the two cell types did respond similarly to the stencils and protocols did not have to be adapted. Only during later experiments where the cells were seeded on the hydrogel, it was found that the FCDI hiPSC-CMs did not adhere to the hydrogel in contrast to the NCardia cells. This was resolved by adding FN to the hydrogel mixture and a FN coating.

7.3 Assessment of the effects of detachment and transfer of small monolayers

In order to stack the micro-patches on top of each other to make a thicker construct, monolayers were detached from the thermoresponsive culture dish and transferred to a new dish to examine the effects of the detachment process on the cells. It was found that the method of detaching was more challenging than initially thought, resulting in a loss of micro-patches and a low success rate (25%). Moreover, the construct size was significantly reduced upon detachment. The 3 mm patch resulted in a monolayer of 1 mm in size (3x reduction), whereas the 2 mm patch practically became a sphere. The process of stacking cellular monolayers to create thicker tissues has shown to be successful in literature (Matsuo et al., 2015a, Haraguchi et al., 2012), however, these studies were done using cm-scale monolayers. This means that our micro-patches are too small to stack and create thicker patches. As an alternative, monolayers could be seeded in a larger mould, *e.g.* 10 mm, that, based on a 3x reduction in size, would become a 3 mm diameter patch after detachment. However, these larger monolayers would need considerably more cells which is cost-limiting in the context of this thesis.

7.4 The use of a biomaterial as support structure for cell delivery

As an alternative to scaffold-free micro-tissues, a biomaterial was used to maintain the monolayer shape and to function as a support structure for cell delivery. In this work, it was chosen to use a recombinant collagen-like peptide (RCP-MA), functionalized with methacrylated sidechains that form covalent bonds following UV-crosslinking. From the three stiffnesses available, RCP-MA_{50} (10 kPa) and RCP-MA_{100} (22 kPa) were of interest as their stiffness is comparable to that of the neonatal myocardium (~20 kPa). Using silicone moulds, hydrogels of 350 µm thickness were developed.

HiPSC-CMs were seeded on top of the hydrogel, as opposed to mixing the cells within the hydrogel, to assure cell-cell bonding and prevent damage caused by UV exposure used to cure the hydrogel. Initial experiments were done using Cor.4U hiPSC-CMs (NCardia), showing sufficient adherence of the cells to the material. However, because of the discontinuation of this cell line, further experiments included hiPSC-CMs from FCDI and, unfortunately, these were unable to adhere to the hydrogel. Cell adhesion improved when coating the hydrogel with FN, indicating that the RCP-MA did not have the correct binding moieties for this cell type. Other ECM matrix components did not result in a comparable adhesion efficiency as FN. In addition to the FN coating, combining the RCP-MA with FN prior to crosslinking enhanced cell adhesion allowed hiPSC-CMs to form a monolayer similar to those obtained through standard culture methods on glass or plastic, but only for the stiffest hydrogel (22 kPa). Importantly, these monolayers were stable in culture for more than a week and were therefore suitable for implantation experiments.

7.5 The establishment of an optical set-up to monitor the EHT post-implantation using fluorescent dyes

It was initially thought to use two fluorescent dyes in a complementary way to measure the functionality of the myocardium and the implanted cells simultaneously. For example, staining the cells with Cal590-AM and the heart with FV. During *in vitro* studies, Ca^{2+} and voltage signals were recorded simultaneously using this optical filter set (Chapter 6). Therefore, the same filter set was used for the *ex vivo* studies, however, we were unable to record Cal590-AM signals in EHTs grafted onto the ventricular epicardium. Further investigation showed the Cal590 signal to be less bright compared to Cal520. The highest possible fluorescence is needed from a construct, because the excited light is scattered when travelling through the layer of myocardial tissue covering the EHT, even though the scatter was minimized by implanting the EHT with the cells facing towards the lightguide, no Cal590 signals were recorded while recording transients using Cal520 was able to be done routinely. Therefore, it was chosen to use Cal520-AM instead of Cal590-AM, eliminating the option to record fluorescent signals from the myocardium with FV and EHT with Cal590 simultaneously. Instead, the ECG (heart) and Ca^{2+} (EHT) traces were linked using formulas that estimated their respective APD_{90} values. Future studies will examine the feasibility of using longer wavelength BeRST voltage sensitive dyes (Huang et al., 2015).

7.6 Optimization of the implantation technique

Two main implantation techniques described in literature are 1) the ectopic implantation of relatively large EHTs onto the epicardial wall and 2) the injection of cells into the myocardium, both with sub-optimal outcomes (Shiba, 2020, Zimmermann, 2017). The method used in this work can be seen as a combination of both, where a micro-EHT is implanted inside a superficial pocket that is made underneath the epicardial layer and can be compared to the implantation of cellular spheres in terms of implanting mini tissues that has shown to survive and integrate before (Gerbin et al., 2015, Rojas et al., 2017).

One of the major things to be optimized was the incision procedure, including the incision shape and the use of materials to close the incision such as glue or sutures that is used in other studies (Jabbour et al., 2021, Weinberger et al., 2016, Miyagawa et al., 2017). The incision shape has evolved over time from a myocardial pocket towards a myocardial band overlaying the construct, allowing the cardiac effluent to drain from the pocket. If the effluent was not drained, the pocket would fill up with effluent, and pushing the EHT out of the socket by positive pressure. While it was hypothesized that the incision would need to be closed post-implantation, e.g. by using glue or sutures, it was found that the myocardium is elastic enough to keep the construct in place without additional measures.

7.7 Inability of the human EHT to follow high pacing frequencies of the rabbit myocardium

It would appear that due to the human origin of hiPSC-CMs, these cells are unable to follow higher pacing frequencies than 3 Hz. It was shown in Chapter 6 that the failure to follow high pacing frequencies arises from failure of intracellular Ca^{2+} handling at these frequencies, which is confirmed by others (Liu et al., 2007, Kane et al., 2015). ECC depends on L-type Ca^{2+} channel and NCX on the cell membrane and minimally involves ryanodine receptors and SERCA on the SR. SR Ca^{2+} release and reuptake via SERCA has an important role in the calcium flux in adult cells (Hwang et al., 2015).

Some published studies show that hiPSC-CMs are able to follow higher pacing frequencies, but these are a minority (Shiba et al., 2012, Gerbin et al., 2015). It is likely that this physiological mismatch of ECC between rabbit heart and human EHT prevents 1:1 coupling of hiPSC-CMs. Importantly, allogenic studies in mice (Rojas et al., 2017), rat (Kadota et al., 2017) and primates (Zhao et al., 2018, Shiba et al., 2016) resulted in successful integration, showing the importance of matching ECC between the EHT and the recipient heart. Similarly, rabbit iPSC-CMs could be implanted into the rabbit myocardium, but unfortunately, not much is published regarding rabbit iPSCs and rabbit iPSC-CMs (Honda et al., 2010, Osteil et al., 2013, Phakdeedindan et al., 2019), complicating this line of work.

Slowing the rabbit heart down to the IR of the EHT could improve the ability of the EHT to follow the heart, for example through AV-ablation. Alternatively, the IR of the EHT could be increased using pharmacological substances such as beta-receptor agonists, however, it might be challenging to find a human specific beta-adrenergic compound as these pathways are genetically conserved within mammals. Alternative strategies could include specific up-regulation or activation of currents that shorten the APD in hiPSC-CMs to enable the tissue to follow rats comparable to rabbit sinus rates, this topic requires further investigation to determine viable options.

7.8 Limitations

The work presented within this thesis had a few limitations which will be discussed below.

7.8.1 Recording signals from one EHT per experiment

One of the limitations of the *ex vivo* platform is that the calcium signals of only one EHT can be recorded at a time. Because the EHTs are small, it is easy to lose signal once the light guide has moved. Initially, the aim was to implant multiple EHTs in the same heart, however, repositioning the lightguide might cause signal loss or a change in signal strength. To be able to compare the sequential recordings from one EHT, it was decided to avoid repositioning the light guide.

7.8.2 Estimation of APD_{90} values

Furthermore, it was aimed to record the APs from both the EHT and myocardium was desired. However, there are currently no bright voltage sensitive dyes available that have the right wavelengths for dual imaging. Instead, it was chosen to only record the calcium signals of the EHT along the ECG of the heart. To be able to compare the electrophysiology of the heart and the implanted cells, it was decided to perform preliminary experiments investigating the ECG:AP and CaT:AP relationship of the heart and EHT, respectively. As these values are only estimates of the actual APD_{90} values, it is difficult to draw firm conclusions.

For direct comparison of physiologically similar transients, the heart could be stained with Cal590-AM, and the cells with Cal520-AM, whereafter the CaT_{50} values can be calculated from both signals and be compared. However, to investigate electrical coupling, it is of interest to measure the electrical signals of the heart and/or the EHT. Measuring the calcium transients would therefore be inadequate.

Another option could be to use a viable long-wavelength voltage sensitive dye (e.g. BeRST) that would allow Cal520 to be retained for the EHT marker (Huang et al., 2015). If BeRST has a comparable brightness as Cal520-AM, it could be used to stain the EHTs prior to implantation and in combination with FV for the rabbit heart to obtain the APs from the EHTs and the direct surrounding myocardium. Alternatively, the rabbit heart could be stained with BeRST and the EHT with Cal520-AM.

7.8.3 Fluorescent dyes are only viable short-term

Furthermore, Cal520-AM or other fluorescent dyes are not long-lasting and will therefore not be useful for *in vivo* experiments. Here, a genetically engineered voltage or calcium indicator is needed, such as the previously discussed GCaMP-6f (paragraph 2.2.3).

7.8.4 Elimination of contraction through contraction uncouplers

Another limitation is that the contractile ability of the myocardium was eliminated through blebbistatin incubation to minimize the moving artifacts during fluorescent recording. Therefore, the effect of myocardial contraction on the implanted cells was not assessed, but this might be an important factor for coupling of the host ECC to that of the EHT. Future studies should look into ways to obtain fluorescent (Cal520) signals without motion artifacts, so that the effect of myocardial contraction on the cellular integration and electro-mechanical coupling can be investigated.

7.8.5 Limitations of the Langendorff perfusion system

The reason for using the Langendorff setup for these studies, is that it is a controlled environment where the beating frequency, flow and systemic pressure can be easily regulated (Langendorff, 1895). Furthermore, the heart could be arrested using the ECC uncoupler blebbistatin and the coronary arteries are continuously perfused, a necessary requirement for maintaining the viable myocardium for the duration of the experiment. However, this approach does not mimic the haemodynamic changes that happen normally in cardiac physiology, including the Frank-Starling mechanism. In contrast, the working heart setup, where the heart is perfused in the ‘normal’, physiological direction, represents the mechanical features of the heart more physiologically (Neely et al., 1967, Au - Dewitt et al., 2016). Thus the isolated working-heart might give a better insight on the acute integration of small EHTs, particularly if mechanical stretch is an important part of the process.

7.9 Future directions

The *ex vivo* platform presented here has shown to be a useful technique to study the acute integration of small EHTs. Now the platform is established, various adaptations to the construct can be investigated in order to improve electro-mechanical coupling at these high rates. For example, focus could lie on improving the calcium handling of the EHTs to shorten the AP and therefore increase the ability of the EHTs to follow the high pacing frequency. This could potentially be done by over express ion channels involved with calcium handling, such as SERCA and the LTCC. Alternatively, maturation of the cells through mechanical or electrical stimulation prior to implantation has also shown to improve calcium handling of constructs (Ronaldson-Bouchard et al., 2019).

In contrast to this, the pacing frequency of the rabbit heart could be manipulated in order to mimic the intrinsic rate of the human CMs. This could be done by AV ablation, so that the electrical impulses generated in the SA node are blocked at the AV node (Loen et al., 2021). Therefore, the much slower intrinsic pulse generation of the LV will determine the frequency of LV depolarization.

Furthermore, the influence of mechanical stimulation in addition to electrical stimulation would also be important to investigate, as this could be an important influence on cellular integration. Future studies should therefore avoid using the ECC uncoupler, such as blebbistatin used in the experiments presented in this thesis. Other factors, such as graft size (hypoxia and arrhythmia's), implantation technique (epicardial vs intramyocardial), and location (healthy vs border zone vs infarct region) could be determining for the successful integration of these EHTs. Eventually, *in vivo* experiments would be the final logical step to investigate the integration and survival of small EHTs for a longer period of time.

7.10 Multiphasic contractile behaviour – A second theme throughout the chapters

Beside the main aim of this study, an interesting observation was made and discussed in Chapter 3, namely the multiphasic contractile behaviour of the hiPSC-CMs. Investigation into the origin of the multiphasic contractility concluded that this phenomenon was not caused by variation in electrical conductivity across the monolayer as all APs were alike. Moreover, these multiphasic patterns were not observed in free floating monolayers or monolayers seeded on a soft substrate (hydrogel), but only in monolayers seeded on stiff surfaces, such as glass or TCP. Interestingly, multiphasic time-courses were not related to cell seeding density, and were not observed in single cells, indicating that cell-cell adhesion as a potential underlying cause. Addition of isoprenaline demonstrated an increase in chronotropy and lusitropy, but not inotropy, and the lusotropic effect was greater in hiPSC-CMs on soft substrates. Furthermore, the ß-adrenergic stimulus did not affect the degree of multiphasic contractile behaviour. These data suggest that the rigid culture surfaces are not suitable for actively contracting tissues such as cardiac cells.

Final conclusion

With the work discussed in this thesis, a novel platform has been developed to investigate functionality of implanted cells within the myocardium in the acute phase post-implantation. This platform includes a micro-EHT, a novel implantation technique, fluorescent dyes to track functionality and an *ex vivo* rabbit heart preparation. It can be used to investigate many factors that might affect the integration and survival of implanted cells during the acute phase in a cost-effective way and is therefore a good intermediate step between *in vitro* and *in vivo* experiments.

Chapter 8 Appendix

8.1 Computational model to investigate the biological findings of the multiphasic contractile behaviour of hiPSC-CMs on rigid surfaces

8.1.1 Introduction

To help understand the contractile signals obtained from hiPSC-CMs in culture, I embarked on a collaboration with a group in Mathematical Sciences, Glasgow University lead by Prof. Radostin Simitev and in particular with a concurrent PhD scholar Peter Mortensen. We simplified the mathematical description of cells cultured on a surface to a one-dimensional array of contractile units connected in series (Fig. 1.1). The units represent cells and sit on a horizontal frictionless surface representing the substrate. The two ends of the chain are connected to the surface by linear elastic springs. Illustrations of this setup are shown in Figure 8.1.

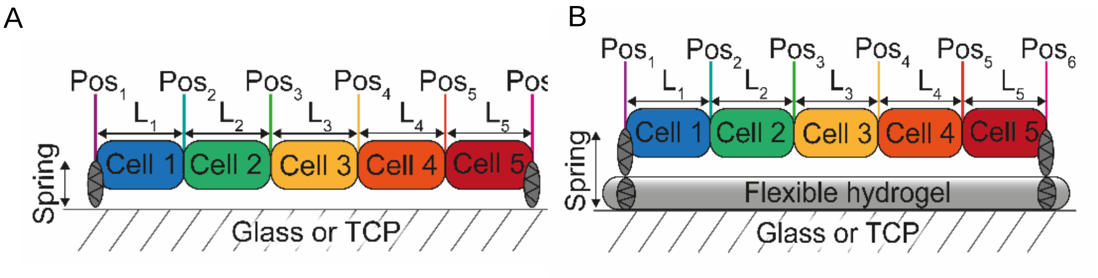

Figure 8.1 Diagrams showing the model for the cell arrangement on the stiff (A) and soft (B) substrates.
The stiff substrate is represented by a spring at each end with value of the spring constant equal to k=1 and soft substrate is represented by a pair of springs at each end with value of the effective spring constant equal to k=0.01.

To vary the stiffness of the substrate in this model we consider different values of the linear string constants. An essential input to the model is the calcium transient profile and here it is determined by a calcium transient derived from the fluorescent measurements reported in this study Figure 8.2**A**, with values of the resting Ca^{2+} and peak Ca^{2+} based on published literature (Hwang et al., 2015). As an output of the model a motion signal equivalent to the output of the MM algorithm (Sala et al., 2018) was computed from the movement of the cell ends. As shown in Figure 8.2B the result and motion signal in response to an appropriate calcium transient has a similar time course to that seen in culture. A diagram of the mathematical model itself is shown in Figure 8.2C.

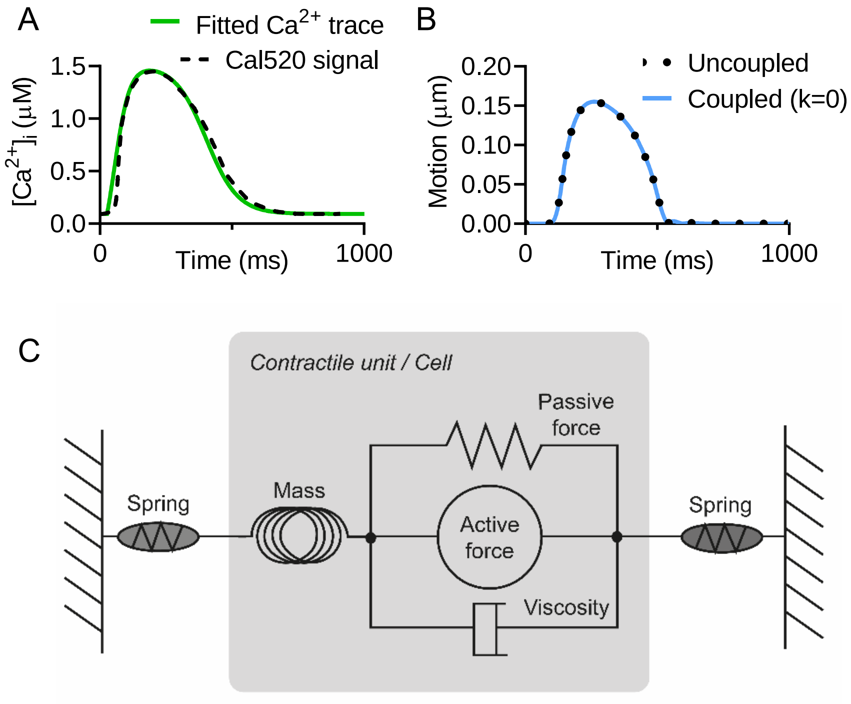

Figure 8.2 Mathematical model specifics.
A) Calcium trace from hiPSC-CMs (Cal590 signal) (solid line) vs the calcium profile used in the mathematical modelling (broken line). B) The motion trace from a single contracting unit in the uncoupled system (dotted line) from the model from Rice et al, compared with the motion traces from a single contracting unit, coupled between two springs with k=0, from the model directly from Timmerman et al (solid blue line). C) A schematic of the force components in the contractile units, based on Figure 1D from Rice et al (Rice et al., 2008).

8.1.2 Mathematical model

The following scheme proposed by Timmermann et al (Timmermann et al., 2019) is used to connect the contractile units and the end springs into a chain,

$$\frac{dL_i}{dt} = \left(2\frac{d\hat{L}_i}{dt} - \frac{d\hat{L}_{i-1}}{dt} - \frac{d\hat{L}_{i+1}}{dt}\right)/2, \forall i \in \{2,3,\ldots,N-1\},$$

$$\frac{dL_1}{dt} = \left(\frac{d\hat{L}_1}{dt} - \frac{d\hat{L}_2}{dt}\right)/2,$$

$$\frac{dL_N}{dt} = \left(\frac{d\hat{L}_N}{dt} - \frac{d\hat{L}_{N-1}}{dt}\right)/2,$$

where, L_i is the length of the contractile unit i at a given timestep, with L_1 and L_N being the elastic springs at the left and right end, and N is the total number of units (including the springs). The hats ^ denote quantities at the preceding timestep and are computed using the myofilament contraction model of Rice et al (Rice et al., 2008),

$$\frac{d\hat{L}_i}{dt} = \frac{p + \left(L_i - L_{i,0}\right) \times viscosity}{mass}, wherep = \int_0^t F dt$$

where, impulse p is the integral of the total force F acting on a unit over a time interval. Forces are scaled with the peak twitch force of a rat sarcomere of 101.8kPa (Daniels et al., 1984).

For the contracting units i=2. N-1, the total force is a sum of active and passive forces, $F = F_a + F_p$, as illustrated in Figure 8.2C. The passive force has contributions from the titin in the sarcomere, and collagen in the extra cellular matrix, see (Rice et al., 2008). A linear elastic force has been added to those considered in (Rice et al., 2008), to ensure that each cell can return to its original length after active contraction and represents passive forces in the whole cell unaccounted for in (Rice et al., 2008), for example isovolumetric forces. This modification is justified by the fact that (Rice et al., 2008) is a myofilament model that we adopt as a model of the whole cell and is critical for reproducing the recorded motion of the myocyte contraction. The active force is taken identical to that specified in the Rice model (Rice et al., 2008) and is dependent on the calcium concentration. As input calcium profiles we use curves fitted to the recorded calcium concentration in the experimental work, as seen in Figure 8.2A. The maximum and minimum concentration used are taken from the Shannon et al (Shannon et al., 2004) model of a rabbit ventricular myocyte, as also used in the Rice model.

For the linear elastic springs i=1 and i=N, the total force is given by Hooke's law, $F = F_S$, with

$$F_S = \mathrm{k}\left(L_i - L_{i,0}\right),$$

where L_i is the current length of the spring, and $L_{i,0}$ is the initial length of the spring. The value k is the stiffness of spring, or the spring constant. This value is a unit normalised force per μm^{-1}. As mentioned, the forces in the Rice model (Rice et al., 2008) are normalised relative to the peak twitch force of a rat sarcomere of 101.8kPa (Daniels et al., 1984), thus k=1 represents a stiffness of 101.8kPa. Although it is understood that stiffness of the stiff plastics or glass would have a stiffness in the order of GPa, k=1 was found to be sufficient to have little movement in the springs, as desired.

A more complete discussion and derivation of the model equations is provided in Mortensen (Mortensen, 2021).

8.1.3 Results

Attachment to a stiff matrix (glass or plastic) was simulated by setting the value of the spring constant k to 1 and attachment to a flexible matrix equivalent to the RCP-MA hydrogel was simulated setting the value of the spring constant k to 0.01. The model was tested for variations in the number of contractile units (N=3, N=5 or N=10) and for the cell-to-cell variation of intracellular calcium ($[Ca^{2+}]_i$) (Cerignoli et al., 2012) on the contractile profiles as shown in Figure 8.3. Here, the variations in $[Ca^{2+}]_i$ tested were 0% (identical), 95-100% (minimal), 75-105% (low), 50-115% (medium) and 25-125% (high), where the maximum calcium level was randomly sampled from a uniform distribution and randomly assigned to each contractile unit.

The contractile behaviour of 3, 5 or 10 contractile units, or cells, in sequence and attached to a stiff (k=1) or soft (k=0.01) surface is simulated using the model. As shown in Figure 8.3A and C, more than 5 units result in multiphasic motion that is incompatible with our biological results.

Our hypothesis is that the heterogeneity of the contractile activity in each contractile unit (cell) is the origin of the complex contractile behaviour on stiff matrices. There may be multiple reasons for the variation, but one identified heterogeneity is the cell-to-cell variation in the amplitude of the intracellular calcium transient (Cerignoli et al., 2012). Various degrees of heterogeneity of peak $[Ca^{2+}]_i$ were investigated and a moderate level that corresponded with the experimental observations (50-115% of 1.5 μM) was used (Figure 8.3A and C, red boxes).

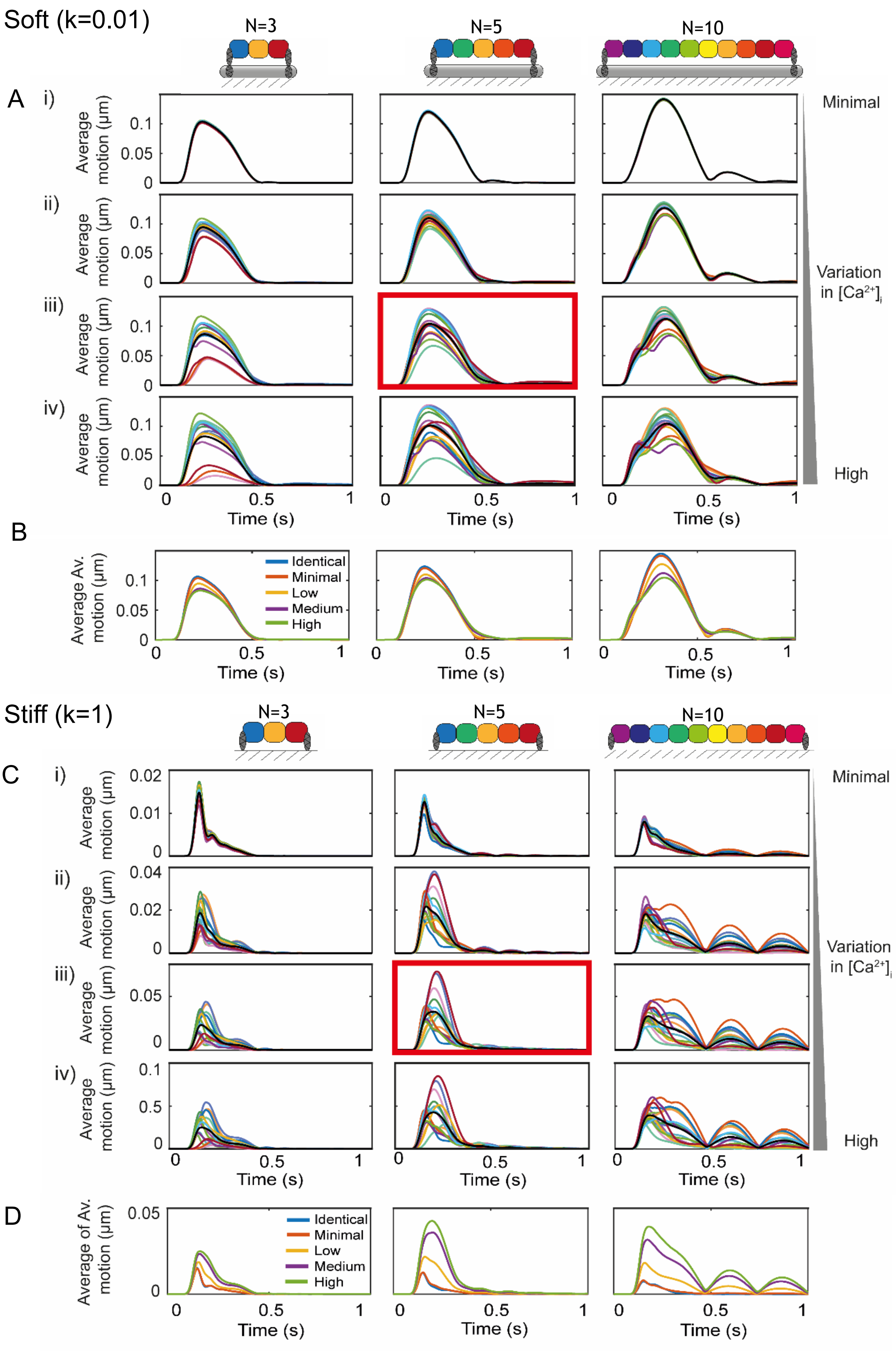
Soft (k=0.01)
N=3
N=5
N=10
A
i)
ii)
iii)
iv)
Average motion (μm)
0.1
0.05
0
Time (s)
0.5
1
Minimal
Variation in [Ca2+]i
High
B
Average Av. motion (μm)
Identical
Minimal
Low
Medium
High
Stiff (k=1)
C
0.02
0.01
0.04
0.05
0.1
0.5
D
Average of Av. motion (μm)

Figure 8.3 (previous page) The effect of variation in intracellular calcium and number of contractile units on the computed motion by the model presented.
A) Average motion from 15 sets of simulations with N=3, 5 and 10 contractile units, with k=0.01 and randomly assigned maximum calcium concentrations within the ranges: i) a minimal range of 95-100%, ii) a low level of variation, 75-105%, iii) a medium level of variation, 50-115%, and iv) the highest level of variation, 25-125%. The red box indicates the set seen in the main body of the text, specifically, the case with N=5 and a medium level of variation of the maximum calcium. The average of the 15 sets of averages is plotted with the thick black line and are plotted in B). C) Average motion from 15 sets of simulations with N=3, 5 and 10 contractile units, with k=1 and randomly assigned maximum calcium concentrations within the ranges: i) a minimal range of 95-100%, ii) a low level of variation, 75-105%, iii) a medium level of variation, 50- 115%, and iv) the highest level of variation, 25-125%. The red box indicates the set seen in the main body of the text, specifically, the case with N=5 and a medium level of variation of the maximum calcium. The average of the 15 sets of averages is plotted with the thick black line and are plotted in D).

The same distribution of $[Ca^{2+}]_i$ (medium, 50-115% of 1.5 µM) was applied to both models to keep all factors identical except for the spring constant (Figure 8.4Ai and ii). Here, the cells on the soft substrate (k=0.01) practically all shortened during the increase in $[Ca^{2+}]_i$ (Figure 8.4Aiv), however, the cells on the rigid substrate (k=1) showed a distinct pattern of both shortening and elongation (Figure 8.4Aiii). As shown in Figure 8.4Av, this resulted in a similar complex motion that we observed in our hiPSC-CM cultures seeded on fixed substrates, including multiple-phasic contraction profiles and delayed transients. In contrast, the transients resulting from the model for the soft substrate only showed twitch-like motion without delay (Figure 8.4Avi). Simulating the same model with other randomized distributions of $[Ca^{2+}]_i$, had similar outcomes, which can be seen in Figure 8.4Bi and Figure 8.4Bii for stiff and soft substrates, respectively.

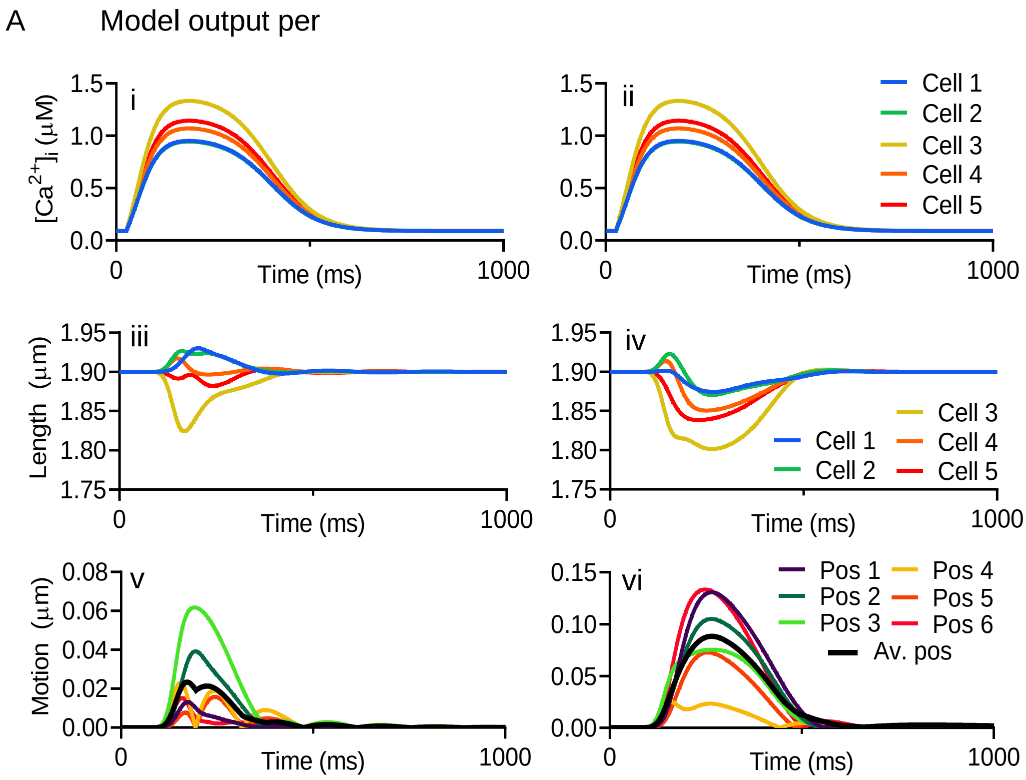

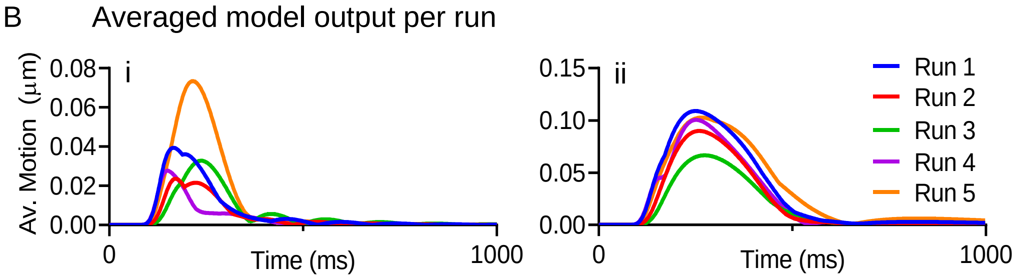

Figure 8.4 Computational model showing the complex contractile behaviour as seen in biological samples.
A) Graphs showing the output per unit (cell) for intracellular calcium (μM) (i and ii), cell length (μm) (iii and iv) and the displacement of the ends of a cell from their initial positions (motion) (μm) (v and vi) of hiPSC-CMs seeded on stiff (i, iii, v) and soft (ii, iv, vi) substrates. Colour schemes of panel (B) are corresponding with the diagram Figure 1.1. The black line in figures Av and Avi represents the average position (Av. Pos) of all the positions (1-6) combined. C) The averaged model output per run for 5 different runs of the same model, but different randomized calcium distribution for each cell. Note that run 2 in both panel Bi and Bii corresponds with the average position of panels Av and Avi, respectively. Pos denotes position. L denotes cell length or unit length.

8.1.4 Conclusion and discussion

The data obtained using this model supports the hypothesis that the complex motion signal arises from cell-to-cell interactions within small groups of cells that are not individually attached to a stiff matrix. Flexible matrixes with a stiffness comparable to a cell allows shortening of the sarcomere within the groups of cells and prevents significant cell-to-cell variation in contraction.

The model showed that in 1-dimensional arrays of up to 5 cells differences in peak calcium between cells generates different contractile forces at the level of the sarcomere, which in cells with high $[Ca^{2+}]_i$ results in sarcomere and cell shortening while adjacent cells with lower $[Ca^{2+}]_i$ are stretched, increasing both sarcomere- and cell length. Due to the dome shaped relationship of the sarcomere length-tension curve, as the cells shorten, these forces cannot be maintained and result in spontaneous stretching as the forces in adjacent cells become greater. These interactions occur during the phase of high calcium within one contraction and generate multi-phasic changes in cell length within each cluster. This behaviour contrasts with that of a flexible substrate where the overall array of cells shortens uniformly because the underlying substrate shortens in parallel (Figure 8.4Error! Reference source not found.). This difference in behaviour does not critically depend on the extensive differences in cell-to-cell calcium, but more complex behaviour arises when the cell array size consists of more than 5 cells (Error! Reference source not found.). Thus, the *in silico* modelling supports the multi-phasic contractile behaviour arises from the cell-to-cell interactions of small clusters of hiPSC-CM differentially attached to the underlying stiff matrix and supports the view that the matrix stiffnesses approximating that of the cells are required for more physiological contraction profiles.

8.2 Cardiac differentiation of hiPSCs (Secondment in the Sullivan's Lab, Oslo, Norway)

8.2.1 Introduction

8.2.1.1 The genetically modified GCaMP6f hiPSC-CM cell line

A hiPSC-CM cell line with a genetically encoded calcium indicator (GECI), such as GCaMP6f (Chen et al., 2013), would be a great tool for long-term calcium imaging and thus for *ex vivo* and *in vivo* experiments. In addition to this, hiPSC have proliferative capacities and thus genetically modifying the hiPSC rather than the hiPSC-CM results in an unlimited GCaMP6f hiPSC-CM cell source.

In collaboration with the Sullivan Lab at the University of Oslo (Oslo, Norway) we aimed to establish a GCaMP6f encoded hiPSC-CM cell line. The Sullivan lab has experience with human fibroblast dedifferentiation and genetical modification of hiPSC lines (Siller and Sullivan, 2017) and they were working on cardiac differentiation following a protocol of Lian *et al*. (Lian et al., 2013). To establish this GCaMP6f encoded hiPSC-CM cell line, hiPSC would be genetically modified whereby the GCaMP6f gene together with a doxycycline sensitive promoter that allows for control of the GCaMP6f expression. In this way, GCaMP6f is only expressed in the presence of doxycycline and could therefore prevent long-term photobleaching of GCaMP6f.

During a one-month secondment at the Sullivan lab in Oslo, all techniques, skills and knowledge needed for hiPSC maintenance and cardiac differentiation were obtained. Moreover, their expertise guided us in the process of setting up a hiPSC and hiPSC-CM lab to be able to culture these cells in our lab in Glasgow. To test the new lab facilities and hiPSC lines, wildtype (non-transfected cells) were sent over from Oslo first to optimize the culture- and differentiation protocols. In the meantime, the Sullivan lab would develop a genetically modified version of the same hiPSC source.

8.2.1.2 Optimization of assays

Beside setting up a hiPSC culture lab, facilities to assess the stemness of the cells and differentiation efficiency are needed too. Examples are immunohistochemistry, karyotyping, RT-qPCR and fluorescence-activated cell sorting (FACS). Immunohistochemistry would not need much optimization, however, the other procedures would. RT-qPCR facilities are present in our lab, however, finding the correct primers can be a challenge. Here, it is important to keep in mind that the progenitor cell or stem cell can have a different housekeeping gene signature compared to its profile when differentiated (Synnergren et al., 2007). This could eventually lead to skewed results. It is therefore important to find housekeeping genes that are similarly expressed in the hiPSC and in the hiPSC-CM (Holmgren et al., 2015).Therefore, multiple housekeeping genes will be assessed. Because immunohistochemistry and RT-qPCR are available in the labs, the hiPSCs and hiPSC-CMs were assessed using those techniques first.

When the hiPSCs are differentiated into CMs they will start beating. Further assessment of their cardiac phenotype and genotype is needed as well.

8.2.2 Methods

8.2.2.1 Dedifferentiation of human fibroblasts

Dedifferentiation of fibroblast was done by the Sullivan’s lab at the university of Oslo, Oslo, Norway. Reprogramming of human fibroblast was done using the Cytotune – iPS 2.0 Sendai Reprogramming Kit (Cat# A16517, A16518, Invitrogen). An overview of the reprogramming procedure is shown in Figure 8.5A. In brief, fibroblasts were grown on vitronectin coated petri-dishes and exposed to the Sendai virus for one day. On day 8, the culture medium was changed from fibroblast culture medium to Essential 8 (E8) medium. Once colonies were formed (2 weeks) and large enough (3-4 weeks), the colonies were collected and transferred to a new dish (Figure 8.5B). Importantly, all colonies were kept separately to be able to distinguish hiPSC properties between colonies (proliferation, morphology, viability, etc.).

We received hiPSCs derived from two different commercial fibroblasts cell lines, namely AG05836 (Coriell Institute, 44 yo female) and Detroit551 (CCL-110, female fetus). The AG cell line performed better, so all results seen in this chapter are from this cell line.

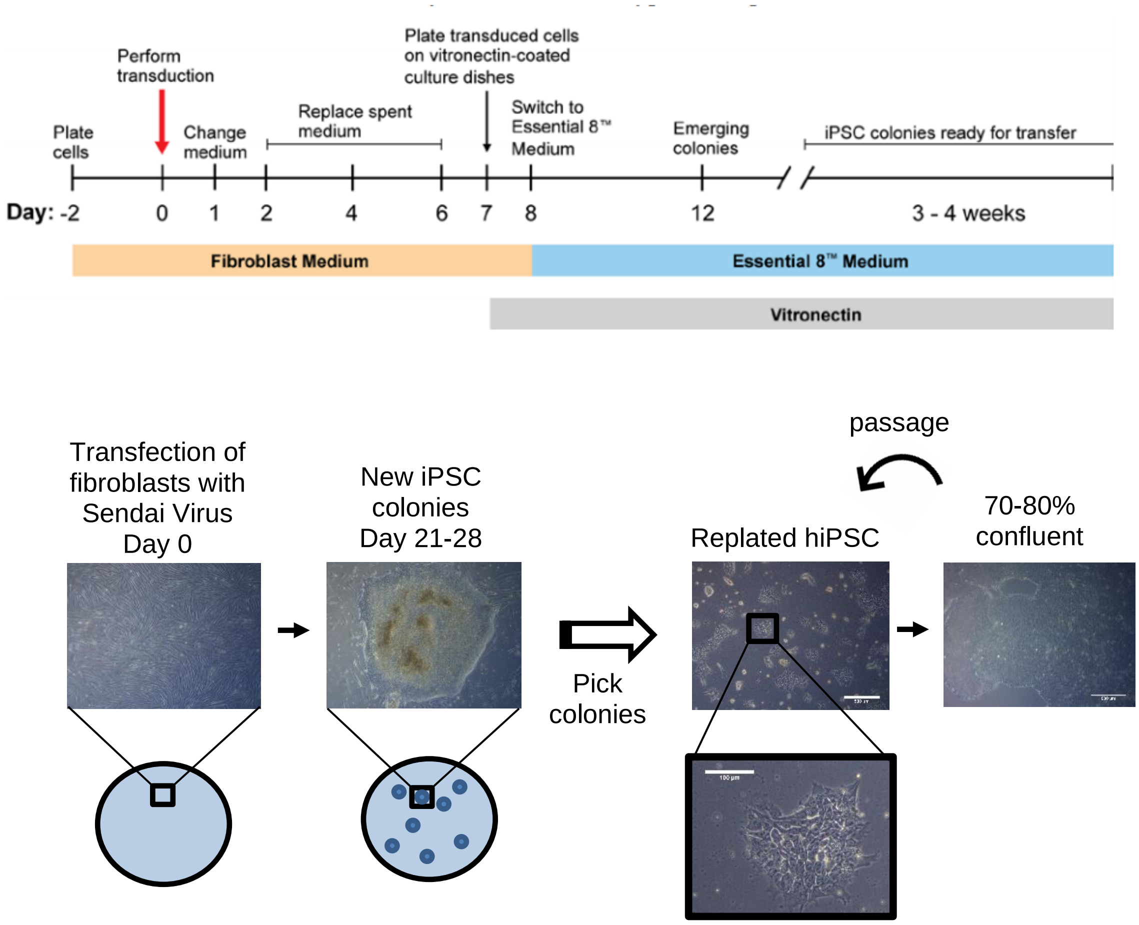

Figure 8.5 Differentiation of fibroblasts towards hiPSCs and hiPSC-CM maintenance. Overview of hiPSC colony picking and passaging. Scalebar represent 500 µm for all pictures except for the insert (black box), which represents 100 µm. The photo's regarding fibroblast culture and colony picking were made by the Sullivan lab. The diagram showing the reprogramming was taken from the CytoTune-iPS 2.0 Sendai Reprogramming Kit brochure.

8.2.2.2 HiPSC maintenance

HiPSC were seeded on Geltrex (A1413302, Life Technologies, 1:100) coated 6-well plates and kept in essential 8 (E8) culture medium. E8 medium was made from scratch as described by Siller and Sullivan (Siller and Sullivan, 2017) and was changed every day. HiPSCs can be used between passage 20-60.

Table 8.1 Components of E8 culture medium (200 ml).

Compound	***Volume***	***Company***	***Cat #***
DMEM/F12, HEPES (with 6.464 mM sodium bicarbonate)	200 ml	Thermo Fisher	11330057
Insulin solution, human	400 ul	Sigma-Aldrich	I9278
Ascorbic acid 2-phosphate	200 ul	Sigma-Aldrich	A8960
Human recombinant transferrin	200 ul	Sigma-Aldrich	T3705
bFGF2	200 ul	Prepotech	100-18B
TGFb1 (human recombinant -CHO)	200 ul	Prepotech	100-21C
Sodium selenite	200 ul	Sigma-Aldrich	S5261
Pen/Strep	2 ml	Thermo-Fisher	15140-122

8.2.2.3 HiPSC passaging

When a 70-80% confluency was reached, hiPSC were detached by incubating them with Ultrapure EDTA (15575-020, Life Technologies, 0.5 mM and pH 8.0) for 3-4 minutes. Subsequently, EDTA was removed, and cells were collected by forcefully adding E8 medium containing ROCK-inhibitor Y-27632 (1254, TOCRIS, 10 µM). Subsequently, hiPSC were seeded 1:3 onto new Geltrex coated plates.

8.2.2.4 Cardiac differentiation of hiPSCs

Single cell seeding

The cardiac differentiation protocol that was used here is previously described by Lian et al (Lian et al., 2013). Briefly, upon a confluency of 70-80%, hiPSC were detached by incubation with Accutase® for 10-15 minutes. Cells were subsequently collected using E8 medium containing 10 µM Y-27632 and pipetted through a 40 µm cell strainer to promote single cell seeding. Then, cells were centrifuged at 300g for 5 minutes and the supernatant was replaced for fresh E8 medium. Finally, hiPSC were counted and plated in the desired cell density.

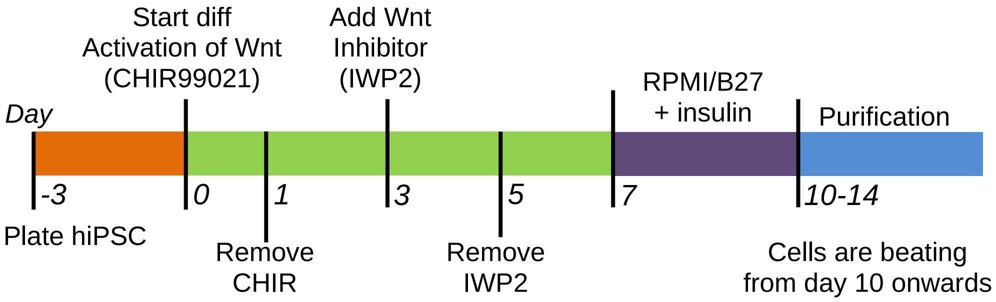

Figure 8.6 Differentiation protocol as described by Lian et al.
Purification of beating cardiomyocytes is done by replacing glucose for lactic acid to mimic anaerobic oxidation as described by Tohyama et al.

Cardiac differentiation protocol

When the replated cells reached a confluency of 70-80%, the cardiac differentiation protocol was initiated through activation of Wnt signalling by adding CHIR99021 (6-12 µM, 4423, TOCRIS) dissolved in RPMI/B27 medium without insulin (day 0). On day 1, medium was replaced for RPMI/B27 without insulin. On day 3 of differentiation, Wnt signalling was inhibited by adding 5 µM

IWP2 (3533, TOCRIS) dissolved in RPMI/B27 medium without insulin, which was replaced for plain RPMI/B27 medium on day 5. From day 7 onwards, RPMI/B27 with insulin was used and replaced every 2 days. Beating cells were observed from day 10 of differentiation. Importantly, CHIR99021 concentrations and cell densities must be optimized for every hiPSC clone. An overview of the differentiation protocol is shown in Figure 8.6.

8.2.2.5 Purification step by replacing glucose for lactic acid

Most cell types, including hiPSCs depend on aerobic glycolysis for ATP production. In contrast, cardiac cells can produce ATP through both aerobic- and anaerobic oxidation and are thus independent of glucose to survive. This feature can be used to eliminate undifferentiated cells in order to purify the cell population after differentiation (Tohyama et al., 2013).

CM purification was initiated by replacing the RPMI/B27+insulin for glucose-free RPMI for 4 days, refreshing the purification-medium halfway (day 2).

8.2.2.6 Immunofluorescence

HiPSCs were washed 2x with PBS and fixed in 4% PFA for 10 min. Subsequently cells were washed another 2x with PBS and permeabilized with 0.2% Triton-X in 1% BSA/PBS for 10 min. Then, cells were blocked with 10% goat serum in 1% BSA/PBS, whereafter the primary antibody was incubated ON at 4°C. The next day, the primary antibody was washed off whereafter the secondary antibody was added and incubated for 60 mins. Finally, DAPI (1:1000) was added for 2 min, followed by more wash steps with PBS. Cells were kept in PBS until they were imaged on the EVOS auto-FL microscope using a 10x objective.

Table 8.2 Primary and secondary antibodies

Antibody	Company	Cat #	Dilution
Primary antibodies			
Rabbit-anti-Sox2	Stemgent	09-0024	1:100
Rabbit-anti-Oct4	Stemgent	09-0023	1:100
Rabbit-anti-Nanog	Stemgent	09-0020	1:100
Rabbit-anti-α-actinin	Abcam	Ab137346	1:50
Mouse-anti-α-actinin	Sigma	A7732	1:500
Mouse-anti-cTnnT	Abcam	Ab8295	1:200
Secondary antibodies			
Alexa Fluor Goat-anti-Mouse	Invitrogen	A11001 (488); A21235 (647)	1:500
Alexa Fluor Goat-anti-Rabbit	Invitrogen	A11034 (488); A21245 (647)	1:500
Nuclear stain			
DAPI	Life technologies, Thermo scientific	62247	1:1000

8.2.2.7 RNA isolation and RT-qPCR

Gene expression profiling was planned as a measure to check the stemness of the hiPSCs and as a method to qualify the hiPSC differentiation. Multiple primers for Sox, Nanog, Oct4, NKX2.5, cTnnT and various housekeeping genes were assessed on binding affinity and specificity, whereafter the primers with the best results were kept (Table 8.1).

Cells were detached from the plate using standard conditions, washed and the cell pellet was frozen until further use. For RNA extraction, the ReliaPrep^{TM} RNA Cell Miniprep System (Z6011, Promega) was used and the protocol of the manufacturer was followed. After RNA isolation, the quality and quantity of the RNA was measured using the nano-drop.

Unfortunately, the optimization took a long time and was not finished once it was decided for me to take a step back from these experiments. Therefore, no RT-qPCR results are shown in this section.

Table 8.3 Overview of genes for RT-qPCR

	Gene	Full name	Function
Housekeeping genes	EID2	EP300 interacting inh of diff 2	Inhibition of TGF-b/SMAD
	CAPN10	Calpain 10,	Cytoskeleton remodelling and signal transduction
	RABEP2	Rab-GTPase binding effector protein 2	Membrane trafficking
	ZNF324B	Zinc Finger 324B	Transcriptional regulation
	ACTB	beta-actin	Cytoskeleton
	GAPDH	Glyceraldehyde-3-phosphate dehydrogenase	Metabolism
Cardiac markers	NKX2.5	NK2 homeobox 5	Heart development
	cTnnT	Cardiac troponin T	Sarcomeric structure
Stem cell markers	Sox2	SRY-box2	Embryonic development and pluripotency
	Oct4/POU5F1	Octomer-binding TF 4 (POU5F1)	Self renewal
	Nanog	Homeobox Protein Nanog	Pluripotency

Table 8.4 Selected primers for RT-qPCR

Gene name	NCBI data base number		Primer sequence	T_m	Amplicon size	Ref/source
Stem cell genes						
SOX2	NM_003106.3	Fwd	ATGGACAGTTACGCGCACAT	60.39	171	Primerblast
		Rev	CGAGCTGGTCATGGAGTTGT	60.04		
POU5F1	NM_002701.5	Fwd	AAGCGAACCAGTATCGAGAAC	58.12	143	(Park et al., 2008)
		Rev	TTACAGAACCACACTCGGAC	57.19		
NANOG	NM_024865.3	Fwd	ATGCCTCACACGGAGACTGT	61.19	103	(Page et al., 2009)
		Rev	AAGTGGGTTGTTTGCCTTTG	57.31		
Cardiac markers						
NKX2.5	NM_004387.3	Fwd	CAAGTGTGCGTCTGCCTTTC	60.04	104	Primerblast
		Rev	CGCACAGCTCTTTCTTTTCGG	60.40		
TnntT2	NM_001001431	Fwd	AGAGCGGAAAAGTGGGAAGA	58.94	171	Primerblast
		Rev	TGCAGGTCGAACTTCTCTGC	60.32		
Housekeeping genes						
EID2	NM_153232.3	Fwd	TGCTCCCGGCAGAATACAAG	60.11	117	Primerbank
		Rev	AGGTCCACCCTGTGAGGATT	60.18		
RABEP2	NM_024816.2	Fwd	TGCCTGCACCATGAGGTAAAG	60.61	231	Primerbank
		Rev	CGTCACGATCTCGATCCGC	60.72		
ACTB	NM_001101.4	Fwd	AGTCATTCCAAATATGAGATGCGTT	59.18	123	Primerbank
		Rev	TGCTATCACCTCCCCTGTGT	60.25		
GAPDH	NM_001289745.2	Fwd	GGAGCGAGATCCCTCCAAAAT	59.86	197	Primerbank
		Rev	GGCTGTTGTCATACTTCTCATGG	59.38		

8.2.2.8 FACS

Fluorescence-activated cell sorting (FACS) was planned to quantify the purity of the cell population. However, because of the change in direction in my project, this part was optimised by Miriam Rol Garcia.

Nonetheless, the idea was to compare undifferentiated cells with differentiated cells and CMs from a purified population. Markers would be Sox and Nanog as stem cell marker and cTnnT as marker for differentiated CMs.

8.2.3 Results

8.2.3.1 HiPSC quality control

To assess the stemness of the hiPSCs, cells were fixed and stained for the stem cell markers Sox2, Nanog and Oct4. The results are shown in Figure 8.7 and confirmed expression of these stem cell markers.

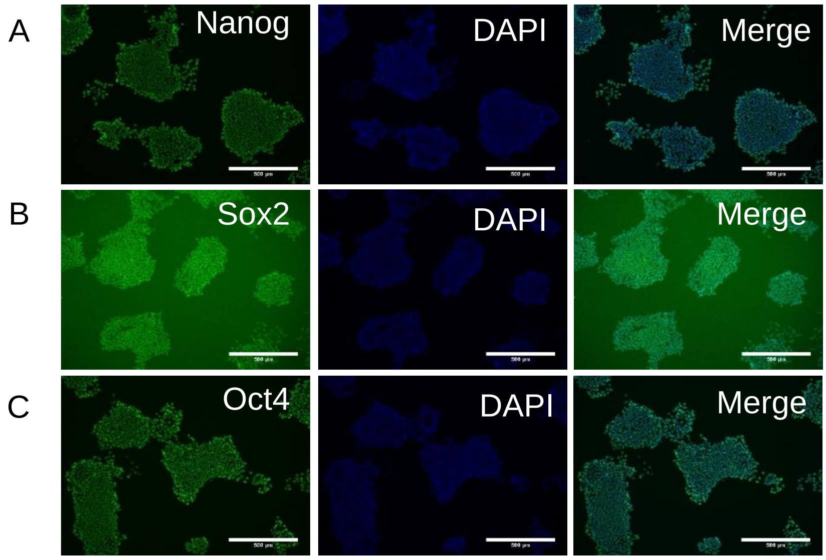

Figure 8.7 Immunofluorescent staining for stem cell markers.
The markers assessed were Nanog (A), Sox2 (B) and Oct4 (C) (left) and for the nuclear stain (DAPI, middle). Merged images are shown on the right. Scalebar represents 500 µm.

8.2.3.2 Optimization of the differentiation protocol: cell seeding densities and CHIR concentration

To optimize the cell seeding density for cardiac differentiation, three different cell densities were tested, namely 24,000 cells/cm^2 (24k), 36,000 cells/cm^2 (36k) and 48,000 cells/cm^2(48k). The confluency is important when starting the differentiation protocol. Underconfluency or overconfluency may result in no or suboptimal cardiac differentiation. In Figure 8.8, the confluency of both the 36k and 48k group is too dense on day 0, therefore, these cell seeding densities are too high and will most likely not result in a good cardiac cell population.

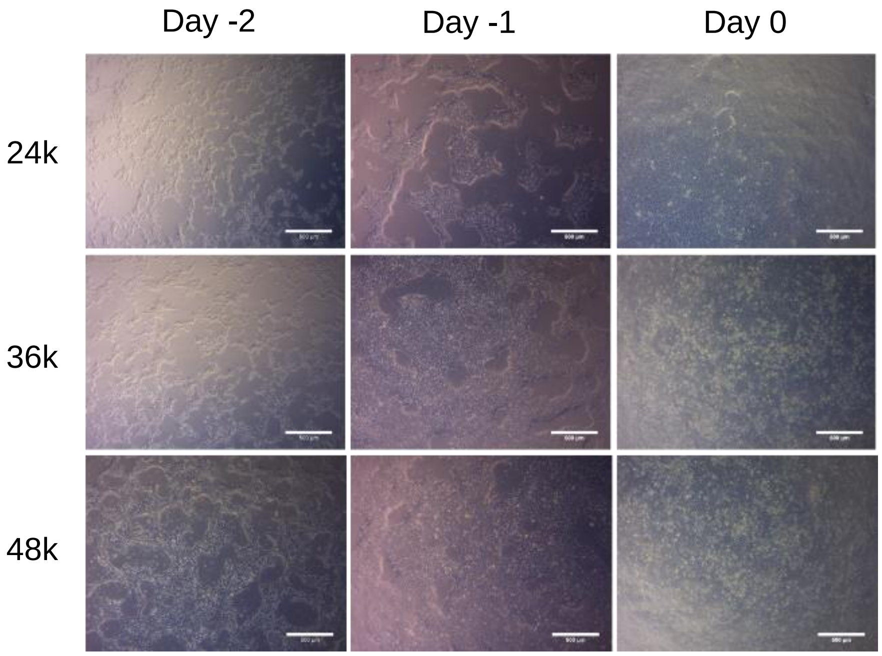

Figure 8.8 Assessment of three different cell seeding densities as preparation for hiPSC differentiation towards CMs.
Cell densities tested were 24,000 cells/cm^2 (24k), 36,000 cells/cm^2 (36k) and 48,000 cells/cm^2 (48k). Scalebar represents 500 µm.

On day 1, Wnt signalling is activated using CHIR (day 0), however, the correct concentration needs to be optimized. Therefore, 4 concentrations of CHIR were assessed, namely 6, 8, 10 and 12 µM simultaneously with the 3 different cell densities mentioned before. One day after Wnt activation, slight differences can be observed between groups as shown in Figure 8.9A. For all three cell densities, 12 µM showed small openings in the monolayer. This was also visible in the 24k group with 10 µM CHIR. The rest of the monolayers looked very confluent. On day 4, on day after inhibiting the Wnt signalling pathway, clear differences were observed between the wells. The groups that showed small open spots within the monolayers now show distinct patterns as shown in Figure 8.9B. The other groups do not show these patters at all or in a more faded fashion. Finally, from this optimization experiment, only 2 conditions resulted in long-term beating, namely 24k and 36k with 12 µM CHIR. In Figure 8.11A

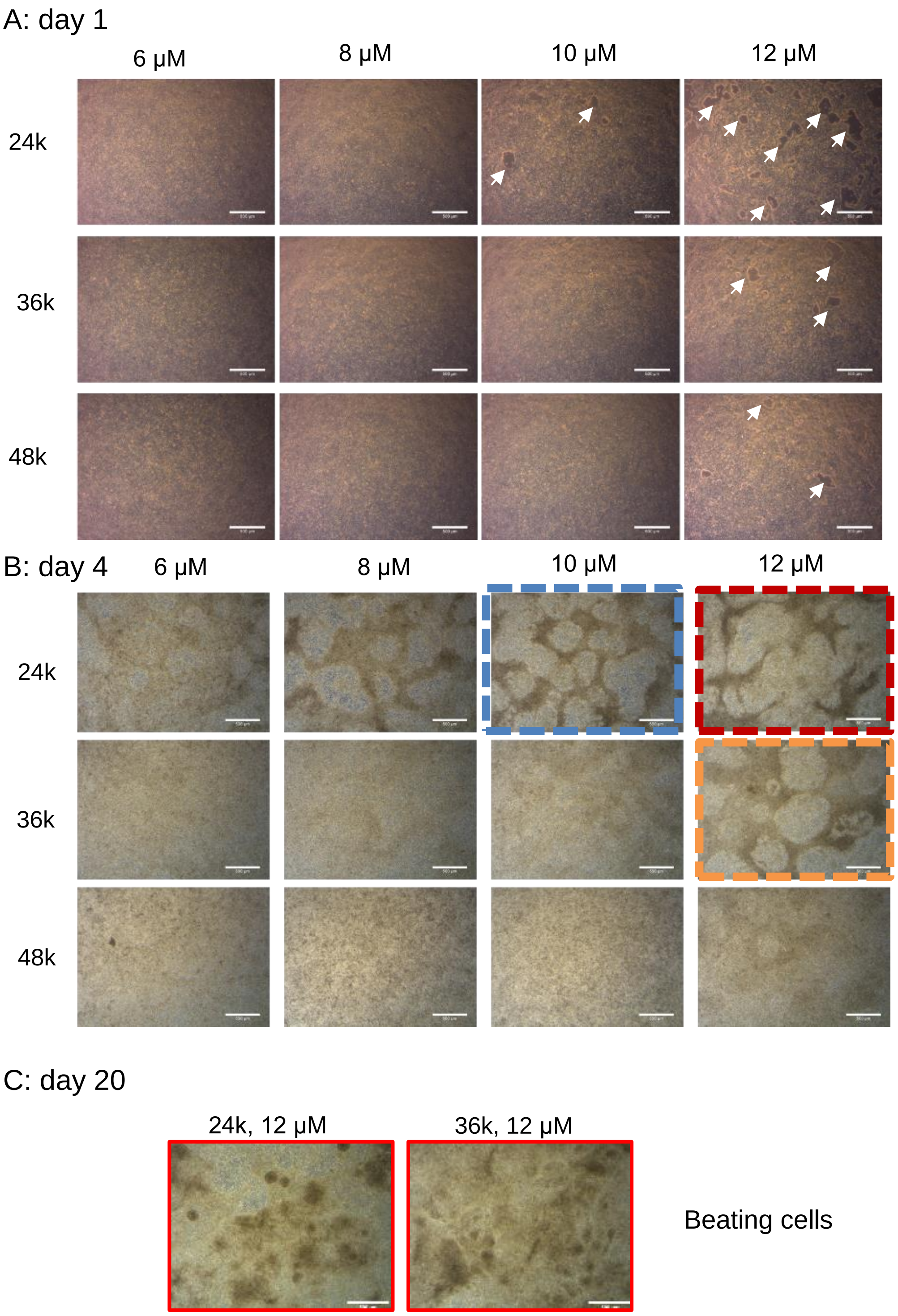

Figure 8.9 Assessment of three different CHIR concentrations and cell seeding densities. Brightfield images taken on day 1 (A), day 4 (B) and day 20 (C) from the start of the differentiation process. The concentrations tested were 6 μM, 8 μM, 10 μM and 12 μM along with the 24k, 36k and 48k cells/cm^2. Arrows indicate small openings within the monolayer. Black box = same wells as in (C and Figure Figure 8.10). Red boxes (C) = cells are beating. Coloured boxes (B): colours are linked to the colours used in Figure 8.10. Scalebar = 500 μm.

8.2.3.3 Replating of hiPSC-CMs

Now optimal conditions for cardiac differentiation of hiPSCs were found and resulted in beating cardiomyocytes, replating of cells is needed in order to use them for experimental procedures. Cells from the two conditions resulting in beating CMs (24k 12 µM and 36k 12 µM) and from one extra well that showed minor beating (24k 10 µM), were detached and replated in 4 different replating densities, namely 40k, 60k, 80k and 100k cells/cm^2. Here, the 80k and 100k groups correspond with the cell densities used for commercial hiPSC-CMs. The results are shown in Figure 8.10. All cell seeding densities resulted in beating cardiomyocytes for the two best conditions (24k 12 µM and 36k 12 µM). Additionally, from the four densities tested, 80k and 100k cells/cm^2 resulted in a confluent monolayer. Unfortunately, the third condition (24k, 10 µM), did not result in a beating monolayer for any of the cell densities.

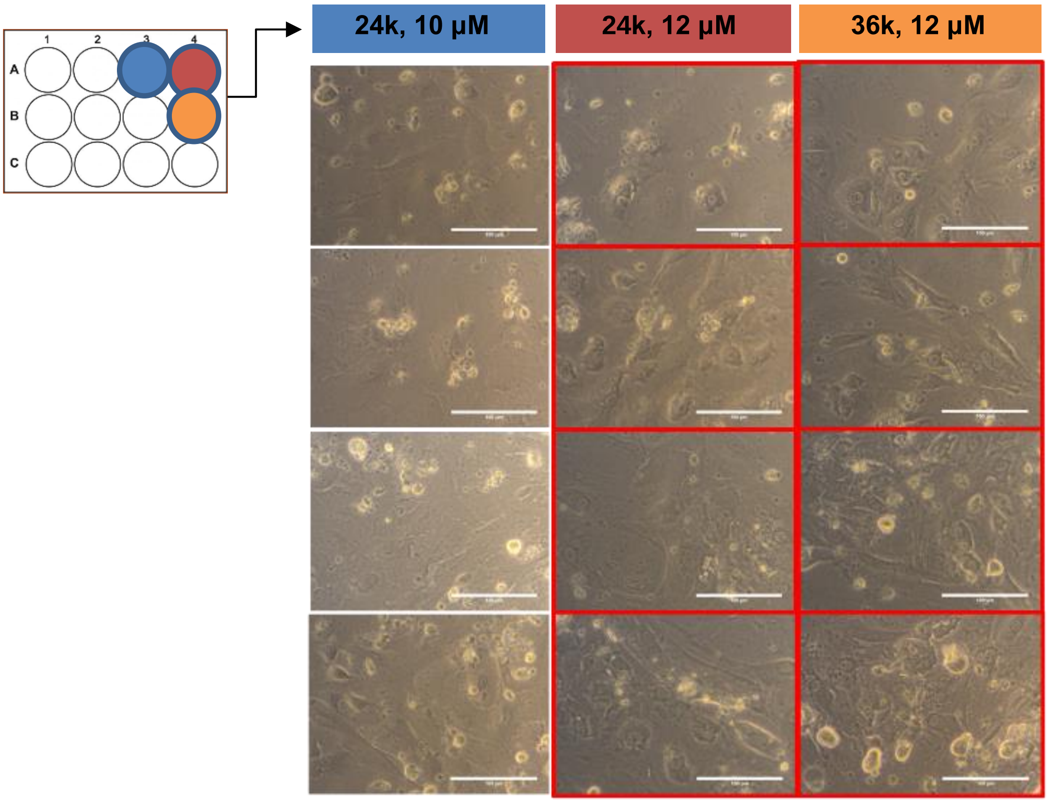

Figure 8.10 Brightfield images of replated hiPSC-CMs.
Images were taken on day 6 after replating. HiPSC-CMs were replated on 40 of the differentiation. Scalebar represents 100 µm. Red boxes indicate cells are beating.

8.2.4 Discussion and conclusion

Culture of a hiPSC and hiPSC-CM line can be a good alternative for commercially available hiPSC-CMs, especially when the cells are genetically modified with a GCaMP6f. During a relatively short amount of time, a hiPSC culture lab was set-up where they were successfully differentiated into cardiomyocytes. A short overview is shown in Figure 8.11.

Unfortunately, the amount of time and resources that are needed for the maintenance, differentiation processes, quality control and assessment was underestimated. Half a year into this direction we realized that the focus to answer the main aim of my thesis was lost and it was therefore decided to stop using/culturing these cells to go back to the commercial cell lines. Nonetheless, all the work is continued by Miriam Rol Garcia, who optimized the differentiation protocols further. Other colleagues are currently working in the hiPSC lab to improve the process further.

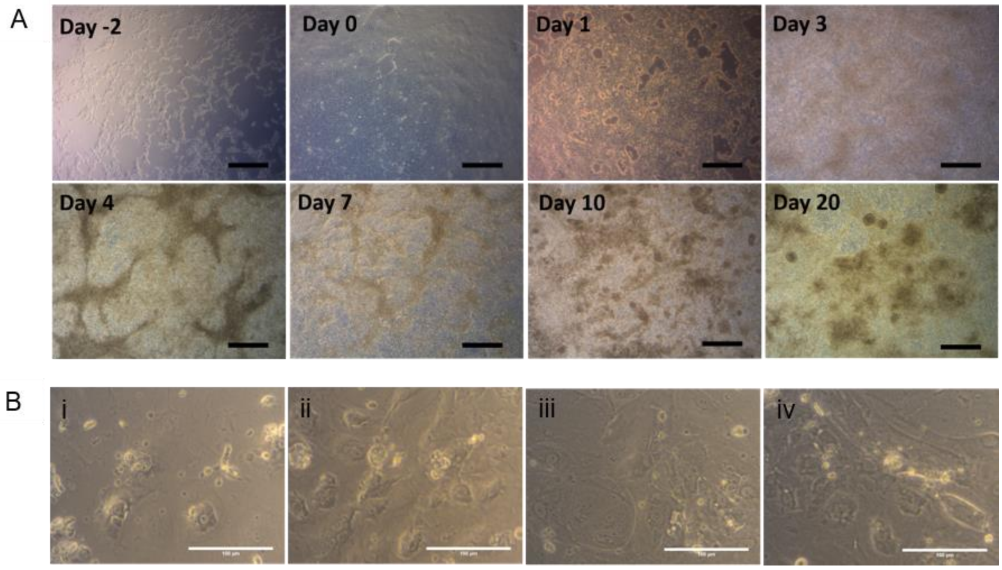

Figure 8.11 Overview of hiPSC and hiPSC-CM differentiation and replating processes. A) Brightfield images showing the morphological changes in time during the cardiac differentiation phases of hiPSCs. B) Brightfield images showing the morphology and spreading of hiPSC-CM after replating. HiPSC-CMs were replated in different cell densities: 40,000 cells/cm^2 (i), 60,000 cells/cm^2 (ii), 80,000 cells/cm^2 (iii) and 100,000 cells/cm^2 (iv). Cells were assessed on day 6 post-replating Scalebar is 100 µm.

Reference list

2020. *RCP Hydrogels based on collagen type 1* [Online]. https://www.fujifilmcellmatrix.com/hydrogels/hydrogels-applications: Fujifilm Manufacturing Europe B.V. [Accessed May 2021].

Allen, D. G., Lee, J. A. & Smith, G. L. 1989. The consequences of simulated ischaemia on intracellular Ca2+ and tension in isolated ferret ventricular muscle. *J Physiol,* 410**,** 297-323.

Antia, M., Baneyx, G., Kubow, K. E. & Vogel, V. 2008. Fibronectin in aging extracellular matrix fibrils is progressively unfolded by cells and elicits an enhanced rigidity response. *Faraday Discuss,* 139**,** 229-49; discussion 309-25, 419-20.

Antzelevitch, C. & Fish, J. 2001. Electrical heterogeneity within the ventricular wall. *Basic Res Cardiol,* 96**,** 517-27.

Antzelevitch, C., Sicouri, S., Litovsky, S. H., Lukas, A., Krishnan, S. C., Di Diego, J. M., Gintant, G. A. & Liu, D. W. 1991. Heterogeneity within the ventricular wall. Electrophysiology and pharmacology of epicardial, endocardial, and M cells. *Circ Res,* 69**,** 1427-49.

Asakura, K., Hayashi, S., Ojima, A., Taniguchi, T., Miyamoto, N., Nakamori, C., Nagasawa, C., Kitamura, T., Osada, T., Honda, Y., Kasai, C., Ando, H., Kanda, Y., Sekino, Y. & Sawada, K. 2015. Improvement of acquisition and analysis methods in multi-electrode array experiments with iPS cell-derived cardiomyocytes. *J Pharmacol Toxicol Methods,* 75**,** 17-26.

Asher, D. M. 1999. The transmissible spongiform encephalopathy agents: concerns and responses of United States regulatory agencies in maintaining the safety of biologics. *Developments in biological standardization,* 100**,** 103-118.

Au - Dewitt, E. S., Au - Black, K. J. & Au - Kheir, J. N. 2016. Rodent Working Heart Model for the Study of Myocardial Performance and Oxygen Consumption. *JoVE***,** e54149.

Baek, J., Cho, Y., Park, H.-J., Choi, G., Lee, J. S., Lee, M., Yu, S. J., Cho, S.-W., Lee, E. & Im, S. G. 2020. A Surface-Tailoring Method for Rapid Non-Thermosensitive Cell-Sheet Engineering via Functional Polymer Coatings. *Advanced Materials,* 32**,** 1907225.

Bar, A. & Cohen, S. 2020. Inducing Endogenous Cardiac Regeneration: Can Biomaterials Connect the Dots? *Frontiers in bioengineering and biotechnology,* 8**,** 126-126.

Barczyk, M., Carracedo, S. & Gullberg, D. 2010. Integrins. *Cell Tissue Res,* 339**,** 269-80.

Bers, D. M. 2002. Cardiac excitation-contraction coupling. *Nature,* 415**,** 198-205.

Bers, D. M., Bridge, J. H. & Spitzer, K. W. 1989. Intracellular Ca2+ transients during rapid cooling contractures in guinea-pig ventricular myocytes. *The Journal of Physiology,* 417**,** 537-553.

Blinova, K., Dang, Q., Millard, D., Smith, G., Pierson, J., Guo, L., Brock, M., Lu, H. R., Kraushaar, U., Zeng, H., Shi, H., Zhang, X., Sawada, K., Osada, T., Kanda, Y., Sekino, Y., Pang, L., Feaster, T. K., Kettenhofen, R., Stockbridge, N., Strauss, D. G. & Gintant, G. 2018. International Multisite Study of Human-Induced Pluripotent Stem Cell-Derived Cardiomyocytes for Drug Proarrhythmic Potential Assessment. *Cell Rep,* 24**,** 3582-3592.

Boothe, S. D., Myers, J. D., Pok, S., Sun, J., Xi, Y., Nieto, R. M., Cheng, J. & Jacot, J. G. 2016. The Effect of Substrate Stiffness on Cardiomyocyte Action Potentials. *Cell Biochem Biophys,* 74**,** 527-535.

Bootman, M. D., Rietdorf, K., Collins, T., Walker, S. & Sanderson, M. 2013. Ca2+-sensitive fluorescent dyes and intracellular Ca2+ imaging. *Cold Spring Harb Protoc,* 2013**,** 83-99.

Braam, B. F. S. 2019. *RE: Discontinuation Cor.4U cardiomyocyte products.* Type to Lab, S.

Breckwoldt, K., Letuffe-Brenière, D., Mannhardt, I., Schulze, T., Ulmer, B., Werner, T., Benzin, A., Klampe, B., Reinsch, M. C., Laufer, S., Shibamiya, A., Prondzynski, M., Mearini, G., Schade, D., Fuchs, S., Neuber, C., Krämer, E., Saleem, U., Schulze, M. L., Rodriguez, M. L., Eschenhagen, T. & Hansen, A. 2017. Differentiation of cardiomyocytes and generation of human engineered heart tissue. *Nat Protoc,* 12**,** 1177-1197.

Buikema, J. W., Lee, S., Goodyer, W. R., Maas, R. G., Chirikian, O., Li, G., Miao, Y., Paige, S. L., Lee, D., Wu, H., Paik, D. T., Rhee, S., Tian, L., Galdos, F. X., Puluca, N., Beyersdorf, B., Hu, J., Beck, A., Venkamatran, S., Swami, S., Wijnker, P., Schuldt, M., Dorsch, L. M., Van Mil, A., Red-Horse, K., Wu, J. Y., Geisen, C., Hesse, M., Serpooshan, V., Jovinge, S., Fleischmann, B. K., Doevendans, P. A., Van Der Velden, J., Garcia, K. C., Wu, J. C., Sluijter, J. P. G. & Wu, S. M. 2020. Wnt Activation and Reduced Cell-Cell Contact Synergistically Induce Massive Expansion of Functional Human iPSC-Derived Cardiomyocytes. *Cell Stem Cell,* 27**,** 50-63.e5.

Burgess, K. A., Frati, C., Meade, K., Gao, J., Castillo Diaz, L., Madeddu, D., Graiani, G., Cavalli, S., Miller, A. F., Oceandy, D., Quaini, F. & Saiani, A. 2021. Functionalised peptide hydrogel for the delivery of cardiac progenitor cells. *Materials Science and Engineering: C,* 119**,** 111539.

Burridge, P. W., Holmström, A. & Wu, J. C. 2015. Chemically Defined Culture and Cardiomyocyte Differentiation of Human Pluripotent Stem Cells. *Curr Protoc Hum Genet,* 87**,** 21.3.1-15.

Cerignoli, F., Charlot, D., Whittaker, R., Ingermanson, R., Gehalot, P., Savchenko, A., Gallacher, D. J., Towart, R., Price, J. H., Mcdonough, P. M. & Mercola, M. 2012. High throughput measurement of Ca^{2+} dynamics for drug risk assessment in human stem cell-derived cardiomyocytes by kinetic image cytometry. *J Pharmacol Toxicol Methods,* 66**,** 246-56.

Chen, G., Li, S., Karakikes, I., Ren, L., Chow, M. Z., Chopra, A., Keung, W., Yan, B., Chan, C. W., Costa, K. D., Kong, C. W., Hajjar, R. J., Chen, C. S. & Li, R. A. 2015. Phospholamban as a crucial determinant of the inotropic response of human pluripotent stem cell-derived ventricular cardiomyocytes and engineered 3-dimensional tissue constructs. *Circ Arrhythm Electrophysiol,* 8**,** 193-202.

Chen, T. W., Wardill, T. J., Sun, Y., Pulver, S. R., Renninger, S. L., Baohan, A., Schreiter, E. R., Kerr, R. A., Orger, M. B., Jayaraman, V., Looger, L. L., Svoboda, K. & Kim, D. S. 2013. Ultrasensitive fluorescent proteins for imaging neuronal activity. *Nature,* 499**,** 295-300.

Chen-Izu, Y. & Izu, L. T. 2017. Mechano-chemo-transduction in cardiac myocytes. *J Physiol,* 595**,** 3949-3958.

Chong, J. J., Yang, X., Don, C. W., Minami, E., Liu, Y. W., Weyers, J. J., Mahoney, W. M., Van Biber, B., Cook, S. M., Palpant, N. J., Gantz, J. A., Fugate, J. A., Muskheli, V., Gough, G. M., Vogel, K. W., Astley, C. A., Hotchkiss, C. E., Baldessari, A., Pabon, L., Reinecke, H., Gill, E. A., Nelson, V., Kiem, H. P., Laflamme, M. A. & Murry, C. E. 2014. Human embryonic-stem-cell-derived cardiomyocytes regenerate non-human primate hearts. *Nature,* 510**,** 273-7.

Chopra, A., Tabdanov, E., Patel, H., Janmey, P. A. & Kresh, J. Y. 2011. Cardiac myocyte remodeling mediated by N-cadherin-dependent mechanosensing. *Am J Physiol Heart Circ Physiol,* 300**,** H1252-66.

Chow, A., Stuckey, D. J., Kidher, E., Rocco, M., Jabbour, R. J., Mansfield, C. A., Darzi, A., Harding, S. E., Stevens, M. M. & Athanasiou, T. 2017. Human Induced Pluripotent Stem Cell-Derived Cardiomyocyte Encapsulating Bioactive Hydrogels Improve Rat Heart Function Post Myocardial Infarction. *Stem Cell Reports,* 9**,** 1415-1422.

Daniels, M., Noble, M. I., Ter Keurs, H. E. & Wohlfart, B. 1984. Velocity of sarcomere shortening in rat cardiac muscle: relationship to force, sarcomere length, calcium and time. *The Journal of physiology,* 355**,** 367-381.

Del Rio, A., Perez-Jimenez, R., Liu, R., Roca-Cusachs, P., Fernandez, J. M. & Sheetz, M. P. 2009. Stretching single talin rod molecules activates vinculin binding. *Science,* 323**,** 638-41.

Dewald, O., Ren, G., Duerr, G. D., Zoerlein, M., Klemm, C., Gersch, C., Tincey, S., Michael, L. H., Entman, M. L. & Frangogiannis, N. G. 2004. Of mice and dogs: species-specific differences in the inflammatory response following myocardial infarction. *Am J Pathol,* 164**,** 665-77.

Dietrichs, E. S., Mcglynn, K., Allan, A., Connolly, A., Bishop, M., Burton, F., Kettlewell, S., Myles, R., Tveita, T. & Smith, G. L. 2020. Moderate but not severe hypothermia causes pro-arrhythmic changes in cardiac electrophysiology. *Cardiovascular Research,* 116**,** 2081-2090.

Dworak, A., Utrata-Wesołek, A., Szweda, D., Kowalczuk, A., Trzebicka, B., Anioł, J., Sieroń, A. L., Klama-Baryła, A. & Kawecki, M. 2013. Poly[tri(ethylene glycol) ethyl ether methacrylate]-coated surfaces for controlled fibroblasts culturing. *ACS Appl Mater Interfaces,* 5**,** 2197-207.

Ellermann, C., Wolfes, J., Eckardt, L. & Frommeyer, G. 2020. Role of the rabbit whole-heart model for electrophysiologic safety pharmacology of non-cardiovascular drugs. *EP Europace*.

Engler, A. J., Carag-Krieger, C., Johnson, C. P., Raab, M., Tang, H. Y., Speicher, D. W., Sanger, J. W., Sanger, J. M. & Discher, D. E. 2008. Embryonic cardiomyocytes beat best on a matrix with heart-like elasticity: scar-like rigidity inhibits beating. *J Cell Sci,* 121**,** 3794-802.

Feaster, T. K., Cadar, A. G., Wang, L., Williams, C. H., Chun, Y. W., Hempel, J. E., Bloodworth, N., Merryman, W. D., Lim, C. C., Wu, J. C., Knollmann, B. C. & Hong, C. C. 2015. Matrigel Mattress: A Method for the Generation of Single Contracting Human-Induced Pluripotent Stem Cell-Derived Cardiomyocytes. *Circ Res,* 117**,** 995-1000.

Fiedler, L. R., Chapman, K., Xie, M., Maifoshie, E., Jenkins, M., Golforoush, P. A., Bellahcene, M., Noseda, M., Faust, D., Jarvis, A., Newton, G., Paiva, M. A., Harada, M., Stuckey, D. J., Song, W., Habib, J., Narasimhan, P., Aqil, R., Sanmugalingam, D., Yan, R., Pavanello, L., Sano, M., Wang, S. C., Sampson, R. D., Kanayaganam, S., Taffet, G. E., Michael, L. H., Entman, M. L., Tan, T. H., Harding, S. E., Low, C. M. R., Tralau-Stewart, C., Perrior, T. & Schneider, M. D. 2019. MAP4K4 Inhibition Promotes Survival of Human Stem Cell-Derived Cardiomyocytes and Reduces Infarct Size In Vivo. *Cell Stem Cell,* 24**,** 579-591.e12.

Fluhler, E., Burnham, V. G. & Loew, L. M. 1985. Spectra, membrane binding, and potentiometric responses of new charge shift probes. *Biochemistry,* 24**,** 5749-55.

Frangogiannis, N. G. 2014. The inflammatory response in myocardial injury, repair, and remodelling. *Nat Rev Cardiol,* 11**,** 255-65.

Frangogiannis, N. G. 2015. Pathophysiology of Myocardial Infarction. *Compr Physiol,* 5**,** 1841-75.

Frangogiannis, N. G. 2017. The extracellular matrix in myocardial injury, repair, and remodeling. *J Clin Invest,* 127**,** 1600-1612.

Fujita, J., Tohyama, S., Kishino, Y., Okada, M. & Morita, Y. 2019. Concise Review: Genetic and Epigenetic Regulation of Cardiac Differentiation from Human Pluripotent Stem Cells. *STEM CELLS,* 37**,** 992-1002.

Gao, L., Gregorich, Z. R., Zhu, W., Mattapally, S., Oduk, Y., Lou, X., Kannappan, R., Borovjagin, A. V., Walcott, G. P., Pollard, A. E., Fast, V. G., Hu, X., Lloyd, S. G., Ge, Y. & Zhang, J. 2018. Large Cardiac Muscle Patches Engineered From Human Induced-Pluripotent Stem Cell-Derived Cardiac Cells Improve Recovery From Myocardial Infarction in Swine. *Circulation,* 137**,** 1712-1730.

Gao, X. M., White, D. A., Dart, A. M. & Du, X. J. 2012. Post-infarct cardiac rupture: recent insights on pathogenesis and therapeutic interventions. *Pharmacol Ther,* 134**,** 156-79.

Garg, P., Garg, V., Shrestha, R., Sanguinetti Michael, C., Kamp Timothy, J. & Wu Joseph, C. 2018. Human Induced Pluripotent Stem Cell–Derived Cardiomyocytes as Models for Cardiac Channelopathies. *Circulation Research,* 123**,** 224-243.

Gee, K. R., Brown, K. A., Chen, W. N. U., Bishop-Stewart, J., Gray, D. & Johnson, I. 2000. Chemical and physiological characterization of fluo-4 Ca2+-indicator dyes. *Cell Calcium,* 27**,** 97-106.

Geiger, B., Spatz, J. P. & Bershadsky, A. D. 2009. Environmental sensing through focal adhesions. *Nat Rev Mol Cell Biol,* 10**,** 21-33.

Gerbin, K. A., Yang, X., Murry, C. E. & Coulombe, K. L. 2015. Enhanced Electrical Integration of Engineered Human Myocardium via Intramyocardial versus Epicardial Delivery in Infarcted Rat Hearts. *PLoS One,* 10**,** e0131446.

Giepmans, B. N. 2004. Gap junctions and connexin-interacting proteins. *Cardiovasc Res,* 62**,** 233-45.

Grant Augustus, O. 2009. Cardiac Ion Channels. *Circulation: Arrhythmia and Electrophysiology,* 2**,** 185-194.

Gutstein, D. E., Liu, F.-Y., Meyers, M. B., Choo, A. & Fishman, G. I. 2003. The organization of adherens junctions and desmosomes at the cardiac intercalated disc is independent of gap junctions. *Journal of Cell Science,* 116**,** 875.

Haraguchi, Y., Shimizu, T., Sasagawa, T., Sekine, H., Sakaguchi, K., Kikuchi, T., Sekine, W., Sekiya, S., Yamato, M., Umezu, M. & Okano, T. 2012. Fabrication of functional three-dimensional tissues by stacking cell sheets in vitro. *Nat Protoc,* 7**,** 850-8.

Harrison, S. M. & Bers, D. M. 1989. Influence of temperature on the calcium sensitivity of the myofilaments of skinned ventricular muscle from the rabbit. *The Journal of general physiology,* 93**,** 411-428.

Helassa, N., Podor, B., Fine, A. & Török, K. 2016. Design and mechanistic insight into ultrafast calcium indicators for monitoring intracellular calcium dynamics. *Sci Rep,* 6**,** 38276.

Heras-Bautista, C. O., Katsen-Globa, A., Schloerer, N. E., Dieluweit, S., Abd El Aziz, O. M., Peinkofer, G., Attia, W. A., Khalil, M., Brockmeier, K., Hescheler, J. & Pfannkuche, K. 2014. The influence of physiological matrix conditions on permanent culture of induced pluripotent stem cell-derived cardiomyocytes. *Biomaterials,* 35**,** 7374-85.

Herron, T. J., Rocha, A. M., Campbell, K. F., Ponce-Balbuena, D., Willis, B. C., Guerrero-Serna, G., Liu, Q., Klos, M., Musa, H., Zarzoso, M., Bizy, A., Furness, J., Anumonwo, J., Mironov, S. & Jalife, J. 2016. Extracellular Matrix-Mediated Maturation of Human Pluripotent Stem Cell-Derived Cardiac Monolayer Structure and Electrophysiological Function. *Circ Arrhythm Electrophysiol,* 9**,** e003638.

Holmgren, G., Ghosheh, N., Zeng, X., Bogestål, Y., Sartipy, P. & Synnergren, J. 2015. Identification of stable reference genes in differentiating human pluripotent stem cells. *Physiol Genomics,* 47**,** 232-9.

Honda, A., Hirose, M., Hatori, M., Matoba, S., Miyoshi, H., Inoue, K. & Ogura, A. 2010. Generation of induced pluripotent stem cells in rabbits: potential experimental models for human regenerative medicine. *J Biol Chem,* 285**,** 31362-9.

Huang, Y. L., Walker, A. S. & Miller, E. W. 2015. A Photostable Silicon Rhodamine Platform for Optical Voltage Sensing. *J Am Chem Soc,* 137**,** 10767-76.

Huethorst, E., Hortigon, M., Zamora-Rodriguez, V., Reynolds, P. M., Burton, F., Smith, G. & Gadegaard, N. 2016. Enhanced Human-Induced Pluripotent Stem Cell Derived Cardiomyocyte Maturation Using a Dual Microgradient Substrate. *ACS Biomater Sci Eng,* 2**,** 2231-2239.

Huethorst, E., Mortensen, P., Simitev, R. D., Gao, H., Pohjolainen, L., Talman, V., Ruskoaho, H., Burton, F. L., Gadegaard, N. & Smith, G. L. 2021. Conventional rigid 2D substrates cause complex contractile signals in monolayers of human induced pluripotent stem cell-derived cardiomyocytes. *The Journal of Physiology,* n/a.

Huo, J., Kamalakar, A., Yang, X., Word, B., Stockbridge, N., Lyn-Cook, B. & Pang, L. 2017. Evaluation of Batch Variations in Induced Pluripotent Stem Cell-Derived Human Cardiomyocytes from 2 Major Suppliers. *Toxicol Sci,* 156**,** 25-38.

Hwang, H. S., Kryshtal, D. O., Feaster, T. K., Sanchez-Freire, V., Zhang, J., Kamp, T. J., Hong, C. C., Wu, J. C. & Knollmann, B. C. 2015. Comparable calcium handling of human iPSC-derived cardiomyocytes generated by multiple laboratories. *J Mol Cell Cardiol,* 85**,** 79-88.

Ichimura, H., Kadota, S., Kashihara, T., Yamada, M., Ito, K., Kobayashi, H., Tanaka, Y., Shiba, N., Chuma, S., Tohyama, S., Seto, T., Okada, K., Kuwahara, K. & Shiba, Y. 2020. Increased predominance of the matured ventricular subtype in embryonic stem cell-derived cardiomyocytes in vivo. *Scientific Reports,* 10**,** 11883.

Iskratsch, T., Wolfenson, H. & Sheetz, M. P. 2014. Appreciating force and shape-the rise of mechanotransduction in cell biology. *Nat Rev Mol Cell Biol.* England.

Isorni, M. A., Casanova, A., Piquet, J., Bellamy, V., Pignon, C., Puymirat, E. & Menasche, P. 2015. Comparative Analysis of Methods to Induce Myocardial Infarction in a Closed-Chest Rabbit Model. *Biomed Res Int,* 2015**,** 893051.

Itzhaki, I., Rapoport, S., Huber, I., Mizrahi, I., Zwi-Dantsis, L., Arbel, G., Schiller, J. & Gepstein, L. 2011. Calcium handling in human induced pluripotent stem cell derived cardiomyocytes. *PLoS One,* 6**,** e18037.

Izu, L. T., Kohl, P., Boyden, P. A., Miura, M., Banyasz, T., Chiamvimonvat, N., Trayanova, N., Bers, D. M. & Chen-Izu, Y. 2019. Mechano-electric and mechano-chemo-transduction in cardiomyocytes. *J Physiol*.

Jabbour, R. J., Owen, T. J., Pandey, P., Reinsch, M., Wang, B., King, O., Couch, L. S., Pantou, D., Pitcher, D. S., Chowdhury, R. A., Pitoulis, F. G., Handa, B. S., Kit-Anan, W., Perbellini, F., Myles, R. C., Stuckey, D. J., Dunne, M., Shanmuganathan, M., Peters, N. S., Ng, F. S., Weinberger, F., Terracciano, C. M., Smith, G. L., Eschenhagen, T. & Harding, S. E. 2021. In vivo grafting of large engineered heart tissue patches for cardiac repair. *JCI Insight,* 6.

Jackman, C. P., Ganapathi, A. M., Asfour, H., Qian, Y., Allen, B. W., Li, Y. & Bursac, N. 2018. Engineered cardiac tissue patch maintains structural and electrical properties after epicardial implantation. *Biomaterials,* 159**,** 48-58.

Jackson, B. M., Gorman, J. H., Salgo, I. S., Moainie, S. L., Plappert, T., St. John-Sutton, M., Edmunds, L. H. & Gorman, R. C. 2003. Border zone geometry increases wall stress after myocardial infarction: contrast echocardiographic assessment. *American Journal of Physiology-Heart and Circulatory Physiology,* 284**,** H475-H479.

Jacot, J. G., Mcculloch, A. D. & Omens, J. H. 2008. Substrate stiffness affects the functional maturation of neonatal rat ventricular myocytes. *Biophys J,* 95**,** 3479-87.

Jia, J., Coyle, R. C., Richards, D. J., Berry, C. L., Barrs, R. W., Biggs, J., James Chou, C., Trusk, T. C. & Mei, Y. 2016. Development of peptide-functionalized synthetic hydrogel microarrays for stem cell and tissue engineering applications. *Acta Biomater,* 45**,** 110-120.

Jugdutt, B. I., Joljart, M. J. & Khan, M. I. 1996. Rate of collagen deposition during healing and ventricular remodeling after myocardial infarction in rat and dog models. *Circulation,* 94**,** 94-101.

Kadota, S., Pabon, L., Reinecke, H. & Murry, C. E. 2017. In Vivo Maturation of Human Induced Pluripotent Stem Cell-Derived Cardiomyocytes in Neonatal and Adult Rat Hearts. *Stem Cell Reports,* 8**,** 278-289.

Kadota, S., Tanaka, Y. & Shiba, Y. 2020. Heart regeneration using pluripotent stem cells. *J Cardiol,* 76**,** 459-463.

Kaestner, L., Scholz, A., Tian, Q., Ruppenthal, S., Tabellion, W., Wiesen, K., Katus, H. A., Müller, O. J., Kotlikoff, M. I. & Lipp, P. 2014. Genetically encoded Ca2+ indicators in cardiac myocytes. *Circ Res,* 114**,** 1623-39.

Kane, C., Couch, L. & Terracciano, C. M. 2015. Excitation-contraction coupling of human induced pluripotent stem cell-derived cardiomyocytes. *Front Cell Dev Biol,* 3**,** 59.

Karakikes, I., Ameen, M., Termglinchan, V. & Wu, J. C. 2015. Human induced pluripotent stem cell-derived cardiomyocytes: insights into molecular, cellular, and functional phenotypes. *Circ Res,* 117**,** 80-8.

Karbassi, E., Fenix, A., Marchiano, S., Muraoka, N., Nakamura, K., Yang, X. & Murry, C. E. 2020. Cardiomyocyte maturation: advances in knowledge and implications for regenerative medicine. *Nature Reviews Cardiology,* 17**,** 341-359.

Kawecki, M., Kraut, M., Klama-Baryła, A., Łabuś, W., Kitala, D., Nowak, M., Glik, J., Sieroń, A. L., Utrata-Wesołek, A., Trzebicka, B., Dworak, A. & Szweda, D. 2016. Transfer of fibroblast sheets cultured on thermoresponsive dishes with membranes. *J Mater Sci Mater Med,* 27**,** 111.

Kehat, I., Khimovich, L., Caspi, O., Gepstein, A., Shofti, R., Arbel, G., Huber, I., Satin, J., Itskovitz-Eldor, J. & Gepstein, L. 2004. Electromechanical integration of cardiomyocytes derived from human embryonic stem cells. *Nat Biotechnol,* 22**,** 1282-9.

Kelly, A., Salerno, S., Connolly, A., Bishop, M., Charpentier, F., Stølen, T. & Smith, G. L. 2018. Normal interventricular differences in tissue architecture underlie right ventricular susceptibility to conduction abnormalities in a mouse model of Brugada syndrome. *Cardiovasc Res,* 114**,** 724-736.

Khan, M., Nickoloff, E., Abramova, T., Johnson, J., Verma, S. K., Krishnamurthy, P., Mackie, A. R., Vaughan, E., Garikipati, V. N., Benedict, C., Ramirez, V., Lambers, E., Ito, A., Gao, E., Misener, S., Luongo, T., Elrod, J., Qin, G., Houser, S. R., Koch, W. J. & Kishore, R. 2015. Embryonic stem cell-derived exosomes promote endogenous repair mechanisms and enhance cardiac function following myocardial infarction. *Circ Res,* 117**,** 52-64.

Kitala, D., Klama-Baryła, A., Kraut, M., Łabuś, W., Glik, J., Kawecki, M., Trzebicka, B., Dworak, A., Adamus-Włodarczyk, A., Komasa, J., Kadłubowski, S., Ulański, P. & Rosiak, J. M. 2020. Amniotic Stem Cells Cultured on Thermoresponsive Polymers Allow Obtaining a Full Cell Sheet. *Transplant Proc,* 52**,** 2198-2203.

Kléber, A. G. 1990. Consequences of acute ischemia for the electrical and mechanical function of the ventricular myocardium. A brief review. *Experientia,* 46**,** 1162-7.

Kopljar, I., Hermans, A. N., Teisman, A., Gallacher, D. J. & Lu, H. R. 2018. Impact of calcium-sensitive dyes on the beating properties and pharmacological responses of human iPS-derived cardiomyocytes using the calcium transient assay. *J Pharmacol Toxicol Methods,* 91**,** 80-86.

Kovács, M., Tóth, J., Hetényi, C., Málnási-Csizmadia, A. & Sellers, J. R. 2004. Mechanism of blebbistatin inhibition of myosin II. *J Biol Chem,* 279**,** 35557-63.

Kubow, K. E., Vukmirovic, R., Zhe, L., Klotzsch, E., Smith, M. L., Gourdon, D., Luna, S. & Vogel, V. 2015. Mechanical forces regulate the interactions of fibronectin and collagen I in extracellular matrix. *Nature Communications,* 6**,** 8026.

Lachaud, Q. 2019a. *Development of a medium-high throughput electrophysiology method to study cellular heterogeneity in the rabbit heart.* Doctor of Philosophy, University of Glasgow.

Lachaud, Q. 2019b. *Development of a medium-high throughput electrophysiology method to study cellular heterogeneity in the rabbit heart.* PhD, University of Glasgow.

Laflamme, M. A., Chen, K. Y., Naumova, A. V., Muskheli, V., Fugate, J. A., Dupras, S. K., Reinecke, H., Xu, C., Hassanipour, M., Police, S., O'sullivan, C., Collins, L., Chen, Y., Minami, E., Gill, E. A., Ueno, S., Yuan, C., Gold, J. & Murry, C. E. 2007. Cardiomyocytes derived from human embryonic stem cells in pro-survival factors enhance function of infarcted rat hearts. *Nat Biotechnol,* 25**,** 1015-24.

Langendorff, O. 1895. Untersuchungen am überlebenden Säugethierherzen. *Archiv für die gesamte Physiologie des Menschen und der Tiere,* 61**,** 291-332.

Legrice, I. J., Smaill, B. H., Chai, L. Z., Edgar, S. G., Gavin, J. B. & Hunter, P. J. 1995. Laminar structure of the heart: ventricular myocyte arrangement and connective tissue architecture in the dog. *Am J Physiol,* 269**,** H571-82.

Lemme, M., Ulmer, B. M., Lemoine, M. D., Zech, A. T. L., Flenner, F., Ravens, U., Reichenspurner, H., Rol-Garcia, M., Smith, G., Hansen, A., Christ, T. & Eschenhagen, T. 2018. Atrial-like Engineered Heart Tissue: An In Vitro Model of the Human Atrium. *Stem Cell Reports,* 11**,** 1378-1390.

Lemoine, M. D., Mannhardt, I., Breckwoldt, K., Prondzynski, M., Flenner, F., Ulmer, B., Hirt, M. N., Neuber, C., Horvath, A., Kloth, B., Reichenspurner, H., Willems, S., Hansen, A., Eschenhagen, T. & Christ,

T. 2017. Human iPSC-derived cardiomyocytes cultured in 3D engineered heart tissue show physiological upstroke velocity and sodium current density. *Sci Rep,* 7**,** 5464.

Lensink, M. A., Jongsma, K. R., Boers, S. N., Van Delden, J. J. M. & Bredenoord, A. L. 2021. Responsible Research with Human Tissues: The Need for Reciprocity Toward Both Collectives and Individuals. *Am J Bioeth,* 21**,** 75-78.

Lewandowski, J., Rozwadowska, N., Kolanowski, T. J., Malcher, A., Zimna, A., Rugowska, A., Fiedorowicz, K., Labedz, W., Kubaszewski, L., Chojnacka, K., Bednarek-Rajewska, K., Majewski, P. & Kurpisz, M. 2018. The impact of in vitro cell culture duration on the maturation of human cardiomyocytes derived from induced pluripotent stem cells of myogenic origin. *Cell Transplant,* 27**,** 1047-1067.

Li, A. H., Liu, P. P., Villarreal, F. J. & Garcia, R. A. 2014. Dynamic changes in myocardial matrix and relevance to disease: translational perspectives. *Circ Res,* 114**,** 916-27.

Li, J., Liu, Y., Jin, Y., Wang, R., Wang, J., Lu, S., Vanburen, V., Dostal, D. E., Zhang, S. L. & Peng, X. 2017. Essential role of Cdc42 in cardiomyocyte proliferation and cell-cell adhesion during heart development. *Dev Biol,* 421**,** 271-283.

Li, K., Wagner, L., Moctezuma-Ramirez, A., Vela, D. & Perin, E. 2021. A Robust Percutaneous Myocardial Infarction Model in Pigs and Its Effect on Left Ventricular Function. *J Cardiovasc Transl Res*.

Lian, X., Zhang, J., Azarin, S. M., Zhu, K., Hazeltine, L. B., Bao, X., Hsiao, C., Kamp, T. J. & Palecek, S. P. 2013. Directed cardiomyocyte differentiation from human pluripotent stem cells by modulating Wnt/β-catenin signaling under fully defined conditions. *Nat Protoc,* 8**,** 162-75.

Lieu, D. K., Liu, J., Siu, C. W., Mcnerney, G. P., Tse, H. F., Abu-Khalil, A., Huser, T. & Li, R. A. 2009. Absence of transverse tubules contributes to non-uniform Ca(2+) wavefronts in mouse and human embryonic stem cell-derived cardiomyocytes. *Stem Cells Dev,* 18**,** 1493-500.

Liu, J., Fu, J. D., Siu, C. W. & Li, R. A. 2007. Functional sarcoplasmic reticulum for calcium handling of human embryonic stem cell-derived cardiomyocytes: insights for driven maturation. *Stem Cells,* 25**,** 3038-44.

Liu, Y. W., Chen, B., Yang, X., Fugate, J. A., Kalucki, F. A., Futakuchi-Tsuchida, A., Couture, L., Vogel, K. W., Astley, C. A., Baldessari, A., Ogle, J., Don, C. W., Steinberg, Z. L., Seslar, S. P., Tuck, S. A., Tsuchida, H., Naumova, A. V., Dupras, S. K., Lyu, M. S., Lee, J., Hailey, D. W., Reinecke, H., Pabon, L., Fryer, B. H., Maclellan, W. R., Thies, R. S. & Murry, C. E. 2018. Human embryonic stem cell-derived cardiomyocytes restore function in infarcted hearts of non-human primates. *Nat Biotechnol,* 36**,** 597-605.

Lock, J. T., Parker, I. & Smith, I. F. 2015. A comparison of fluorescent Ca^{2+} indicators for imaging local Ca^{2+} signals in cultured cells. *Cell Calcium,* 58**,** 638-48.

Loen, V., Vos, M. A. & Van Der Heyden, M. A. G. 2021. The canine chronic atrioventricular block model in cardiovascular preclinical drug research. *British Journal of Pharmacology,* n/a.

Lou, Q., Li, W. & Efimov, I. R. 2012. The role of dynamic instability and wavelength in arrhythmia maintenance as revealed by panoramic imaging with blebbistatin vs. 2,3-butanedione monoxime. *Am J Physiol Heart Circ Physiol,* 302**,** H262-9.

Lundy, S. D., Zhu, W. Z., Regnier, M. & Laflamme, M. A. 2013. Structural and functional maturation of cardiomyocytes derived from human pluripotent stem cells. *Stem Cells Dev,* 22**,** 1991-2002.

Majid, Q. A., Fricker, A. T. R., Gregory, D. A., Davidenko, N., Hernandez Cruz, O., Jabbour, R. J., Owen, T. J., Basnett, P., Lukasiewicz, B., Stevens, M., Best, S., Cameron, R., Sinha, S., Harding, S. E. & Roy, I. 2020. Natural Biomaterials for Cardiac Tissue Engineering: A Highly Biocompatible Solution. *Frontiers in Cardiovascular Medicine,* 7**,** 192.

Mancuso, S. 2003. Stem cell research need not be carried out utilizing human embryos. *Reprod Biomed Online,* 6**,** 168-9.

Mannhardt, I., Saleem, U., Mosqueira, D., Loos, M. F., Ulmer, B. M., Lemoine, M. D., Larsson, C., Améen, C., De Korte, T., Vlaming, M. L. H., Harris, K., Clements, P., Denning, C., Hansen, A. & Eschenhagen, T. 2020. Comparison of 10 Control hPSC Lines for Drug Screening in an Engineered Heart Tissue Format. *Stem Cell Reports,* 15**,** 983-998.

Manring, H. R., Dorn, L. E., Ex-Willey, A., Accornero, F. & Ackermann, M. A. 2018. At the heart of inter- and intracellular signaling: the intercalated disc. *Biophys Rev,* 10**,** 961-971.

Maruthamuthu, V., Sabass, B., Schwarz, U. S. & Gardel, M. L. 2011. Cell-ECM traction force modulates endogenous tension at cell-cell contacts. *Proc Natl Acad Sci U S A,* 108**,** 4708-13.

Masumoto, H., Nakane, T., Tinney, J. P., Yuan, F., Ye, F., Kowalski, W. J., Minakata, K., Sakata, R., Yamashita, J. K. & Keller, B. B. 2016. The myocardial regenerative potential of three-dimensional engineered cardiac tissues composed of multiple human iPS cell-derived cardiovascular cell lineages. *Scientific Reports,* 6**,** 29933.

Matsuo, T., Masumoto, H., Tajima, S., Ikuno, T., Katayama, S., Minakata, K., Ikeda, T., Yamamizu, K., Tabata, Y., Sakata, R. & Yamashita, J. K. 2015a. Efficient long-term survival of cell grafts after myocardial infarction with thick viable cardiac tissue entirely from pluripotent stem cells. *Scientific Reports,* 5**,** 16842.

Matsuo, T., Masumoto, H., Tajima, S., Ikuno, T., Katayama, S., Minakata, K., Ikeda, T., Yamamizu, K., Tabata, Y., Sakata, R. & Yamashita, J. K. 2015b. Efficient long-term survival of cell grafts after myocardial infarction with thick viable cardiac tissue entirely from pluripotent stem cells. *Sci Rep,* 5**,** 16842.

Mcglynn, K. P. 2017. *The effect of hypothermia and rewarming on cardiac electrophysiology and mechanical function.* PhD, University of Glasgow.

Menasché, P. 2018. Cell therapy trials for heart regeneration - lessons learned and future directions. *Nat Rev Cardiol,* 15**,** 659-671.

Mesirca, P., Alig, J., Torrente, A. G., Müller, J. C., Marger, L., Rollin, A., Marquilly, C., Vincent, A., Dubel, S., Bidaud, I., Fernandez, A., Seniuk, A., Engeland, B., Singh, J., Miquerol, L., Ehmke, H., Eschenhagen, T., Nargeot, J., Wickman, K., Isbrandt, D. & Mangoni, M. E. 2014. Cardiac arrhythmia induced by genetic silencing of ‘funny’ (f) channels is rescued by GIRK4 inactivation. *Nature Communications,* 5**,** 4664.

Miller, E. W., Lin, J. Y., Frady, E. P., Steinbach, P. A., Kristan, W. B. & Tsien, R. Y. 2012. Optically monitoring voltage in neurons by photo-induced electron transfer through molecular wires. *Proc Natl Acad Sci U S A,* 109**,** 2114-9.

Miyagawa, S., Domae, K., Yoshikawa, Y., Fukushima, S., Nakamura, T., Saito, A., Sakata, Y., Hamada, S., Toda, K., Pak, K., Takeuchi, M. & Sawa, Y. 2017. Phase I Clinical Trial of Autologous Stem Cell-Sheet Transplantation Therapy for Treating Cardiomyopathy. *J Am Heart Assoc,* 6.

Miyagawa, S., Sawa, Y., Sakakida, S., Taketani, S., Kondoh, H., Memon, I. A., Imanishi, Y., Shimizu, T., Okano, T. & Matsuda, H. 2005. Tissue cardiomyoplasty using bioengineered contractile cardiomyocyte sheets to repair damaged myocardium: their integration with recipient myocardium. *Transplantation,* 80**,** 1586-95.

Monemian Esfahani, A., Rosenbohm, J., Reddy, K., Jin, X., Bouzid, T., Riehl, B., Kim, E., Lim, J. Y. & Yang, R. 2019. Tissue Regeneration from Mechanical Stretching of Cell-Cell Adhesion. *Tissue Eng Part C Methods,* 25**,** 631-640.

Moore, J. C., Tsang, S. Y., Rushing, S. N., Lin, D., Tse, H. F., Chan, C. W. & Li, R. A. 2008. Functional consequences of overexpressing the gap junction Cx43 in the cardiogenic potential of pluripotent human embryonic stem cells. *Biochem Biophys Res Commun,* 377**,** 46-51.

Morrissey, P. J., Murphy, K. R., Daley, J. M., Schofield, L., Turan, N. N., Arunachalam, K., Abbott, J. D. & Koren, G. 2017. A novel method of standardized myocardial infarction in aged rabbits. *Am J Physiol Heart Circ Physiol,* 312**,** H959-h967.

Mortensen, P. 2021. *Mathematical modelling of the electrical and*

mechanical properties of cardiac cells coupled with non-muscle cells. University of Glasgow.

Mummery Christine, L., Zhang, J., Ng Elizabeth, S., Elliott David, A., Elefanty Andrew, G. & Kamp Timothy, J. 2012. Differentiation of Human Embryonic Stem Cells and Induced Pluripotent Stem Cells to Cardiomyocytes. *Circulation Research,* 111**,** 344-358.

Munarin, F., Kant, R. J., Rupert, C. E., Khoo, A. & Coulombe, K. L. K. 2020. Engineered human myocardium with local release of angiogenic proteins improves vascularization and cardiac function in injured rat hearts. *Biomaterials,* 251**,** 120033.

Myles, R. C., Burton, F. L., Cobbe, S. M. & Smith, G. L. 2011. Alternans of action potential duration and amplitude in rabbits with left ventricular dysfunction following myocardial infarction. *J Mol Cell Cardiol,* 50**,** 510-21.

Nakai, J., Ohkura, M. & Imoto, K. 2001. A high signal-to-noise Ca2+ probe composed of a single green fluorescent protein. *Nature Biotechnology,* 19**,** 137-141.

Neely, J. R., Liebermeister, H., Battersby, E. J. & Morgan, H. E. 1967. Effect of pressure development on oxygen consumption by isolated rat heart. *Am J Physiol,* 212**,** 804-14.

Okano, T., Yamada, N., Sakai, H. & Sakurai, Y. 1993. A novel recovery system for cultured cells using plasma-treated polystyrene dishes grafted with poly(N-isopropylacrylamide). *J Biomed Mater Res,* 27**,** 1243-51.

Osteil, P., Tapponnier, Y., Markossian, S., Godet, M., Schmaltz-Panneau, B., Jouneau, L., Cabau, C., Joly, T., Blachère, T., Gócza, E., Bernat, A., Yerle, M., Acloque, H., Hidot, S., Bosze, Z., Duranthon, V., Savatier, P. & Afanassieff, M. 2013. Induced pluripotent stem cells derived from rabbits exhibit some characteristics of naïve pluripotency. *Biol Open,* 2**,** 613-28.

Page, R. L., Ambady, S., Holmes, W. F., Vilner, L., Kole, D., Kashpur, O., Huntress, V., Vojtic, I., Whitton, H. & Dominko, T. 2009. Induction of stem cell gene expression in adult human fibroblasts without transgenes. *Cloning Stem Cells,* 11**,** 417-26.

Pandey, P., Hawkes, W., Hu, J., Megone, W. V., Gautrot, J., Anilkumar, N., Zhang, M., Hirvonen, L., Cox, S., Ehler, E., Hone, J., Sheetz, M. & Iskratsch, T. 2018. Cardiomyocytes Sense Matrix Rigidity through a Combination of Muscle and Non-muscle Myosin Contractions. *Dev Cell,* 44**,** 326-336.e3.

Parikh, S. S., Blackwell, D. J., Gomez-Hurtado, N., Frisk, M., Wang, L., Kim, K., Dahl, C. P., Fiane, A., Tonnessen, T., Kryshtal, D. O., Louch, W. E. & Knollmann, B. C. 2017. Thyroid and Glucocorticoid Hormones Promote Functional T-Tubule Development in Human-Induced Pluripotent Stem Cell-Derived Cardiomyocytes. *Circ Res,* 121**,** 1323-1330.

Park, I. H., Zhao, R., West, J. A., Yabuuchi, A., Huo, H., Ince, T. A., Lerou, P. H., Lensch, M. W. & Daley, G. Q. 2008. Reprogramming of human somatic cells to pluripotency with defined factors. *Nature,* 451**,** 141-6.

Park, S. E., Yeon, G. B., Goo, H. G., Seo, D. S., Dayem, A. A., Lee, K. E., Park, H. M., Cho, S. G. & Kim, D. S. 2020. Maintenance and differentiation of human ES cells on polyvinylidene fluoride scaffolds immobilized with a vitronectin-derived peptide. *J Cell Physiol*.

Parvizi, M., Petersen, A. H., Van Spreuwel-Goossens, C., Kluijtmans, S. & Harmsen, M. C. 2018. Perivascular scaffolds loaded with adipose tissue-derived stromal cells attenuate development and progression of abdominal aortic aneurysm in rats. *J Biomed Mater Res A,* 106**,** 2494-2506.

Parvizi, M., Plantinga, J. A., Van Speuwel-Goossens, C. A., Van Dongen, E. M., Kluijtmans, S. G. & Harmsen, M. C. 2016. Development of recombinant collagen-peptide-based vehicles for delivery of adipose-derived stromal cells. *J Biomed Mater Res A,* 104**,** 503-16.

Pecha, S., Yorgan, K., Röhl, M., Geertz, B., Hansen, A., Weinberger, F., Sehner, S., Ehmke, H., Reichenspurner, H., Eschenhagen, T. & Schwoerer, A. P. 2019. Human iPS cell-derived engineered heart tissue does not affect ventricular arrhythmias in a guinea pig cryo-injury model. *Sci Rep,* 9**,** 9831.

Pekkanen-Mattila, M., Kerkelä, E., Tanskanen, J. M. A., Pietilä, M., Pelto-Huikko, M., Hyttinen, J., Skottman, H., Suuronen, R. & Aalto-Setälä, K. 2009. Substantial variation in the cardiac differentiation of human embryonic stem cell lines derived and propagated under the same conditions—a comparison of multiple cell lines. *Annals of Medicine,* 41**,** 360-370.

Pfeffer, M. A., Pfeffer, J. M., Fishbein, M. C., Fletcher, P. J., Spadaro, J., Kloner, R. A. & Braunwald, E. 1979. Myocardial infarct size and ventricular function in rats. *Circ Res,* 44**,** 503-12.

Phakdeedindan, P., Setthawong, P., Tiptanavattana, N., Rungarunlert, S., Ingrungruanglert, P., Israsena, N., Techakumphu, M. & Tharasanit, T. 2019. Rabbit induced pluripotent stem cells retain capability of in vitro cardiac differentiation. *Exp Anim,* 68**,** 35-47.

Pillekamp, F., Haustein, M., Khalil, M., Emmelheinz, M., Nazzal, R., Adelmann, R., Nguemo, F., Rubenchyk, O., Pfannkuche, K., Matzkies, M., Reppel, M., Bloch, W., Brockmeier, K. & Hescheler, J. 2012. Contractile properties of early human embryonic stem cell-derived cardiomyocytes: beta-adrenergic stimulation induces positive chronotropy and lusitropy but not inotropy. *Stem Cells Dev,* 21**,** 2111-21.

Pluijmert, N. J., Bart, C. I., Bax, W. H., Quax, P. H. A. & Atsma, D. E. 2020. Effects on cardiac function, remodeling and inflammation following myocardial ischemia-reperfusion injury or unreperfused myocardial infarction in hypercholesterolemic APOE*3-Leiden mice. *Sci Rep,* 10**,** 16601.

Pope, A. J., Sands, G. B., Smaill, B. H. & Legrice, I. J. 2008. Three-dimensional transmural organization of perimysial collagen in the heart. *Am J Physiol Heart Circ Physiol,* 295**,** H1243-H1252.

Prajapati, C., Ojala, M., Lappi, H., Aalto-Setälä, K. & Pekkanen-Mattila, M. 2021. Electrophysiological evaluation of human induced pluripotent stem cell-derived cardiomyocytes obtained by different methods. *Stem Cell Research,* 51**,** 102176.

Ramadan, S., Paul, N. & Naguib, H. E. 2017. Standardized static and dynamic evaluation of myocardial tissue properties. *Biomed Mater,* 12**,** 025013.

Ribeiro, A. J., Ang, Y. S., Fu, J. D., Rivas, R. N., Mohamed, T. M., Higgs, G. C., Srivastava, D. & Pruitt, B. L. 2015. Contractility of single cardiomyocytes differentiated from pluripotent stem cells depends on physiological shape and substrate stiffness. *Proc Natl Acad Sci U S A,* 112**,** 12705-10.

Ribeiro, M. C., Slaats, R. H., Schwach, V., Rivera-Arbelaez, J. M., Tertoolen, L. G. J., Van Meer, B. J., Molenaar, R., Mummery, C. L., Claessens, M. & Passier, R. 2020. A cardiomyocyte show of force: A fluorescent alpha-actinin reporter line sheds light on human cardiomyocyte contractility versus substrate stiffness. *J Mol Cell Cardiol,* 141**,** 54-64.

Rice, J. J., Wang, F., Bers, D. M. & De Tombe, P. P. 2008. Approximate model of cooperative activation and crossbridge cycling in cardiac muscle using ordinary differential equations. *Biophys J,* 95**,** 2368-90.

Richardson, W. J., Clarke, S. A., Quinn, T. A. & Holmes, J. W. 2015. Physiological Implications of Myocardial Scar Structure. *Compr Physiol,* 5**,** 1877-909.

Rodriguez, Anthony g., Han, Sangyoon j., Regnier, M. & Sniadecki, Nathan j. 2011. Substrate Stiffness Increases Twitch Power of Neonatal Cardiomyocytes in Correlation with Changes in Myofibril Structure and Intracellular Calcium. *Biophysical Journal,* 101**,** 2455-2464.

Rojas, S. V., Kensah, G., Rotaermel, A., Baraki, H., Kutschka, I., Zweigerdt, R., Martin, U., Haverich, A., Gruh, I. & Martens, A. 2017. Transplantation of purified iPSC-derived cardiomyocytes in myocardial infarction. *PLOS ONE,* 12**,** e0173222.

Ronaldson-Bouchard, K., Ma, S. P., Yeager, K., Chen, T., Song, L., Sirabella, D., Morikawa, K., Teles, D., Yazawa, M. & Vunjak-Novakovic, G. 2018. Advanced maturation of human cardiac tissue grown from pluripotent stem cells. *Nature,* 556**,** 239-243.

Ronaldson-Bouchard, K., Yeager, K., Teles, D., Chen, T., Ma, S., Song, L., Morikawa, K., Wobma, H. M., Vasciaveo, A., Ruiz, E. C., Yazawa, M. & Vunjak-Novakovic, G. 2019. Engineering of human cardiac muscle electromechanically matured to an adult-like phenotype. *Nat Protoc,* 14**,** 2781-2817.

Sala, L., Van Meer, B. J., Tertoolen, L. G. J., Bakkers, J., Bellin, M., Davis, R. P., Denning, C., Dieben, M. A. E., Eschenhagen, T., Giacomelli, E., Grandela, C., Hansen, A., Holman, E. R., Jongbloed, M. R. M., Kamel, S. M., Koopman, C. D., Lachaud, Q., Mannhardt, I., Mol, M. P. H., Mosqueira, D., Orlova, V. V., Passier, R., Ribeiro, M. C., Saleem, U., Smith, G. L., Burton, F. L. & Mummery, C. L. 2018. MUSCLEMOTION: A Versatile Open Software Tool to Quantify Cardiomyocyte and Cardiac Muscle Contraction In Vitro and In Vivo. *Circ Res,* 122**,** e5-e16.

Salameh, A. & Dhein, S. 2013. Effects of mechanical forces and stretch on intercellular gap junction coupling. *Biochim Biophys Acta,* 1828**,** 147-56.

Saldin, L. T., Cramer, M. C., Velankar, S. S., White, L. J. & Badylak, S. F. 2017. Extracellular matrix hydrogels from decellularized tissues: Structure and function. *Acta Biomater,* 49**,** 1-15.

Saleem, U., Van Meer, B. J., Katili, P. A., Mohd Yusof, N. A. N., Mannhardt, I., Garcia, A. K., Tertoolen, L., De Korte, T., Vlaming, M. L. H., Mcglynn, K., Nebel, J., Bahinski, A., Harris, K., Rossman, E., Xu, X., Burton, F. L., Smith, G. L., Clements, P., Mummery, C. L., Eschenhagen, T., Hansen, A. & Denning, C. 2020. Blinded, Multicenter Evaluation of Drug-induced Changes in Contractility Using Human-induced Pluripotent Stem Cell-derived Cardiomyocytes. *Toxicol Sci,* 176**,** 103-123.

Salerno, S., Garten, K., Smith, G. L., Stølen, T. & Kelly, A. 2020. Two-photon excitation of FluoVolt allows improved interrogation of transmural electrophysiological function in the intact mouse heart. *Prog Biophys Mol Biol,* 154**,** 11-20.

Samarel, A. M. 2005. Costameres, focal adhesions, and cardiomyocyte mechanotransduction. *Am J Physiol Heart Circ Physiol,* 289**,** H2291-301.

Santoro, R., Perrucci, G. L., Gowran, A. & Pompilio, G. 2019. Unchain My Heart: Integrins at the Basis of iPSC Cardiomyocyte Differentiation. *Stem Cells Int,* 2019**,** 8203950.

Saucerman, J. J., Tan, P. M., Buchholz, K. S., Mcculloch, A. D. & Omens, J. H. 2019. Mechanical regulation of gene expression in cardiac myocytes and fibroblasts. *Nat Rev Cardiol,* 16**,** 361-378.

Scientific, T. *FluoVolt ™ Membrane Potential Kit Description.* [Online]. https://www.thermofisher.com/order/catalog/product/F10488#/F10488. Available: https://www.thermofisher.com/order/catalog/product/F10488#/F10488.

Scuderi, G. J. & Butcher, J. 2017. Naturally Engineered Maturation of Cardiomyocytes. *Front Cell Dev Biol,* 5**,** 50.

Sengupta, S., Rothenberg, K. E., Li, H., Hoffman, B. D. & Bursac, N. 2019. Altering integrin engagement regulates membrane localization of Kir2.1 channels. *J Cell Sci,* 132.

Senyo, S. E., Steinhauser, M. L., Pizzimenti, C. L., Yang, V. K., Cai, L., Wang, M., Wu, T.-D., Guerquin-Kern, J.-L., Lechene, C. P. & Lee, R. T. 2013. Mammalian heart renewal by pre-existing cardiomyocytes. *Nature,* 493**,** 433-436.

Sewanan, L. R., Schwan, J., Kluger, J., Park, J., Jacoby, D. L., Qyang, Y. & Campbell, S. G. 2019. Extracellular Matrix From Hypertrophic Myocardium Provokes Impaired Twitch Dynamics in Healthy Cardiomyocytes. *JACC Basic Transl Sci,* 4**,** 495-505.

Shannon, T. R., Wang, F., Puglisi, J., Weber, C. & Bers, D. M. 2004. A mathematical treatment of integrated Ca dynamics within the ventricular myocyte. *Biophys J,* 87**,** 3351-71.

Shiba, Y. 2020. Pluripotent Stem Cells for Cardiac Regeneration - Current Status, Challenges, and Future Perspectives. *Circ J,* 84**,** 2129-2135.

Shiba, Y., Fernandes, S., Zhu, W. Z., Filice, D., Muskheli, V., Kim, J., Palpant, N. J., Gantz, J., Moyes, K. W., Reinecke, H., Van Biber, B., Dardas, T., Mignone, J. L., Izawa, A., Hanna, R., Viswanathan, M., Gold, J. D., Kotlikoff, M. I., Sarvazyan, N., Kay, M. W., Murry, C. E. & Laflamme, M. A. 2012. Human ES-cell-derived cardiomyocytes electrically couple and suppress arrhythmias in injured hearts. *Nature,* 489**,** 322-5.

Shiba, Y., Filice, D., Fernandes, S., Minami, E., Dupras, S. K., Biber, B. V., Trinh, P., Hirota, Y., Gold, J. D., Viswanathan, M. & Laflamme, M. A. 2014. Electrical Integration of Human Embryonic Stem Cell-Derived Cardiomyocytes in a Guinea Pig Chronic Infarct Model. *J Cardiovasc Pharmacol Ther,* 19**,** 368-381.

Shiba, Y., Gomibuchi, T., Seto, T., Wada, Y., Ichimura, H., Tanaka, Y., Ogasawara, T., Okada, K., Shiba, N., Sakamoto, K., Ido, D., Shiina, T., Ohkura, M., Nakai, J., Uno, N., Kazuki, Y., Oshimura, M., Minami, I. & Ikeda, U. 2016. Allogeneic transplantation of iPS cell-derived cardiomyocytes regenerates primate hearts. *Nature,* 538**,** 388-391.

Shimizu, T., Yamato, M., Akutsu, T., Shibata, T., Isoi, Y., Kikuchi, A., Umezu, M. & Okano, T. 2002a. Electrically communicating three-dimensional cardiac tissue mimic fabricated by layered cultured cardiomyocyte sheets. *J Biomed Mater Res,* 60**,** 110-7.

Shimizu, T., Yamato, M., Isoi, Y., Akutsu, T., Setomaru, T., Abe, K., Kikuchi, A., Umezu, M. & Okano, T. 2002b. Fabrication of pulsatile cardiac tissue grafts using a novel 3-dimensional cell sheet manipulation technique and temperature-responsive cell culture surfaces. *Circ Res,* 90**,** e40.

Shinde, A. V., Humeres, C. & Frangogiannis, N. G. 2017. The role of α-smooth muscle actin in fibroblast-mediated matrix contraction and remodeling. *Biochim Biophys Acta Mol Basis Dis,* 1863**,** 298-309.

Siller, R. & Sullivan, G. J. 2017. Rapid Screening of the Endodermal Differentiation Potential of Human Pluripotent Stem Cells. *Curr Protoc Stem Cell Biol,* 43**,** 1G.7.1-1G.7.23.

Swift, L. M., Jaimes, R., 3rd, Mccullough, D., Burke, M., Reilly, M., Maeda, T., Zhang, H., Ishibashi, N., Rogers, J. M. & Posnack, N. G. 2019. Optocardiography and Electrophysiology Studies of Ex Vivo Langendorff-perfused Hearts. *J Vis Exp*.

Synnergren, J., Giesler, T. L., Adak, S., Tandon, R., Noaksson, K., Lindahl, A., Nilsson, P., Nelson, D., Olsson, B., Englund, M. C., Abbot, S. & Sartipy, P. 2007. Differentiating human embryonic stem cells express a unique housekeeping gene signature. *Stem Cells,* 25**,** 473-80.

Tachibana, A., Santoso, M. R., Mahmoudi, M., Shukla, P., Wang, L., Bennett, M., Goldstone, A. B., Wang, M., Fukushi, M., Ebert, A. D., Woo, Y. J., Rulifson, E. & Yang, P. C. 2017. Paracrine Effects of the Pluripotent Stem Cell-Derived Cardiac Myocytes Salvage the Injured Myocardium. *Circ Res,* 121**,** e22-e36.

Tada, M., Takeuchi, A., Hashizume, M., Kitamura, K. & Kano, M. 2014. A highly sensitive fluorescent indicator dye for calcium imaging of neural activity in vitro and in vivo. *Eur J Neurosci,* 39**,** 1720-8.

Takahashi, K., Tanabe, K., Ohnuki, M., Narita, M., Ichisaka, T., Tomoda, K. & Yamanaka, S. 2007. Induction of pluripotent stem cells from adult human fibroblasts by defined factors. *Cell,* 131**,** 861-72.

Takahashi, K. & Yamanaka, S. 2006. Induction of pluripotent stem cells from mouse embryonic and adult fibroblast cultures by defined factors. *Cell,* 126**,** 663-76.

Thomson, J. A., Itskovitz-Eldor, J., Shapiro, S. S., Waknitz, M. A., Swiergiel, J. J., Marshall, V. S. & Jones, J. M. 1998. Embryonic stem cell lines derived from human blastocysts. *Science,* 282**,** 1145-7.

Thygesen, K., Alpert, J. S., Jaffe, A. S., Simoons, M. L., Chaitman, B. R., White, H. D., Katus, H. A., Apple, F. S., Lindahl, B., Morrow, D. A., Clemmensen, P. M., Johanson, P., Hod, H., Underwood, R., Bax, J. J., Bonow, J. J., Pinto, F., Gibbons, R. J., Fox, K. A., Atar, D., Newby, L. K., Galvani, M., Hamm, C. W., Uretsky, B. F., Steg, P. G., Wijns, W., Bassand, J. P., Menasche, P., Ravkilde, J., Ohman, E. M., Antman, E. M., Wallentin, L. C., Armstrong, P. W., Januzzi, J. L., Nieminen, M. S., Gheorghiade, M., Filippatos, G., Luepker, R. V., Fortmann, S. P., Rosamond, W. D., Levy, D., Wood, D., Smith, S. C., Hu, D., Lopez-Sendon, J. L., Robertson, R. M., Weaver, D., Tendera, M., Bove, A. A., Parkhomenko, A. N., Vasilieva, E. J., Mendis, S., Baumgartner, H., Ceconi, C., Dean, V., Deaton, C., Fagard, R., Funck-Brentano, C., Hasdai, D., Hoes, A., Kirchhof, P., Knuuti, J., Kolh, P., Mcdonagh, T., Moulin, C., Popescu, B. A., Reiner, Z., Sechtem, U., Sirnes, P. A., Torbicki, A., Vahanian, A., Windecker, S., Morais, J., Aguiar, C., Almahmeed, W., Arnar, D. O., Barili, F., Bloch, K. D., Bolger, A. F., Botker, H. E., Bozkurt, B., Bugiardini, R., Cannon, C., De Lemos, J., Eberli, F. R., Escobar, E., Hlatky, M., James, S., Kern, K. B., Moliterno, D. J., Mueller, C., Neskovic, A. N., Pieske, B. M., Schulman, S. P., Storey, R. F., Taubert, K. A., Vranckx, P., Wagner, D. R., Infarction, J. E. A. A. W. T. F. F. U. D. O. M., Chairpersons, A. T. F. M., et al. 2012. Third universal definition of myocardial infarction. *J Am Coll Cardiol,* 60**,** 1581-98.

Timmermann, V., Edwards, A. G., Wall, S. T., Sundnes, J. & Mcculloch, A. D. 2019. Arrhythmogenic Current Generation by Myofilament-Triggered Ca(2+) Release and Sarcomere Heterogeneity. *Biophys J,* 117**,** 2471-2485.

Tischbirek, C. H., Birkner, A. & Konnerth, A. 2017. In vivo deep two-photon imaging of neural circuits with the fluorescent Ca(2+) indicator Cal-590. *J Physiol,* 595**,** 3097-3105.

Tohyama, S., Hattori, F., Sano, M., Hishiki, T., Nagahata, Y., Matsuura, T., Hashimoto, H., Suzuki, T., Yamashita, H., Satoh, Y., Egashira, T., Seki, T., Muraoka, N., Yamakawa, H., Ohgino, Y., Tanaka, T., Yoichi, M., Yuasa, S., Murata, M., Suematsu, M. & Fukuda, K. 2013. Distinct metabolic flow enables large-scale purification of mouse and human pluripotent stem cell-derived cardiomyocytes. *Cell Stem Cell,* 12**,** 127-37.

Travers, J. G., Kamal, F. A., Robbins, J., Yutzey, K. E. & Blaxall, B. C. 2016. Cardiac Fibrosis: The Fibroblast Awakens. *Circ Res,* 118**,** 1021-40.

Tsuruyama, S., Matsuura, K., Sakaguchi, K. & Shimizu, T. 2019. Pulsatile tubular cardiac tissues fabricated by wrapping human iPS cells-derived cardiomyocyte sheets. *Regenerative Therapy,* 11**,** 297-305.

Tully, A. & Bishop, M. A. 2021. Coronary Artery Surgery. *StatPearls.* Treasure Island (FL): StatPearls Publishing

Copyright © 2021, StatPearls Publishing LLC.

Tytgat, L., Markovic, M., Qazi, T. H., Vagenende, M., Bray, F., Martins, J. C., Rolando, C., Thienpont, H., Ottevaere, H., Ovsianikov, A., Dubruel, P. & Van Vlierberghe, S. 2019. Photo-crosslinkable recombinant collagen mimics for tissue engineering applications. *J Mater Chem B,* 7**,** 3100-3108.

Ulmer, B. M., Stoehr, A., Schulze, M. L., Patel, S., Gucek, M., Mannhardt, I., Funcke, S., Murphy, E., Eschenhagen, T. & Hansen, A. 2018. Contractile Work Contributes to Maturation of Energy Metabolism in hiPSC-Derived Cardiomyocytes. *Stem Cell Reports,* 10**,** 834-847.

Van Deel, E. D., Najafi, A., Fontoura, D., Valent, E., Goebel, M., Kardux, K., Falcao-Pires, I. & Van Der Velden, J. 2017. In vitro model to study the effects of matrix stiffening on Ca(2+) handling and myofilament function in isolated adult rat cardiomyocytes. *J Physiol,* 595**,** 4597-4610.

Vermij, S. H., Abriel, H. & Van Veen, T. A. B. 2017. Refining the molecular organization of the cardiac intercalated disc. *Cardiovascular Research,* 113**,** 259-275.

Walker, N. L., Burton, F. L., Kettlewell, S., Smith, G. L. & Cobbe, S. M. 2007. Mapping of Epicardial Activation in a Rabbit Model of Chronic Myocardial Infarction. *Journal of Cardiovascular Electrophysiology,* 18**,** 862-868.

Wang, L., Morotti, S., Tapa, S., Francis Stuart, S. D., Jiang, Y., Wang, Z., Myles, R. C., Brack, K. E., Ng, G. A., Bers, D. M., Grandi, E. & Ripplinger, C. M. 2019. Different paths, same destination: divergent action potential responses produce conserved cardiac fight-or-flight response in mouse and rabbit hearts. *J Physiol,* 597**,** 3867-3883.

Ward, M. & Iskratsch, T. 2020. Mix and (mis-)match - The mechanosensing machinery in the changing environment of the developing, healthy adult and diseased heart. *Biochim Biophys Acta Mol Cell Res,* 1867**,** 118436.

Weinberger, F., Breckwoldt, K., Pecha, S., Kelly, A., Geertz, B., Starbatty, J., Yorgan, T., Cheng, K. H., Lessmann, K., Stolen, T., Scherrer-Crosbie, M., Smith, G., Reichenspurner, H., Hansen, A. &

Eschenhagen, T. 2016. Cardiac repair in guinea pigs with human engineered heart tissue from induced pluripotent stem cells. *Sci Transl Med,* 8**,** 363ra148.

Weinberger, F. & Eschenhagen, T. 2020. Heart regeneration: from mouse to human. *Current Opinion in Physiology,* 14**,** 7-12.

Weinberger, F., Mannhardt, I. & Eschenhagen, T. 2017. Engineering Cardiac Muscle Tissue: A Maturating Field of Research. *Circ Res,* 120**,** 1487-1500.

Wickline, E. D., Dale, I. W., Merkel, C. D., Heier, J. A., Stolz, D. B. & Kwiatkowski, A. V. 2016. alphaT-Catenin Is a Constitutive Actin-binding alpha-Catenin That Directly Couples the Cadherin.Catenin Complex to Actin Filaments. *J Biol Chem,* 291**,** 15687-99.

Williams, C., Quinn, K. P., Georgakoudi, I. & Black, L. D. 2014. Young developmental age cardiac extracellular matrix promotes the expansion of neonatal cardiomyocytes in vitro. *Acta Biomater,* 10**,** 194-204.

Yamada, N., Okano, T., Sakai, H., Karikusa, F., Sawasaki, Y. & Sakurai, Y. 1990. Thermo-responsive polymeric surfaces; control of attachment and detachment of cultured cells. *Die Makromolekulare Chemie, Rapid Communications,* 11**,** 571-576.

Yang, X., Pabon, L. & Murry, C. E. 2014. Engineering adolescence: maturation of human pluripotent stem cell-derived cardiomyocytes. *Circ Res,* 114**,** 511-23.

Yeung, E., Fukunishi, T., Bai, Y., Bedja, D., Pitaktong, I., Mattson, G., Jeyaram, A., Lui, C., Ong, C. S., Inoue, T., Matsushita, H., Abdollahi, S., Jay, S. M. & Hibino, N. 2019. Cardiac regeneration using human-induced pluripotent stem cell-derived biomaterial-free 3D-bioprinted cardiac patch in vivo. *J Tissue Eng Regen Med,* 13**,** 2031-2039.

Yonemura, S., Wada, Y., Watanabe, T., Nagafuchi, A. & Shibata, M. 2010. α-Catenin as a tension transducer that induces adherens junction development. *Nature Cell Biology,* 12**,** 533-542.

Yue, K., Trujillo-De Santiago, G., Alvarez, M. M., Tamayol, A., Annabi, N. & Khademhosseini, A. 2015. Synthesis, properties, and biomedical applications of gelatin methacryloyl (GelMA) hydrogels. *Biomaterials,* 73**,** 254-71.

Zeng, D., Ou, D.-B., Wei, T., Ding, L., Liu, X.-T., Hu, X.-L., Li, X. & Zheng, Q.-S. 2013. Collagen/β(1) integrin interaction is required for embryoid body formation during cardiogenesis from murine induced pluripotent stem cells. *BMC cell biology,* 14**,** 5-5.

Zentilin, L., Puligadda, U., Lionetti, V., Zacchigna, S., Collesi, C., Pattarini, L., Ruozi, G., Camporesi, S., Sinagra, G., Pepe, M., Recchia, F. A. & Giacca, M. 2010. Cardiomyocyte VEGFR-1 activation by VEGF-B induces compensatory hypertrophy and preserves cardiac function after myocardial infarction. *Faseb j,* 24**,** 1467-78.

Zhao, C., Tian, S., Liu, Q., Xiu, K., Lei, I., Wang, Z. & Ma, P. X. 2020. Biodegradable nanofibrous temperature-responsive gelling microspheres for heart regeneration. *Adv Funct Mater,* 30.

Zhao, M., Fan, C., Ernst, P. J., Tang, Y., Zhu, H., Mattapally, S., Oduk, Y., Borovjagin, A. V., Zhou, L., Zhang, J. & Zhu, W. 2019. Y-27632 preconditioning enhances transplantation of human-induced pluripotent stem cell-derived cardiomyocytes in myocardial infarction mice. *Cardiovasc Res,* 115**,** 343-356.

Zhao Q, G. H., Yi G, Liao J, Diwu Z,. A novel red fluorescence calcium indicator for functional analysis of GPCRs and calcium targets. 2015. Biophys J, 109a-110a.

Zhao, X., Chen, H., Xiao, D., Yang, H., Itzhaki, I., Qin, X., Chour, T., Aguirre, A., Lehmann, K., Kim, Y., Shukla, P., Holmström, A., Zhang, J. Z., Zhuge, Y., Ndoye, B. C., Zhao, M., Neofytou, E., Zimmermann, W. H., Jain, M. & Wu, J. C. 2018. Comparison of Non-human Primate versus Human Induced Pluripotent Stem Cell-Derived Cardiomyocytes for Treatment of Myocardial Infarction. *Stem Cell Reports,* 10**,** 422-435.

Zhu, K., Wu, Q., Ni, C., Zhang, P., Zhong, Z., Wu, Y., Wang, Y., Xu, Y., Kong, M., Cheng, H., Tao, Z., Yang, Q., Liang, H., Jiang, Y., Li, Q., Zhao, J., Huang, J., Zhang, F., Chen, Q., Li, Y., Chen, J., Zhu, W., Yu, H., Zhang, J., Yang, H. T., Hu, X. & Wang, J. 2018. Lack of Remuscularization Following Transplantation of Human Embryonic Stem Cell-Derived Cardiovascular Progenitor Cells in Infarcted Nonhuman Primates. *Circ Res,* 122**,** 958-969.

Zimmerman, A. N. E., Daems, W., Hülsmann, W. C., Snijder, J., Wisse, E. & Durrer, D. 1967. Morphological Changes of Heart Muscle Caused by Successive Perfusion with Calcium-free and Calcium-containing Solutions (Calcium Paradox). *Cardiovascular Research,* 1**,** 201-209.

Zimmermann, W. H. 2017. Remuscularization of the failing heart. *J Physiol,* 595**,** 3685-3690.

Ziv, O., Schofield, L., Lau, E., Chaves, L., Patel, D., Jeng, P., Peng, X., Choi, B. R. & Koren, G. 2012. A novel, minimally invasive, segmental myocardial infarction with a clear healed infarct borderzone in rabbits. *Am J Physiol Heart Circ Physiol,* 302**,** H2321-30.